Vegetation/Forest Effects in Microwave Remote Sensing of Soil Moisture

by

Huanting Huang

A dissertation submitted in partial fulfillment
of the requirements for the degree of
Doctor of Philosophy
(Electrical Engineering)
in the University of Michigan
2019

Doctoral Committee:

Professor Leung Tsang, Chair
Professor Christopher Ruf
Professor Kamal Sarabandi
Professor Fawwaz Ulaby

Huanting Huang

huanght@umich.edu

ORCID iD: 0000-0002-3986-5920

To my family,
With love and gratitude.

ACKNOWLEDGEMENTS

First and foremost, I would like to express my very great appreciation to my advisor, Professor Leung Tsang. He inspired me by his hardworking, immense knowledge and enthusiasm for research and innovation. He is always energetic and one of the smartest people I know. He taught me how to deal with problems, derive from the first physical principle, correlate different research topics and come up with new ideas. He trained me in making slides, giving presentations, writing papers, technical reports, ect. I am grateful for his great guidance, enthusiastic encouragement and contributions of time, ideas, and funding throughout my PhD research study.

I would like to offer my special thanks to Professor Christopher Ruf, Professor Kamal Sarabandi and Professor Fawwaz Ulaby for serving as my dissertation committee members, asking insightful questions, giving constructive comments and offering invaluable advice.

I would like to thank the instructors of the courses I took in both University of Michigan, Ann Arbor and University of Washington, Seattle. These courses helped my research as well as broadening my views beyond my research area.

My sincere thanks also go to my collaborators in other institutions. For example, my collaborators at NASA Jet Propulsion Laboratory (JPL) provided me insightful thoughts and invaluable comments during our discussions, assisted me with ground data analysis, and gave me unwavering support and encouragement. My collaborators at US Department of Agriculture (USDA) taught me how to conduct ground measurements so that I had a better understanding of the data. I was lucky enough to have a chance to collaborate with them.

I would also like to thank my friends and fellow labmates, for the stimulating discussions, wholehearted support and encouragement, positive attitude, respect, kindness, comfortable workplace, friendly working atmosphere, collaborations on projects and for all the fun we had.

Last but not least, I would like to express my sincere gratitude to my family, my parents, my grandparents and my boyfriend, for their unconditional love and support. They cheered me up whenever I was down. They were patient with me. They were always the strongest support behind me in all my pursuits.

Huanting Huang

University of Michigan, Ann Arbor

August 2019

TABLE OF CONTENTS

LIST OF TABLES

LIST OF FIGURES

ABSTRACT

This thesis includes (1) the distorted Born approximation (DBA) and an improved coherent model for vegetation-covered surfaces at L-band for data-cube based soil moisture retrieval; (2) a unified approach for combined active and passive remote sensing of vegetation-covered surfaces with the same input physical parameters; (3) Numerical Maxwell Model in 3D (NMM3D) simulations of a vegetation canopy comprising randomly distributed dielectric cylinders; and (4) a hybrid method based on the generalized T matrix of single objects and Foldy-Lax equations for NMM3D full-wave simulations of the realistic vegetation/forest with vector spherical, spheroidal and cylindrical wave expansoins.

The main contributions and novelty of this thesis are NMM3D full-wave simulations of vegetation/forest canopy using the generalized T matrix of the single object and Foldy-Lax equations of multiple scattering among many objects. Before this work, the large-scale full-wave simulations of vegetation/forst such as many tree trunks were deemed very difficult. The NMM3D full-wave simulation results showed that the results of past models significantly overestimate attenuation in a vegetation/forest canopy. The NMM3D full-wave models predict transmissions that are several times greater than that of past models. A much greater microwave transmission means the microwave can better penetrate a vegetation/forest canopy and thus it can be used to retrieve soil moisture.

The thesis starts with the DBA to compute the backscattering coefficients for various kinds of vegetation-covered surfaces such as pasture, wheat and canola fields. For the soybean fields, an improved coherent branching model is used by taking into account the correlated scattering among scatterers. The novel feature of the analytic coherent model consists of conditional probability functions to eliminate the overlapping effects of branches in the former branching models. In order to make use of complex physical models for real time retrieval for satellite missions, the outputs of the physical model are provided as lookup-tables (with three axes; therefore, called data cube). The three axes are: vegetation water content (VWC), root mean square (RMS) height of the rough soil surface and soil permittivity which is directly related to the soil moisture, each of which covering the full range of natural conditions. By inverting the data cubes, time-series retrieval of soil moisture is performed. Next, the DBA is extended to calculate the bistatic scattering coefficients. Emissivities are calculated by integrating the bistatic scattering coefficients over the hemispherical solid angle. The backscattering coefficients and emissivities calculated using this approach form a consistent model for combined active and passive microwave remote sensing. This has the advantage that the active and passive models are founded on the same theoretical basis and hence allow the use of the same physical parameters. In comparison, current approaches generally use different models and different parameters for active and passive with the tau-omega model most frequently used as the passive model with empirical input parameters. The modeled backscattering coefficients, brightness temperatures and soil moisture retrieval results are validated with the measurements from the Soil Moisture Active Passive Validation Experiment 2012 (SMAPVEX12).

In the analytical physical models mentioned above, as well as in another commonly used approach of the radiative transfer equation (RTE), the attenuation of the wave is accounted for by

the attenuation rate per unit distance κ_e, which originates from the concept of an "effective medium". Such a model is unsuitable for a vegetation canopy. κ_e is calculated using $\kappa_e = n_0(\sigma_a + \sigma_s)$, where n_0 is the number density of scatterers, and σ_a and σ_s are the scattering cross section and the absorption cross section of a single scatterer, respectively. In calculating the scattering cross section, the scatterers are assumed to be illuminated uniformly which is not valid due to the influence of other scatterers. Moreover, RTE/DBA does not account for gaps and gives the same results independent of the existence of gaps. Because of these issues, NMM3D full-wave simulations of vegetation are pursued. At first, the scattering of a vegetation canopy consisting of cylindrical scatterers is calculated. The approach for solving Maxwell's equations is based on the Foldy-Lax multiple scattering equations (FL) combined with the body of revolution (BOR). For a layer of extended-cylinders distributed in clusters, the NMM3D simulations at C-band show very different results from DBA/RTE, with NMM3D giving a much larger transmission coefficient (i.e much smaller optical thickness τ). The quantity τ has been used in active and passive microwave remote sensing. For example, the radar sensitivity to soil moisture of vegetation-covered surfaces depends strongly on the value of τ of the vegetation canopy. The method FL-BOR is limited for rotationally symmetric objects such as cylinders and circular disks. Realistic vegetation/forests, that are what we see with our eyes (unlike the models generated using Lindenmayer Systems), consist of arbitrarily-shaped scatterers. To perform NMM3D full-wave simulations for realistic vegetation/forests, a hybrid method is used, which is a hybrid of the off-the-shelf techniques (e.g. HFSS) and newly developed techniques. The newly developed techniques are the three key steps of the hybrid method: (1) extracting the generalized T matrix of each single object using vector spheroidal/cylindrical waves, (2) vector spheroidal/cylindrical wave transformations, and (3) solving FL for all the objects. The hybrid method is much more efficient than the HFSS brute force

(FEM) and MoM methods for vegetation scattering and applicable to a wide range of conditions including full-wave simulations of trees.

CHAPTER I

Introduction

The focus of my research is physical modelling of microwave interactions with vegetation and forest cover for applications in microwave remote sensing of soil moisture. The research is aimed at the use of satellite remote sensing of Earth for the monitoring of soil moisture, which is important for the global climate change, the water cycle and the carbon cycle [1]. In recent years, many satellites have been launched by NASA, the European Space Agency, China, as well as other countries in North America, Europe, Asia and South America. There have been major advancements in instruments such as radiometers, radars, SAR (Synthetic Aperture Radar), InSAR (Interferometric SAR) and the recent usage of signals of opportunity such as GNSS-R (Global Navigation Satellite System Reflectometry) [2]. The mapping of soil moisture is important for hydrologic modelling, climate prediction, and flood and drought monitoring [3]. Soil moisture acts as a storage of water between rainfall and evaporation and influences the infiltration and runoff prediction in hydrologic processes [3]. Much of the soil is covered by vegetation/forest, and it is in these arable regions and croplands where measuring soil moisture is particularly useful for agriculture and environmental monitoring. Thus, understanding the effects of vegetation/forests on microwave transmission/emission is important for remote sensing of soil moisture. Vegetation/forest is characterized as random media [4]. The electromagnetic modelling of microwave interaction with random media is important to these satellite missions in the following three aspects. Firstly, in the mission design stage, the modelling provides the theoretical basis to

predict the microwave signals and builds foundations for mission design such as the choice of microwave frequencies, incident angles and polarizations to be used for maximal sensitivity. Secondly, in the mission calibration/validation stage, airborne and ground measurements are performed, and the modelling interprets the microwave measurements and provides calibration and validation for the data. Finally, after the satellite is launched, electromagnetic modelling provides the basis for the application of physically based retrieval algorithms of parameters such as soil moisture, snow water equivalent, biomass, forests height etc.

In the first two years of my PhD research, I used a method that combines DBA for a vegetation canopy with NMM3D full-wave simulations for soil surfaces to compute the backscattering coefficient for various kinds of vegetation-covered surfaces such as pasture, wheat and canola fields. For the soybean fields, an improved coherent branching model is developed by taking into account the correlated scattering among scatterers [5]. This provides the physical model for the Soil Moisture Active Passive (SMAP) baseline radar algorithm [3]. In order to make use of the complex physical models for real-time retrieval for satellite missions, the outputs of the physical models are provided as lookup-tables (with three axes; therefore, called data cube) [6]. By inverting the data cubes, time-series retrievals of soil moisture, vegetation biomass and RMS soil roughness are performed. The data cubes, together with the retrieval algorithm, have been validated with extensive field campaigns. SMAP was launched in Jan 2015 [3]. The baseline algorithm has been applied to provide global soil moisture maps using the SMAP radar data over the entire observation period [7].

Combined active and passive microwave remote sensing of soil moisture is of great interest and importance, given the increasing number of active and passive satellite microwave missions and datasets available for studies in land hydrology and ecology [1]. Complementary information

contained in active and passive multi-frequency and multi-polarization measurements can be used to retrieve detailed soil and vegetation characteristics. However, the commonly used passive and active models are quite different, requiring different sets of parameters for the same vegetatation-covered surface scenes. Passive microwave models used in satellite retrieval algorithms (including the SMAP mission) are mostly based on the omega-tau model [8], which is a zeroth-order radiative transfer solution. Roughness effects in the omega-tau model are based on the h-Q formulation. For active remote sensing, such as for the SMAP "data-cube" retrieval [6], a first-order radiative transfer model is used, which is inconsistent with the passive model. Empirical parameters are used for the passive model while physical parameters are used for the active model. Because of these issues, consistent active and passive microwave remote sensing models were used to enable a truly synergistic retrieval approach that makes full use of information in the passive and active signatures [9]. The active model (DBA for a vegetation canopy and the NMM3D full-wave simulations for soil surfaces designed to compute the backscattering coefficients) was extended to calculate the bistatic scattering coefficients. Emissivities are calculated by integrating the bistatic scattering coefficients over the hemispherical solid angle. The backscattering coefficients and emissivities calculated using this approach form a consistent pair for combined active and passive microwave remote sensing. This has the advantage that the active and passive models are founded on the same theoretical basis and hence allow the use of the same physical parameters. The modeled backscattering coefficients (active measurements), brightness temperatures (passive measurements) and soil moisture retrieval results are validated using the measurements from the Soil Moisture Active Passive Validation Experiment 2012 (SMAPVEX12) [10].

Understanding how vegetation/forests interact with microwaves is important for remote sensing of soil moisture. Of particular importance is the attenuation properties of the vegetation

canopy. For three decades, the two most commonly used models have been the radiative transfer equation (RTE) [4] and DBA [11]. There are two key assumptions associated with the past RTE/DBA models: (1) the positions of the scatterers are assumed to be statistically homogeneous in 3D and (2) each scatterer is uniformly illuminated. However, these two assumptions are invalid for most types of vegetation/forests. For example, trees have trunks, branches and leaves in a correlated structure and there are gaps among branches and different trees. In my most recent research, innovative methods were developed for Numerical Maxwell Model in 3D (NMM3D) simulations of vegetation/forest. At first, the Foldy-Lax equations were combined with the Z matrix from the Body of Revolution (BOR) [12] (FL-BOR) for NMM3D full-wave simulations of grass canopy modeled by dielectric cylinders [13]. The NMM3D results show much greater transmission and smaller optical thickenss τ than the values predicted by RTE/DBA at C-band. However, this method of FL-BOR is limited to multiple scattering of objects with rotational symmetry such as cylinders. Moreover, this method is difficult to extend to cylinders with large radii compared with the wavelength, such as the case for trees at L-band. Because of these limits, an innovative hybrid method is developed for calculating the scattering from areas of vegetation/forests. With the use of the hybrid method, NMM3D simulations can be performed for realistic plants such as stalks with complicated branches, in addition to cylinders and disks. To perform NMM3D full-wave simulations efficiently for vegetation/forests, the hybrid method combines:

(i) Off-the-shelf technique for single objects. Off-the-shelf technique such as HFSS, BOR[12], ICA [4], and FEKO can solve Maxwell's equations for a complicated single object such as long cylinders, branches with leaves.

(ii) Extract T matrices for single objects for vector spheroidal and cylindrical waves, apply vector wave transformations and use the Foldy-Lax multiple scattering equations to compute multiple scattering among the single objects.

In (ii), three innovative steps were implemented: (1) extracting the T matrix for each single object using vector spheroidal waves, (2) vector spheroidal wave transformations, and (3) solving Foldy-Lax multiple scattering equations (FL) for all the objects. The T matrix relates the incident fields to the scattered fields for an arbitrarily-shaped scatterer. Previously, vector spherical wave expansions were used for the T matrix, where a circumscribing sphere is defined. However, when the objects are closely packed, it is impractical to enclose each object within a spherical surface without overlap. In general, spheroidal/cylindrical surfaces are more compact to enclose closely packed objects. Thus, vector spheroidal/cylindrical wave expansions are used, which are more complicated than the spherical waves. In the hybrid method, Maxwell's equations are solved using the Foldy-Lax multiple scattering equations (FL) with generalized T matrix. The Foldy-Lax equations were derived rigorously from Maxwell's equations. The wave interactions among scatterers are taken into account in the Foldy-Lax equations. Thus, the effects of complex vegetation structure, including canopy clustering and gaps, are accounted for. Using the hybrid method, forests environment with 196 tree trunks at height of 20m and diameter of 20cm was simulated at L-band frequency. Before this work, the large-scale full-wave simulations of many tree trunks were deemed very difficult. The NMM3D full-wave simulation results showed that the results of past models significantly overestimate attenuation in a vegetation/forest canopy. The NMM3D full-wave models predict transmissions that are several times greater than that of past models. A much greater microwave transmission means the microwave can better penetrate a vegetation/forest canopy and thus it can be used to retrieve soil moisture.

This thesis is organized as follows. In chapter II, DBA is derived from the Foldy-Lax equation with first-order iteration. DBA for vegetation is combined with NMM3D for rough surfaces. For soybean fields, an improved coherent model is developed, consisting of conditional probability functions to eliminate the overlapping effects of branches in the former branching models. DBA and the improved coherent model are used to generate data-cubes at L-band for the data-cube based soil moisture retrieval for SMAP. In chapter III, a unified combined active and passive model is constructed, with the active and passive microwave remote sensing models founded on the same theoretical basis and hence allow the use of the same physical parameters. DBA combined with NMM3D for rough surfaces is extended to calculate the bistatic scattering coefficients and then integrating the bistatic scattering coefficients over the hemispherical solid angle to compute the emissivity. The vegetation models in chapter II and III are single scattering models where multiple scattering among scatterers is not considered. In chapter IV, Foldy-Lax multiple scattering equations are combined with BOR for NMM3D full-wave simulations of vegetation with scatterers of rotational symmetry. This full-wave method accounts for all the interactions and multiple scattering among vegetation scatterers. Grass canopy of different vegetation water content (VWC) modeled by a layer of dielectric cylinders at C-band is simulated. In chapter V, an innovative hybrid method is developed for NMM3D full-wave simulations of vegetation/forest. The hybrid method combines off-the-shelf techniques for single scatterer and developed techniques of Foldy-Lax techniques. The fields are expanded in terms of vector spherical/spheroidal/cylindrical waves. The off-the-shelf techniques such as the commercial software HFSS is suitable for complicated single object with moderate size such as branches with realistic leaves and a single soybean plant. The developed techniques account for the multiple scattering among single objects and solve the Maxwell's equations for the vegetation/forest

canopy, including extracting the T matrix, vector wave translation addition and solving the Foldy-Lax equations.

CHAPTER II

DBA and an Improved Coherent Model for Vegetation-covered Surfaces at L-Band for Data-Cube Based Soil Moisture Retrieval

In this Chapter, two models are used to calculate the backscattering coefficient for the vegetation-covered surfaces: the distorted Born approximation (DBA) (section 2.2) and an improved coherent model (section 2.3). The two models are used for the data-cube based soil moisture retrieval at L-band (section 2.4).

For wheat and canola fields, DBA is used. DBA is derived from the Foldy-Lax equation with first-order iteration. DBA has three scattering terms: volume scattering, double-bounce scattering and surface scattering. The coherent reflectivity in the double-bounce scattering and the surface scattering are determined by the numerical solutions of Maxwell's equations (NMM3D). Using DBA, forward lookup-tables (data-cubes) for VV and HH backscattering coefficients at L-band are developed for wheat and canola fields. The data-cubes have three axes: vegetation water content (VWC), root mean square (RMS) height of rough soil surface and soil permittivity. The results of the data-cubes are compared with airborne radar measurements collected during the Soil Moisture Active Passive Validation Experiment 2012 (SMAPVEX12) for ten wheat fields and five canola fields. The results show good agreement between the data-cube simulation and the airborne data: the root mean squared error (RMSE) of 0.82 dB and 0.78 dB for HH backscattering coefficients, and 0.97 dB and 1.30 dB for VV backscattering coefficients for wheat and canola fields, respectively. The data-cubes are next used to perform the time-series retrieval of the soil

moisture, which was the baseline active retrieval algorithm for the NASA's Soil Moisture Active Passive (SMAP) mission. The RMSE of the soil moisture retrieval is 0.043 cm^3/cm^3 for wheat fields and 0.082 cm^3/cm^3 for canola fields. The larger RMSE for canola fields is attributed to the dominance of volume scattering which does not depend on soil moisture.

For soybean fields, an improved coherent branching model is developed by taking into account the correlated scattering among scatterers. The novel feature of the analytical coherent model consists of conditional probability functions to eliminate the overlapping effects of branches in the former branching models. Backscattering coefficients are considered for a variety of scenarios over the full growth cycle for VWC and the complete dry-down conditions for soil moisture. The results of the coherent model show that HH scattering has a significant difference up to 3 dB, from that computed on the basis of the independent scattering when VWC is low; for example, 0.2 kg/m^2. Forward model calculations are performed for the scattering from the soybean field for the full range of the three axes of the data-cubes using the coherent model. The soybean volume scattering including the double-bounce term is combined with the forward scattering model of bare soil from the numerical Maxwell solutions that incorporates RMS height, soil permittivity and correlation length, to form the forward model lookup-table for the vegetation-covered soil. The results are compared with data from 13 soybean fields collected as part of the SMAPVEX12. Time-series retrieval of soil moisture is also applied to the soybean fields by inverting the forward model lookup-table. During the retrieval, the VWC is optimized with physical constraints obtained from ground measurements. The retrieval performances are significantly improved by using the proposed coherent model: the root mean squared error (RMSE) of the soil moisture retrieval is decreased from 0.09 to 0.05 cm^3/cm^3 and the correlation coefficient is increased from 0.66 to 0.92.

2.1 Introduction

The mapping of soil moisture on a golobal scale has many potential benefits including flood assessment, drought monitoring, global carbon balance quantification, and more. Providing this information is one of the important goals of NASA's Soil Moisture Active Passive (SMAP) mission [1, 3]. SMAP, which was launched in January 2015, utilized a L-band radar and radiometer to provide global maps of soil moisture at 3-, 9-, and 36-km resolutions [1, 14]. Empirical and semi-empirical models have been developed to retrieve the soil moisture information for vegetation-covered surfaces [15-17] using backscattering coefficients, but they have limited capability on a global scale because the empirical equations were derived using a small set of measurements. Complex physical scattering models have also been used to calculate the backscattering [18-21]. In order to make use of the complex physical models for real time-retrieval during the SMAP mission, lookup-tables of backscattering are constructed. Using the measured data and the lookup-tables, time-series retrieval of soil moisture can be carried out in real time [6, 10]. In the SMAP baseline active radar retrieval algorithm, the data-cubes are inverted. The soil permittivity directly related to the soil moisture [22, 23]. The SMAP baseline algorithm for radar-based retrieval inverts the data-cubes. The data-cubes were validated against airborne and field measurements and were also used for retrieval of soil moisture from the airborne radar measurements. Previously, the validation and soil moisture retrieval for soybean and corn covered surfaces were published [5]. In this chapter, we report on the validation and soil moisture retrieval of wheat and canola vegetation-covered surfaces using airborne and field measurements of SMAPVEX12 [10]. Wheat is the most abundant crop in terms of the acreage in the world [24]. Canola is a major crop in North America. Accurate retrieval of soil moisture for these crops is a critical step towards soil moisture retrieval at SMAP's 3-km resolution for croplands.

In vegetation-covered surfaces, the commonly used physical models of radar backscattering at L-band are based on the incoherent addition of three contributions: volume scattering, double-bounce and surface scattering. There are also models accounting for the interactions between different vegetation scatterers [25], and the vegetation and slightly rough surface [26]. These models are more complicated than the incoherent model. In previous studies [27], physical models for wheat and canola fields were derived using MIMICS (Michigan Microwave Canopy Scattering) model [28] where the first-order radiative transfer equation is used to calculate volume and double-bounce scattering while the surface-scattering component is computed using the physical optics model [4, 28]. However, in the backscattering direction, the forward and reverse going ground-vegetation interaction scattering fields are exactly in phase according to reciprocity, and thus their coherent interaction cannot be neglected. This backscattering enhancement effect in double-bounce scattering is accounted for by the field-based distorted Born approximation [11, 29] which gives a factor of 2 difference for the double-bounce term. In this chapter, the distorted Born approximation [11] is used to compute scattering from a vegetation medium. The distorted Born approximation is derived from the Foldy-Lax equation with the use of the T matrix [30, 31] and half-space Green's function with the effective propagation constant. For surface scattering, we use the numerical solutions of Maxwell's equations in 3-dimensional simulations (NMM3D) for backscattering. We also use the rough surface coherent reflectivity derived from NMM3D for the specular reflection in the double-bounce term. In the previous soybean model [5], we used the coherent addition of scattered fields which gives significant improvement when compared with backscattering data. For wheat and canola, we found that the incoherent addition model suffices.

The wheat canopy is modeled as a layer of uniformly distributed finite cylinders, while two kinds of cylinders with different sizes and circular disks are used for canola to model its main stem,

branches and leaves, respectively. The scatterers are treated as embedded in the equivalent media [11] whose dielectric constant is computed from the Foldy's approximation [4]. The imaginary part of the equivalent dielectric constant accounts for the attenuation through the vegetation layer. The surface-scattering component is determined by NMM3D for a random rough surface [32]. NMM3D results are based on the Method of Moments (MoM) with Rao-Wilton-Glisson (RWG) basis function using Gaussian random rough surfaces with exponential correlation functions. The NMM3D simulation results have been shown to be in good agreement with experimental data for surfaces with RMS height varying from 0.55cm to 3.47cm at L-band [32]. The agreement has been shown to be superior to the predictions of the small perturbation method (SPM), physical optics (PO), small slope approximation (SSA) and advanced integral equation model (AIEM). The soil medium is considered to be homegeneious in this section. There are models to calculate scattering from rough surface with inhomogeneous dielectric profiles [33]. According to the ground]data from the Soil Moisture Active Passive Validation Experiment 2012 (SMAPVEX12) [34], the RMS height for more than half of the wheat and canola fields is within the range of 0.55cm to 1cm. The data-cubes computed from the forward model are validated with the VV and HH backscattering coefficient measurements from SMAPVEX12 [34], taking into account the growth of the crops as determined from ground measurements during the summer season. SMAPVEX12 started at the period of early crop development and finished at the point where crops had reached maximum biomass during which soil moisture also significantly varied [34]. The long-duration measurements over a wide range of soil moisture and vegetation conditions are a unique and valuable attribute of this field campaign when compared with previous airborne experiment and provide an extensive data set critical to test the vegetation scattering models and radar-based soil moisture retrieval algorithm for SMAP [34]. The retrieved soil moisture derived

by inverting the data-cubes is also compared with the ground truth data from the SMAPVEX12 field campaign [10].

In the models of the distorted Born approximation and first-order radiative transfer equation, the results are in terms of the absolute square of the scattering amplitude of a single scatterer. The incoherent addition of the scattering from a single scatter can be referred to as the "incoherent scattering model" since the collective scattering effects of the scatterers are not accounted for [2, 28]. For example, when two scatterers are close to each other within a $\lambda/4$ scale, there is a relatively small phase difference (less than $\pi/2$) and the individual scattering superimposes on each other collectively, producing significant constructive interference. Models taking into account these relative phase shifts are known as "coherent scattering models". Generalized coherent models for dissimilar plant elements, crops in a growing cycle and multilayer vegetation have been proposed. It was suggested that an agricultural crop could be considered a statistically uniform random medium and represented with a *n*th-scale branching model. Different parameters were used for different stages of the crops in a growing cycle obtained from ground measurements [35]. Yueh et al. [36] proposed an analytical branching model for soybean and showed that the geometry and internal structure of vegetation affect the coherent scattering. Monte Carlo simulations of soybean field were also carried out to simulate the statistical properties of the backscatter at different incidence angles, by averaging over many realizations untill convergence is realized. For each realization, a group of soybean plants was generated using random number generators with a pre-described probability distribution function, and then the scattered fields were computed. It was shown that the contributions from the second-order near field and the double ground-bounce mechanism are negligible at L band [37]. The coherent model was also applied to other canopies such as alfalfa. Each alfalfa plant was represented by a clump defined as a collection

of stems in a conical shape with leaflets clustered on each stem. The scattering from the alfalfa was substantially increased by including the coherent wave interactions. It was shown that the proximity of the scatterers in relation to wavelength is important and should be included in the calculation of the backscattering from the canopy. [38] In the previous coherent model for soybean [36], different branches overlap physically, which is unrealistic. In this chapter, we use an improved branching model that introduces conditional probabilities of non-overlap of branches both in locations and in orientations for the soybean, which has a typical main stem attached with branches. The analytical simulation results are significantly different from those by the prior branching models in that they either allow the physical overlap or are based on the incoherent model. We initially constructed the data-cube based on the incoherent scattering models. But they are not in good agreement with the magnitudes of backscattering nor the polarization ratios observed during the SMAPVEX12 campaign. The new data-cube based on the improved coherent model enhances the forward matching with experimental data of the 13 soybean fields from SMAPVEX12, as well as the soil moisture retrieval accuracy.

2.2 The Distorted Born Approximation (DBA) for Wheat and Canola Fields

Wheat and canola are two of the major crops studied during the Soil Moisture Active Passive Validation Experiment 2012 (SMAPVEX12) conducted to support NASA's Soil Moisture Active Passive (SMAP) mission. The models are used in the baseline active retrieval algorithm for the SMAP mission. Forward lookup-tables (data-cubes) for VV and HH backscattering coefficients at L-band are developed for wheat and canola fields. The volume scattering and double-bounce scattering of the fields are calculated using the distorted Born approximation derived from the Foldy-Lax equation with first-order iteration. The coherent reflectivity in the

double-bounce scattering and the surface scattering are determined by the numerical solutions of Maxwell's equations (NMM3D). The results of the data-cubes are compared with airborne radar measurements collected during SMAPVEX12 for ten wheat fields and five canola fields. The results show good agreement between the data-cube simulation and the airborne data: the root mean squared error (RMSE) is 0.82 dB and 0.78 dB for HH backscattering coefficients, and 0.97 dB and 1.30 dB for VV backscattering coefficients for wheat and canola fields, respectively. In this section, the distorted Born approximation (DBA) is derived based on the Foldy-Lax equation with first-order iteration. The results are compared the first-order radiative transfer equation. After that, the DBA is applied to generate the data-cubes for wheat and canola fields and the modeled data-cubes are compared with SMAPVEX12 airborne UAVSAR data.

2.2.1 Derivation of DBA

We consider a vegetation field as shown in Figure II.1. There are three regions: air, vegetation and soil. The reflection at the artificial boundary between the air and vegetation is ignored. The distorted Born approximation (DBA) calculates the final backscattering in terms of volume scattering, double-bounce scattering and surface scattering. The derivations for the three terms are given below based on the Foldy-Lax equation with first-order iteration. The derivations are different from the traditional method as in [11].

The effective propagation constant in the vegetation layer is [39],

$$k_v = k + \frac{2\pi n_0}{k} < f_{vv}(\theta_i, \phi_i; \theta_i, \phi_i) > \tag{2.2.1}$$

$$k_h = k + \frac{2\pi n_0}{k} < f_{hh}(\theta_i, \phi_i; \theta_i, \phi_i) > \tag{2.2.2}$$

where k is the propagation constant in free space and n_0 is the number density of the vegetation scatterers with unit m^{-3}. (θ_i, ϕ_i) defines the incident angle. $f_{vv}(\theta_i, \phi_i; \theta_i, \phi_i)$ and $f_{hh}(\theta_i, \phi_i; \theta_i, \phi_i)$ are the scattering amplitudes of single scatterers in the forward direction for the porlarizations VV and HH, respectively. The angle bracket means average over orientations of scatterers.

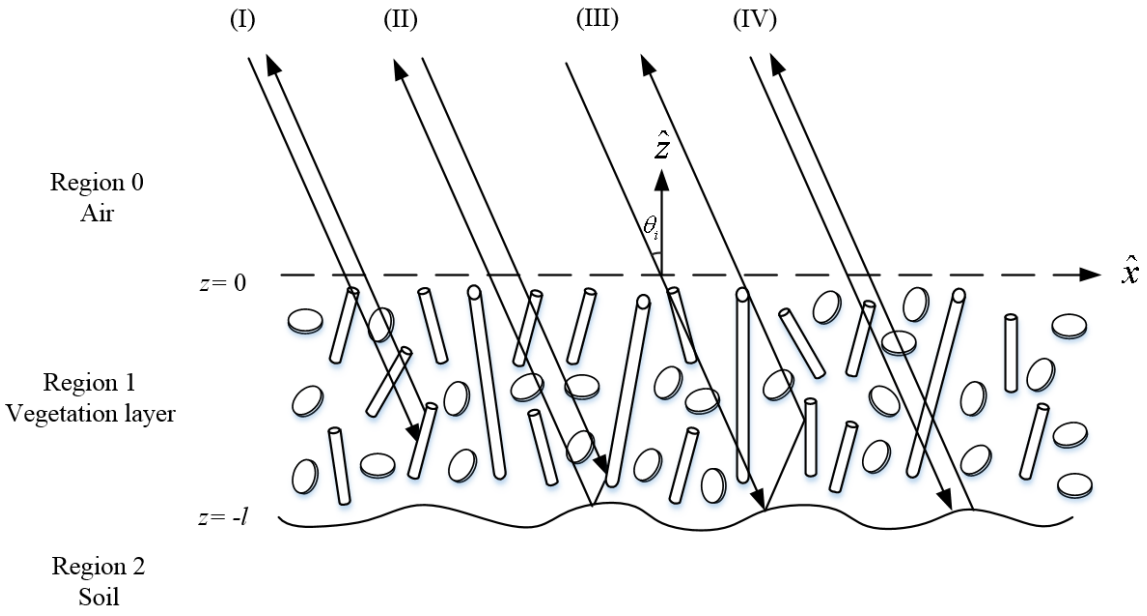

Figure II.1. Backscattering of vegetation-covered surface. The four scattering terms are: (I) volume scattering, (II) double-bounce scattering (scattering from the scatterer and then reflected by the surface), (III) double-bounce scattering (scattering of the reflected wave by a scatterer), and (IV) surface scattering.

Because of the phase matching condition [39], the z component of the effective propagation constant in the vegetation layer is

$$
\begin{aligned}
k_{pz} &= \sqrt{k_p^2 - (k\sin\theta_0)^2} \\
&= k\cos\theta_0 \sqrt{1 + \frac{4\pi n_0 < f_{pp}(\theta_i, \phi_i; \theta_i, \phi_i) > + \left(\frac{2\pi n_0}{k} < f_{pp}(\theta_i, \phi_i; \theta_i, \phi_i) >\right)^2}{k^2 \cos^2\theta_0}} \\
&\simeq k\cos\theta_0 \left(1 + \frac{4\pi n_0 < f_{pp}(\theta_i, \phi_i; \theta_i, \phi_i) >}{2k^2 \cos^2\theta_0}\right)
\end{aligned}
\qquad (2.2.3)
$$

where the subscript 'p' is either 'v' or 'h' polarization. θ_0 is the incident angle.

The k_{pz} can be written using the real part and imaginary part as $k_{pz} = k_{pz}^{'} + ik_{pz}^{''}$, with

$$k_{pz}^{'} = k\cos\theta_0 + \mathrm{Re}\left(\frac{4\pi n_0 < f_{pp}(\theta_i,\phi_i;\theta_i,\phi_i) >}{2k\cos\theta_0}\right) \tag{2.2.4}$$

$$k_{pz}^{''} = \mathrm{Im}\left(\frac{4\pi n_0 < f_{pp}(\theta_i,\phi_i;\theta_i,\phi_i) >}{2k\cos\theta_0}\right) \tag{2.2.5}$$

Next, the dyadic Green's function for free space is used to calculate volume scattering. The dyadic Green's function for free space is [39]

$$\overline{\overline{G}}_P(\bar{r}) = \begin{cases} \dfrac{i}{8\pi^2}\displaystyle\int_{-\infty}^{\infty}dk_x\int_{-\infty}^{\infty}dk_y\left[\hat{e}(k_z)\hat{e}(k_z)+\hat{h}(k_z)\hat{h}(k_z)\right]\dfrac{\exp\left(ik_x x+ik_y y+ik_z z\right)}{k_z} & \text{for } z>0 \\ \dfrac{i}{8\pi^2}\displaystyle\int_{-\infty}^{\infty}dk_x\int_{-\infty}^{\infty}dk_y\left[\hat{e}(-k_z)\hat{e}(-k_z)+\hat{h}(-k_z)\hat{h}(-k_z)\right]\dfrac{\exp\left(ik_x x+ik_y y-ik_z z\right)}{k_z} & \text{for } z<0 \end{cases} \tag{2.2.6}$$

where for TE polarization (h-pol) : $\hat{e}(k_z) = \dfrac{\hat{k}\times\hat{z}}{|\hat{k}\times\hat{z}|} = \dfrac{1}{k_\rho}\left(\hat{x}k_y - \hat{y}k_x\right)$ and for TM polarization (v-pol) : $\hat{h}(k_z) = \hat{e}\times\hat{k} = -\dfrac{k_z}{kk_\rho}\left(\hat{x}k_x + \hat{y}k_y\right) + \dfrac{k_\rho}{k}\hat{z}$.

In the vegetation layer, the dyadic Green's function of free space is modified using the effective propagation constant

$$\overline{\overline{G}}_P(\bar{r}) = \begin{cases} \dfrac{i}{8\pi^2}\displaystyle\int_{-\infty}^{\infty}dk_x\int_{-\infty}^{\infty}dk_y\left[\hat{e}(k_z)\hat{e}(k_z)\exp(ik_{hz}z)+\hat{h}(k_z)\hat{h}(k_z)\exp(ik_{vz}z)\right]\dfrac{\exp\left(ik_x x+ik_y y\right)}{k_z} & \text{for } z>0 \\ \dfrac{i}{8\pi^2}\displaystyle\int_{-\infty}^{\infty}dk_x\int_{-\infty}^{\infty}dk_y\left[\hat{e}(-k_z)\hat{e}(-k_z)\exp(-ik_{hz}z)+\hat{h}(-k_z)\hat{h}(-k_z)\exp(-ik_{vz}z)\right]\dfrac{\exp\left(ik_x x+ik_y y\right)}{k_z} & \text{for } z<0 \end{cases} \tag{2.2.7}$$

It is noted that only the phase-dependent terms are changed to the effective propagation constant while the amplitude-dependent terms are not changed. It is because the effects are small for amplitude. Generally, for the vegetation canopy, more than 99% is empty air and less than 1% contains vegetation scatterers. Thus, the effective propagation constant of the vegetation layer is close to that in free space. The change in the amplitude can be ignored. However, the change in the phase terms cannot be ignored.

The Green's function of the reflective wave from the soil surface in the vegetation layer is

$$\overline{\overline{G}}_R\left(\bar{r},\bar{r}'\right)=$$
$$\frac{i}{8\pi^2}\int_{-\infty}^{\infty}dk_x\int_{-\infty}^{\infty}dk_y\left[\begin{array}{l}R^{TE}\exp\left(ik_{hz}z+2ik_{hz}d\right)\hat{e}\left(k_z\right)\hat{e}\left(-k_z\right)\exp\left(ik_{hz}z'\right)\\+R^{TM}\exp\left(ik_{vz}z+2ik_{vz}d\right)\hat{h}\left(k_z\right)\hat{h}\left(-k_z\right)\exp\left(ik_{vz}z'\right)\end{array}\right]\frac{\exp\left(ik_x\left(x-x'\right)+ik_y\left(y-y'\right)\right)}{k_z} \tag{2.2.8}$$

where d is the height of the vegetation canopy.

Thus, at the observation point of z = 0 in Figure II.1, Green's function for the total wave, which is the sum of that of the free space and the reflective wave, is

$$\overline{\overline{G}}_{11}\left(\bar{r},\bar{r}'\right)=\overline{\overline{G}}_P\left(\bar{r},\bar{r}'\right)+\overline{\overline{G}}_R\left(\bar{r},\bar{r}'\right)=$$
$$\frac{i}{8\pi^2}\int_{-\infty}^{\infty}dk_x\int_{-\infty}^{\infty}dk_y\left\{\begin{array}{l}\hat{e}\left(k_z\right)\left[\hat{e}\left(k_z\right)\exp\left(-ik_{hz}z'\right)+R^{TE}\exp\left(2ik_{hz}d\right)\hat{e}\left(-k_z\right)\exp\left(ik_{hz}z'\right)\right]\\+\hat{h}\left(k_z\right)\left[\hat{h}\left(k_z\right)\exp\left(-ik_{vz}z'\right)+R^{TM}\exp\left(2ik_{xz}d\right)\hat{h}\left(-k_z\right)\exp\left(ik_{vz}z'\right)\right]\end{array}\right\} \tag{2.2.9}$$
$$\times\frac{\exp\left(ik_x\left(x-x'\right)+ik_y\left(y-y'\right)\right)}{k_z}$$

where the subscript '11' means that both the source point and the observation point are in region 1 (i.e., the vegetation region).

For z>0, the phase continues as $\exp(ik_z z)$ because there is no physical reflection at z=0 which is the artificial boundary between the air and the vegetation layer. Hence,

$$\overline{\overline{G}}_{01}\left(\bar{r},\bar{r}'\right)=$$

$$\frac{i}{8\pi^2}\int_{-\infty}^{\infty}dk_x\int_{-\infty}^{\infty}dk_y\begin{Bmatrix}\hat{e}\left(k_z\right)\left[\hat{e}\left(k_z\right)\exp\left(-ik_{hz}z'\right)+R^{TE}\exp\left(2ik_{hz}d\right)\hat{e}\left(-k_z\right)\exp\left(ik_{hz}z'\right)\right]\\+\hat{h}\left(k_z\right)\left[\hat{h}\left(k_z\right)\exp\left(-ik_{vz}z'\right)+R^{TM}\exp\left(2ik_{xz}d\right)\hat{h}\left(-k_z\right)\exp\left(ik_{vz}z'\right)\right]\end{Bmatrix} \quad (2.2.10)$$

$$\times\frac{\exp\left(ik_x\left(x-x'\right)+ik_y\left(y-y'\right)+ik_z z\right)}{k_z}$$

where the subscript '01' means that both the source point is in region 1 (i.e., vegetation region) while the observation point is in region 0 (i.e., air region).

After some mathematical manipulations, the expressions becomes

$$\overline{\overline{G}}_{01}\left(\bar{r},\bar{r}'\right)=$$

$$\frac{i}{8\pi^2}\int_{-\infty}^{\infty}dk_x\int_{-\infty}^{\infty}dk_y\begin{Bmatrix}\hat{e}\left(k_z\right)\left[\hat{e}\left(k_z\right)\exp\left(-ik_{hz}z'\right)+R^{TE}\exp\left(2ik_{hz}d\right)\hat{e}\left(-k_z\right)\exp\left(ik_{hz}z'\right)\right]\\+\hat{h}\left(k_z\right)\left[\hat{h}\left(k_z\right)\exp\left(-ik_{vz}z'\right)+R^{TM}\exp\left(2ik_{vz}d\right)\hat{h}\left(-k_z\right)\exp\left(ik_{vz}z'\right)\right]\end{Bmatrix} \quad (2.2.11)$$

$$\times\frac{\exp(i\bar{k}\cdot\bar{r})}{k_z}\exp\left(-ik_x x'-ik_y y'\right)$$

In the far field, using the stationary-phase method, $k_x=k\sin\theta_s\cos\phi_s$, $k_y=k\sin\theta_s\sin\phi_s$, $k_z=k\cos\theta_s$ and $\frac{i}{8\pi^2}\int_{-\infty}^{\infty}dk_x\int_{-\infty}^{\infty}dk_y\frac{\exp(i\bar{k}\cdot\bar{r})}{k_z}\to\frac{\exp(ikr)}{4\pi r}$. Thus,

$$\overline{\overline{G}}_{01}\left(\bar{r},\bar{r}'\right)=$$

$$\frac{\exp(ikr)}{4\pi r}\begin{Bmatrix}\hat{e}\left(k_z\right)\left[\hat{e}\left(k_z\right)\exp\left(-ik_{hz}z'\right)+R^{TE}\exp\left(2ik_{hz}d\right)\hat{e}\left(-k_z\right)\exp\left(ik_{hz}z'\right)\right]\\+\hat{h}\left(k_z\right)\left[\hat{h}\left(k_z\right)\exp\left(-ik_{vz}z'\right)+R^{TM}\exp\left(2ik_{vz}d\right)\hat{h}\left(-k_z\right)\exp\left(ik_{vz}z'\right)\right]\end{Bmatrix}\exp\left(-ik_x x'-ik_y y'\right)$$

(2.2.12)

where

$$\hat{e}\left(k_z\right)=\left(\hat{x}\sin\phi_s-\hat{y}\cos\phi_s\right)=-\hat{h}_s\left(\theta_s,\phi_s\right)=-\hat{h}_s\left(\pi-\theta_s,\phi_s\right) \quad (2.2.13)$$

$$\hat{e}\left(-k_z\right)=\left(\hat{x}\sin\phi_s-\hat{y}\cos\phi_s\right)=-\hat{h}_s\left(\theta_s,\phi_s\right)=-\hat{h}_s\left(\pi-\theta_s,\phi_s\right) \quad (2.2.14)$$

$$\hat{h}(k_z) = -\cos\theta_s(\hat{x}\cos\phi_s + \hat{y}\sin\phi_s) + \sin\theta_s\hat{z} = -\hat{v}_s(\theta_s, \phi_s) \tag{2.2.15}$$

$$\hat{h}(-k_z) = \cos\theta_s(\hat{x}\cos\phi_s + \hat{y}\sin\phi_s) + \sin\theta_s\hat{z} = -\hat{v}_s(\pi - \theta_s, \phi_s) \tag{2.2.16}$$

Next, the Green's function $\overline{\overline{G}}_{01}(\bar{r}, \bar{r}')$ can be written into two parts as

$$\overline{\overline{G}}_{01}(\bar{r}, \bar{r}') = \overline{\overline{G}}_{01}^{(0)}(\bar{r}, \bar{r}') + \overline{\overline{G}}_{01}^{(R)}(\bar{r}, \bar{r}') \tag{2.2.17}$$

where

$$\overline{\overline{G}}_{01}^{(0)}(\bar{r}, \bar{r}') = \frac{\exp(ikr)}{4\pi r}\begin{bmatrix}\hat{e}(k_z)\hat{e}(k_z)\exp(-ik_{hz}z') + \\ \hat{h}(k_z)\hat{h}(k_z)\exp(-ik_{vz}z')\end{bmatrix}\exp(-ik_x x' - ik_y y') \tag{2.2.18}$$

$$\overline{\overline{G}}_{01}^{(R)}(\bar{r}, \bar{r}') = \frac{\exp(ikr)}{4\pi r}\begin{bmatrix}\hat{e}(k_z)R^{TE}\exp(2ik_{hz}d)\hat{e}(-k_z)\exp(ik_{hz}z') + \\ \hat{h}(k_z)R^{TM}\exp(2ik_{vz}d)\hat{h}(-k_z)\exp(ik_{vz}z')\end{bmatrix}\exp(-ik_x x' - ik_y y') \tag{2.2.19}$$

Let the incident wave be

$$\bar{E}_{inc} = E_{vi}\hat{v}(\pi - \theta_i, \phi_i)\exp(i\bar{K}_{iv}\cdot\bar{r}) + E_{hi}\hat{h}(\pi - \theta_i, \phi_i)\exp(i\bar{K}_{ih}\cdot\bar{r}) \tag{2.2.20}$$

where $\bar{K}_{ip} = k_{ix}x + k_{iy}y - k_{izp}\hat{z}$, indicating that the wave is travelling downward.

The reflected wave is

$$\bar{E}_{ref} = E_{vi}R_{vi}\exp(2ik_{ivz}d)\hat{v}(\theta_i, \phi_i)\exp(i\bar{k}_{iv}\cdot\bar{r}) + E_{hi}R_{hi}\exp(2ik_{ihz}d)\hat{h}(\theta_i, \phi_i)\exp(i\bar{k}_{ih}\cdot\bar{r}) \tag{2.2.21}$$

where $R_v = R^{TM}, R_h = R^{TE}$ and the phase shift caused by the vegetation canopy is included.

According to [30], the Foldy-Lax equation is

$$\bar{E} = \bar{E}_{inc} + \bar{E}_{ref} + \sum_{j=1}^{N}\overline{\overline{G}}_{01}\overline{\overline{T}}_j\bar{E}_j^{ex} \tag{2.2.22}$$

where N is the total number of vegetation scatterers.

For first-order iteration,

$$\overline{E} = \overline{E}_{inc} + \overline{E}_{ref} + \sum_{j=1}^{N} \overline{\overline{G}}_{01} \overline{\overline{T}}_j \left(\overline{E}_{inc} + \overline{E}_{ref} \right) \tag{2.2.23}$$

Thus, the scattered fields from the vegetation canopy is

$$\overline{E}_s = \sum_{j=1}^{N} \overline{\overline{G}}_{01} \overline{\overline{T}}_j \left(\overline{E}_{inc} + \overline{E}_{ref} \right) \tag{2.2.24}$$

Let $\overline{E}_s = \sum_{j=1}^{N} \overline{E}_{sj}$, the summation of the scattered fields from each vegetation scatterer, and substituting $\overline{\overline{G}}_{01}\left(\overline{r},\overline{r}'\right) = \overline{\overline{G}}_{01}^{(0)}\left(\overline{r},\overline{r}'\right) + \overline{\overline{G}}_{01}^{(R)}\left(\overline{r},\overline{r}'\right)$ leads to

$$\overline{E}_{sj} = \overline{\overline{G}}_{01}^{(0)} \overline{\overline{T}}_j \overline{E}_{inc} + \overline{\overline{G}}_{01}^{(R)} \overline{\overline{T}}_j \overline{E}_{inc} + \overline{\overline{G}}_{01}^{(0)} \overline{\overline{T}}_j \overline{E}_{ref} + \overline{\overline{G}}_{01}^{(R)} \overline{\overline{T}}_j \overline{E}_{ref} \tag{2.2.25}$$

The first term represents the volume scattering, the second and third terms are the double-bounce scattering and the last term is the triple bounce scattering. The last term is ignored in the distorted Born approximation. Hence,

$$\overline{E}_{sj} = \overline{\overline{G}}_{01}^{(0)} \overline{\overline{T}}_j \overline{E}_{inc} + \overline{\overline{G}}_{01}^{(R)} \overline{\overline{T}}_j \overline{E}_{inc} + \overline{\overline{G}}_{01}^{(0)} \overline{\overline{T}}_j \overline{E}_{ref} \tag{2.2.26}$$

(a) Volume Scattering

In this subsection, the expressions for volume scattering $\overline{E}_{sj}^{(1)} = \overline{\overline{G}}_{01}^{(0)} \overline{\overline{T}}_j \overline{E}_{inc}$ is calculated as below.

$$\overline{E}_{sj}^{(1)}(\overline{r}) = \int d\overline{r}' \overline{\overline{G}}_{01}^{(0)} \int d\overline{r}'' < \overline{r}' \left| \overline{\overline{T}}_j \right| \overline{r}'' >< \overline{r}'' \mid \overline{E}_{inc} > \tag{2.2.27}$$

Substituting the expressions for the Green's function and the incident field leads to

$$\begin{aligned} \overline{E}_{sj}^{(1)}(\overline{r}) &= \frac{\exp(ikr)}{4\pi r} \int d\overline{r}' \left[\hat{e}\left(k_z\right) \hat{e}\left(k_z\right) \exp\left(-i\overline{k}_h \cdot \overline{r}'\right) + \hat{h}\left(k_z\right) \hat{h}\left(k_z\right) \exp\left(-i\overline{k}_v \cdot \overline{r}'\right) \right] \\ &\times \int d\overline{r}'' < \overline{r}' \left| \overline{\overline{T}}_j \right| \overline{r}'' > \left[E_{vi} \hat{v}\left(\pi - \theta_i, \phi_i\right) \exp\left(i\overline{K}_{iv} \cdot \overline{r}''\right) + E_{hi} \hat{h}\left(\pi - \theta_i, \phi_i\right) \exp\left(i\overline{K}_{ih} \cdot \overline{r}''\right) \right] \end{aligned} \tag{2.2.28}$$

According to [30],

$$
\begin{aligned}
&< \bar{r}' \left| \bar{\bar{T}}_j \right| \bar{r}'' >= \int \frac{d\bar{p}}{(2\pi)^3} \int \frac{d\bar{p}'}{(2\pi)^3} < \bar{r}' \mid \bar{p} >< \bar{p} \mid \bar{\bar{T}}_j \left| \bar{p}' \right. >< \bar{p}' \left| \bar{r}'' \right. > \\
&= \int \frac{d\bar{p}}{(2\pi)^3} \int \frac{d\bar{p}'}{(2\pi)^3} \exp\left(i\bar{p} \cdot \bar{r}' - i\bar{p}' \cdot \bar{r}'' \right) < \bar{p} \left| \bar{\bar{T}}_j \right| \bar{p}' >
\end{aligned}
\tag{2.2.29}
$$

$$
< \bar{p} \left| \bar{\bar{T}}_j \right| \bar{p}' >= \exp\left(-i\left(\bar{p} - \bar{p}' \right) \cdot \bar{r}_j \right) \bar{\bar{T}}_p \left(\bar{p}, \bar{p}' \right) \tag{2.2.30}
$$

Substituting these into $\bar{E}_{sj}^{(1)}(\bar{r})$ leads to

$$
\begin{aligned}
&\bar{E}_{sj}^{(1)}(\bar{r}) = \frac{\exp(ikr)}{4\pi r} \int d\bar{r}' \left[\hat{e}\left(k_z \right) \hat{e}\left(k_z \right) \exp\left(-i\bar{k}_h \cdot \bar{r}' \right) + \hat{h}\left(k_z \right) \hat{h}\left(k_z \right) \exp\left(-i\bar{k}_v \cdot \bar{r}' \right) \right] \\
&\times \int d\bar{r}'' \int \frac{d\bar{p}}{(2\pi)^3} \int \frac{d\bar{p}'}{(2\pi)^3} \exp\left(i\bar{p} \cdot \bar{r}' - i\bar{p}' \cdot \bar{r}'' \right) \exp\left(-i\left(\bar{p} - \bar{p}' \right) \cdot \bar{r}_j \right) \bar{\bar{T}}_p \left(\bar{p}, \bar{p}' \right) \\
&\times \left[E_{vi} \hat{v}\left(\pi - \theta_i, \phi_i \right) \exp\left(i\bar{K}_{iv} \cdot \bar{r}'' \right) + E_{hi} \hat{h}\left(\pi - \theta_i, \phi_i \right) \exp\left(i\bar{K}_{ih} \cdot \bar{r}'' \right) \right]
\end{aligned}
\tag{2.2.31}
$$

Because $\int d\bar{r}' \exp\left(-i\bar{k}_h \cdot \bar{r}' \right) \exp\left(i\bar{p} \cdot \bar{r}' \right) = (2\pi)^3 \delta\left(\bar{p} - \bar{k}_h \right)$, then

$$
\begin{aligned}
&\bar{E}_{sj}^{(1)}(\bar{r}) = \frac{\exp(ikr)}{4\pi r} \int d\bar{r}'' \int \frac{d\bar{p}'}{(2\pi)^3} \begin{bmatrix} \hat{e}\left(k_z \right) \hat{e}\left(k_z \right) \exp\left(-i\left(\bar{k}_h - \bar{p}' \right) \cdot \bar{r}_j \right) \bar{\bar{T}}_p \left(\bar{k}_h, \bar{p}' \right) \\ + \hat{h}\left(k_z \right) \hat{h}\left(k_z \right) \exp\left(-i\left(\bar{k}_v - \bar{p}' \right) \cdot \bar{r}_j \right) \bar{\bar{T}}_p \left(\bar{k}_v, \bar{p}' \right) \end{bmatrix} \\
&\times \exp\left(-i\bar{p}' \cdot \bar{r}'' \right) \begin{bmatrix} E_{vi} \hat{v}\left(\pi - \theta_i, \phi_i \right) \exp\left(i\bar{K}_{iv} \cdot \bar{r}'' \right) \\ + E_{hi} \hat{h}\left(\pi - \theta_i, \phi_i \right) \exp\left(i\bar{K}_{ih} \cdot \bar{r}'' \right) \end{bmatrix}
\end{aligned}
\tag{2.2.32}
$$

Because $\int d\bar{r}'' \exp\left(-i\bar{p}' \cdot \bar{r}'' \right) \exp\left(i\bar{K}_{iv} \cdot \bar{r}'' \right) = (2\pi)^3 \delta\left(\bar{p}' - \bar{K}_{iv} \right)$ and use of (2.2.13) – (2.2.16), then

$$
\bar{E}_{sj}^{(1)}(\bar{r}) = \frac{\exp(ikr)}{4\pi r} \begin{Bmatrix} \hat{h}\left(\theta_s, \phi_s \right) \hat{h}\left(\theta_s, \phi_s \right) \exp\left(-i\left(\bar{k}_h - \bar{K}_{iv} \right) \cdot \bar{r}_j \right) \cdot \bar{\bar{T}}_p \left(\bar{k}_h, \bar{K}_{iv} \right) \cdot E_{vi} \hat{v}\left(\pi - \theta_i, \phi_i \right) \\ + \hat{h}\left(\theta_s, \phi_s \right) \hat{h}\left(\theta_s, \phi_s \right) \exp\left(-i\left(\bar{k}_h - \bar{K}_{ih} \right) \cdot \bar{r}_j \right) \cdot \bar{\bar{T}}_p \left(\bar{k}_h, \bar{K}_{ih} \right) \cdot E_{hi} \hat{h}\left(\pi - \theta_i, \phi_i \right) \\ + \hat{v}\left(\theta_s, \phi_s \right) \hat{v}\left(\theta_s, \phi_s \right) \exp\left(-i\left(\bar{k}_v - \bar{K}_{iv} \right) \cdot \bar{r}_j \right) \cdot \bar{\bar{T}}_p \left(\bar{k}_v, \bar{K}_{iv} \right) \cdot E_{vi} \hat{v}\left(\pi - \theta_i, \phi_i \right) \\ + \hat{v}\left(\theta_s, \phi_s \right) \hat{v}\left(\theta_s, \phi_s \right) \exp\left(-i\left(\bar{k}_v - \bar{K}_{th} \right) \cdot \bar{r}_j \right) \cdot \bar{\bar{T}}_p \left(\bar{k}_v, \bar{K}_{ih} \right) \cdot E_{hi} \hat{h}\left(\pi - \theta_i, \phi_i \right) \end{Bmatrix}
\tag{2.2.33}
$$

The relationship between the scattering amplitude and the T matrix is

$$\overline{\overline{F}}(\theta_s,\phi_s;\theta_i,\phi_i)\cdot\hat{e}_i = \frac{1}{4\pi}\left(\hat{v}(\theta_s,\phi_s)\hat{v}(\theta_s,\phi_s)+\hat{h}(\theta_s,\phi_s)\hat{h}(\theta_s,\phi_s)\right)\cdot\overline{\overline{T}}_p\left(k\hat{k}(\theta_s,\phi_s),k\hat{k}(\theta_i,\phi_i)\right)\cdot\hat{e}_i \tag{2.2.34}$$

This means that

$$\begin{aligned}
f_{vv}(\theta_s,\phi_s;\theta_i,\phi_i) &= \frac{1}{4\pi}\hat{v}(\theta_s,\phi_s)\cdot\overline{\overline{T}}_p\left(k\hat{k}(\theta_s,\phi_s),k\hat{k}(\theta_i,\phi_i)\right)\cdot\hat{v}(\theta_i,\phi_i)\\
f_{vh}(\theta_s,\phi_s;\theta_i,\phi_i) &= \frac{1}{4\pi}\hat{v}(\theta_s,\phi_s)\cdot\overline{\overline{T}}_p\left(k\hat{k}(\theta_s,\phi_s),k\hat{k}(\theta_i,\phi_i)\right)\cdot\hat{h}(\theta_i,\phi_i)\\
f_{hv}(\theta_s,\phi_s;\theta_i,\phi_i) &= \frac{1}{4\pi}\hat{h}(\theta_s,\phi_s)\cdot\overline{\overline{T}}_p\left(k\hat{k}(\theta_s,\phi_s),k\hat{k}(\theta_i,\phi_i)\right)\cdot\hat{v}(\theta_i,\phi_i)\\
f_{hh}(\theta_s,\phi_s;\theta_i,\phi_i) &= \frac{1}{4\pi}\hat{h}(\theta_s,\phi_s)\cdot\overline{\overline{T}}_p\left(k\hat{k}(\theta_s,\phi_s),k\hat{k}(\theta_i,\phi_i)\right)\cdot\hat{h}(\theta_i,\phi_i)
\end{aligned} \tag{2.2.35}$$

For vegetation scatterers, the main stems, stalks and branches are usually modeled as dielectric cylinders and in this case, the Infinite Cylinder Approximation (ICA) [39, 40] can be used to calculate the scattering amplitude f for a single vegetation scatterer in the above equation. The leaves are usually modeled as dielectric disks, and in this case, the Generalized Rayleigh-Gans Approximation [4, 41] can be used to calculate the scattering amplitude. There are also other methods [42] to calculate the scattering from dielectric disks.

From equations (2.2.33) – (2.2.35),

$$\overline{E}_{sj}^{(1)}(\overline{r}) = \frac{\exp(ikr)}{r}\begin{Bmatrix}
\hat{h}(\theta_s,\phi_s)\exp\left(-i\left(\overline{k}_h-\overline{K}_{iv}\right)\cdot\overline{r}_j\right)f_{hv}(\theta_s,\phi_s;\pi-\theta_i,\phi_i)E_{vi}\\
+\hat{h}(\theta_s,\phi_s)\exp\left(-i\left(\overline{k}_h-\overline{K}_{ih}\right)\cdot\overline{r}_j\right)f_{hh}(\theta_s,\phi_s;\pi-\theta_i,\phi_i)E_{hi}\\
+\hat{v}(\theta_s,\phi_s)\exp\left(-i\left(\overline{k}_v-\overline{K}_{iv}\right)\cdot\overline{r}_j\right)f_{vv}(\theta_s,\phi_s;\pi-\theta_i,\phi_i)E_{vi}\\
+\hat{v}(\theta_s,\phi_s)\exp\left(-i\left(\overline{k}_v-\overline{K}_{ih}\right)\cdot\overline{r}_j\right)f_{vh}(\theta_s,\phi_s;\pi-\theta_i,\phi_i)E_{hi}
\end{Bmatrix} \tag{2.2.36}$$

Substituting into $\overline{E}_s = \sum_{j=1}^{N}\overline{E}_{sj}$ leads to

$$\overline{E}_s^{(1)}(\overline{r}) = \frac{\exp(ikr)}{r}\left[\hat{h}(\theta_s,\phi_s)\left(S_{hv}^{(1)}E_{vi}+S_{hh}^{(1)}E_{hi}\right)+\hat{v}(\theta_s,\phi_s)\left(S_{vv}^{(1)}E_{vi}+S_{vh}^{(1)}E_{hi}\right)\right] \tag{2.2.37}$$

where

$$S_{hv}^{(1)} = \sum_{j=1}^{N} \exp\left(-i\left(\bar{k}_h - \bar{K}_{iv}\right)\cdot \bar{r}_j\right) f_{hv}\left(\theta_s, \phi_s; \pi - \theta_i, \phi_i\right) \tag{2.2.38}$$

$$S_{hh}^{(1)} = \sum_{j=1}^{N} \exp\left(-i\left(\bar{k}_h - \bar{K}_{ih}\right)\cdot \bar{r}_j\right) f_{hh}\left(\theta_s, \phi_s; \pi - \theta_i, \phi_i\right) \tag{2.2.39}$$

$$S_{vv}^{(1)} = \sum_{j=1}^{N} \exp\left(-i\left(\bar{k}_v - \bar{K}_{iv}\right)\cdot \bar{r}_j\right) f_{vv}\left(\theta_s, \phi_s; \pi - \theta_i, \phi_i\right) \tag{2.2.40}$$

$$S_{vh}^{(1)} = \sum_{j=1}^{N} \exp\left(-i\left(\bar{k}_v - \bar{K}_{ih}\right)\cdot \bar{r}_j\right) f_{vh}\left(\theta_s, \phi_s; \pi - \theta_i, \phi_i\right) \tag{2.2.41}$$

Assuming that (1) there is no correlation between vegetation scatterers and the scattering from the vegetation scatterers are independent of each other, and (2) the vegetation scatterers are statistically identical and uniformly distributed in the vegetation layer, then

$$\begin{aligned}
&\left\langle S_{pp}^{(1)} S_{pp}^{(1)*} \right\rangle \\
&= \sum_{j=1}^{N} \frac{1}{V} \int d\bar{r}_j \exp\left(-i\left[\left(\bar{k}_p - \bar{K}_{ip}\right) - \left(\bar{k}_p^* - \bar{K}_{ip}^*\right)\right]\cdot \bar{r}_j\right) \left\langle f_{ppj}\left(\theta_s, \phi_s; \pi - \theta_i, \phi_i\right) f_{ppj}^*\left(\theta_s, \phi_s; \pi - \theta_i, \phi_i\right)\right\rangle \\
&= n_0 \int d\bar{r}_j \exp\left(-i\left[\left(\bar{k}_p - \bar{K}_{ip}\right) - \left(\bar{k}_p^* - \bar{K}_{ip}^*\right)\right]\cdot \bar{r}_j\right) \left\langle f_{ppj}\left(\theta_s, \phi_s; \pi - \theta_i, \phi_i\right) f_{ppj}^*\left(\theta_s, \phi_s; \pi - \theta_i, \phi_i\right)\right\rangle
\end{aligned} \tag{2.2.42}$$

In the backscattering direction,

$$\theta_s = \theta_i, \phi_s = \pi + \phi_i \tag{2.2.43}$$

After integration, the following results are obtained

$$\left\langle S_{pp}^{(1)} S_{pp}^{(1)*} \right\rangle = n_0 A \frac{1 - \exp\left(-4k_{ipz}^{"} d\right)}{4k_{ipz}^{"}} \left\langle \left| f_{pp}\left(\theta_i, \pi + \phi_i; \pi - \theta_i, \phi_i\right)\right|^2 \right\rangle \tag{2.2.44}$$

Hence, the backscattering coefficient for volume scattering is given by

$$\sigma_{pp}^{vol} = 4\pi n_0 \frac{1-\exp\left(-4k_{ipz}^{"}d\right)}{4k_{ipz}^{"}} \left\langle \left| f_{pp}\left(\theta_i, \pi+\phi_i; \pi-\theta_i, \phi_i\right)\right|^2 \right\rangle \tag{2.2.45}$$

In this chapter, only the backscattering coefficient for co-pol is calculated, because only co-pol is used for the data-cube based soil moisture retrieval as will be explained later. The backscattering coefficient for cross-pol can be calculated using a similar method by computing $\left\langle S_{pq}^{(1)} S_{pq}^{(1)*} \right\rangle$.

(b) Double-bounce Scattering

In this subsection, the expressions for double-bounce scattering are derived as below. The double-bounce scattering has two terms: (1) $\overline{E}_{sj}^{(2)}(\overline{r}) = \overline{\overline{G}}_{01}^{(R)} \overline{\overline{T}}_j \overline{E}_{inc}$, scattered by the vegetation scatterer and then reflected by the rough surface, and (2) $\overline{E}_{sj}^{(3)}(\overline{r}) = \overline{\overline{G}}_{01}^{(0)} \overline{\overline{T}}_j \overline{E}_{ref}$, reflected by the rough surface and then scattered by the vegetation scatterer:

$$\overline{E}_{sj}^{(2)}(\overline{r}) = \int d\overline{r}' \overline{\overline{G}}_{01}^{(R)} \int d\overline{r}'' < \overline{r}' \left| \overline{\overline{T}}_j \right| \overline{r}'' >< \overline{r}'' \mid \overline{E}_{inc} > \tag{2.2.46}$$

Substituting the expressions for $\overline{\overline{G}}_{01}^{(R)}$ and $\overline{E}_{inc}$, and using (2.2.29) – (2.2.30), we obtain that

$$\begin{aligned} \overline{E}_{sj}^{(2)}(\overline{r}) = {} & \frac{\exp(ikr)}{4\pi r} \int d\overline{r}' \left[\begin{array}{l} \hat{e}\left(k_z\right) R^{TE} \exp\left(2ik_{kz}d\right) \hat{e}\left(-k_z\right) \exp\left(-i\overline{K}_h \cdot \overline{r}'\right) \\ +\hat{h}\left(k_z\right) R^{TM} \exp\left(2ik_{vz}d\right) \hat{h}\left(-k_z\right) \exp\left(-i\overline{K}_v \cdot \overline{r}'\right) \end{array} \right] \\ & \int d\overline{r}'' \int \frac{d\overline{p}}{(2\pi)^3} \int \frac{d\overline{p}'}{(2\pi)^3} \exp\left(i\overline{p} \cdot \overline{r}' - i\overline{p}' \cdot \overline{r}''\right) \exp\left(-i\left(\overline{p} - \overline{p}'\right) \cdot \overline{r}_j\right) \overline{\overline{T}}_p\left(\overline{p}, \overline{p}'\right) \\ & \left[E_{vi} \hat{v}\left(\pi - \theta_i, \phi_i\right) \exp\left(i\overline{K}_{iv} \cdot \overline{r}''\right) + E_{hi} \hat{h}\left(\pi - \theta_i, \phi_i\right) \exp\left(i\overline{K}_{ih} \cdot \overline{r}''\right) \right] \end{aligned} \tag{2.2.47}$$

Using the following properties,

$$\begin{aligned}
&\int d\bar{r}' \exp\left(-i\bar{K}_h \cdot \bar{r}'\right)\exp\left(i\bar{p}\cdot\bar{r}'\right) = (2\pi)^3\delta\left(\bar{p}-\bar{K}_h\right)\\
&\int d\bar{r}' \exp\left(-i\bar{K}_v \cdot \bar{r}'\right)\exp\left(i\bar{p}\cdot\bar{r}'\right) = (2\pi)^3\delta\left(\bar{p}-\bar{K}_v\right)\\
&\int d\bar{r}'' \exp\left(-i\bar{p}' \cdot \bar{r}''\right)\exp\left(i\bar{K}_{iv}\cdot\bar{r}''\right) = (2\pi)^3\delta\left(\bar{p}'-\bar{K}_{iv}\right)\\
&\int d\bar{r}'' \exp\left(-i\bar{p}' \cdot \bar{r}''\right)\exp\left(i\bar{K}_{ih}\cdot\bar{r}''\right) = (2\pi)^3\delta\left(\bar{p}'-\bar{K}_{ih}\right)
\end{aligned} \tag{2.2.48}$$

Together with (2.2.13) – (2.2.16) and the relationship between the scattering amplitude and the T matrix, we obtain that

$$\begin{aligned}
&\bar{E}_{sj}^{(2)}(\bar{r}) = \frac{\exp(ikr)}{r}\times\\
&\left\{\begin{aligned}
&\hat{h}\left(\theta_s,\phi_s\right)R^{TE}\exp\left(2ik_{kz}d\right)\exp\left(-i\left(\bar{K}_h-\bar{K}_{iv}\right)\cdot\bar{r}_j\right)f_{hv}\left(\pi-\theta_s,\phi_s;\pi-\theta_i,\phi_i\right)E_{vi}\\
&+\hat{h}\left(\theta_s,\phi_s\right)R^{TE}\exp\left(2ik_{hz}d\right)\exp\left(-i\left(\bar{K}_h-\bar{K}_{ih}\right)\cdot\bar{r}_j\right)f_{hh}\left(\pi-\theta_s,\phi_s;\pi-\theta_i,\phi_i\right)E_{hi}\\
&+\hat{v}\left(\theta_s,\phi_s\right)R^{TM}\exp\left(2ik_{vz}d\right)\exp\left(-i\left(\bar{K}_v-\bar{K}_{iv}\right)\cdot\bar{r}_j\right)f_{vv}\left(\pi-\theta_s,\phi_s;\pi-\theta_i,\phi_i\right)E_{vi}\\
&+\hat{v}\left(\theta_s,\phi_s\right)R^{TM}\exp\left(2ik_{vz}d\right)\exp\left(-i\left(\bar{K}_v-\bar{K}_{ih}\right)\cdot\bar{r}_j\right)f_{vh}\left(\pi-\theta_s,\phi_s;\pi-\theta_i,\phi_i\right)E_{hi}
\end{aligned}\right\}
\end{aligned} \tag{2.2.49}$$

where

$$\begin{aligned}
f_{wv}\left(\pi-\theta_s,\phi_s;\pi-\theta_i,\phi_i\right) &= \frac{1}{4\pi}\hat{v}\left(\pi-\theta_s,\phi_s\right)\cdot\bar{\bar{T}}_p\left(k\hat{k}\left(\pi-\theta_s,\phi_s\right),k\hat{k}\left(\pi-\theta_i,\phi_i\right)\right)\cdot\hat{v}\left(\pi-\theta_i,\phi_i\right)\\
f_{vh}\left(\pi-\theta_s,\phi_s;\pi-\theta_i,\phi_i\right) &= \frac{1}{4\pi}\hat{v}\left(\pi-\theta_s,\phi_s\right)\cdot\bar{\bar{T}}_p\left(k\hat{k}\left(\pi-\theta_s,\phi_s\right),k\hat{k}\left(\pi-\theta_i,\phi_i\right)\right)\cdot\hat{h}\left(\pi-\theta_i,\phi_i\right)\\
f_{hv}\left(\pi-\theta_s,\phi_s;\pi-\theta_i,\phi_i\right) &= \frac{1}{4\pi}\hat{h}\left(\pi-\theta_s,\phi_s\right)\cdot\bar{\bar{T}}_p\left(k\hat{k}\left(\pi-\theta_s,\phi_s\right),k\hat{k}\left(\pi-\theta_i,\phi_i\right)\right)\cdot\hat{v}\left(\pi-\theta_i,\phi_i\right)\\
f_{hh}\left(\pi-\theta_s,\phi_s;\pi-\theta_i,\phi_i\right) &= \frac{1}{4\pi}\hat{h}\left(\pi-\theta_s,\phi_s\right)\cdot\bar{\bar{T}}_p\left(k\hat{k}\left(\pi-\theta_s,\phi_s\right),k\hat{k}\left(\pi-\theta_i,\phi_i\right)\right)\cdot\hat{h}\left(\pi-\theta_i,\phi_i\right)
\end{aligned} \tag{2.2.50}$$

Next, substituting into $\bar{E}_s = \sum_{j=1}^{N}\bar{E}_{sj}$ and using $R_v = R^{TM}, R_h = R^{TE}$ leads to

$$\bar{E}_s^{(2)}(\bar{r}) = \frac{\exp(ikr)}{r}\left[\hat{h}\left(\theta_s,\phi_s\right)\left(S_{hv}^{(2)}E_{vi}+S_{hh}^{(2)}E_{hi}\right)+\hat{v}\left(\theta_s,\phi_s\right)\left(S_{vv}^{(2)}E_{vi}+S_{vh}^{(2)}E_{hi}\right)\right] \tag{2.2.51}$$

where

$$S_{hv}^{(2)} = \sum_{j=1}^{N} R_{hs} \exp\left(2ik_{hz}d\right) \exp\left(-i\left(\bar{K}_h - \bar{K}_{iv}\right)\cdot \bar{r}_j\right) f_{hv}\left(\pi-\theta_s,\phi_s;\pi-\theta_i,\phi_i\right) \tag{2.2.52}$$

$$S_{hh}^{(2)} = \sum_{j=1}^{N} R_{hs} \exp\left(2ik_{hz}d\right) \exp\left(-i\left(\bar{K}_h - \bar{K}_{ih}\right)\cdot \bar{r}_j\right) f_{hh}\left(\pi-\theta_s,\phi_s;\pi-\theta_i,\phi_i\right) \tag{2.2.53}$$

$$S_{wv}^{(2)} = \sum_{j=1}^{N} R_{vs} \exp\left(2ik_{vz}d\right) \exp\left(-i\left(\bar{K}_v - \bar{K}_{iv}\right)\cdot \bar{r}_j\right) f_{vv}\left(\pi-\theta_s,\phi_s;\pi-\theta_i,\phi_i\right) \tag{2.2.54}$$

$$S_{vh}^{(2)} = \sum_{j=1}^{N} R_{vs} \exp\left(2ik_{vz}d\right) \exp\left(-i\left(\bar{K}_v - \bar{K}_{ih}\right)\cdot \bar{r}_j\right) f_{vh}\left(\pi-\theta_s,\phi_s;\pi-\theta_i,\phi_i\right) \tag{2.2.55}$$

The subscript 's' of R means the reflection coefficient in the specular direction.

Next, for the other term in the double-bounce scattering contribution,

$$\bar{E}_{sj}^{(3)}(\bar{r}) = \int d\bar{r}' \bar{G}_{01}^{(0)} \int d\bar{r}'' < \bar{r}' \left| \overline{\overline{T}}_j \right| \bar{r}'' >< \bar{r}'' \mid \bar{E}_{ref} > \tag{2.2.56}$$

Substituting the expressions for $\overline{\overline{G}}_{01}^{(0)}$ and $\bar{E}_{ref}$, and using (2.2.29) – (2.2.30) leads to

$$\begin{aligned}
&\bar{E}_{sj}^{(3)}(\bar{r}) = \frac{\exp(ikr)}{4\pi r} \int d\bar{r}' \left[\hat{e}\left(k_z\right)\hat{e}\left(k_z\right)\exp\left(-i\bar{k}_h\cdot\bar{r}'\right) + \hat{h}\left(k_z\right)\hat{h}\left(k_z\right)\exp\left(-i\bar{k}_v\cdot\bar{r}'\right)\right] \\
&\int d\bar{r}'' \int \frac{d\bar{p}}{(2\pi)^3} \int \frac{d\bar{p}'}{(2\pi)^3} \exp\left(i\bar{p}\cdot\bar{r}' - i\bar{p}'\cdot\bar{r}''\right)\exp\left(-i\left(\bar{p}-\bar{p}'\right)\cdot\bar{r}_j\right) T_p\left(\bar{p},\bar{p}'\right) \\
&\left[E_{vi}R_{vi}\exp\left(2ik_{ivz}d\right)\hat{v}\left(\theta_i,\phi_i\right)\exp\left(i\bar{k}_{iv}\cdot\bar{r}''\right) + E_{hi}R_{hi}\exp\left(2ik_{ihz}d\right)\hat{h}\left(\theta_i,\phi_i\right)\exp\left(i\bar{k}_{ih}\cdot\bar{r}''\right)\right]
\end{aligned} \tag{2.2.57}$$

Similarly, using the properties in (2.2.48) and (2.2.13) – (2.2.16) leads to

$$\bar{E}_{sj}^{(3)}(\bar{r}) = \frac{\exp(ikr)}{4\pi r} \begin{Bmatrix}
\hat{h}\left(\theta_s,\phi_s\right)\exp\left(-i\left(\bar{k}_h - \bar{k}_{iv}\right)\cdot\bar{r}_j\right) f_{hv}\left(\theta_s,\phi_s;\theta_i,\phi_i\right) E_{vi}R_{vi}\exp\left(2ik_{ivz}d\right) \\
+\hat{h}\left(\theta_s,\phi_s\right)\exp\left(-i\left(\bar{k}_h - \bar{k}_{ih}\right)\cdot\bar{r}_j\right) f_{hh}\left(\theta_s,\phi_s;\theta_i,\phi_i\right) E_{hi}R_{hi}\exp\left(2ik_{ihz}d\right) \\
+\hat{v}\left(\theta_s,\phi_s\right)\exp\left(-i\left(\bar{k}_v - \bar{k}_{iv}\right)\cdot\bar{r}_j\right) f_{vv}\left(\theta_s,\phi_s;\theta_i,\phi_i\right) E_{vi}R_{vi}\exp\left(2ik_{ivz}d\right) \\
+\hat{v}\left(\theta_s,\phi_s\right)\exp\left(-i\left(\bar{k}_v - \bar{k}_{ih}\right)\cdot\bar{r}_j\right) f_{vh}\left(\theta_s,\phi_s;\theta_i\right) E_h R_{hi}\exp\left(2ik_{ik}d\right)
\end{Bmatrix} \tag{2.2.58}$$

where

$$
\begin{aligned}
f_{wv}(\theta_s,\phi_s;\theta_i,\phi_i) &= \frac{1}{4\pi}\hat{v}(\theta_s,\phi_s)\cdot\overline{\overline{T}}_p\left(k\hat{k}(\theta_s,\phi_s),k\hat{k}(\theta_i,\phi_i)\right)\cdot\hat{v}(\theta_i,\phi_i)\\
f_{vh}(\theta_s,\phi_s;\theta_i,\phi_i) &= \frac{1}{4\pi}\hat{v}(\theta_s,\phi_s)\cdot\overline{\overline{T}}_p\left(k\hat{k}(\theta_s,\phi_s),k\hat{k}(\theta_i,\phi_i)\right)\cdot\hat{h}(\theta_i,\phi_i)\\
f_{hv}(\theta_s,\phi_s;\theta_i,\phi_i) &= \frac{1}{4\pi}\hat{h}(\theta_s,\phi_s)\cdot\overline{\overline{T}}_p\left(k\hat{k}(\theta_s,\phi_s),k\hat{k}(\theta_i,\phi_i)\right)\cdot\hat{v}(\theta_i,\phi_i)\\
f_{hh}(\theta_s,\phi_s;\theta_i,\phi_{ii}) &= \frac{1}{4\pi}\hat{h}(\theta_s,\phi_s)\cdot\overline{\overline{T}}_p\left(k\hat{k}(\theta_s,\phi_s),k\hat{k}(\theta_i,\phi_i)\right)\cdot\hat{h}(\theta_i,\phi_i)
\end{aligned}
\tag{2.2.59}
$$

Next, substituting into $\overline{E}_s=\sum_{j=1}^{N}\overline{E}_{sj}$, we obtain that

$$
\overline{E}_s^{(3)}(\overline{r})=\frac{\exp(ikr)}{r}\left[\hat{h}(\theta_s,\phi_s)\left(S_{hv}^{(3)}E_{vi}+S_{hh}^{(3)}E_{hi}\right)+\hat{v}(\theta_s,\phi_s)\left(S_{vv}^{(3)}E_{vi}+S_{vh}^{(3)}E_{hi}\right)\right] \tag{2.2.60}
$$

where

$$
S_{hv}^{(3)}=\sum_{j=1}^{N}\exp\left(-i\left(\overline{k}_h-\overline{k}_{iv}\right)\cdot\overline{r}_j\right)f_{hv}(\theta_s,\phi_s;\theta_i,\phi_i)R_{vi}\exp\left(2ik_{ivz}d\right) \tag{2.2.61}
$$

$$
S_{hh}^{(3)}=\sum_{j=1}^{N}\exp\left(-i\left(\overline{k}_h-\overline{k}_{ih}\right)\cdot\overline{r}_j\right)f_{hh}(\theta_s,\phi_s;\theta_i,\phi_i)R_{hi}\exp\left(2ik_{ihz}d\right) \tag{2.2.62}
$$

$$
S_{vv}^{(3)}=\sum_{j=1}^{N}\exp\left(-i\left(\overline{k}_v-\overline{k}_{iv}\right)\cdot\overline{r}_j\right)f_{vv}(\theta_s,\phi_s;\theta_i,\phi_i)R_{vi}\exp\left(2ik_{ivz}d\right) \tag{2.2.63}
$$

$$
S_{vh}^{(3)}=\sum_{j=1}^{N}\exp\left(-i\left(\overline{k}_v-\overline{k}_{ih}\right)\cdot\overline{r}_j\right)f_{vh}(\theta_s,\phi_s;\theta_i,\phi_i)R_{hi}\exp\left(2ik_{ihz}d\right) \tag{2.2.64}
$$

The scattering matrix of the double-bounce scattering is the sum of two terms,

$$
S_{pq}^{db}=S_{pq}^{(2)}+S_{pq}^{(3)} \tag{2.2.65}
$$

According to reciprocity [39],

$$
f_{pp}(\pi-\theta_i,\pi+\phi_i;\pi-\theta_s,\pi+\phi_s)=f_{pp}(\theta_s,\phi_s;\theta_i,\phi_i) \tag{2.2.66}
$$

In the backscattering direction, $k_{ipz} = k_{pz}$ and $\theta_s = \theta_i$. Thus, the following equality relations are established:

$$\exp\left(2ik_{pz}d\right) = \exp\left(2ik_{ipz}d\right) ;$$

$$\left(\overline{K}_p - \overline{K}_{ip}\right) = \left(\overline{k}_p - \overline{k}_{ip}\right) = k\left(\sin\theta_s\cos\phi_s - \sin\theta_i\cos\phi_i\right)\hat{x} + k\left(\sin\theta_s\sin\phi_s - \sin\theta_i\sin\phi_i\right)\hat{y} ;$$

$$\exp\left(-i\left(\overline{K}_p - \overline{K}_{ip}\right)\bullet\overline{r}_j\right) = \exp\left(-i\left(\overline{k}_p - \overline{k}_{ip}\right)\bullet\overline{r}_j\right) ;$$

$$R_{ps} = R_{pi} .$$

Therefore, in the backscattering direction, the forward and reverse going ground-vegetation interaction scattering fields are exactly the same, $S_{pp}^{(2)} = S_{pp}^{(3)}$.

Hence,

$$S_{pp}^{db} = \sum_{j=1}^{N} 2R_{ps}\exp\left(2ik_{pz}d\right)\exp\left(-i\left(\overline{K}_p - \overline{K}_{ip}\right)\cdot\overline{r}_j\right) f_{pp}\left(\pi-\theta_s,\phi_s;\pi-\theta_i,\phi_i\right) \qquad (2.2.67)$$

Similarly, assuming independent scattering, statistically identical and uniformly distributed vegetation scatterers, we obtain

$$\begin{aligned}\left\langle S_{pp}^{db}S_{pp}^{db^*}\right\rangle &= 4n_0\int d\overline{r}_j R_{ps}\exp\left(2ik_{pz}d\right)R_{ps}^{\ *}\exp\left(-2ik_{pz}^{*}d\right)\times \\ &\exp\left(-i\left[\left(\overline{K}_p - \overline{K}_{ip}\right) - \left(\overline{K}_p^{*} - \overline{K}_{ip}^{*}\right)\right]\cdot\overline{r}_j\right)\left\langle f_{ppj}\left(\pi-\theta_s,\phi_s;\pi-\theta_i,\phi_i\right) f_{ppj}^{*}\left(\pi-\theta_s,\phi_s;\pi-\theta_i,\phi_i\right)\right\rangle \qquad (2.2.68) \\ &= 4n_0 Ad\left|R_{ps}\right|^2\exp\left(-4k_{ipz}^{"}d\right)\left\langle\left|f_{pp}\left(\theta_i,\phi_i+\pi;\theta_i,\phi_i\right)\right|^2\right\rangle\end{aligned}$$

Thus, the backscattering coefficient for double scattering is

$$\sigma_{pp}^{db} = \frac{4\pi}{A}\left\langle S_{pp}^{db} S_{pp}^{db*}\right\rangle = 16\pi n_0 d\left|R_{ps}\right|^2 \exp\left(-4k_{ipz}^{"} d\right)\left\langle\left|f_{pp}\left(\theta_i,\phi_i+\pi;\theta_i,\phi_i\right)\right|^2\right\rangle \quad (2.2.69)$$

When there are several kinds of scatterers, such as the case for the canola canopy where the main stems, branches and leaves are modeled by different shapes, the effective propagation constant in the vegetation layer, the backscattering coefficient for volume scattering and the backscattering coefficient for double-bounce scattering are calculated as follows

$$k_p = k + \frac{2\pi}{k}\sum_{t=1}^{T} n_{0,t}\left\langle f_{pp,t}\left(\pi-\theta_i,\phi_i;\pi-\theta_i,\phi_i\right)\right\rangle \quad (2.2.70)$$

$$\sigma_{pp}^{vol} = 4\pi\frac{1-\exp\left(-4k_{ipz}^{"} d\right)}{4k_{ipz}^{"}}\sum_{t=1}^{T} n_{0,t}\left\langle\left|f_{pp,t}\left(\theta_i,\pi+\phi_i;\pi-\theta_i,\phi_i\right)\right|^2\right\rangle \quad (2.2.71)$$

$$\sigma_{pp}^{db} = 16\pi d\left|R_{ps}\right|^2 \exp\left(-4k_{ipz}^{"} d\right)\sum_{t=1}^{T} n_{0,t}\left\langle\left|f_{pp,t}\left(\theta_i,\phi_i+\pi;\theta_i,\phi_i\right)\right|^2\right\rangle \quad (2.2.72)$$

where T is the total number of scatterers' types (three for the canola: main stems, stalks and leaves), $n_{0,t}$ is the number of scatters of type t per unit volume and f_{ppt} is the scattering amplitude of the scatterer of type t.

Finally, the surface-scattering component in the backscattering direction is the bare rough-surface scattering coefficient reduced by the attenuation by the vegetation canopy,

$$\sigma_{pp}^{surf} = \exp\left(-4k_{ipz}^{"} d\right)\sigma_{pp}^{surf,bare} \quad (2.2.73)$$

where $\sigma_{pp}^{surf,bare}$ is the backscattering coefficient of the bare rough surface computed from NMM3D [32].

In the DBA, the total backscattering is the sum of the volume scattering, double-bounce scattering and surface scattering,

$$\sigma_{pp}^{total} = \sigma_{pp}^{vol} + \sigma_{pp}^{db} + \sigma_{pp}^{surf} \tag{2.2.74}$$

(c) Comparison with the First-Order Radiative Transfer Model

In this section, we compare the formulas of DBA with that of the first-order radiative transfer equation as used in the MIMIC model [2, 28, 43].

The effective propagation constant for *p* polarization k_p is a sum of real part k_p' and the imaginary part k_p''

$$k_p = k_p' + ik_p'' \tag{2.2.75}$$

Similarly, $k_{ipz} = k_{ipz}' + ik_{ipz}''$. Substituting them into $k_{ipz} = \sqrt{k_p^2 - k^2 \sin^2\theta_i}$ and then squaring both sides lead to

$$k_{ipz}'^2 - k_{ipz}''^2 + i2k_{ipz}'k_{ipz}'' = k_p'^2 - k_p''^2 + 2ik_p'k_p'' - k^2 sin^2\theta_i \tag{2.2.76}$$

Balancing the real and imaginary parts, and ignoring $k_{ipz}''^2$ and $k_p''^2$, because they are much smaller than the other terms, we obtain

$$k_{ipz}'^2 = k_p'^2 - k^2 sin^2\theta_i \tag{2.2.77}$$

$$k_{ipz}'' = \frac{k_p'k_p''}{k_{ipz}'} \tag{2.2.78}$$

In the vector radiative transfer equation, the imaginary part, k_p'', is equal to half of the extinction coefficient $\kappa_{e,p}$ [43]

$$k_p'' = \frac{\kappa_{e,p}}{2} \tag{2.2.79}$$

Since the fractional volume of vegetation is no more than 0.5% with the other 99.5% being air, $k_p' = k$, $k_{ipz}' = kcos\theta_i$. Hence,

$$k_{ipz}'' = \frac{\kappa_{e,p}}{2} sec\theta_i \tag{2.2.80}$$

Substituting into equation (2.2.45) leads to

$$\sigma_{pp}^{vol} = \frac{1-\exp\left(-2\tau_p sec\theta_i\right)}{2\kappa_{e,p} sec\theta_i}\left(n_0 4\pi\left\langle\left|f_{pp}\left(\theta_i, \pi+\phi_i; \pi-\theta_i, \phi_i\right)\right|^2\right\rangle\right) \tag{2.2.81}$$

where $\tau_p = \kappa_{e,p} d$ is the optical thickness and the quantity $4\pi\left\langle\left|f_{pp}\left(\theta_i, \pi+\phi_i; \pi-\theta_i, \phi_i\right)\right|^2\right\rangle$ is the averaged *pp*-polarized backscattering cross section of a single particle.

Similarly, the double-bounce scattering term becomes

$$\sigma_{pp}^{db} = 4d\left|\mathrm{R}_p\right|^2 \exp\left(-2\tau_p sec\theta_i\right)\left(n_0 4\pi\left\langle\left|f_{pp}\left(\theta_i, \pi; \theta_i, 0\right)\right|^2\right\rangle\right) \tag{2.2.82}$$

The surface-scattering term becomes

$$\sigma_{pp}^{surf} = \exp\left(-2\tau_p sec\theta_i\right)\sigma_{pp}^{surf,bare} \tag{2.2.83}$$

Equations (2.2.81) and (2.2.83) are the same as equations (11.10) and (11.4) in [2], respectively, derived from the first-order radiative transfer equation. (It is noted that the optical thickness is defined as $\tau_p = \kappa_{e,p} dsec\theta_i$ in [2].) Equation (2.2.82) is the same as equation (11.15a) in [2] except that equation (2.2.83) has a factor of 4 instead of 2. It is because the radiative transfer equation deals with power instead of electric fields [2] and ignores the coherent effects in the double-bounce direction. Thus, the DBA agrees with the first-order radiative transfer equation except that the double-bounce term in the DBA is two times larger than that in the first-order radiative transfer equation. This difference in the DBA is also called the backscattering enhancement, which is not considered in the radiative transfer equation.

Two modifications included in this section are the NMM3D for bare rough-surface scattering in the surface-scattering term and the coherent reflectivity (i.e., *R* in (2.2.69)) in the double-bounce term.

2.2.2 Computation and Validation for the Wheat and Canola Data-cubes

The variables defined in the three axes of the data-cubes [44] are the parameters which affect the backscattering coefficients mostly. The ranges of the data-cube axes are 0.1cm ~ 4.0cm for RMS height and 3 ~ 30 for the real part of $epsr_{soil}$, the combination of of which covers a wide range of natural conditions. The range for VWC depends on the typical VWC values for the particular crop. The wheat data-cubes are plotted in Figure II.2. The corresponding soil moisture can be obtained via the dielectric model for soil given in [22]. It is observed that the backscattering coefficients generally increase with the increase of rough surface RMS height and soil permittivity. When the RMS height is small, the backscattering coefficients first increases with VWC and then decreases with VWC when VWC is large. This is because, when RMS height is small, volume scattering and double-bounce scattering dominate. The scattering from the vegetation scatterers increases with VWC but larger VWC also provides larger attenuation. When the RMS height is large, the backscattering coefficients generally decreases with VWC. In this case, surface scattering dominates and larger VWC results in larger attenuation for the surface-scattering term.

In this section, we explain how to generate the data-cubes for wheat and canola fields. The data-cubes are then validated using the SMAPVEX12 data.

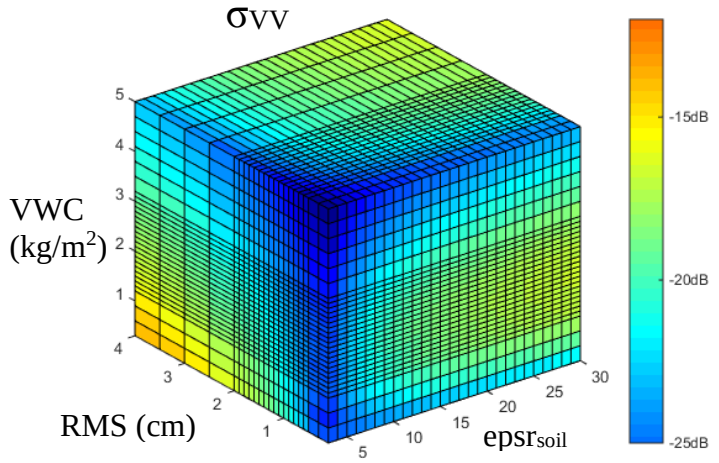

(a)

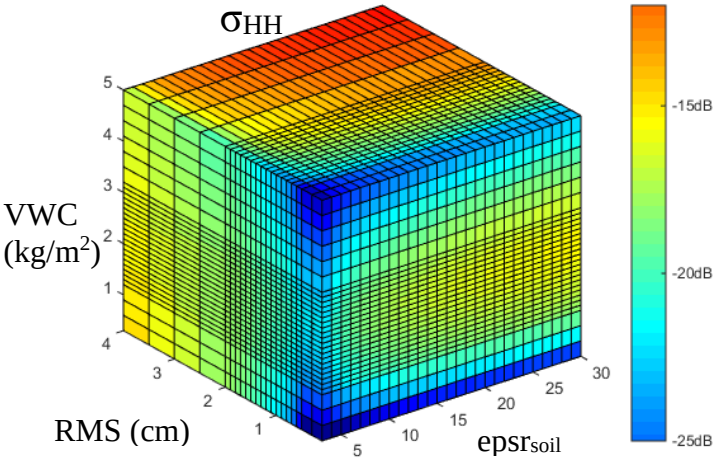

(b)

Figure II.2. Wheat data-cube, (a) σ_{VV}, (b) σ_{HH}. $epsr_{soil}$, stands for the real part of the soil permittivity.

As detailed in [10, 34], SMAPVEX12 was designed to support the development and assessment of SMAP soil moisture products in an agricultural region with an area of about 15km × 70km, located within the larger Red River Watershed south of Winnipeg, Manitoba (Canada). SMAPVEX12 was conducted between June 7 and July 19, 2012 during which soil moisture and vegetation conditions varied significantly, which provides extended-duration measurements that exceed those of any past soil moisture remote sensing field experiment. Uninhabited Aerial

Vehicle Synthetic Aperture Radar (UAVSAR) [45], an aircraft-based fully polarimetric L-band radar, provided high-quality backscatter data, with its high spatial resolution, stable platform, and reliable calibration. The aircraft carrying the UAVSAR was flown several times per week, a frequency similar to that of the SMAP satellite. Data within the UAVSAR swath were collected over a wide range of incidence angles. These σ_0 values were normalized to an incidence angle of 40 degrees for this algorithm test in order to be applicable to the SMAP data, using the histogram-matching method [46]. The residual error in the normalization is smaller than 1 dB stdev. The speckle noise was nearly removed by averaging over a large number of single looks at ~7m resolution over each field (~800m×800m). The measured backscatter coefficients are compared with the outputs from the data-cubes and also serve as the inputs for the time-series retrieval of soil moisture, which will be presented in later sections. The VWC, RMS rough-surface height and soil permittivity (and hence, soil moisture) were also measured, which are the inputs to sample the data-cube of VV and HH backscattering coefficients. VWC was measured through destructive sampling at three sample points for each field by cutting and collecting the plants on the ground in a small area with all the measurements scaled to 1 m^2 area. The water content is the wet weight minus dry weight obtained by drying the sampled plants in an oven for several days, then multiplied by a conversion factor to account for the little remained water after the drying process. The RMS height of each field is assumed to be constant during SMAPVEX12 because the experiment began after seeding and without further tillage operations to affect the roughness. The surface topography was approximately flat for the vegetation fields. The RMS height of each field was acquired by post-processing the data measured using the 1m long profilometer together with a digital camera. Repeated measurements were performed to obtain a 3m profile consisting of three 1m profiles for each site. During flight days, the soil moisture, which changed rapidly, was

measured concurrently with the airborne acquisitions so that the backscatter and soil moisture data collection were nearly coincident. The handheld Stevens Water Hydra Probe connected to a Personal Digital Assistant was used to measure the surface soil moisture with site-specific calibrations [47, 48] where individual calibration equations were developed for each of the fields. There were 16 soil moisture sample points for each field with three replicate volumetric soil moisture measurements at each point so as to capture spatial variability. Vegetation attributes, such as crop density, plant height, stem diameter, stalk height, stalk angle, leaf thickness and leaf width were also measured, which provided a basis for specifying the parameters of the physical forward models used to compute the data-cubes. For each field, the plant density was obtained by counting the number of plants in ten rows with 1m row length. Plant height and stem diameter were measured at the sample points for VWC just before cutting the vegetation samples, with ten measurements at each point. The other vegetation attributes were measured at four wheat fields and three canola fields five to six times during the campaign. [34].

(a) Vegetation and Roughness Parameters for the Wheat and Canola

Wheat is modeled as a layer of uniformly distributed cylinders with different orientations as shown in Figure II.3. The model parameters for the wheat data-cube presented in Table II-1 are estimated from the ground measurements of SMAPVEX12.

Table II-1. Model parameters for the wheat data-cube.

The probability function for scatterer elevation angle (β, measured from vertical, as shown in Figure II.3 (a)) is chosen to be $p(\beta)=C\sin^2(\beta)\cos^2(\beta)$ so that a good agreement between the data-cube and measurements is achieved, where the coefficient C is determined so that the integration of $p(\beta)$ over $0 \sim 30^\circ$ is 1. The distribution of scatterer azimuth angle (α as shown in Figure II.3 (a)) is uniform over all the angles.

Diameter (mm)	M_{veg}	N_a (m^{-2})	β	α
3.6	50%	350	$0 \sim 30^\circ$	$0 \sim 360^\circ$

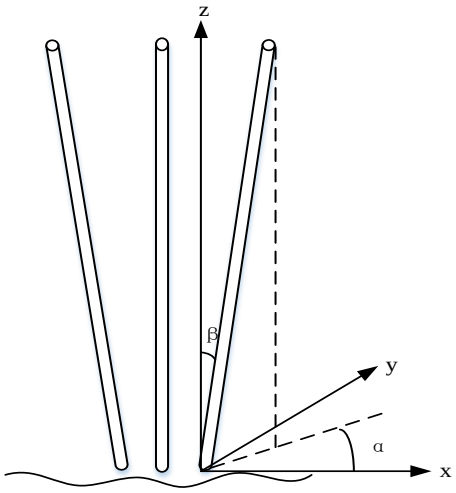

(a)

(b)

Figure II.3. (a) Wheat model, (b) picture of wheat from the SMAPVEX12 campaign.

The length of the cylinders is calculated from VWC using:

$$l = \frac{VWC}{\pi a^2 \rho_{water} N_a Mveg_{wheat}} \tag{2.2.84}$$

Where a, ρ_{water}, N_a and M_{veg} stand for radius, water density, number of cylinders per m^2 and volumetric water content of vegetation, respectively. The measured length is not used because it was not necessarily synchronized with UAVSAR data; however, VWC was synchronized with UAVSAR data. M_{veg} is estimated from the gravimetric water content (M_g) measured during SMAPVEX12 which determines the dielectric constant [49] of a plant organ and subsequently affects the scattering by the vegetation. These parameters are used to calculate VV and HH backscattering coefficients to form the wheat data-cubes using the scattering model developed in section 2.2 for different ratios of cl/s (correlation length to RMS height) [5].

(a) (b) (c)

Figure II.4. (a) Canola model; picture of canola from SMAPVEX12 taken at (b) June 25th, (c) July 17th .

For canola, two different types of cylinders with different radii and lengths are used to model the main stem and branches while circular disks are used to model the leaves, as shown in Figure II.1 and Figure II.4 (a). These elements are assumed to be uniformly distributed in the canola layer, similar to the wheat case.

Table II-2. Experimental data of SMAPVEX12 canola Field 84 at two different dates. Mv is the volumetric soil moisture, hereinafter the same.

Date	Mv	VWC	VV backscattering coefficients	HH backscattering coefficients
June 25th	0.14 cm^3/cm^3	2.23 kg/m^2	-13.34 dB	-10.21 dB
July 17th	0.13 cm^3/cm^3	2.37 kg/m^2	-16.95 dB	-14.74 dB

Table II-2 lists the measured volumetric soil moisture (Mv), VWC, and the VV and HH backscattering coefficients for the same field on two different dates in June and July during SMAPVEX12. There is about a 4dB difference for both VV and HH backscattering coefficients between those two dates even though the soil moisture and the VWC are similar. The RMS height

and cl/s ratio for the same field are approximately the same during the experiment, since they are expected to vary very little in the absence of tillage. The reason for the backscatter difference is that the leaves take larger portion of the total VWC in June than in July. It can be seen from Figure II.4 (b) and (c) that there were more leaves with larger radii in June than in July. The backscattering of leaves increases with their radius and density. Generally, the volume scattering, which is mostly contributed by the leaves, dominates the total backscattering for canola (i.e., the total backscattering is mainly determined by the scattering by leaves.). Thus, for the two cases with the same VWC which is the sum of VWC, from leaves, branches and main stems, the one with more leaves generates more backscattering.

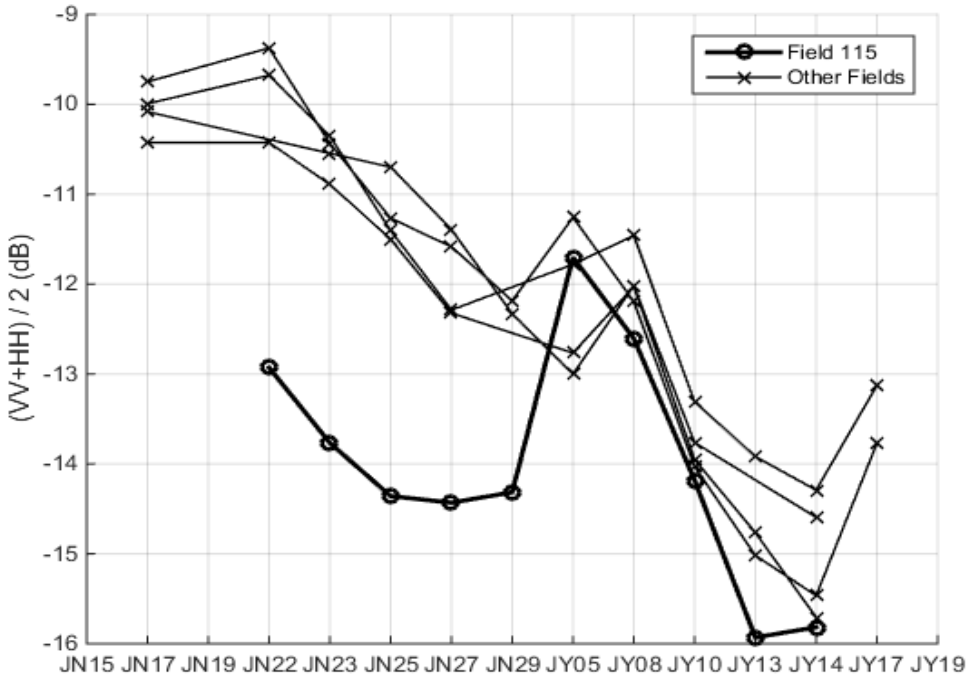

Figure II.5. (VV+HH)/2 data for the five SMAPVEX12 canola fields: large decrease observed between July 8th and 10th. The x-axis presents time: "JN" stands for "June" while "JY" stands for "July", hereinafter the same.

In the data-cubes, each set of input (Mv, VWC, RMS height, and cl/s ratio) should produce only one unique set of VV and HH backscattering coefficients. Thus, two different data-cubes

computed from different model parameters are needed for canola in order to account for the two significantly different values of VV and HH backscattering coefficients in Table II-2. In the evaluation of the data-cube and its inversion for soil moisture retrieval, it will be necessary to know when to use the appropriate data-cube. As shown in Figure II.5, there was a large decrease in the measured (VV+HH)/2 between July 8th and July 10th for all the canola fields despite the fact that there was no significant decrease in soil moisture or VWC based upon the ground measurement in Table II-3. Therefore, a switch is made in the data-cube used beginning July 10th (July data-cube). It is also noticed in Figure II.5 that the (VV+HH)/2 for canola Field 115 was much smaller than that of the other fields in June, so the July data-cube which produces smaller VV and HH backscattering coefficients is used for Field 115 over the entire period. The parameters used to generate the two data-cubes are listed in Table II-4. The M_{veg} and leaf radius are adjusted to smaller values for the July data-cube based on the ground measurement, which can also be seen from Figure II.4 (b) and (c) where the canola in July appears to be withered compared to conditions in June.

Table II-3. Change of Mv and VWC for the canola fields (July 10th minus July 8th).

Field No.	61	84	115	122	124
ΔMv (cm^3/cm^3)	0.056	0.084	-0.064	0.0048	0.029
ΔVWC (kg/m^2)	0.10	0.10	0.074	-0.20	-0.38

From the in-situ measurements, the average number of canola plants per m^2 (N_a) is about 60 and the number of leaves per plant (N_l) is about bN_s with b = 2 and 1 for June and July data-cubes, respectively and N_s is the number of branches per plant. The main stem diameter (d), which increases with VWC, is calculated from the allometric relationship with VWC obtained from the data through curve fitting:

$d = -0.03135VWC^2 + 0.938VWC + 4.87$ in mm,

as shown in Figure II.6 (a). Similarly, the main stem length (l) is obtained from: $l = -121.4VWC^{-1.186} + 130.2$ in cm,

as shown in Figure II.6 (b). N_s can be calculated from VWC using the following formula:

$$N_s = \frac{VWC - \rho_{water} N_a Vol_{stem} Mveg_{stem}}{N_a \rho_{water} (Vol_{branch} Mveg_{branch} + bVol_{leaf} Mveg_{leaf})} \quad (2.2.85)$$

where Vol_{stem}, Vol_{branch} and Vol_{leaf} are the volume of stem, branch and leaf, respectively.

Table II-4. Model parameters for the canola data-cubes.
The M_{veg} values in plain font and in parentheses are used for June and July data-cube, respectively. M_{veg} is estimated from the measured M_g in the way as the wheat [49]. VWC is measured in situ. d and l are derived from VWC based on the empirical allometry relationships. The distribution of azimuthal angle (α as shown in Figure II.4 (a)) is uniform over $0 \sim 360^\circ$ for the stem, branch and leave.

	Diameter (mm)	Length (cm)	M_{veg}	Distribution of β
Stem	d	l	60% (*40%*)	Uniform over $0 \sim 5^\circ$
Branch	$d/2$	$l/3$	60% (*40%*)	Uniform over $0 \sim 35^\circ$
Leaf	140 (*80*)	0.03	60% (*40%*)	Uniform over $40^\circ \sim 90^\circ$

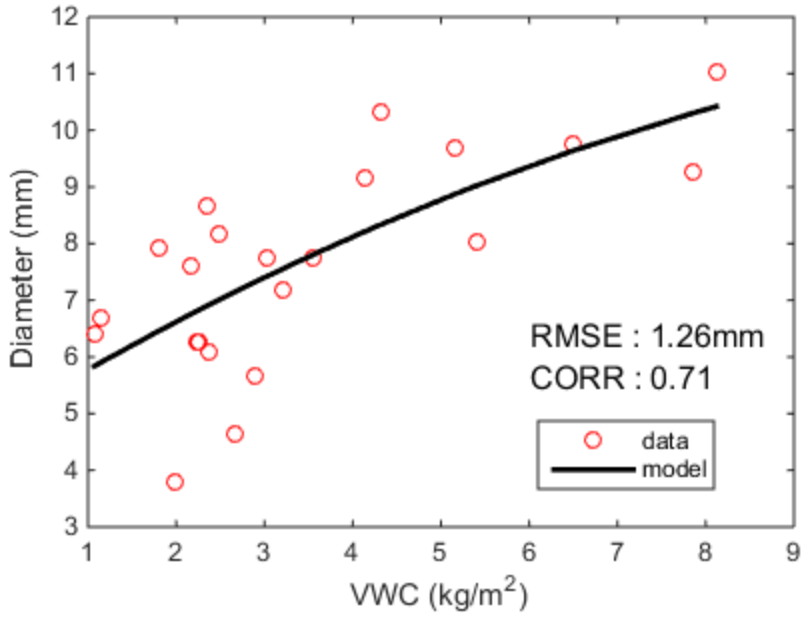

(a)

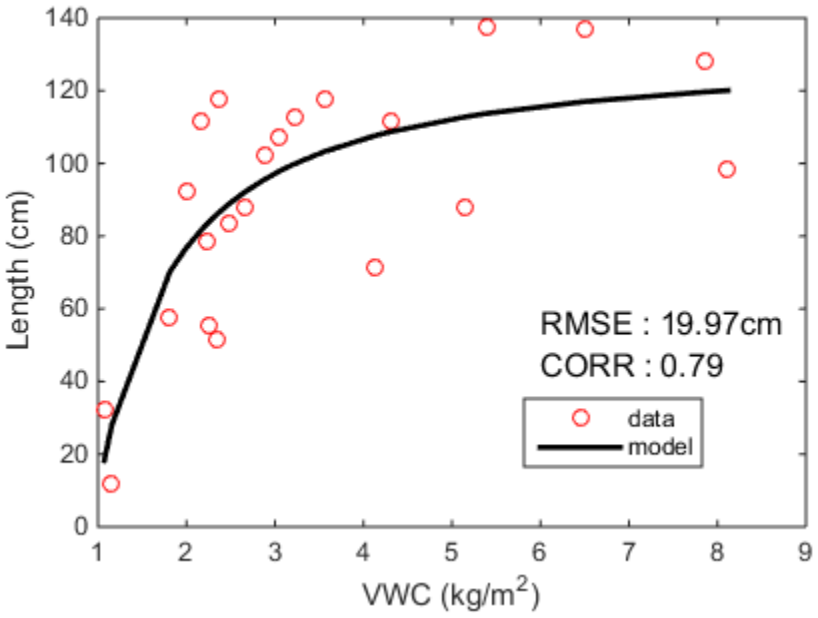

(b)

Figure II.6. Vegetation parameters during SMAPVEX12: (a) Main stem diameter as a function of VWC, (b) Main stem length as a function of VWC.

(b) Validation for the Wheat and Canola Data-cubes

First, we compute the data-cubes using the model described in section 2.2.2 (a) and using vegetation and roughness parameters as measured in section 2.2.2 (b).

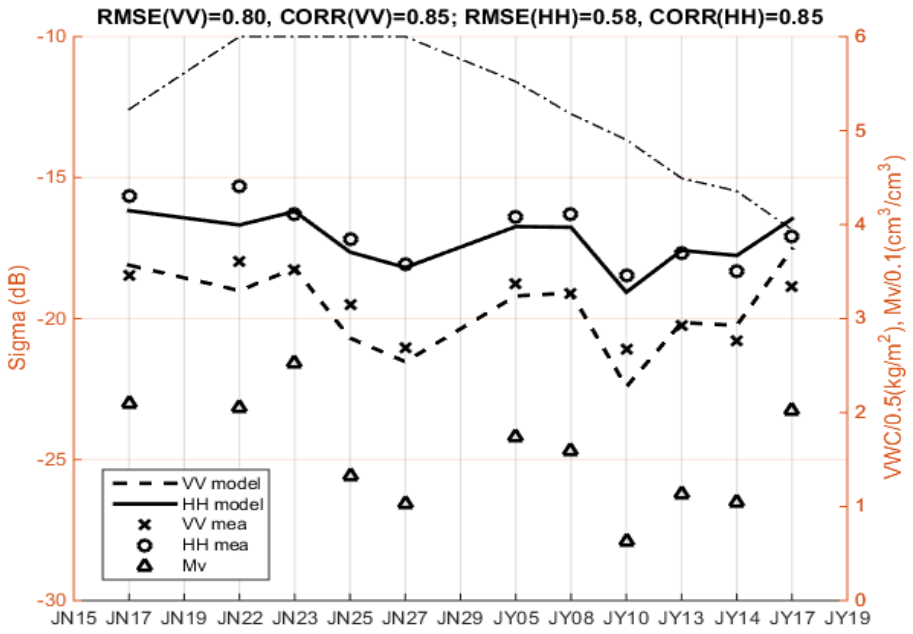

Figure II.7. Wheat data-cube applied to SMAPVEX12 wheat Field 91 with cl/s=15. 'CORR' is short for 'correlation coefficient'. The dash-dot curve plots VWC, hereinafter the same. 'VV model' and 'HH model' indicate the backscatters from the data-cube. 'VV mea' and 'HH mea' represent the measured backscatters from the UAVSAR. Soil moisture (Mv) and VWC are scaled as Mv/0.1 and VWC/0.5 for plot, respectively.

Next, the data-cubes are evaluated by comparing the predictons to the backscatter measurements from the UAVSAR for the ten wheat fields and five canola fields studied during SMAPVEX12. The measured RMS height, VWC and in-situ soil moisture are used as inputs to the data-cube to estimate the VV and HH backscattering coefficients, and then compared to the UAVSAR data for each day of flight. An example of the time-series forward comparison between the data-cube and the UAVSAR data for one of the wheat fields is presented in Figure II.7, which has an RMSE of 0.80 dB and 0.58 dB for VV and HH backscattering coefficients, respectively.

Here,

$$RMSE = \sqrt{\frac{1}{N}\sum_{i=1}^{N}\left(\sigma_{data,\mathrm{i}} - \sigma_{cube,\mathrm{i}}\right)^2} \tag{2.2.86}$$

where N is the number of samples, σ_{data} is the measured backscattering coefficient and σ_{cube} is the predicted backscattering coefficient from the data-cube.

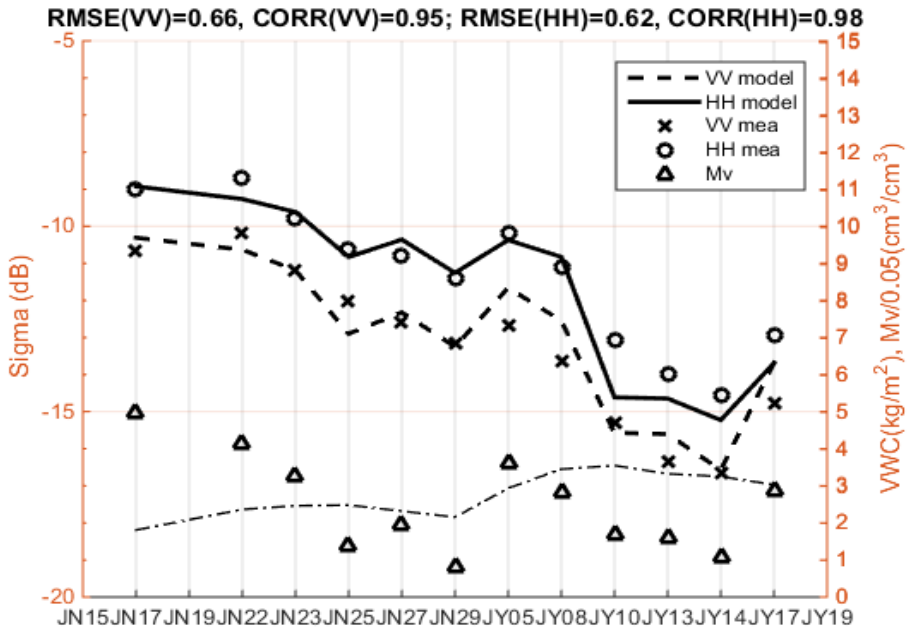

Figure II.8. Canola data-cubes applied to SMAPVEX12 canola Field 61 with cl/s=4. Soil moisture (Mv) is scaled as Mv/0.05 for plot.

Similarly, Figure II.8 is one example for the canola fields (RMSE values of 0.66 dB and 0.62 dB and correlation coefficients of 0.95 and 0.98 for VV and HH backscattering coefficients, respectively). The forward comparisons for all the wheat and canola fields are presented using the scatter plots in Figure II.9 and Figure II.10. The RMSE and correlation coefficient for each field are listed in Table II-5 and Table II-6. The RMSE for all the wheat fields is 0.97 dB for VV backscattering coefficients and 0.82 dB for HH backscattering coefficients while the RMSE for

the all canola fields is 1.30 dB for VV backscattering coefficients and 0.78 dB for HH backscattering coefficients.

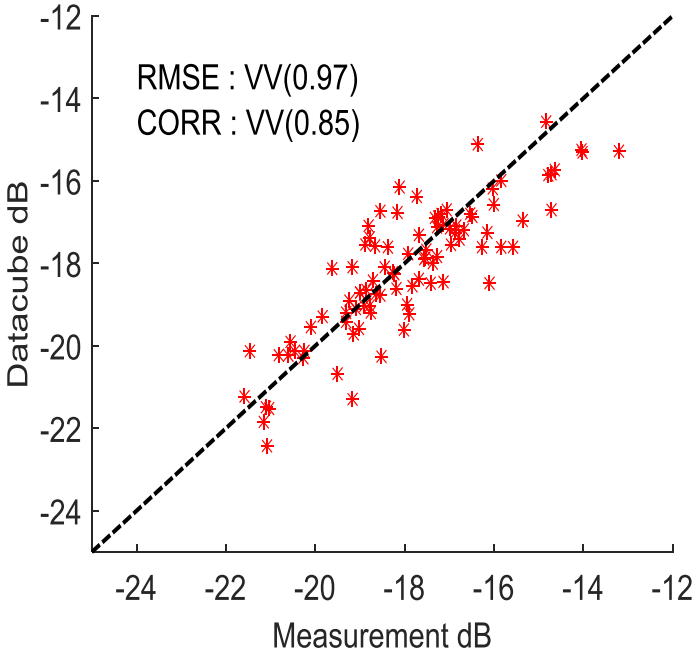

(a)

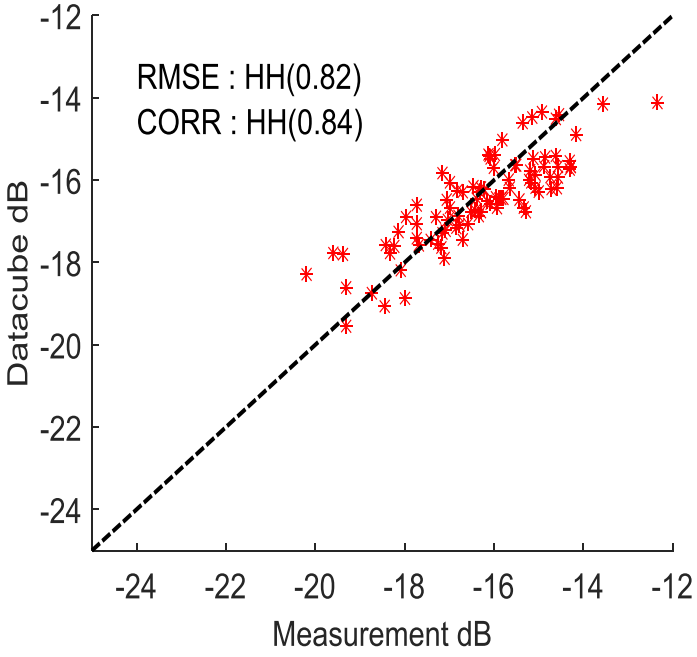

(b)

Figure II.9. Comparison between the data-cube and UAVSAR measurements for the ten SMAPVEX12 wheat fields (a) VV backscattering coefficients, (b) HH backscattering coefficients.

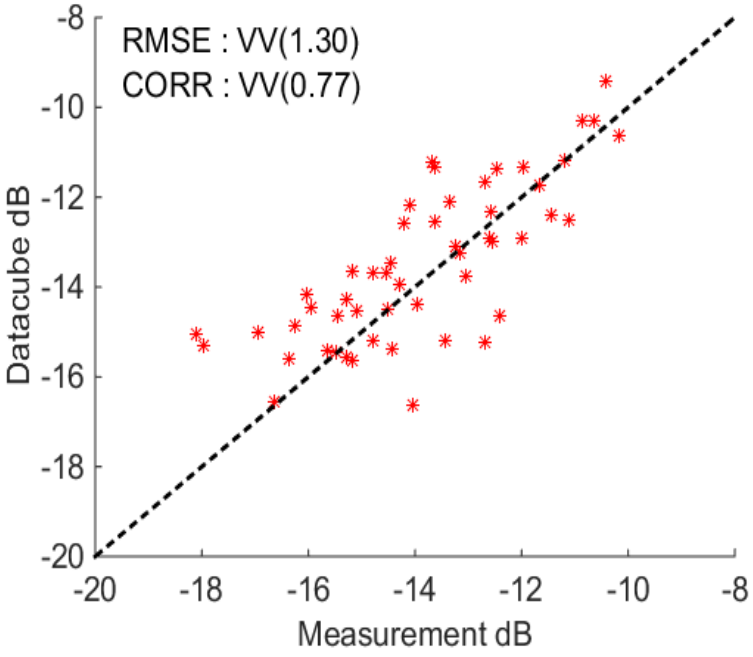

(a)

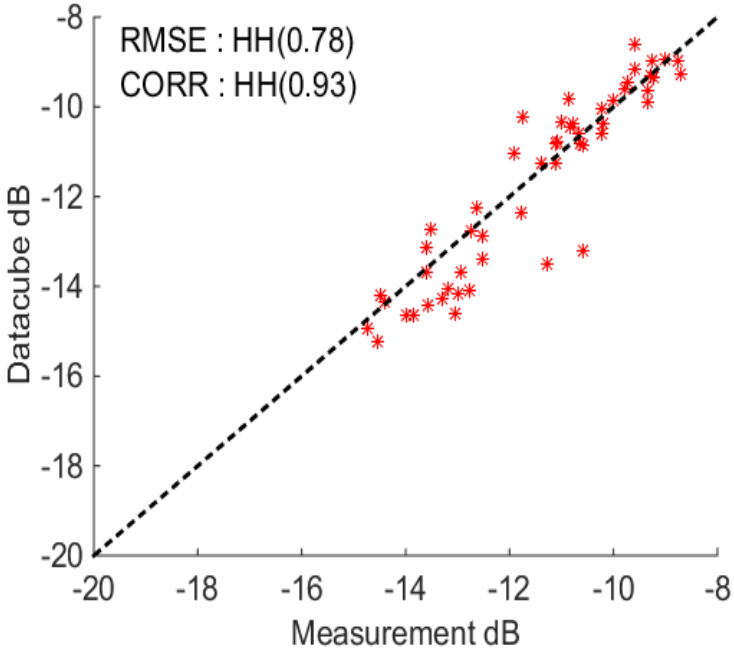

(b)

Figure II.10. Comparison between the data-cube and UAVSAR measurements for the five SMAPVEX12 canola fields (a) VV backscattering coefficients, (b) HH backscattering coefficients.

Table II-5. RMSE and correlation coefficient of backscatters between data-cube simulations and UAVSAR observations for the ten wheat fields.

Field No.	RMSE (dB)		Correlation Coefficient	
	VV	HH	VV	HH
91	0.80	0.58	0.85	0.85
85	0.91	0.87	0.62	0.87
81	1.37	0.84	0.88	0.94
74	0.66	0.98	0.88	0.91
73	0.56	1.03	0.99	0.92
65	1.51	0.64	0.95	0.96
44	1.04	0.87	0.83	0.89
42	1.04	0.74	0.82	0.89
41	0.62	0.56	0.90	0.98
31	1.02	0.91	0.82	0.97

Table II-6. RMSE and correlation coefficient of backscatters between data-cube simulations and UAVSAR observations for the five canola fields.

Field No.	RMSE (dB)		Correlation Coefficient	
	VV	HH	VV	HH
124	1.75	0.47	0.45	0.95
122	0.94	0.60	0.87	0.96
115	1.46	1.23	0.79	0.57
84	1.55	0.78	0.86	0.95
61	0.66	0.62	0.95	0.98

Table II-7. Error of estimated backscatters for wheat, compared with [27].

	E_{sys} (dB)		E_{res} (dB)		E_{tot} (dB)	
	VV	HH	VV	HH	VV	HH
Site #12 of [27]	-1.17	-0.10	0.91	0.68	1.48	0.96
Site #13 of [27]	-0.57	0.63	0.76	0.47	0.95	0.79
Ten SMAPVEX12 Fields	0.20	0.17	0.82	0.68	0.84	0.70

Table II-8. Error of estimated backscatters for canola, compared with [27].

	E_{sys} (dB)		E_{res} (dB)		E_{tot} (dB)	
	VV	HH	VV	HH	VV	HH
Site #23 of [27]	-2.27	-0.51	1.06	0.70	2.51	0.86
Site #31 of [27]	-0.18	0.18	1.08	0.73	1.09	0.75
Five SMAPVEX12 Fields	-0.34	0.18	1.03	0.66	1.08	0.69

The systematic error (E_{sys}), residual error (E_{res}) and total error (E_{tot}) defined as below [27] are also calculated for all the wheat and canola fields.

$$E_{sys} = \frac{1}{N}\sum_{i=1}^{N}\left(\sigma_{data,\mathrm{i}} - \sigma_{cube,\mathrm{i}}\right) \tag{2.2.87}$$

$$E_{res} = \sqrt{\frac{1}{N}\sum_{i=1}^{N}\left(\left|\sigma_{data,\mathrm{i}} - \sigma_{cube,\mathrm{i}}\right| - \left|E_{sys}\right|\right)^2} \tag{2.2.88}$$

$$E_{tot} = \sqrt{E_{sys}^2 + E_{res}^2} \tag{2.2.89}$$

The results are compared with [27] at 40 degrees incident angle and L-band as shown in Table II-7 and Table II-8 for wheat and canola, respectively. In terms of the number of fields, SMAPVEX12 with ten wheat fields and five canola fields provides more extensive data than [27] which has two wheat fields and two canola fields. The total error from the wheat data-cube is smaller than that from [27], especially compared to the VV backscattering coefficients for site #12 where the total error from the data-cube is smaller by 0.64 dB. For the canola data-cubes, the total error is also smaller than that from [27] and is smaller by 1.42 dB than the VVbackscattering coefficients for site #23.

Some sources of error to be considered when interpreting the results are: (1) the ground measurements of RMS height, VWC and soil moisture (e.g., the RMS height was likely to be influenced by the rain which would flatten the soil surface but a constant RMS height was used during the whole study period for each field), (2) UAVSAR data (e.g., there is a normalization error when normalizing the raw data to 40º and the RMSE is about 1 dB [34]), (3) Data-cube parameters (e.g., the plant density is generally different for different fields and only an average value is used in the data-cube that is applied to all the fields), (4) Scattering model (e.g., the scatterers are assumed to be uniformly distributed in the vegetation layer which is unlikely to be true for the crop fields. Furthermore, the space between rows is not taken into account, where the

surface scattering is larger than that from the current model because of no attenuation by the vegetation layer).

The results of Figure II.9 and Figure II.10 show that the data-cube model predictions are in good agreement with airborne radar measurements.

2.3 An Improved Coherent Model for Soybean Fields

In this section, an improved coherent branching model for L-band radar remote sensing of soybean is proposed by taking into account the correlated scattering among scatterers. The novel feature of the analytical coherent model consists of conditional probability functions to eliminate the overlapping effects of branches in the former branching models. There are models using fractal-generated plants to eliminate overlap [50-52]. They can be more computationally intenstive compared with the one using conditional probalility functions. Backscattering coefficients are considered for a variety of scenarios over the full growth cycle for vegetation water content (VWC) and the complete drydown conditions for soil moisture. The results of the coherent model show that HH scattering has a significant difference of up to 3 dB from that of the independent scattering when VWC is low (~ 0.2 kg/m^2). Forward model calculations are performed for scattering from the soybean field for the full range of the three axes of data-cubes using the coherent model. The soybean volume scattering including the double-bounce term is combined with the forward scattering model of bare soil from the numerical Maxwell solutions that incorporates RMS height, soil permittivity and correlation length, to form the forward model lookup-table for the vegetation-covered soil. The results are compared with data from 13 soybean fields collected as part of the Soil Moisture Active Passive Validation Experiment 2012 (SMAPVEX12).

2.3.1 Incoherent and Coherent Models

Soybean is a branching plant composed of a main stem and several stalks attached with a compound leaf which is comprised of three leaflets [36], as shown in Figure II.11 (a). The soybean plant is modeled as a vertical cylinder (main stem) with several attached branches, drawn in Figure II.11 (b). Each branch is a combination of a cylinder (stalk) and three disks (leaves). The orientation angles of the stem, stalk and disk are based on the Eulerian angle system [28]. As shown in Figure II.11 (c), (α, β) and (α_d, β_d) are the orientation angles of cylinder and disk, respectively, with alpha and beta referring to the azimuth and elevation angles. The lengths of stem and stalk are d and l, respectively. (x_j, y_j, z_j) is the position of scatterer j and (α_s, β_s), which defines the orientation angle of stem are not illustrated in the simplified sketch.

Let the direction of the incident wave be (θ_i, ϕ_i) and $\hat{K}_i$ be the incident wave vector

$$\hat{K}_i = \sin\theta_i \cos\phi_i \hat{x} + \sin\theta_i \sin\phi_i \hat{y} - \cos\theta_i \hat{z} \tag{2.3.1}$$

Then the specular reflected direction is

$$\hat{k}_i = \sin\theta_i \cos\phi_i \hat{x} + \sin\theta_i \sin\phi_i \hat{y} + \cos\theta_i \hat{z} \tag{2.3.2}$$

Let $k_{xi} = k\sin\theta_i \cos\phi_i, k_{yi} = k\sin\theta_i \sin\phi_i$ and $k_{zi} = k\cos\theta_i$, where k is the wave number in free space. Let $f_{pp}(\hat{k}_s, \hat{k})$ be the scattering amplitude from direction $\hat{k}$ to $\hat{k}_s$. The function f is calculated by ICA [4] for the cylinder (f^c) and Generalized Rayleigh-Gans Approximation [4] for the disk (f^d). The subscript p denotes the polarization.

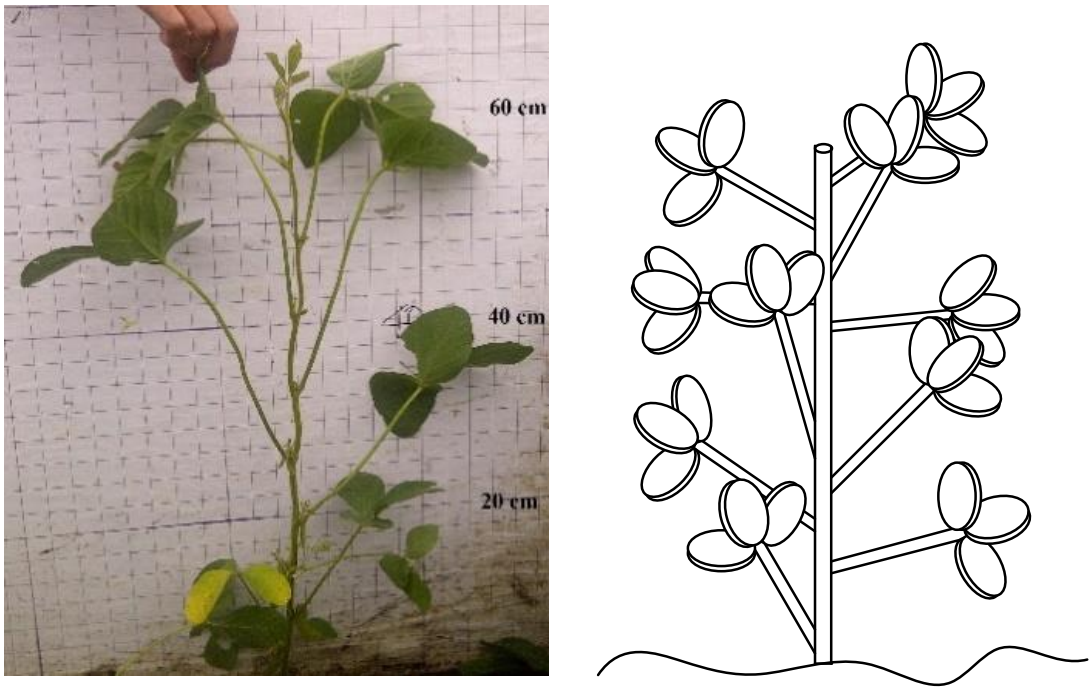

(a) (b)

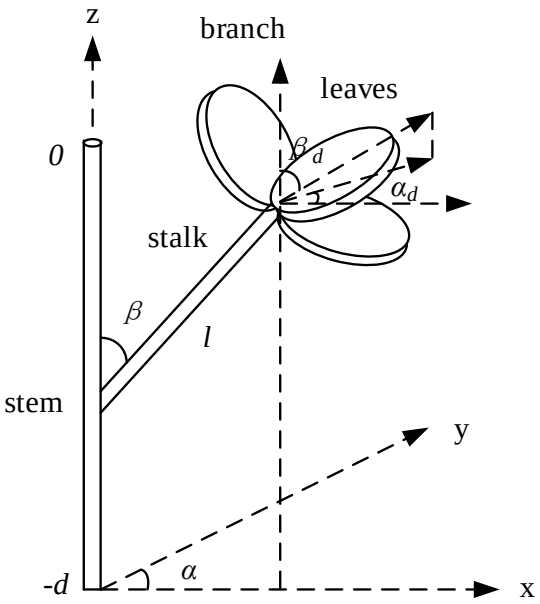

(c)

Figure II.11. (a) Picture of a soybean plant from SMAPVEX12, (b) Diagram of a soybean plant, (c) Sketch of coordinate system and characteristic parameters.

We only consider like polarization (i.e., VV and HH) in this chapter. Let us first ignore the difference between the propagation constants in the air and vegetation layer. As shown in Figure II.12, $f_{pp}(-\hat{K}_i, \hat{K}_i)$ is the scattering amplitude for volume scattering (term 1), while $f_{pp}(-\hat{k}_i, \hat{K}_i)$ is the scattering amplitude in the double-bounce direction (terms 2 and 3). A factor of 2 is added to account for terms 2 and 3 which are the same because of reciprocity. In the case of soybean fields, the triple bounce term is likely to be weak and thus ignored.

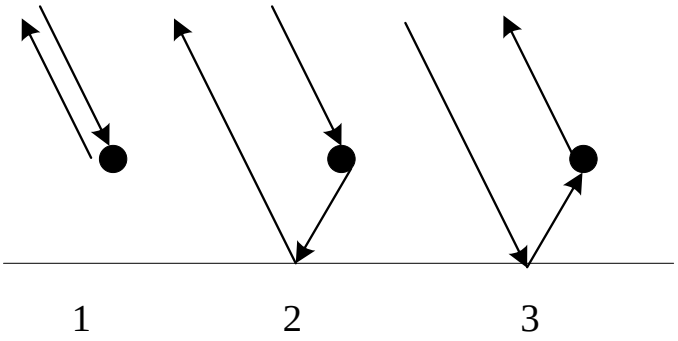

Figure II.12. Backscattering Terms.

For the coherent model, we need to include the phase term associated with the position of the scatterer and the path of the wave in the random medium. For volume and double-bounce scattering:

$$F_{vol} = \exp\left[2i\left(k_{xi}x_j + k_{yi}y_j - k_{zi}z_j\right)\right] f_{pp}(-\hat{K}_i, \hat{K}_i) \tag{2.3.3}$$

$$F_{db} = 2R_p \cdot \exp\left[2i\left(k_{xi}x_j + k_{yi}y_j + k_{zi}d\right)\right] f_{pp}(-\hat{k}_i, \hat{K}_i) \tag{2.3.4}$$

where the subscripts "vol" and "db" stand for volume scattering and double-bounce scattering, respectively. The corresponding subscript pp in F indicating either VV or HH is omitted for simplicity. The symbol d is the vegetation layer thickness, which is assumed to be the same as the length of the main stem in the case of soybean. R_p is the Fresnel reflection coefficient determined by numerical solutions of Maxwell's equations in 3 dimensional simulations (NMM3D)

for random rough-surface scattering [32]. It is worth noting that the double-bounce scattering does not depend on the z component of the scatter's coordinate.

(a) Incoherent Model

For the incoherent model, since a branch consists of a stalk (cylinder) and a compound leaf (disk), the scattering by one branch is given by

$$\left\langle \left| F_{inco}^{branch} \right|^2 \right\rangle = \left\langle \left| F_{vol}^{c} \right|^2 \right\rangle + \left\langle \left| F_{db}^{c} \right|^2 \right\rangle + \left\langle \left| F_{vol}^{d} \right|^2 \right\rangle + \left\langle \left| F_{db}^{d} \right|^2 \right\rangle \tag{2.3.5}$$

where the superscripts c and d stand for cylinder and disk, respectively, and the subscript "$inco$" stands for incoherent. The angle brackets represent averaging. Let N_L be the number of branches per soybean plant. Hence, the scattering by one plant is

$$\left\langle \left| F_{inco}^{plant} \right|^2 \right\rangle = \left\langle \left| F^{stem} \right|^2 \right\rangle + N_L \left\langle \left| F_{inco}^{branch} \right|^2 \right\rangle \tag{2.3.6}$$

Let N_S be the number of soybean plants in a unit area (1 m^2) field. The overall scattering is therefore

$$\left\langle \left| F_{inco}^{field} \right|^2 \right\rangle = N_S \left\langle \left| F_{inco}^{plant} \right|^2 \right\rangle \tag{2.3.7}$$

(b) Coherent Model

For the coherent model, we use the analytical branching model proposed by Yueh et al. [36]. For one branch, the scattering amplitude of the branch j is the coherent summation of the scattering from the cylinder and the disk

$$\begin{aligned} F_{vol}^{branch,j} = & \exp\left[2i\left(k_{xi} x_j^c + k_{yi} y_j^c - k_{zi} z_j^c \right) \right] f_{pp}^{c}(-\hat{K}_i, \hat{K}_i) \\ & + \exp\left[2i\left(k_{xi} x_j^d + k_{yi} y_j^d - k_{zi} z_j^d \right) \right] f_{pp}^{d}(-\hat{K}_i, \hat{K}_i) \end{aligned} \tag{2.3.8}$$

$$F_{db}^{branch,j} = 2R_p \left\{ \exp\left[2i\left(k_{xi} x_j^c + k_{yi} y_j^c + k_{zi} d \right) \right] f_{pp}^{c}(-\hat{k}_i, \hat{K}_i) + \exp\left[2i\left(k_{xi} x_j^d + k_{yi} y_j^d + k_{zi} d \right) \right] f_{pp}^{d}(-\hat{k}_i, \hat{K}_i) \right\} \tag{2.3.9}$$

where (x_j^c, y_j^c, z_j^c) and (x_j^d, y_j^d, z_j^d) are the coordinates of the j^{th} branch's stalk center and leaf center, respectively.

Using subscript "*co*"for coherent, then

$$F_{co}^{branch,j} = F_{vol}^{branch,j} + F_{db}^{branch,j} \tag{2.3.10}$$

$$\left\langle \left| F_{co}^{branch} \right|^2 \right\rangle = \left\langle \left| F_{vol}^{branch} \right|^2 \right\rangle + \left\langle \left| F_{db}^{branch} \right|^2 \right\rangle + 2\left\langle \mathrm{Re}(F_{vol}^{branch} F_{db}^{branch*}) \right\rangle \tag{2.3.11}$$

The coherent scattering amplitude of a soybean plant with N_L branches is

$$F_{co}^{plant} = F^{stem} + \sum_{j=1}^{N_L} F_{co}^{branch,j} \tag{2.3.12}$$

When calculating the intensity $\left\langle \left| F_{co}^{plant} \right|^2 \right\rangle$, there are additional terms of correlation between the scattering amplitudes.

$$\left\langle \left| F_{co}^{plant} \right|^2 \right\rangle = \left\langle \left| F^{stem} \right|^2 \right\rangle + 2\,\mathrm{Re}\left(\sum_{j=1}^{N_L} \left\langle F^{stem*} F_{co}^{branch,j} \right\rangle\right) + \sum_{j=1}^{N_L} \left\langle \left| F_{co}^{branch,j} \right|^2 \right\rangle + \sum_{j=1}^{N_L} \sum_{m=1, m\neq j}^{N_L} \left\langle F_{co}^{branch,j} F_{co}^{branch,m*} \right\rangle \tag{2.3.13}$$

Assuming the branches are statistically identical, the correlation between two different branches $\left\langle F_{co}^{branch,j} F_{co}^{branch,m*} \right\rangle$ is the same for each two branches and there are $N_L\left(N_L\text{-}1\right)$ terms, so it leads to

$$\left\langle \left| F_{co}^{plant} \right|^2 \right\rangle = \left\langle \left| F_{co}^{stem} \right|^2 \right\rangle + 2N_L\,\mathrm{Re}\left(\left\langle F^{stem*} F_{co}^{branch} \right\rangle\right) + N_L \left\langle \left| F_{co}^{branch} \right|^2 \right\rangle + N_L\left(N_L\text{-}1\right)\left\langle F_{co}^{branch,j} F_{co}^{branch,m*} \right\rangle \tag{2.3.14}$$

where $\mathrm{Re}\left(\left\langle F^{stem*} F_{co}^{branch} \right\rangle\right)$ is the real part of the average of the correlation between stem and branch. For soybean, the distance between stem center and branch center is usually much larger than $\lambda/4$ ($\pi/2$ in phase difference) and the real part of the correlation can be either positive or negative, resulting in a small average value. Comparing the coherent and incoherent models, we find that the extra term $N_L\left(N_L\text{-}1\right)\left\langle F_{co}^{branch,j} F_{co}^{branch,m*} \right\rangle$ can make significant difference, particularly when N_L is large as demonstrated in section 2.3.3. Thus, it is important to accurately calculate correlation of scattering between two different branches $\left\langle F_{co}^{branch,j} F_{co}^{branch,m*} \right\rangle$. In the previous coherent model [36], $\left\langle F_{co}^{branch,j} F_{co}^{branch,m*} \right\rangle$ is calculated as $\left\langle F_{co}^{branch} \right\rangle \left\langle F_{co}^{branch*} \right\rangle$. This formulation implies the case that two branches overlap and therefore their scattering fields are completely in phase which results in large total scattering intensity. In reality, there is some space between two branches, which we refer to as "mutual exclusion". We will introduce conditional probabilities to formulate the mutual exclusion in section 2.3.2.

Figure II.13. SMAPVEX12 soybean Field 64 illustrating the spacing between soybean plants.

Next, consider the coherent scattering amplitude of the soybean field with N_S plants. In our model, it is assumed that each soybean plant occupies a certain area with radius *R* where other

plants are not allowed to grow (as shown in Figure II.13), while outside that region the other soybean plants are uniformly distributed. According to [36],

$$\left\langle \left| F_{co}^{field} \right|^2 \right\rangle = N_S \left\langle \left| F_{co}^{plant} \right|^2 \right\rangle + N_S \left(N_S - 1 \right) \frac{\pi R J_1(2k_\rho R)}{k_\rho} \left\langle F_{co}^{plant} \right\rangle \left\langle F_{co}^{plant*} \right\rangle \tag{2.3.15}$$

where $k_\rho = \sqrt{k_{xi}^2 + k_{yi}^2}$ and $J_1(2k_\rho R)$ is the Bessel function of the first kind.

2.3.2 Coherent Model with Conditional Probabilities

(a) Conditional Probability for Branch Geometry

The mutual exclusion method avoids the unrealistic situation that two branches overlap in space, thereby constructing more reasonable geometry for a soybean plant. To implement the mutual exclusion, the improved coherent model applies the conditional probability to two factors: the positions of the bottom of the branches *z*, and the orientation angles α of the branches. Let $s = d / \left[2(N_L - 1) \right]$ be half of the average spacing between two adjacent branches. In the calculations below, it is assumed that the main stem is parallel to the *z* axis. The conditional probability that scatterers exist within given *z* is zero if two branches are within half of the average spacing (s) and uniform otherwise.

Let z_j and z_m be the *z* coordinates of the attachment of the branches j and m to the main stem, respectively. Then the conditional probability is

$$p_2(z_m \mid z_j) = \begin{cases} 0, & \text{if } \left| z_m - z_j \right| < s \\ A(z_j), & \text{otherwise} \end{cases} \tag{2.3.16}$$

where $A(z_j)$ is chosen so that $\int_{-d}^{0} dz_m \, p_2(z_m \mid z_j) = 1$.

For the case when z_j is less than s from the top, $-s < z_j < 0$,

$$A(z_j)=\frac{1}{d-s+z_j}, z_m \in \left[-d, z_j - s\right] \tag{2.3.17}$$

If z_j is at distance more than s from the top or from the bottom, $-d+s \le z_j \le -s$, according to equation (2.3.16), there is an exclusion zone within the distance s on each side of z_j where a neighbor branch cannot exist.

$$A(z_j)=\frac{1}{d-2s}, z_m \in \left[z_j + s, 0\right] or \left[-d, z_j - s\right] \tag{2.3.18}$$

For the case when z_j is less than s from the bottom, $-d < z_j < -d+s$,

$$A(z_j)=\frac{1}{-z_j - s}, z_m \in \left[z_j + s, 0\right] \tag{2.3.19}$$

In summary,

$$A(z_j) = \begin{cases} \dfrac{1}{d-s+z_j}, -s < z_j < 0, z_m \in \left[-d, z_j - s\right] \\ \dfrac{1}{d-2s}, -d+s \le z_j \le -s, z_m \in \left[z_j + s, 0\right] or \left[-d, z_j - s\right] \\ \dfrac{1}{-z_j - s}, -d < z_j < -d+s, z_m \in \left[z_j + s, 0\right] \end{cases} \tag{2.3.20}$$

The joint probability is

$$p(z_m, z_j) = p_2(z_m \mid z_j) p(z_j), \text{ with } p(z_j) = \frac{1}{d} \tag{2.3.21}$$

(b) Calculation of the Term of Correlation between Two Branches

As explained in section 2.3.1, $\left\langle F_{co}^{branch,\,j} F_{co}^{branch,m*} \right\rangle$ is a critical term distinguishing coherent model from incoherent model.

$$\begin{aligned}\left\langle F_{co}^{branch,j} F_{co}^{branch,m*} \right\rangle &= \left\langle \left(F_{vol}^{branch,j} + F_{db}^{branch,j} \right) \left(F_{vol}^{branch,m*} + F_{db}^{branch,m*} \right) \right\rangle \\ &= \left\langle F_{vol}^{branch,j} F_{vol}^{branch,m*} \right\rangle + \left\langle F_{vol}^{branch,j} F_{db}^{branch,m*} \right\rangle \\ &+ \left\langle F_{db}^{branch,j} F_{vol}^{branch,m*} \right\rangle + \left\langle F_{db}^{branch,j} F_{db}^{branch,m*} \right\rangle \end{aligned} \tag{2.3.22}$$

We define x and y coordinates of the main stem of each soybean plant to be (0, 0). Then the coordinates of the cylinder and the disk of branch j are as follows.

$$\begin{aligned} x_j^c &= \frac{l}{2} \sin\beta_j \cos\alpha_j \\ y_j^c &= \frac{l}{2} \sin\beta_j \sin\alpha_j \\ z_j^c &= z_j + \frac{l}{2} \cos\beta_j \end{aligned} \tag{2.3.23}$$

$$\begin{aligned} x_j^d &= l \sin\beta_j \cos\alpha_j \\ y_j^d &= l \sin\beta_j \sin\alpha_j \\ z_j^d &= z_j + l \cos\beta_j \end{aligned} \tag{2.3.24}$$

where l, β_j and α_j are the parameters of the branch j as shown in Figure II.11 (c). Then equation (2.3.8) becomes,

$$\begin{aligned} F_{vol}^{branch,j} = \exp(-2ik_{zi}z_j) \Bigg\{ &\exp\left[2i \left(k_{xi} \frac{l}{2} \sin\beta_j \cos\alpha_j + k_{yi} \frac{l}{2} \sin\beta_j \sin\alpha_j - k_{zi} \frac{l}{2} \cos\beta_j \right) \right] f_{pp}^c(-\hat{K}_i, \hat{K}_i) \\ &+ \exp\left[2i \left(k_{xi} l \sin\beta_j \cos\alpha_j + k_{yi} l \sin\beta_j \sin\alpha_j - k_{zi} l \cos\beta_j \right) \right] f_{pp}^d(-\hat{K}_i, \hat{K}_i) \Bigg\} \end{aligned} \tag{2.3.25}$$

Let

$$\begin{aligned} F_{vol0}^{branch,j} = &\exp\left[2i \left(k_{xi} \frac{l}{2} \sin\beta_j \cos\alpha_j + k_{yi} \frac{l}{2} \sin\beta_j \sin\alpha_j - k_{zi} \frac{l}{2} \cos\beta_j \right) \right] f_{pp}^c(-\hat{K}_i, \hat{K}_i) \\ &+ \exp\left[2i \left(k_{xi} l \sin\beta_j \cos\alpha_j + k_{yi} l \sin\beta_j \sin\alpha_j - k_{zi} l \cos\beta_j \right) \right] f_{pp}^d(-\hat{K}_i, \hat{K}_i) \end{aligned} \tag{2.3.26}$$

Then

$$F_{vol}^{branch,j} = \exp(-2ik_{zi}z_j) F_{vol0}^{branch,j} \tag{2.3.27}$$

We assume that the positions and orientation angles are statistically independent

$$\left\langle F_{vol}^{branch,j} F_{vol}^{branch,m*} \right\rangle = \left\langle \exp\left[-2ik_{zi}\left(z_j - z_m\right)\right] \right\rangle \left\langle F_{vol0}^{branch,j} F_{vol0}^{branch,m*} \right\rangle \tag{2.3.28}$$

where

$$\left\langle \exp\left[-2ik_{zi}\left(z_j - z_m\right)\right] \right\rangle = \int_{-d}^{0} dz_m \int_{-d}^{0} dz_j \, p(z_m, z_j) \exp\left[-2ik_{zi}(z_j - z_m)\right] = A + B + C + D \tag{2.3.29}$$

where the integrations are separated into four parts, A, B, C, and D as follows

$$\begin{aligned} \int_{-d}^{0} dz_m \int_{-d}^{0} dz_j \, p(z_m, z_j) = & \int_{z_j+s}^{0} dz_m \int_{-d}^{-d+s} dz_j \, p_2(z_m \mid z_j) p(z_j) \\ & + \int_{-d}^{z_j-s} dz_m \int_{-d+s}^{-s} dz_j \, p_2(z_m \mid z_j) p(z_j) \\ & + \int_{z_j+s}^{0} dz_m \int_{-d+s}^{-s} dz_j \, p_2(z_m \mid z_j) p(z_j) \\ & + \int_{-d}^{z_j-s} dz_m \int_{-s}^{0} dz_j \, p_2(z_m \mid z_j) p(z_j) \end{aligned} \tag{2.3.30}$$

After calculations, the following four expressions are obtained.

$$A = \frac{1}{2idk_{zi}} \int_{-d}^{-d+s} dz_j \left[\frac{\exp(-2ik_{zi} z_j) - \exp(2ik_{zi} s)}{-z_j - s} \right] \tag{2.3.31}$$

$$B = \frac{\exp(-2ik_{zi} s)}{2idk_{zi}} - \frac{\left\{\exp\left[-2ik_{zi}(d-s)\right] - \exp\left(-2ik_{zi} s\right)\right\}}{4k_{zi}^2 d\left(d - 2s\right)} \tag{2.3.32}$$

$$C = -\frac{\exp(2ik_{zi} s)}{2idk_{zi}} + \frac{\left\{\exp\left(2ik_{zi} s\right) - \exp\left[2ik_{zi}(d-s)\right]\right\}}{4k_{zi}^2 d\left(d - 2s\right)} \tag{2.3.33}$$

$$D = \frac{1}{2ik_{zi} d} \int_{-s}^{0} dz_j \left[\frac{\exp(-2ik_{zi} s) - \exp(-2ik_{zi}(z_j + d))}{d - s + z_j} \right] \tag{2.3.34}$$

The correlation between the volume scattering and double-bounce scattering is

$$\left\langle F_{vol}^{branch,j} F_{db}^{branch,m*} \right\rangle = \left\langle \exp\left(-2ik_{zi} z_j\right) \right\rangle \left\langle F_{vol0}^{branch,j} F_{db}^{branch,m*} \right\rangle \tag{2.3.35}$$

where

$$F_{db}^{branch,m} = 2R_p \left\{ \exp\left[2i\left(k_{xi}\frac{l}{2}\sin\beta_j\cos\alpha_j + k_{yi}\frac{l}{2}\sin\beta_j\sin\alpha_j + k_{zi}d \right)\right] f_{pp}^{c}(-\hat{k}_i, \hat{K}_i) \right.$$
$$\left. + \exp\left[2i\left(k_{xi}l\sin\beta_j\cos\alpha_j + k_{yi}l\sin\beta_j\sin\alpha_j + k_{zi}d \right)\right] f_{pp}^{d}(-\hat{k}_i, \hat{K}_i) \right\} \tag{2.3.36}$$

which does not depend on z .

$$\left\langle \exp\left(-2ik_{zi}z_j\right)\right\rangle = \int_{-d}^{0} dz_j\, p(z_j)\exp\left(-2ik_{zi}z_j\right) = \frac{\exp\left(2ik_{zi}d\right)-1}{2ik_{zi}d} \tag{2.3.37}$$

Similarly,

$$\left\langle F_{db}^{branch,j}F_{vol}^{branch,m*}\right\rangle = \left\langle \exp\left(2ik_{zi}z_m\right)\right\rangle \left\langle F_{db}^{branch,j}F_{vol0}^{branch,m*}\right\rangle = \frac{1-\exp\left(-2ik_{zi}d\right)}{2ik_{zi}d}\left\langle F_{db}^{branch,j}F_{vol0}^{branch,m*}\right\rangle \tag{2.3.38}$$

For mutual exclusion of orientation angles, we use the conditional probability

$$p_3(\alpha_m \mid \alpha_j) = \begin{cases} 0, & \text{if } \left|\alpha_m - \alpha_j\right| < \dfrac{\pi}{2} \\ \dfrac{1}{\pi}, & \text{otherwise} \end{cases} \tag{2.3.39}$$

The joint probability of α_m and α_j is

$$p(\alpha_m, \alpha_j) = p_3(\alpha_m \mid \alpha_j)\, p(\alpha_j), \text{ with } p(\alpha_j) = \frac{1}{2\pi} \tag{2.3.40}$$

Since $F_{vol0}^{branch,j}F_{vol0}^{branch,m*}$, $F_{vol0}^{branch,j}F_{db}^{branch,m*}$, $F_{db}^{branch,j}F_{vol0}^{branch,m*}$ and the remaining term in equation (2.3.22) $F_{db}^{branch,j}F_{db}^{branch,m*}$ are independent of *z* and depend on α and β, their averages are calculated as below,

$$\left\langle F_{t1}^{branch,j}F_{t2}^{branch,m*}\right\rangle = \int_0^{\frac{\pi}{2}} p(\beta)d\beta \int_0^{2\pi} d\alpha_m \int_0^{2\pi} d\alpha_j\, p(\alpha_m, \alpha_j) F_{t1}^{branch,j}F_{t2}^{branch,m*} \tag{2.3.41}$$

where the subscripts "*t1*" and "*t2*" represent "*vol0*" or "*db*". *p(β)* is the probability of β as in Figure II.11 (c). The integrations in equation (2.3.41) are calculated numerically.

2.3.3 Simulation Results and Comparison

The three models illustrated above are simulated for one soybean plant. The values of the major parameters describing the plant geometry used for simulations are: number of branches $N_L = 10$; length of main stem $d = 12$ cm, length of stalk $l = 6$ cm, leaf thickness is 0.3 mm; radius of stem and stalk are both 1.5 mm, radius of compound leaf is 4.3 cm; distribution of stem, stalk and leaf orientation angles are uniform inclination (β as shown in Figure II.11) over $0 \sim 5^\circ$, $0 \sim 60^\circ$ and $0 \sim 90^\circ$, respectively. Other kinds of distributions such as cosine distribution were used for leaf orientation angles [53], and uniform distribution which is closer to the measurement is used here. The incident angle θ=40° and the radar frequency *f*=1.26 GHz.

Table II-9. Simulation results for three scattering models of one soybean plant. Models 1 to 3 are incoherent model, coherent model with no mutual exclusion, and coherent model with conditional probabilities, respectively. S1-S5 are $\left\langle \left| F^{plant} \right|^2 \right\rangle$, $\left\langle \left| F^{stem} \right|^2 \right\rangle$, $N_L \left\langle \left| F^{branch} \right|^2 \right\rangle$, $2N_L \,\mathrm{Re}\left(\left\langle F^{stem*} \right\rangle \left\langle F_{co}^{branch} \right\rangle \right)$, $N_L (N_L\text{-}1) \left\langle F_{co}^{branch} F_{co}^{branch*} \right\rangle$, respectively. Two values in italics means they are out of phase with the other terms.

	Model	S1 [dB]	S2 [dB]	S3 [dB]	S4 [dB]	S5 [dB]
HH	1	-47.8	-83.0	-47.8	N/A	N/A
	2	-42.3	-83.0	-47.1	-61.0	-44.2
	3	-44.7	-83.0	-47.1	-61.0	-48.6
VV	1	-50.6	-64.9	-50.8	N/A	N/A
	2	-49.1	-64.9	-49.6	*-58.0*	-55.9
	3	-49.4	-64.9	-49.6	*-58.0*	-57.6

The simulation results of the three models are presented in Table II-9. It is noticed that among the terms S2-S5, S5 ($N_L (N_L\text{-}1) \left\langle F_{co}^{branch} F_{co}^{branch*} \right\rangle$) causes the largest difference among the three models. For the incoherent model, there is no correlation between two different branches. The coherent model with conditional probabilities decreases the correlation (S5) by 4.4 dB and 1.7 dB for HH

and VV backscattering coefficients, respectively, compared with the coherent model with no mutual exclusion.

For the HH backscattering coefficient simulation results, the difference between the incoherent model and coherent model with no mutual exclusion is 5.5 dB. When the conditional probabilities are introduced, the difference decreases to 3.1 dB. This means our method works well to decrease the overlap effect in soybean scattering. In model 2, the dominant term is the coherent scattering between branches. In model 3, the scattering by branches and the coherent scattering between branches are close. This demonstrates that the effect of the overlap needs to be removed through the mutual exclusion.

For the VV backscattering coefficient simulation results, the difference between the incoherent and coherent models is smaller than the case for the HH backscattering coefficients, because the scattering by branches dominates. In comparison, the difference between the two coherent models originating from the term $N_L\left(N_L\text{-}1\right)\left\langle F_{co}^{branch,j}F_{co}^{branch,m*}\right\rangle$ is small. Thus, the results of the coherent model with mutual exclusion are only slightly different from those of the previous coherent model.

2.3.4 Computation and Validation for the Soybean Data-Cube

Data-cube is used in the time-series retrieval of soil moisture, and is a pre-computed lookup-table developed from a physically-based forward model [6]. The backscattering coefficients σ_{VV} and σ_{HH} are computed using the coherent model over the full observed range of the three variables of the data-cubes.

(a) Data-cubes with Different Correlation Length to RMS Height (cl/s) Ratios

Each data-cube has only one cl/s ratio. It was observed during SMAPVEX12 that different soybean fields had different cl/s ratios. Thus, the method to construct data-cubes with different cl/s ratios is needed. According to the Kirchhoff approximation [54], the double-bounce scattering depends on RMS height instead of correlation length. The results from NMM3D show a similar conclusion that the double-bounce term has almost no dependence on the correlation length (i.e., cl/s ratios). To generate the data-cube, we used the coherent reflectivity from the results of NMM3D for rough-surface scattering.

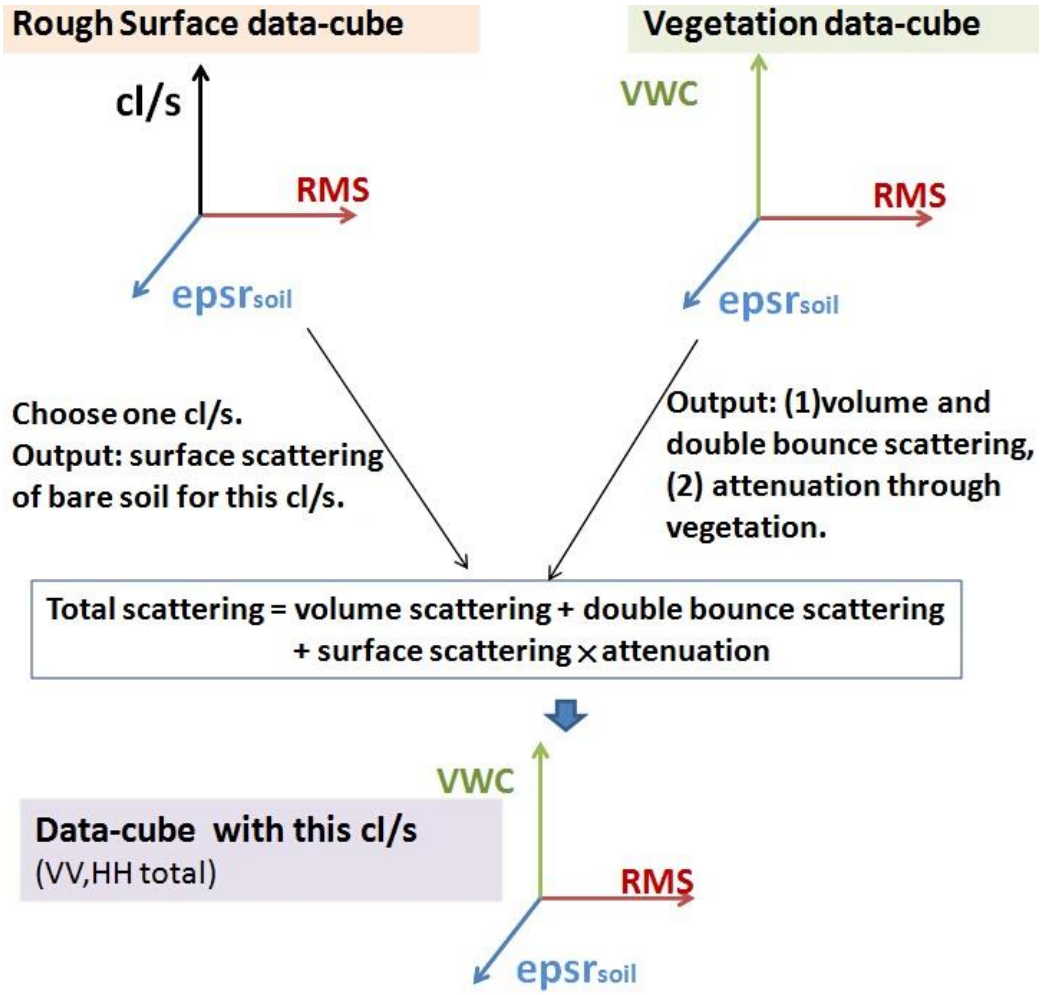

Figure II.14. Method of generating data-cubes with different cl/s ratios.

As shown in Figure II.14, two different types of data-cubes (i.e., Rough Surface data-cube and Vegetation data-cube) are used to construct the data-cube of vegetation-covered soil for a certain cl/s ratio. The output of Rough Surface data-cube is the surface scattering by bare soil for different combinations of soil permittivity ($epsr_{soil}$), RMS height and cl/s ratio. On the other hand, since volume scattering does not depend on the cl/s ratio and double-bounce scattering is only weakly dependent on cl/s ratio, the two scattering mechanisms as well as the attenuation through vegetation can be calculated independently of cl/s ratio. The total backscattering is the summation of volume scattering, double-bounce scattering and the surface scattering with attenuation. Once a cl/s ratio is chosen, the surface scattering for this certain cl/s ratio is provided by the Rough Surface data-cube. The remaining parts to compute the total backscattering are available from the Vegetation data-cube. This way of generating data-cubes with different cl/s ratios improves computational efficiency significantly because it avoids 4 independent axes. Instead, it uses two data-cubes each with 3 independent axes. The present scheme avoids repeating the calculations of the volume and double-bounce scattering as well as the attenuation through vegetation.

(b) Backscattering Coefficient

The attenuation caused by the vegetation layer is calculated as follows. According the Foldy's approximation [4], k_1 for polarization *p* in the vegetation layer is

$$k_{1p} = k + \frac{2\pi}{k}\left(n_{leaf} \left\langle f_{pp}^{leaf}(\hat{K}_i, \hat{K}_i) \right\rangle + n_{stalk} \left\langle f_{pp}^{stalk}(\hat{K}_i, \hat{K}_i) \right\rangle + n_{stem} \left\langle f_{pp}^{stem}(\hat{K}_i, \hat{K}_i) \right\rangle \right) \qquad (2.3.42)$$

where $\left\langle f_{pp}(\hat{K}_i, \hat{K}_i) \right\rangle$ is the forward scattering and averaged over the orientation angles; n_{leaf}, n_{stalk} and n_{stem} are the number of leaves, stalks and stems per m^3, respectively. Then the volume and double-bounce scattering become

$$F_{vol} = \exp\left[2i \left(k_{xi} x_j + k_{yi} y_j - \left(\frac{k_{1p}}{\cos\theta_i} - \frac{k_\rho^2}{k \cos\theta_i} \right) z_j \right) \right] f_{pp}(-\hat{K}_i, \hat{K}_i) \tag{2.3.43}$$

$$F_{db} = 2R_p \exp\left[2i \left(k_{xi} x_j + k_{yi} y_j + \left(\frac{k_{1p}}{\cos\theta_i} - \frac{k_\rho^2}{k \cos\theta_i} \right) d \right) \right] f_{pp}(-\hat{k}_i, \hat{K}_i) \tag{2.344}$$

$k_{1z} = \sqrt{k_1^2 - k_\rho^2}$ and the imaginary part of k_{1z} introduces the attenuation. The attenuation for surface scattering is $\left\{ \exp\left[-2\,\mathrm{Im}\left(k_{1z} \right) d \right] \right\}^2$.

The backscattering coefficient for one soybean branch using the distorted Born approximation [11] is:

$$\sigma_{co,pp}^{branch} = 4\pi \left\langle \left| F_{vol}^{branch} + F_{db}^{branch} \right|^2 \right\rangle \tag{2.3.45}$$

A factor of 4π is multiplied to the scattering intensity [55]. Considering the surface scattering $\sigma_{pp}^{surface}$, the total backscattering coefficient computed in the data-cube is

$$\sigma_{co,pp}^{field} = 4\pi \left\langle \left| F_{co}^{field} \right|^2 \right\rangle + \sigma_{pp}^{surface} \tag{2.3.46}$$

(c) Parameters Used for the Soybean Data-cube

During SMAPVEX12 the VWC and geometry parameters of soybean plants were measured every week for multiple soybean fields. Both stem diameter and length are dynamic properties which increase with VWC. Allometric equations are derived empirically (Figure II.15 and Table II-10).

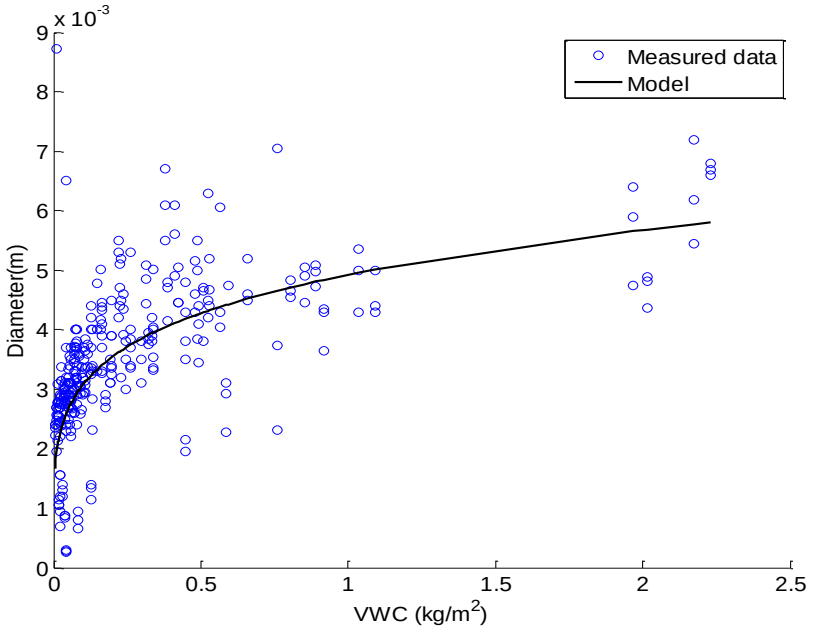

(a)

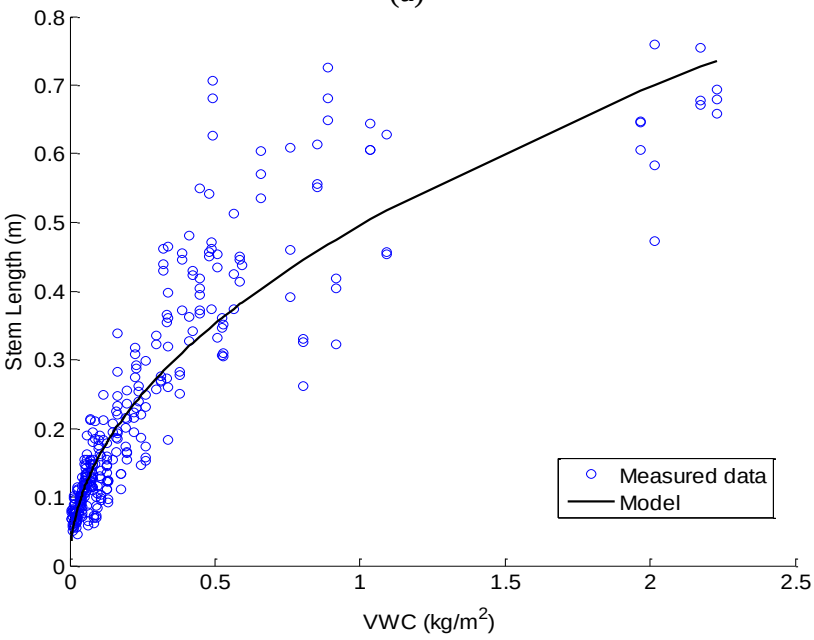

(b)

Figure II.15. (a) Stem diameter as a function of VWC, (b) Stem length as a function of VWC.

Table II-10. Allometric relationship between VWC and plant geometry parameters.
This relationship is obtained from the data, shown in Figure II.15 (a) and (b), through curve fitting. Volumetric water content (M_{veg}) which is used to calculate the dielectric constant is estimated from the gravimetric water content (M_g) measured in SMAPVEX12 [49]. The M_{veg} for leaf is adjusted to a smaller value than that for stalk since the permittivity of soybean leaf is generally smaller than

the permittivity of stalk[14]. The distribution of azimuthal angle (α as shown in Figure II.11) is uniform over $0 \sim 360^{\circ}$ for all of steam, stalk, and leaf.

	Diameter [m]	Length [m]	M_{veg}	Distribution of β
Stem	$0.0049\ VWC^{0.204}$	$0.496\ VWC^{0.49}$	60%	Uniform over $0 \sim 5^{\circ}$
Stalk	$0.0033\ VWC^{0.204}$	$0.248\ VWC^{0.49}$	60%	Uniform over $0 \sim 60^{\circ}$
Leaf	5×10^{-2}	0.3×10^{-3}	40%	Uniform over $0 \sim 90^{\circ}$

With the equations, a given VWC evaluates the geometry parameters that in turn are used to run the forward model and generate the data-cube. There are about 36 soybean plants per m^2 (N_S = 36). The number of branches per plant (N_L) can be calculated from VWC using the following formula:

$$N_L = \frac{VWC - \rho_{water} N_S Vol_{stem} Mveg_{stem}}{\rho_{water} N_S \left(Vol_{stalk} Mveg_{stalk} + Vol_{leaf} Mveg_{leaf} \right)} \tag{2.3.47}$$

where ρ_{water} is water density. $Mveg_{stem}$, $Mveg_{stalk}$ and $Mveg_{leaf}$ are the volumetric water content of stem, stalk and leaf, respectively. Vol_{stem}, Vol_{stalk} and Vol_{leaf} are the volume of stem, stalk and leaf, respectively.

The forward model calculation is performed at a 40° incident angle. Previously, the soybean data-cube was based on the incoherent model whose results are also listed for comparison. For the incoherent data-cube, the soybean field was regarded as a combination of cylinders (stalks and stems) and disks (leaves) without the branching configuration because the positions of the scatterers do not matter. To simplify calculations, we assumed that the stems were the same as stalks since they were both cylinders with similar radius and the number of stems was much smaller than that of stalks. Some other parameters were adjusted to produce the best forward model

matching with data: uniform inclination over $0 \sim 90^{\circ}$ for both cylinders and disks. The soybean data-cube at one cl/s ratio is plotted in Figure II.16.

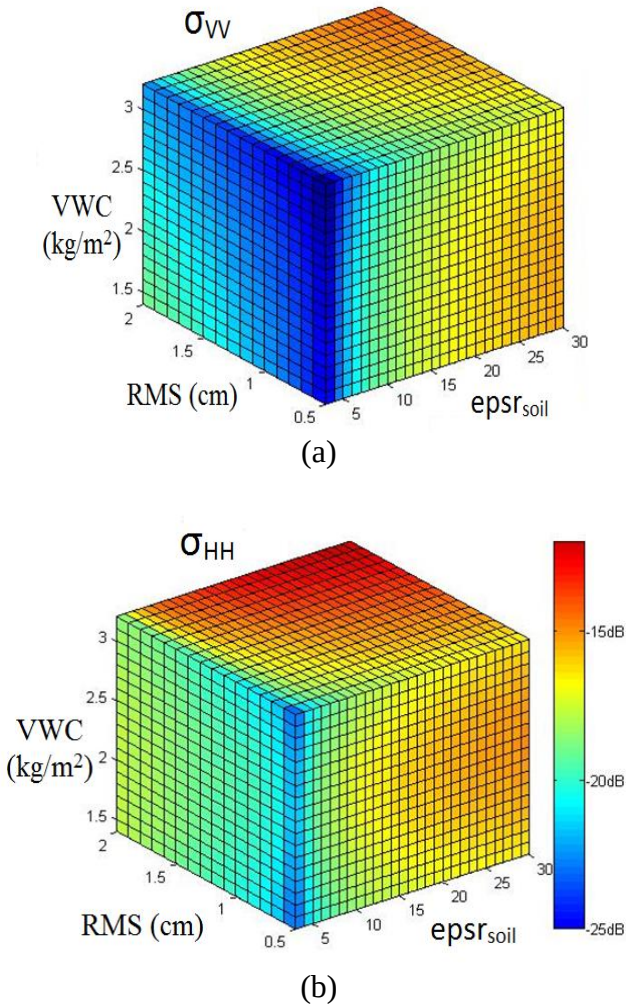

Figure II.16. Examples of soybean data-cube (a) σ_{VV}, (b) σ_{HH}. The corresponding soil moisture can be calculated from soil permittivity by dielectric model for soil [22].

(d) Validation for Data-cubes With Airborne SAR Data

As described in section 2.2.2, SMAPVEX12 [34] was designed to support the requirements of soil moisture retrieval algorithms and products by providing extended time-series measurements

for diverse vegetation conditions. Both RMS height and cl/s ratio are assumed to be constant over the study period. For each day of flight, the in-situ values of RMS height, VWC and soil moisture (used to compute $epsr_{soil}$) are input to sample σ_{VV} and σ_{HH} from the soybean data-cube. These predicted values are compared with the UAVSAR data. The cl/s ratio is chosen so that the difference between the UAVSAR and data-cube values is minimized over the entire 13 flights. The optimal cl/s often does not match the observed cl/s, which may be explained by the well-known uncertainty in the observation of cl (~50% error [23]).

Table II-11. RMSE and correlation coefficient of data-cube and UAVSAR measurement comparison for backscattering coefficients,

Field No.	RMSE (dB)				Correlation Coefficient			
	Incoherent Data-cube		Coherent Data-cube		Incoherent Data-cube		Coherent Data-cube	
	VV	HH	VV	HH	VV	HH	VV	HH
11	0.77	1.76	0.67	1.30	0.87	0.98	0.93	0.98
12	1.34	0.98	1.30	0.98	0.74	0.43	0.74	0.44
14	1.39	0.92	1.19	0.65	0.84	0.91	0.87	0.93
33	1.74	1.03	1.47	0.93	0.68	0.71	0.71	0.63
34	1.05	0.92	1.08	0.86	0.81	0.85	0.77	0.85
51	1.94	1.77	1.04	0.76	0.77	0.96	0.91	0.99
52	1.18	1.11	0.71	0.60	0.87	0.88	0.82	0.95
63	1.09	1.39	0.83	0.59	0.84	0.92	0.92	0.95
64	0.92	0.79	0.88	0.75	0.89	0.72	0.88	0.77
102	2.09	1.07	0.82	0.88	0.22	0.89	0.86	0.93
103	1.74	1.41	1.53	1.09	-0.07	0.74	0.29	0.87
111	1.94	1.77	1.04	0.76	0.77	0.96	0.91	0.99
112	2.09	0.80	0.46	0.79	0.28	0.94	0.95	0.94

It can be seen from Table II-11 that the coherent model with conditional probabilities in general improves the agreement with the measurement compared with the incoherent model in terms of correlation coefficient and RMSE. For the incoherent model, when VWC is low in June the volume and double-bounce scattering are very small and thus the backscattering is primarily from the surface scattering. For the incoherent data-cube, a small cl/s ratio is chosen to ensure an appropriate HH backscattering coefficient to match the data. However, VV simulation is larger than the

measurement as shown in Figure II.17 (b) and Figure II.18 (b). Thus, the polarization ratio of VV to HH backscattering coefficients from the incoherent model is larger than the measurement when VWC is small, which cannot be reduced by selecting a different cl/s ratio. Using the coherent model, this apparent dilemma of not being able to match HH and VV backscattering coefficients simultaneously was resolved. For the coherent model, when VWC is low, the soybean plant is small and the branches and leaves are close to each other, so the coherent effect increases the volume and double-bounce scattering significantly, especially for HH backscattering coefficients. A larger cl/s ratio is chosen so that VV is sufficiently small and improves the agreement with the observation (VV is also mostly contributed by surface scattering when VWC is low in the coherent model). The surface scattering of HH backscattering also becomes smaller; however, the coherent model increases the volume and double-bounce scattering of HH backscattering to match the data. Overall, both VV and HH backscattering coefficients match the measurement well using the coherent data-cube. The polarization ratio between VV and HH backscattering coefficients is used during the dual-polarized time-series retrieval [6]. As a result of the coherent scattering effect, the polarization ratio agrees well with the observations when the VWC is small. When VWC becomes large in July, the soybean plant grows tall and the branches and leaves are far apart, where the coherent model with conditional probabilities also restricts the branches not to be too close to each other. Thus, the coherent effect generally becomes less significant than that in June. The improvement is significant when the volume and double-bounce scattering are comparable to the surface scattering by the soybean fields such as Field 63 and Field 112 shown in Figure II.17 and Figure II.18. To better illustrate the coherent data-cube, the previous coherent model with no mutual exclusion is also applied to the Field 112 as shown in Figure II.18 (c) where HH backscattering coefficients are overestimated with RMSE of 1.49 dB.

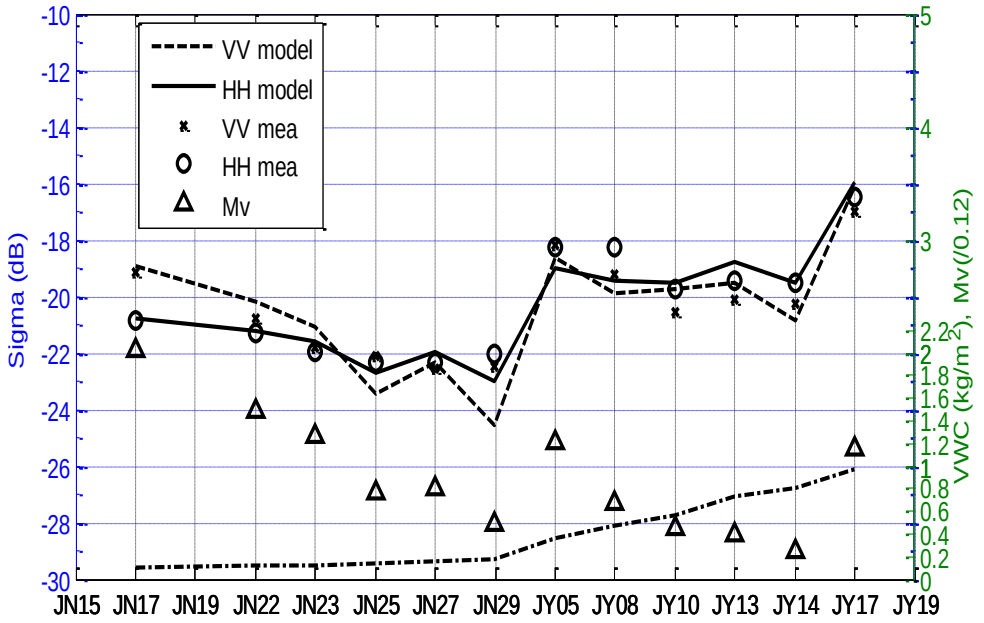

(a)

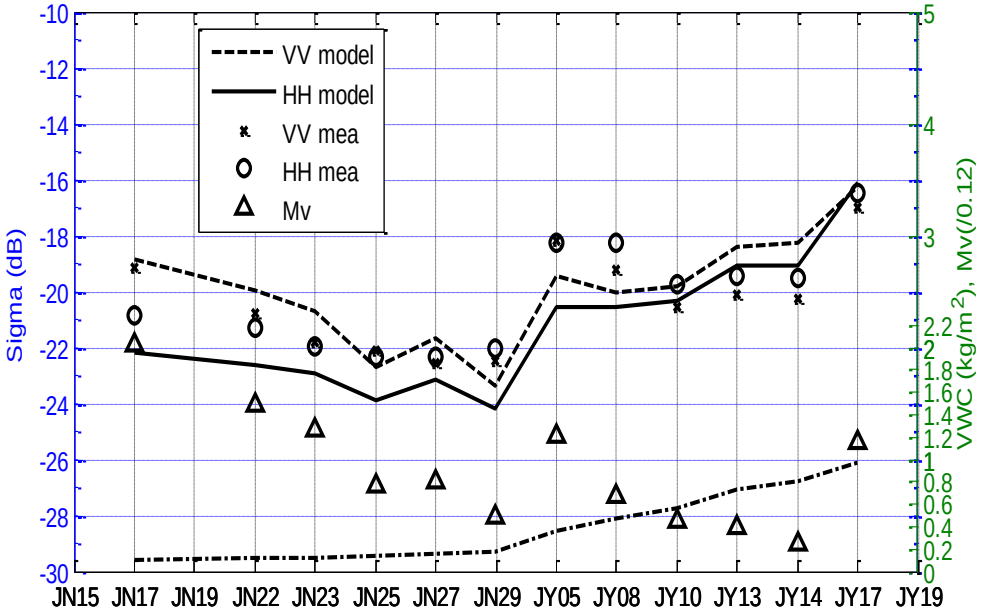

(b)

Figure II.17. (a) Coherent data-cube applied to SMAPVEX12 Field 63 with cl/s=30, (b) Incoherent data-cube applied to soybean Field 63 with cl/s=20. Different cl/s ratios are chosen for the best matching of both models. The dash-dot curve indicates VWC and the x-axis presents time: "JN" stands for "June" while "JY" stands for "July", hereinafter the same.

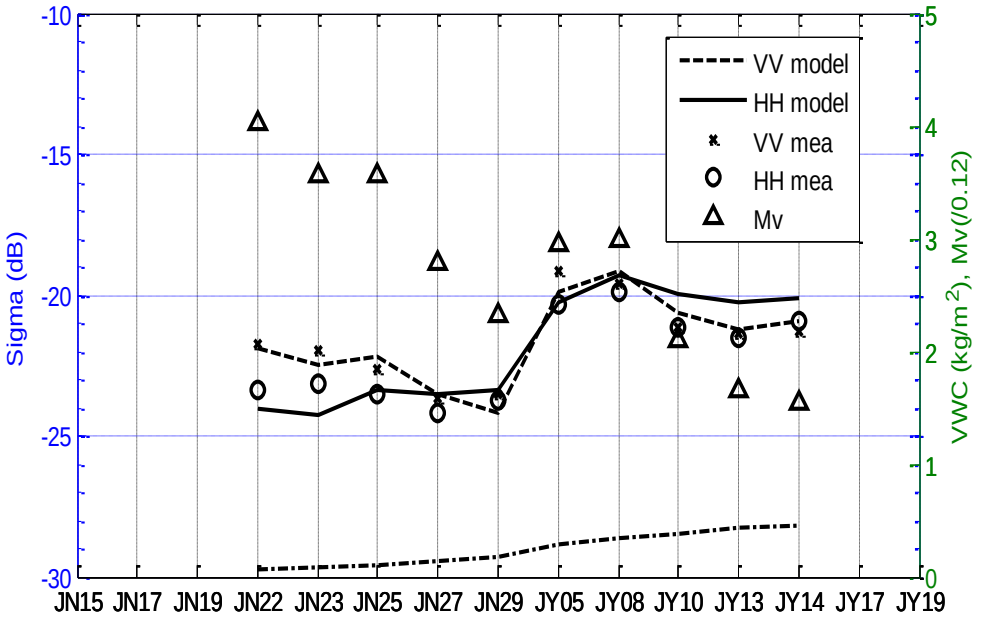
VV model
HH model
VV mea
HH mea
Mv
Sigma (dB)
VWC (kg/m2), Mv(/0.12)
-10
-15
-20
-25
-30
5
4
3
2
1
0
JN15 JN17 JN19 JN22 JN23 JN25 JN27 JN29 JY05 JY08 JY10 JY13 JY14 JY17 JY19

(a)

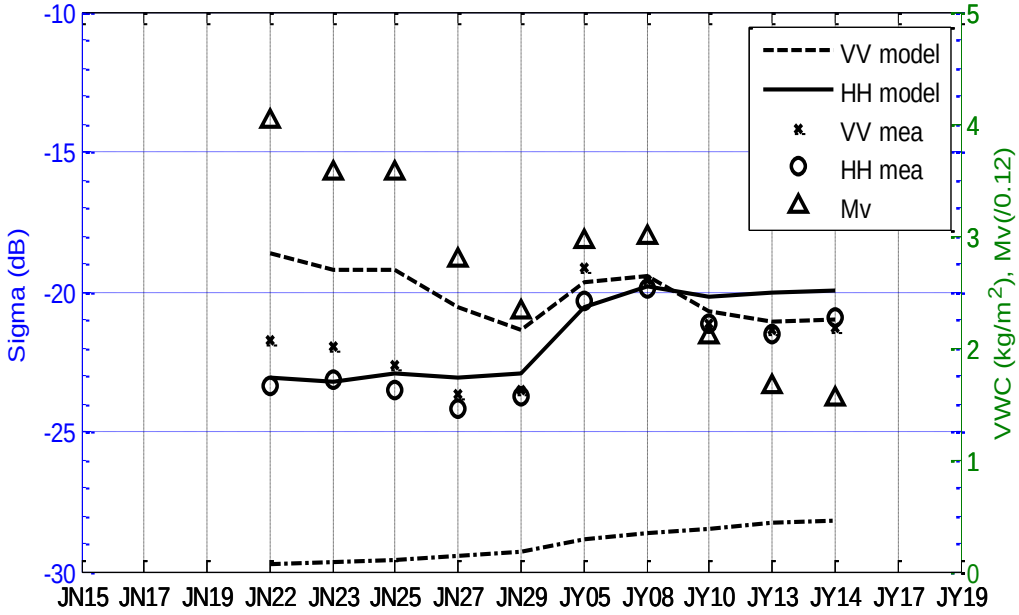
VV model
HH model
VV mea
HH mea
Mv
Sigma (dB)
VWC (kg/m2), Mv(/0.12)
-10
-15
-20
-25
-30
5
4
3
2
1
0
JN15 JN17 JN19 JN22 JN23 JN25 JN27 JN29 JY05 JY08 JY10 JY13 JY14 JY17 JY19

(b)

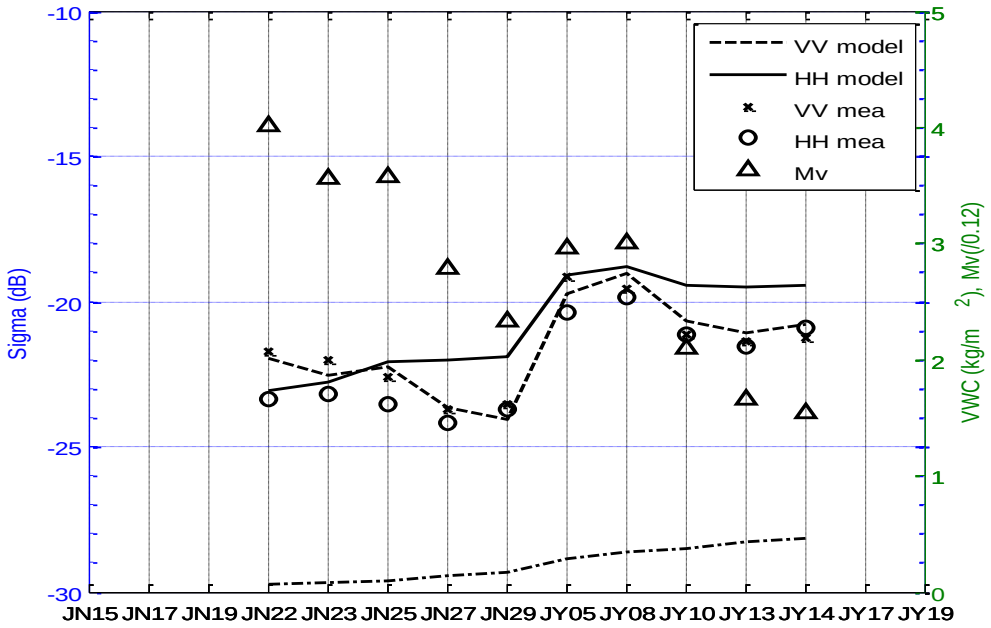

(c)

Figure II.18. (a) The coherent data-cube applied to SMAPVEX12 Field 112 with cl/s=120, (b) The incoherent data-cube applied to SMAPVEX12 Field 112 with cl/s=40, (c) The coherent model with no mutually exclusion applied to SMAPVEX12 Field 112 with cl/s=120.

The coherent and incoherent data-cubes are compared with the data for 13 soybean fields from SMAPVEX12, as shown in Figure II.19 and Figure II.20. The comparison results are variable depending on the soil moisture, RMS height and VWC growth. The coherent model with conditional probabilities decreases the RMSE and increases the correlation coefficient for both VV and HH backscattering coefficients. The forward model presented in this chapter is based on the physical principles of scattering as well as the numerical and analytical solutions based on the principles. The scattering mechanisms do not depend on specific set of measurements, unlike empirical models such as water-cloud model [56] for the vegetation scattering. This suggests that the current model may be applicable to independent observations of soybean fields. This capability will benefit SMAP mission where the goal is the global retrieval of soil moisture. The dependence of the model parameterization on the particular SMAPVEX12 fields is limited to the empirical

derivation of the allometric equation, and some choices of the vegetation parameters. Other data-cubes are needed for soybean fields which have very different properties. For example, the soybean Field 92 has similar VWC, soil moisture and RMS height as the soybean Field 102, but much larger measured VV and HH backscattering coefficients. Some reasons for the mismatch are: (1) Field 92 is not suitable for the data-cube (e.g., its plant density may be much higher than 36 per m^2.); (2) there is measurement error (e.g., the RMS height which is assumed to be constant was measured only once during the campaign but it may be changed by erosion. There may also be error in the VWC data.). Since the data-cube generated in this chapter is suitable for most of the SMAPVEX12 soybean fields, the necessity to build another data-cube for Field 92 will be analyzed when more data are available. Model performance will be assessed with independent observations in the future, to test its general applicability.

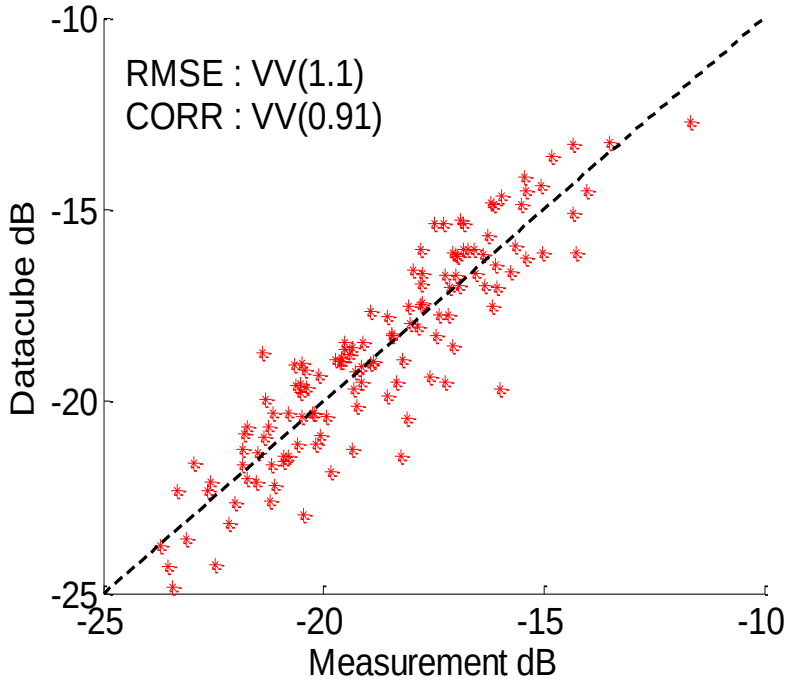

(a)

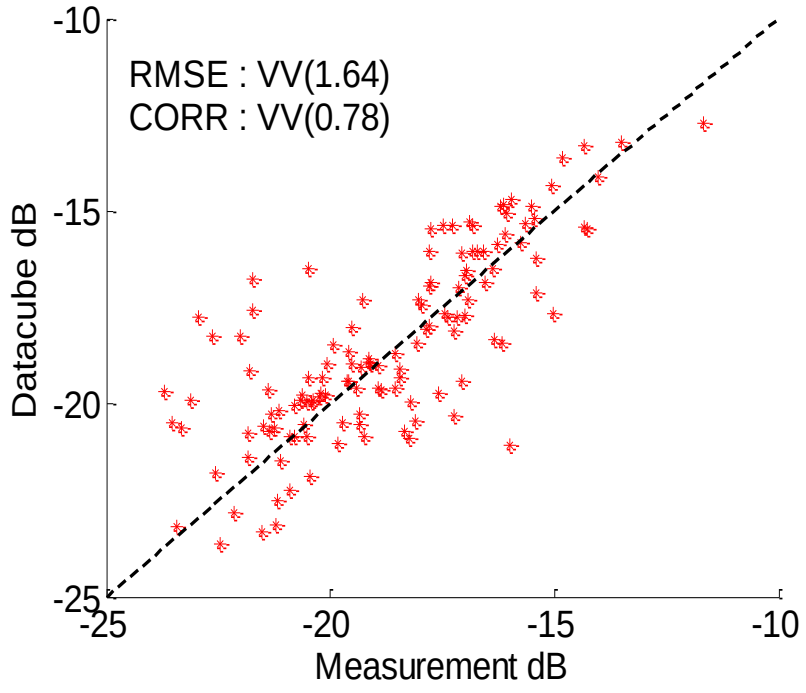

(b)

Figure II.19. VV comparison between data-cube and observation over the 13 SMAPVEX12 soybean fields (a) the coherent data-cube, (b) the incoherent data-cube.

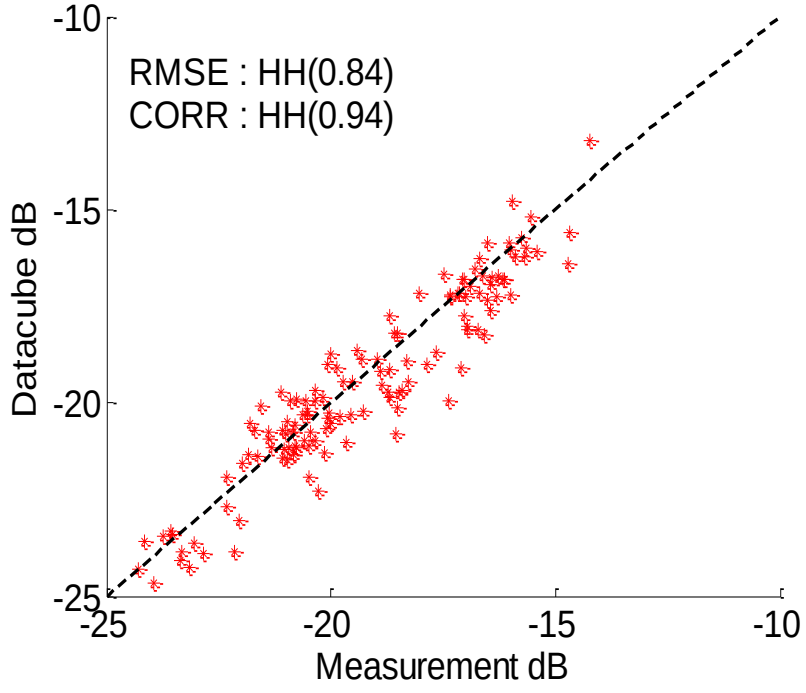

(a)

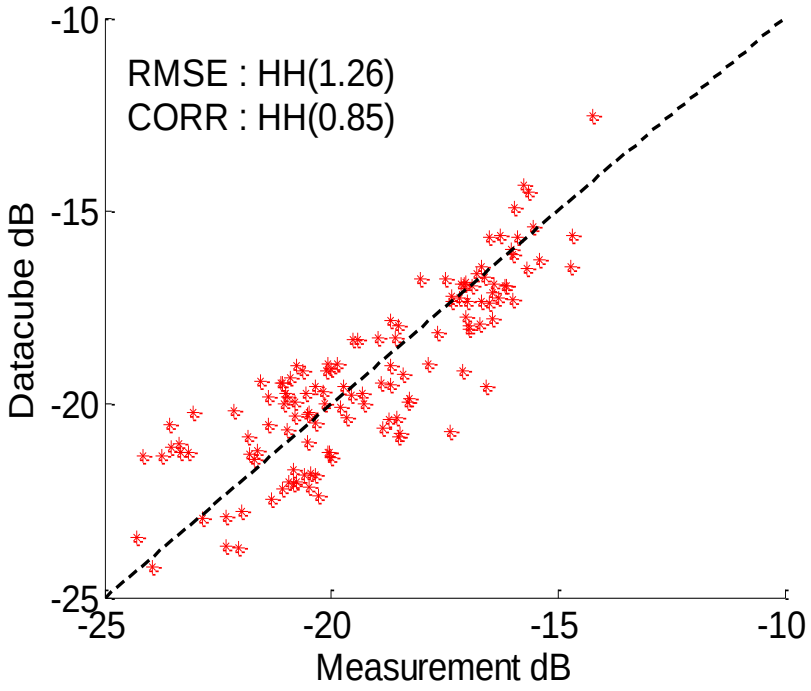

(b)

Figure II.20. HH backscattering coefficients comparison between data-cube and observation over the 13 SMAPVEX12 soybean fields (a) the coherent data-cube, (b) the incoherent data-cube.

2.4 Data-cube Based Soil Moisture Retrieval

The data-cubes developed above are used here to retrieve the soil moisture. Based on the time-series retrieval algorithm developed for the SMAP mission [6], the measured VV and HH of all the N days collected in a specific field are the inputs. The outputs are N values of VWC and $epsr_{soil}$ as well as the RMS height. $epsr_{soil}$ is then converted to soil moisture using the Mironov dielectric model [22] with the ancillary data on the clay fraction of the soil. It is assumed that the RMS height remains unchanged over the retrieval period. The retrieval approach then minimizes the difference between the measurement and the data-cube over all the N days as defined in the

cost function below where w_{VV} and w_{HH} are the weighting factors which are uniform in time and also the same for VV and HH backscattering coefficients in the case of SMAP radar [10].

$$\text{cost} = \sum_{day=1}^{N} \left[w_{VV} \left(VV_{data} - VV_{cube} \right)^2 + w_{HH} \left(HH_{data} - HH_{cube} \right)^2 \right] \tag{2.4.1}$$

The number of unknowns (2N+1) is larger than that of inputs (2N), so some constraints should be added during the retrieval to avoid the improper solutions.

2.4.1 Soil Moisture Retrieval for Wheat and Canola Fields

In this section, a VWC constraint is used under the assumption that the vegetation will not change significantly during an observation cycle. The ratio of the VWC between two sequential observation days (larger one divided by the smaller one) is assumed to be less than 1.10 and 1.14 for wheat and canola, respectively, according to the measured VWC of all the fields as shown in Figure II.21 and Figure II.22.

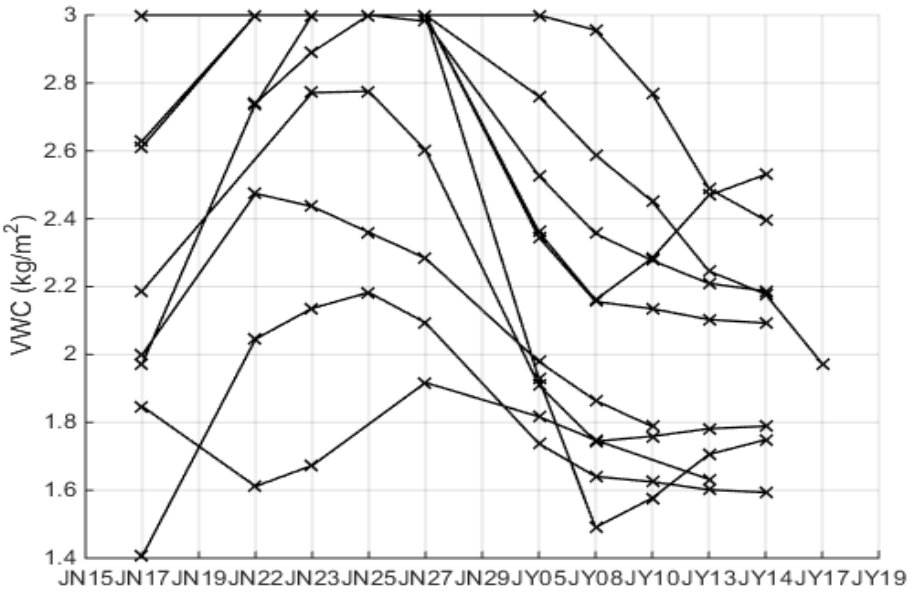

Figure II.21. VWC of the ten SMAPVEX12 wheat fields.

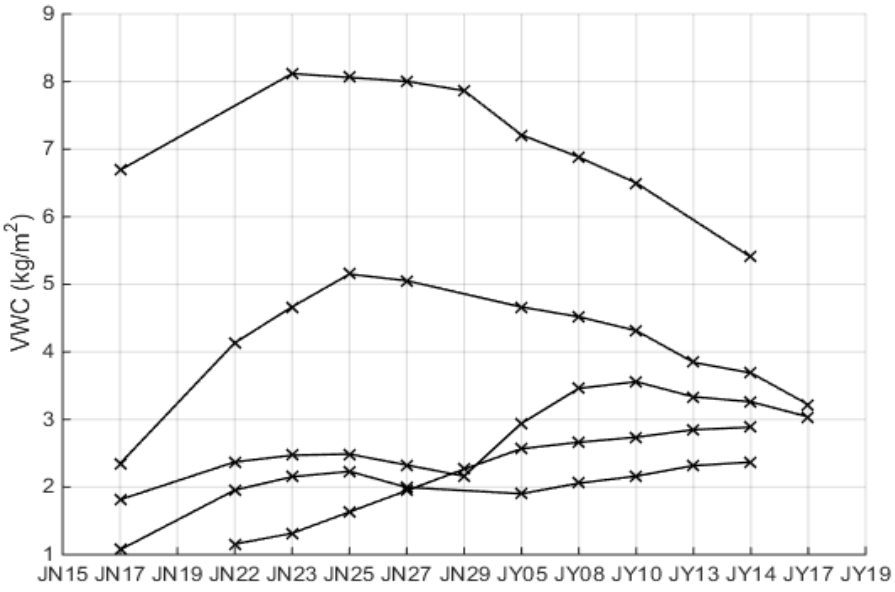

Figure II.22. VWC of the five SMAPVEX12 canola fields (The scale of the y axis is different from that of Figure II.21).

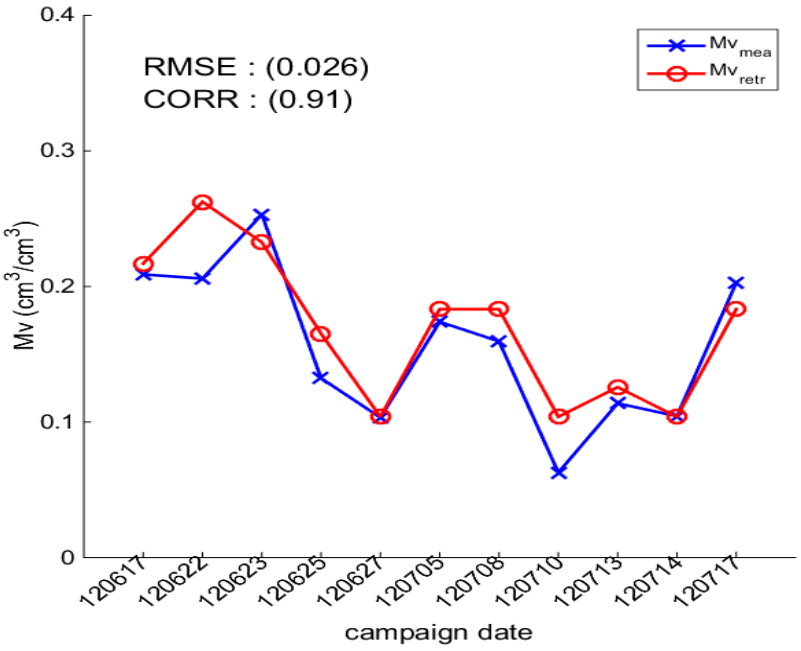

Figure II.23. Time-series soil moisture retrieval for SMAPVEX12 wheat Field 91. Mv_{mea} stands for the measured soil moisture while Mv_{retr} stands for the data-cube retrieved soil moisture, hereinafter the same.

The wheat data-cube is applied to the soil moisture retrieval of the ten wheat fields. Figure II.23 shows one example for the time-series retrieval of wheat Field 91 where the RMSE is 0.026 cm^3/cm^3 with correlation coefficient of 0.91. The retrieval results for all the ten wheat fields are presented in Figure II.24. The RMSE and correlation coefficient values for each field are listed in Table II-12. The correlation coefficient is 0.94 and the RMSE is 0.043 cm^3/cm^3 which is about the same as that obtained for bare soil [10] despite the fact that there was substantial levels of vegetation effect during SMAPVEX12. The RMSE is better than that for the pasture fields [6] (the vegetation structure is similar between pasture and wheat although the scatterer orientation angle may differ).

As described earlier, there are two data-cubes for canola, so it is important to decide which data-cube to use during the soil moisture retrieval. The approach based upon the campaign date used in the forward comparison is not suitable for retrieval because SMAP is designed for global soil moisture retrieval and the canola growth stage could vary at the same time in different areas. Based on Figure II.5 where (VV+HH)/2 became less than -13 dB since July 10th, thus when (VV+HH)/2 is less than -13 dB, the July data-cube should be used; otherwise, the other data-cube should be used. Similarly, the retrieval results are presented in Figure II.25, Figure II.26 and Table II-13 with the averaged RMSE of 0.082 cm^3/cm^3 for all the five canola fields.

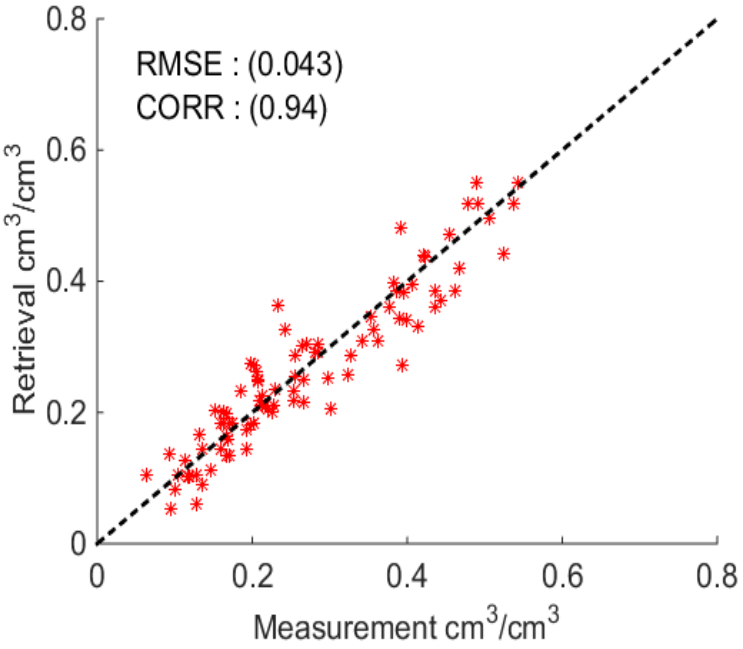

Figure II.24. Retrieved soil moisture compared with measurements for the ten SMAPVEX12 wheat fields. The x and y axes represent the measured soil moisture and data-cube based retrieval results, respectively.

Table II-12. RMSE and correlation coefficient of soil moisture between retrieval results and ground measurements for the ten wheat fields.

Field No.	RMSE (cm^3/cm^3)	Correlation Coefficient
91	0.026	0.91
85	0.034	0.89
81	0.025	0.91
74	0.034	0.99
73	0.053	0.97
65	0.042	0.96
44	0.056	0.88
42	0.051	0.92
41	0.032	0.96
31	0.061	0.94

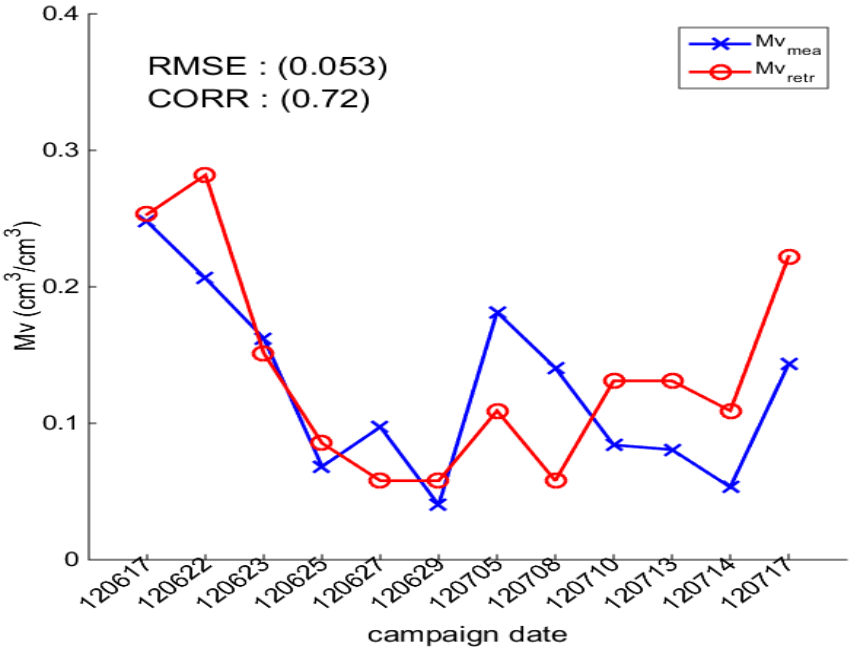

Figure II.25. Time-series soil moisture retrieval for SMAPVEX12 canola Field 61.

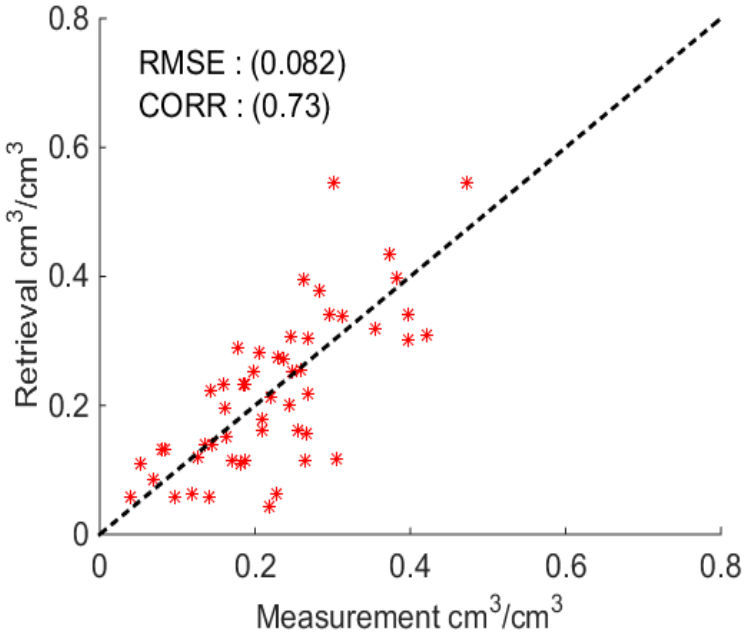

Figure II.26. Retrieved soil moisture compared with measurements for the five SMAPVEX12 canola fields. The x and y axes represent the measured soil moisture and data-cube based retrieval results, respectively.

Table II-13. RMSE and correlation coefficient of soil moisture between retrieval results and ground measurements for the five canola fields.

Field No.	RMSE (cm^3/cm^3)	Correlation Coefficient
124	0.082	0.66
122	0.075	0.65
115	0.10	0.83
84	0.089	0.43
61	0.053	0.72

As presented in section 2.2, the averaged RMSE of the backscattering coefficients between the data-cube and the measurement for all the fields in the forward comparison is similar for the wheat and canola which is around 1 dB. However, the soil moisture retrieval results for wheat are much better than those for canola. The main reason is that the backscattering coefficient of wheat is more sensitive to the soil moisture than that of canola, especially for VV. This is because the double-bounce and surface scattering, which depend significantly on the soil permittivity, usually dominate among the three backscattering mechanisms for wheat. On the other hand, volume scattering, which is independent of the soil moisture and only depends on the VWC, usually dominates for canola while the soil surface scattering is relatively small because of the significant attenuation from the generally large VWC as shown in Figure II.22. Another reason for the retrieval error of canola is its large VWC range (1 kg/m^2 ~ 9 kg/m^2) and the uncertainties associated with estimating it over this large range.

The data-cubes are applicable to the SMAP retrieval over the wheat and canola land cover classes, since the empirical tuning was performed only on the vegetation parameterization over the entire field, not for individual fields. The retrieval error mainly originates from the radar measurements, data-cube modeling and dielectric model, as discussed in more detail in [6]. Considering the uncertainties of in-situ soil moisture measurement (<0.03 cm^3/cm^3 [48]), the actual error could be smaller. The retrieval error can be further reduced by updating the data-cubes

with more data. Generally, the retrieval soil moisture based on the data-cubes are in good agreement with ground measured soil moisture.

2.4.2 Soil Moisture Retrieval of Soybean Fields

The constraints of VWC for the soybean fields are derived through the analysis of the soybean VWC measured during SMAPVEX12. As shown in Figure II.27, the VWC generally increases with time. Also, the soybean plants cannot grow too fast. The VWC growth rate that is defined as the ratio of the VWC of two alternate days has a maximum of 1.24. For example, if the retrieved VWC values contradict the VWC constraints, this series of retrieval results (one RMS height and N sets of VWC and $epsr_{soil}$) will be abandoned. Then another set associated with the minimum cost will be selected if it satisfies the VWC constraints.

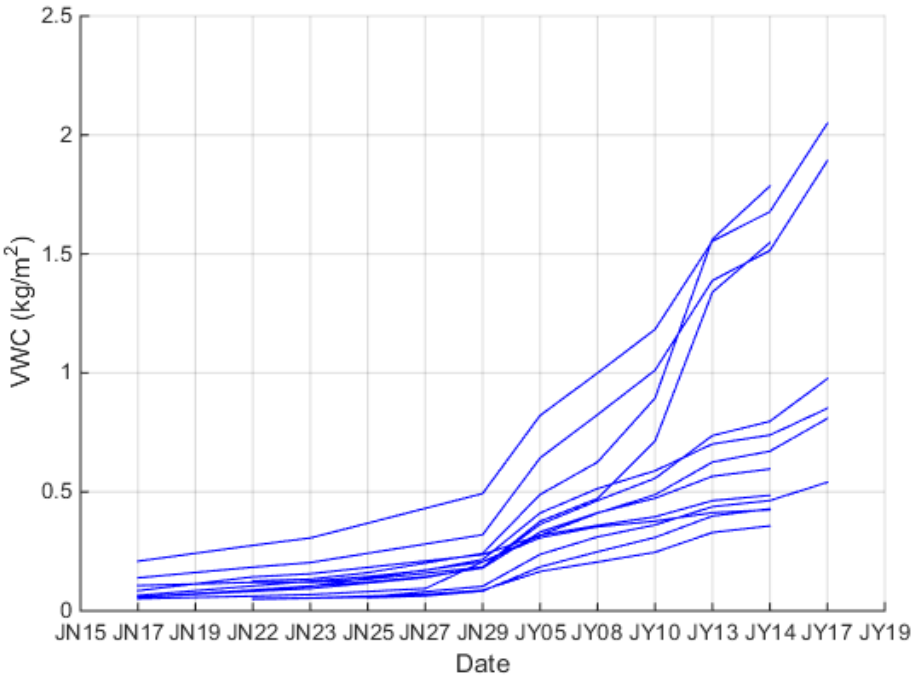

Figure II.27. Measured VWC of the 13 soybean fields.

The time series retrievals of soil moisture are shown in Figure II.28. The coherent data-cube results in more accurate soil moisture retrievals than the incoherent one. The retrieval method is now applied to the 13 soybean fields from SMAPVEX12 and the results are presented in Figure II.29. The coherent model data-cube yields better soil moisture retrievals with a lower RMSE of 0.05 cm^3/cm^3 and higher correlation coefficient of 0.92 compared with the incoherent data-cube. The retrieval error is about the same as that obtained for bare soil [57], despite the fact that the vegetation effect is substantial during SMAPVEX12. The forward model employs the physically based solution to radar scattering. The empirical tuning was performed only on the vegetation parameterization over the entire field, not for individual fields. These aspects of the forward model and retrieval suggest that this approach may be applicable to other observations of soybean.

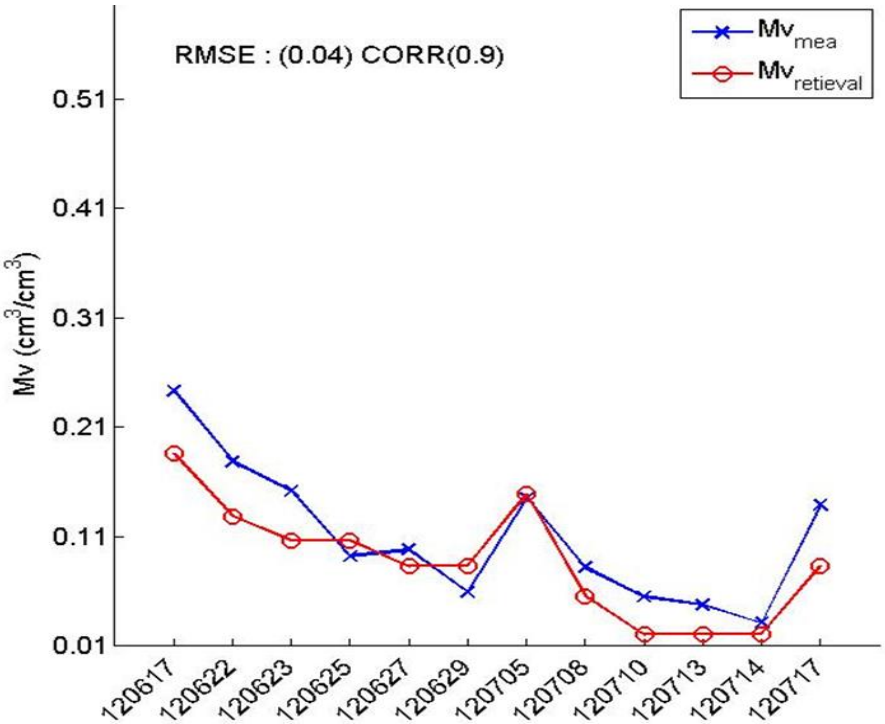

(a)

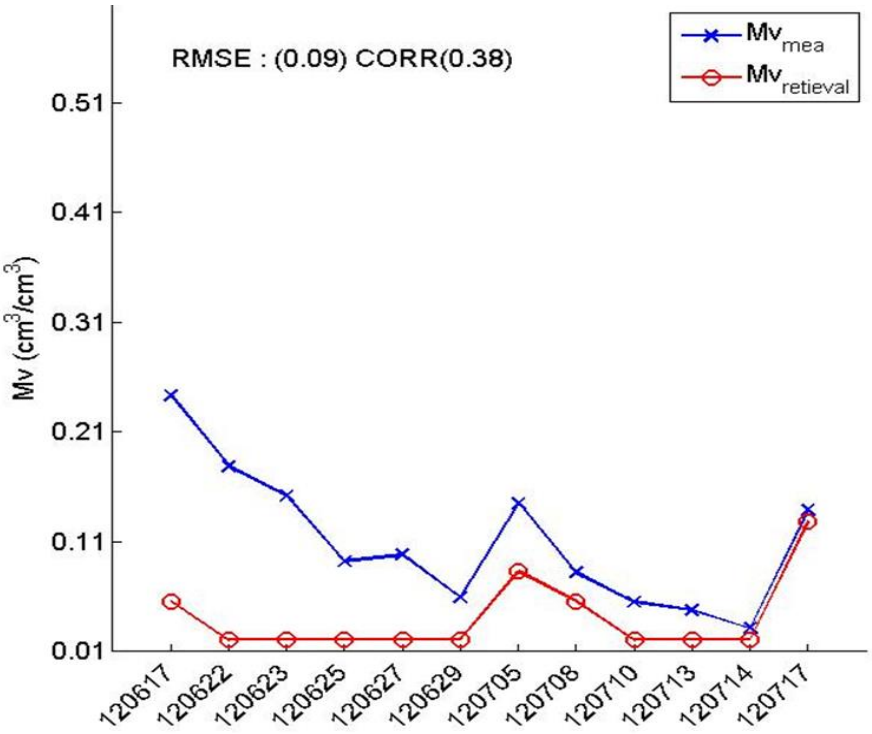

(b)

Figure II.28. Field 63 soil moisture (Mv) retrieval using (a) the coherent data-cube, (b) the incoherent data-cube. X-axis represents time: "120617" stands for June 17th 2012, hereinafter the same.

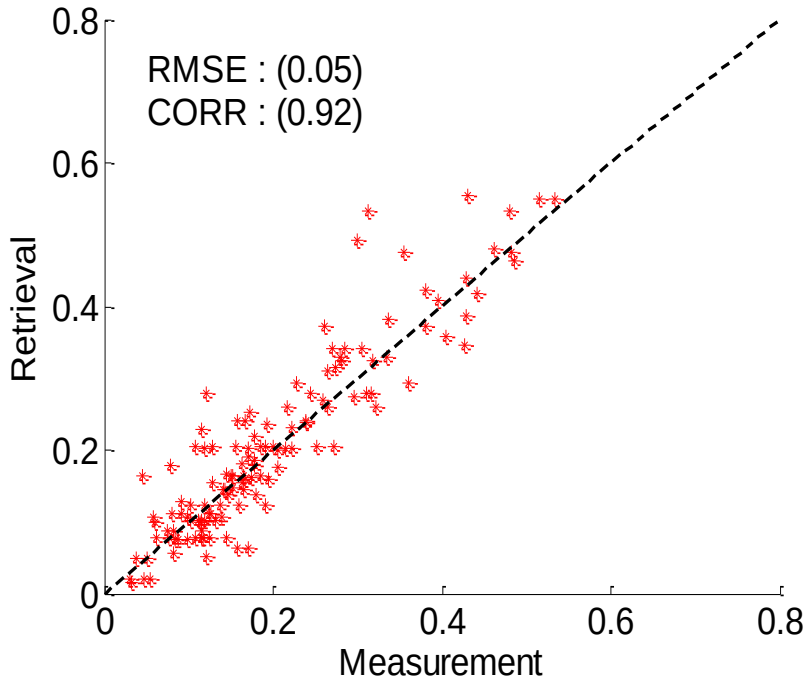

(a)

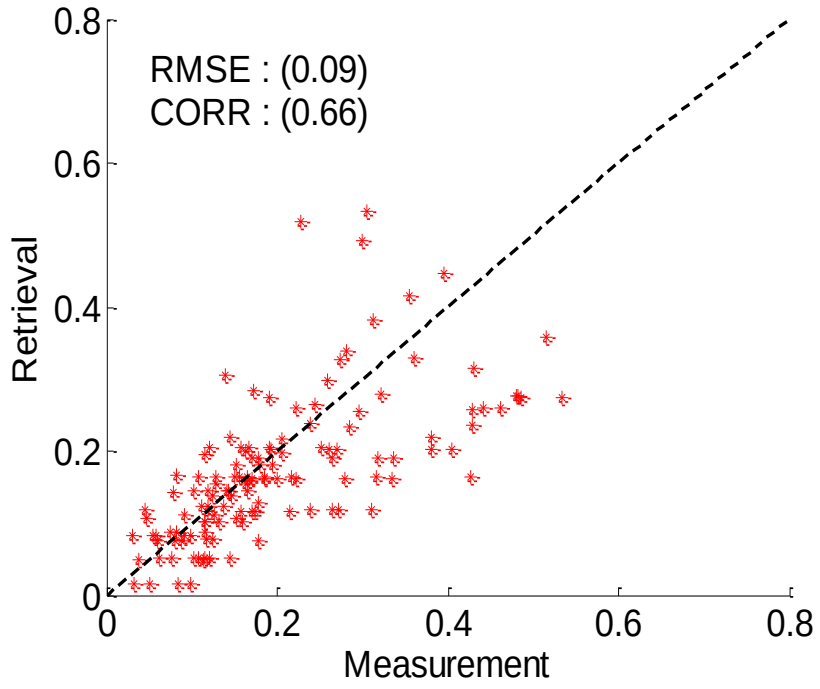

(b)

Figure II.29. Mv retrieval compared with data using (a) the coherent data-cube, (b) the incoherent data-cube.

2.5 Conclusions

Wheat and canola data-cubes are developed based on a physical scattering model to support soil moisture retrieval for the SMAP mission. The physical model combines the distorted Born approximation with the NMM3D. The distorted Born approximation is derived from the Foldy-lax equation with first-order iteration using the half-space Green's function and the T matrix. The backscattering coefficients of the data-cubes compare well with the UAVSAR data collected during the SMAPVEX12 field campaign over a wide range of VWC and soil moisture. Correlation coefficient are 0.84 and 0.93 for HH backscattering coefficients, and 0.85 and 0.77 for VV backscattering coefficients of wheat and canola fields, respectively. The RMSE are 0.82 dB and 0.78 dB for HH backscattering coefficients, and 0.97 dB and 1.30 dB for VV backscattering

coefficients of wheat and canola fields, respectively. The total error for the backscattering coefficient from the data-cubes is generally smaller than that from the MIMICS model applied in [27] for the wheat and canola fields at 40 degrees incident angle and L-band. The time-series retrieval algorithm developed for the SMAP mission is implemented to retrieve the soil moisture using the data-cubes, resulting in a RMSE of 0.043 cm^3/cm^3 for the wheat fields, compared with the in-situ soil moisture from SMAPVEX12. The retrieval performance for the canola fields is not as good, a RMSE of 0.082 cm^3/cm^3, mainly because the volume scattering, which is independent of soil moisture, dominates among the backscattering mechanisms. The satisfactory results in the chapter will contribute to SMAP's global soil moisture retrieval since there is no empirical tuning for individual fields. In the future, the data-cubes will be refined with more field campaign data sets so that the retrieval accuracy can be further improved, especially for the canola data-cubes. Recently, the SMAP baseline active retrieval algorithm based on data-cubes has been applied to the SMAP satellite data [7].

A coherent model with conditional probabilities is developed to compute the radar scattering from soybean fields. With the use of conditional probabilities, the unrealistic overlap of two branches at the same location is avoided. The new model is closer to the reality than the previous models, and produces smaller scattering compared with the previous coherent model predictions. However, it also generates significantly larger scattering than the incoherent model. By comparisons with SMAPVEX 12 data, we are able to show that this approach agrees well with observations in both the absolute values of backscattering and the polarization ratios between VV and HH backscattering coefficients. Using the coherent model with conditional probabilities, the RMSE of the data-cube prediction decreases to 1.1 dB for VV backscattering coefficients and 0.84 dB for HH backscattering coefficients. The accuracy of the time-series retrieval of soil moisture

also improves by using the new data-cube based on the coherent model with conditional probabilities, compared with the incoherent data-cube. By imposing a constraint on the VWC in retrieval, the RMSE of the retrieved soil moisture for the 13 SMAPVEX12 soybean fields was as small as 0.05 cm^3/cm^3. Moreover, the current model with improved physical representation may be applicable to other soybean fields because it does not depend on the characteristics of individual field or flight campaign. The data-cube method of soil moisture retrieval depends on the accuracy of the data-cube which requires that long enough time-series should be acquired to train the data-cube before the retrieval of soil moisture. Thus, SMAPVEX12 is necessary before the launch of SMAP. Although the retrieval performance will vary somewhat with the SMAP data due to the difference in speckle and landcover heterogeneity, the satisfactory retrieval reported in this chapter adds confidence to the algorithm and will benefit SMAP mission's goal of the global soil moisture retrieval.

CHAPTER III

A Unified Combined Active and Passive Model for Microwave Remote Sensing of Agricultural Vegetation at L-Band

The distorted Born approximation (DBA) of volume scattering was combined with the numerical solution of Maxwell's equations (NMM3D) for rough surfaces to calculate radar backscattering coefficients for the Soil Moisture Active Passive (SMAP) mission, in chapter II. The model results were validated with the Soil Moisture Active Passive Validation Experiment 2012 (SMAPVEX12) data. In this chapter, this existing model is extended to calculate the bistatic scattering coefficients for each of the three scattering mechanisms: volume, double-bounce and surface scattering. Emissivities are calculated by integrating the bistatic scattering coefficients over the hemispherical solid angle. The backscattering coefficients and emissivities calculated using this approach form a consistent model for combined active and passive microwave remote sensing. This has the advantage that the active and passive microwave remote sensing models are founded on the same theoretical basis and hence allow the use of the same physical parameters such as crop density, plant height, stalk orientation, leaf radii, and surface roughness, amongst others. In this chapter, this combined active and passive model, DBA/NMM3D, is applied to four vegetation types to calculate both backscattering coefficients and brightness temperature: wheat, winter wheat, pasture and canola. We demonstrate the use of the DBA/NMM3D for both active and passive using the same input parameters for matching active and passive coincident data. The model results are validated using coincident airborne Passive Active L-band System (PALS) low-

altitude radiometer data and Uninhabited Aerial Vehicle Synthetic Aperture Radar (UAVSAR) data taken during the SMAPVEX12 field campaign. Results show an average root mean squared error (RMSE) of 1.04 dB and 1.21 dB for backscatter at VV and HH backscattering coefficients, respectively, and 4.65 K and 6.44 K for brightness temperature at V-pol and H-pol, respectively. The results are comparable to those from the tau-omega model which is commonly used to compute the brightness temperature, though the physical parameters used in this model are different from the empirically adjusted parameters used in the tau-omega model.

3.1 Introduction

Combined active and passive microwave remote sensing of vegetation-covered surfaces is of great interest and importance given the increasing number of active and passive satellite microwave missions and datasets available for studies of land surfaces for application in hydrology and terrestrial ecology [1]. For example, L-band radar and radiometer data can be used to retrieve soil moisture over crop fields. According to the previous research, L-band is the optimal choice for remote sensing of near surface soil moisture of vegetation-covered surfaces with moderate vegetation water content (VWC) [58, 59]. At L-band, the atmosphere can be near transparent even under cloudy and rain conditions and the transmissivity through the vegetation canopy with moderate *VWC* is relatively high; so that the L-band radar or radiometer data has considerable sensitivity to the near surface soil moisture of the agricultural fields [2, 3, 58, 59]. Soil moisture is closely linked to crop water stress and its availability hence provides better crop supply and demand information. This in turn enables improvements in crop productivity [3]. The VWC is closely related to the crop development and can also be estimated from the radar and radiometer data. This further enables crop assessment and monitoring [3]. For many years, passive microwave

retrieval algorithms for satellite missions such as Advanced Microwave Scanning Radiometer-E (AMSR-E), Soil Moisture Ocean Salinity (SMOS), and SMAP have been based on the tau-omega model [58, 60], which is derived from a zeroth order solution of the radiative transfer equation. Since the zeroth order solution ignores the phase matrix term [4], an empirically adjusted scattering albedo ω, which is usually smaller than the physical parameter, must be used to fit this model to observations. The vegetation parameter b used in the tau-omega model to relate VWC to the optical thickness τ is also empirical. In modeling the rough surface effects in the tau-omega model, the h-Q formulation [61] is used; it includes only the coherent wave specular reflection while ignoring the bistatic scattering. Thus, empirical "best-fit" parameters rather than physical parameters are used in the tau-omega model. For active remote sensing modeling, we previously used the distorted Born approximation (DBA) [11] and the numerical solutions of the Maxwell's equations (NMM3D) [32] (this method is called NMM3D-DBA for short), where the coherent reflectivity and rough-surface scattering are calculated by NMM3D [32]. This model was used to calculate the VV and HH backscatter at L-band for pasture [6], wheat, winter wheat and canola fields. The active model has been validated using data from the Soil Moisture Active Passive Validation Experiment 2012 (SMAPVEX12) [6, 10]. The distorted Born approximation is valid for these vegetation types because the optical thickness at L-band is small.

Combined active and passive approaches for remote sensing of vegetation-covered surfaces have been studied extensively. In many studies, the analyses for radiometer and radar data were based on different models: the tau-omega model was used as a passive model [62, 63], while an empirical model [62] or the water-cloud model [63] was used as an active model. Ferrazzoli *et al.* [64] and Guerriero *et al.* [65] discussed the interrelations between emission and scattering for vegetation-covered surfaces. In [64, 65], the emissivity and backscattering coefficient were

computed in a unified approach using the radiative transfer theory and the "matrix doubling" algorithm. Chauhan *et al.* [66] used DBA to compute both the backscattering coefficient and brightness temperature for corn. But the direct scattering from the soil surface was not taken into account, which can be important for rough soil surface [67]. Furthermore, only brightness temperature data at H-polarization over a one-week period were used for comparison. In this chapter, we study active and passive microwave remote sensing in a consistent manner using NMM3D-DBA for both active and passive. The active model NMM3D-DBA is extended to calculate bistatic scattering, and integration of the bistatic scattering over the hemispherical solid angle is used to calculate emissivity. Thus, the active and passive microwave remote sensing models are founded on the same theoretical basis and allow the use of the same physical parameters such as crop density, plant height, stalk orientation, leaf radii, surface roughness, amongst others. The vegetation canopy is modeled as a layer of uniformly distributed dielectric cylinders and disks representing stalks and leaves, respectively [11]. The distorted Born approximation is derived from the Foldy-Lax equation with first-order iteration using the half-space Green's function and the T matrix [4]. The attenuation through the vegetation layer is accounted for by the imaginary part of the effective propagation constant calculated by Foldy's approximation [4]. NMM3D results are based on the Method of Moments (MoM) with the Rao-Wilton-Glisson (RWG) basis function using Gaussian random rough surfaces with exponential correlation functions, which have been shown to agree well with experimental data for various root mean square (RMS) height values and soil moisture conditions [32]. The total bistatic scattering is expressed as the incoherent sum of three scattering mechanisms: volume scattering, double-bounce scattering and surface scattering. In the coherent model [36, 68], the collective scattering between the vegetation scatterers is taken into account, and then the scattering from the vegetation and the scattering from the rough surface

are added incoherently. The coherent model is more difficult to implement than the incoherent model, especially for calculating emissivity which includes integration over the upper hemispherical solid angle. The coherent model also requires more input parameters such as the relative positions of the scatterers. In this chapter, it is the first time that the incoherent model is combined with NMM3D for emissivity calculations. The MIMICS model [28] uses first-order radiative transfer (RT) and the rough-surface scattering is calculated by one of the three methods: Geometrical Optical Model (GO), Physical Optics Model (PO) and Small Perturbation Model (SPM). In this chapter, we use NMM3D-DBA. The DBA is the same as the first-order RT theory except that it includes backscattering enhancement [43] in the double-bounce term. In the backscattering direction, the double-bounce term from DBA is twice (3dB) larger than that from the first-order RT for co-pol. The rough-surface scattering is calculated by the numerical solution of Maxwell's equations (NMM3D).

Here, the NMM3D-DBA model is applied to the analysis of SMAPVEX12 data for wheat, winter wheat, pasture and canola fields to calculate both brightness temperatures and radar backscatter coefficients. The collective and multiple scattering effects do not contribute significantly for the fields studied in this chapter since bistatic surface scattering mostly dominates among the three scattering mechanisms and the scattering parameter ω as well as the optical thickness τ is not large for these fields. Thus the distorted Born approximation which is easier to implement and requires less input parameters than the coherent model [36] and the multiple scattering model [5] is applied to these fields. The model results are compared with the brightness temperature and backscatter observations from SMAPVEX12 [34]. SMAPVEX12 was a pre-launch Soil Moisture Active Passive (SMAP) field experiment. Observations began during the period of early crop development and finished at the point where crops had reached maximum

biomass. Soil moisture also varied significantly [34]. These long-duration measurements, over a wide range of soil moisture and vegetation conditions, are a unique and valuable attribute of this field campaign when compared with previous airborne experiment, and provide an extensive data set critical to test the vegetation scattering models and radar-based soil moisture retrieval algorithm for SMAP [34].

The outline of the chapter is as follows: section 3.2 presents the derivations of the bistatic scattering coefficients using NMM3D-DBA that are used to calculate the emissivity. In section 3.3, the NMM3D-DBA model uses the same physical parameters to compute both brightness temperature and backscatter, which are evaluated by the SMAPVEX12 PALS low-altitude radiometer data and UAVSAR data, respectively. Section 3.4 presents the comparison between the NMM3D-DBA and the tau-omega model.

3.2 Unified Combined Active and Passive Model Based on NMM3D-DBA

Emissivity (e_q) related to brightness temperature through the physical temperature of the object, is calculated by integrating the bistatic scattering coefficients over the hemispherical solid angle as given in the equation below [64, 65]

$$e_q = 1 - \frac{1}{4\pi}\int_0^{\pi/2} d\theta_s \sin\theta_s \int_0^{2\pi} d\phi_s \sum\nolimits_{p=v \text{ or } h} \gamma_{pq}\left(\theta_s, \phi_s; \theta_i, \phi_i\right) \tag{3.2.1}$$

where the subscripts 'p' and 'q' stand for polarization, either 'v' or 'h'. γ_{pq} is the bistatic scattering coefficient with 'q' denoting the polarization of transmitting and 'p' denoting the polarization of receiving. θ_i and ϕ_i as used in a spherical coordinate system define the incident

direction, while θ_s and ϕ_s define the scattering direction. The integration is calculated numerically using the Trapezoid rule. The convergence of the integration with regard to the number of points used has been checked. To calculate the bistatic scattering coefficient γ we use the distorted Born approximation for the vegetation volume scattering, which is derived below, and NMM3D [32] for coherent reflectivity and bistatic rough-surface scattering by the soil surface. In the derivations below, the crucial assumptions are: (1) the vegetation scatterers are uniformly distributed in the vegetation layer; (2) each type of vegetation scatterer, such as stalks or leaves, is statistically identical in terms of the size, shape and permittivity; (3) there is no correlation between the scattered fields of different vegetation scatterers, hence the incoherent model can be used; and (4) the first-order scattering contributions are significantly larger than the high-order scattering contributions in the vegetation, such that a single scattering approximation is applicable.

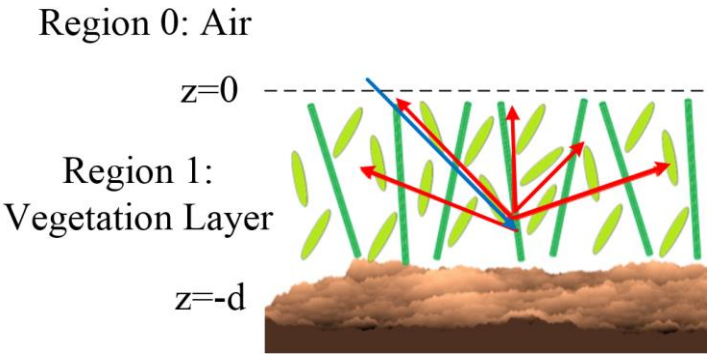

(a)

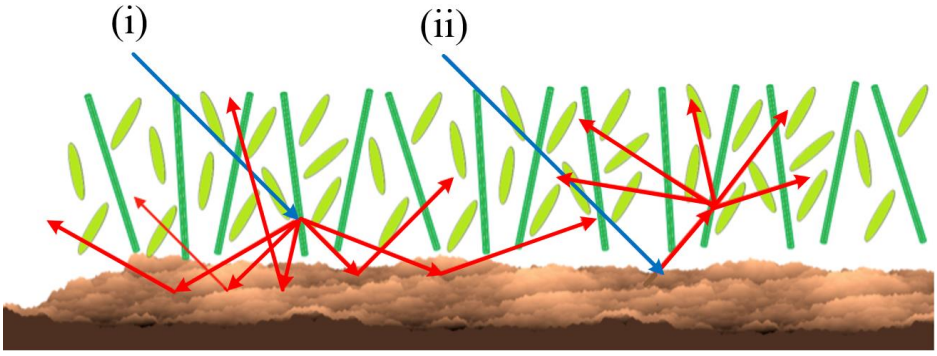

(b)

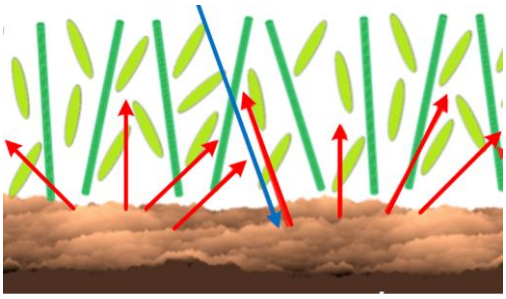

(c)

Figure III.1 Scattering from a vegetation-covered surface. The three scattering mechanisms are: (a) volume scattering; (b) double-bounce scattering (i) scattering from the scatterer and then reflected by the surface, (ii) scattering of the reflected wave by a scatterer; (c) surface scattering.

As shown in Figure III.1, let the vegetation layer be region 1 and the air above the vegetation layer be region 0. Then, the total field in region 0 is according to the Foldy-Lax equation [4] with first-order iteration:

$$\overline{E} = \overline{E}_{inc} + \overline{E}_{ref} + \sum_{j=1}^{N} \overline{\overline{G}}_{01} \overline{\overline{T}}_{j} \left(\overline{E}_{inc} + \overline{E}_{ref} \right) \tag{3.2.2}$$

where N is the total number of scatterers and $\overline{\overline{T}}_{j}$ is the transfer operator for scatterer j [4]. The subscript '01' of the Green's function ($\overline{\overline{G}}_{01}$) indicates that the scatterers are in region 1 while the observation is in region 0. $\overline{E}_{inc}$ and $\overline{E}_{ref}$ are the incident and reflected field by the rough surface under the vegetation, respectively.

The vegetation scatterers are in the upper space over a lower space of soil, as shown in Figure III.1. There is reflection at the boundary between the vegetation layer and the soil while there is no physical reflection at z = 0 (between the vegetation layer and air). Thus, the half space Green's function [4] is used and can be separated into two terms ($\overline{\overline{G}}_{01}^{(0)}$ and $\overline{\overline{G}}_{01}^{(R)}$ as below). The total scattered field from the N vegetation particles can be written as [4]:

$$\overline{E}_s = \sum_{j=1}^{N} \overline{\overline{G}}_{01} \overline{\overline{T}}_j \left(\overline{E}_{inc} + \overline{E}_{ref} \right) = \sum_{j=1}^{N} \left(\overline{\overline{G}}_{01}^{(0)} + \overline{\overline{G}}_{01}^{(R)} \right) \overline{\overline{T}}_j \left(\overline{E}_{inc} + \overline{E}_{ref} \right) \tag{3.2.3a}$$

where $\overline{\overline{G}}_{01}^{(R)}$ with the superscript '(*R*)' represents the part of Green's function with reflection by the soil below while $\overline{\overline{G}}_{01}^{(0)}$ with the superscript '(*0*)' represents the remaining part of the Green's function.

Multiplying out the two brackets yields

$$\overline{E}_s = \sum_{j=1}^{N} \left(\overline{\overline{G}}_{01}^{(0)} \overline{\overline{T}}_j \overline{E}_{inc} + \overline{\overline{G}}_{01}^{(R)} \overline{\overline{T}}_j \overline{E}_{inc} + \overline{\overline{G}}_{01}^{(0)} \overline{\overline{T}}_j \overline{E}_{ref} + \overline{\overline{G}}_{01}^{(R)} \overline{\overline{T}}_j \overline{E}_{ref} \right) \tag{3.2.3b}$$

$$\overline{E}_s \approx \sum_{j=1}^{N} \left(\overline{\overline{G}}_{01}^{(0)} \overline{\overline{T}}_j \overline{E}_{inc} + \overline{\overline{G}}_{01}^{(R)} \overline{\overline{T}}_j \overline{E}_{inc} + \overline{\overline{G}}_{01}^{(0)} \overline{\overline{T}}_j \overline{E}_{ref} \right) \tag{3.2.3c}$$

The first term ($\sum_{j=1}^{N} \overline{\overline{G}}_{01}^{(0)} \overline{\overline{T}}_j \overline{E}_{inc}$) is the volume scattering while the second and third terms ($\sum_{j=1}^{N} \overline{\overline{G}}_{01}^{(R)} \overline{\overline{T}}_j \overline{E}_{inc}$ and $\sum_{j=1}^{N} \overline{\overline{G}}_{01}^{(0)} \overline{\overline{T}}_j \overline{E}_{ref}$) are the double-bounce scattering, as illustrated in Figure III.1 (a) and (b). The last term ($\sum_{j=1}^{N} \overline{\overline{G}}_{01}^{(R)} \overline{\overline{T}}_j \overline{E}_{ref}$) in is the triple bounce scattering, which is likely to be weak in the case of grass, wheat, canola and soybean fields at L-band [27]; it is ignored here as shown in equation (3.2. 3c).

According to the analysis above, the total bistatic scattering is calculated as the sum of the three scattering mechanisms shown in Figure III.1: volume scattering, double-bounce scattering and surface scattering.

$$\gamma_{pq} = \gamma_{pq}^{vol} + \gamma_{pq}^{db} + \gamma_{pq}^{surf} \tag{3.2.4}$$

where the superscript '*vol*' is short for volume scattering, '*db*' is short for double-bounce scattering and '*surf*' is short for surface scattering.

The bistatic scattering coefficient is calculated as [2]:

$$\gamma_{pq} = \frac{4\pi}{A\cos\theta_i}\left\langle S_{pq}S_{pq}^{*}\right\rangle \tag{3.2.5}$$

where *A* is the illumination area, S_{pq} is the element in the scattering matrix and the angle brackets $\langle\ \rangle$ in the expressions indicate the statistical average over the orientations of different scatterers. The calculations of S_{pq} was explained in details in chapter II.

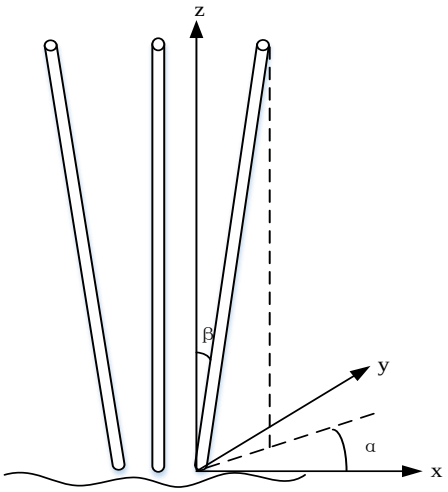

Figure III.2 Cylinder scatterer elevation angle (β) and azimuth angle (α).

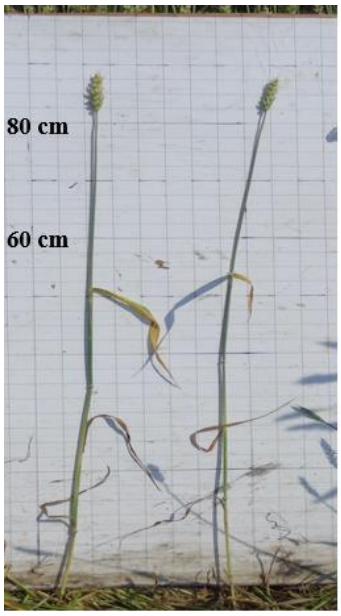

Figure III.3 Photos of wheat from SMAPVEX12.

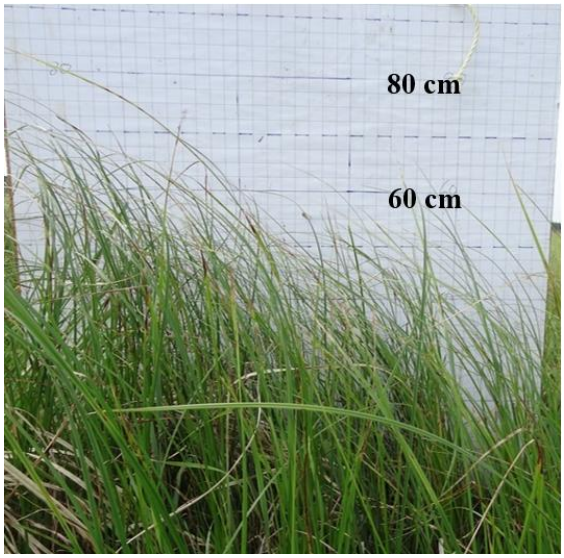

Figure III.4 Photos of pasture from SMAPVEX12.

The S_{pq} for volume scattering is

$$S_{pq}^{vol} = \sum_{j=1}^{N} \exp\left(-i\left(\bar{k}_{sp} - \overline{K}_{iq}\right)\bullet \bar{r}_j\right) f_{pq,j}\left(\theta_s, \phi_s; \pi - \theta_i, \phi_i\right) \tag{3.2.6}$$

$$\text{with, } \bar{k}_{sp} = k\sin\theta_s\cos\phi_s\hat{x} + k\sin\theta_s\sin\phi_s\hat{y} + k_{spz}\hat{z},\ \overline{K}_{iq} = k\sin\theta_i\cos\phi_i\hat{x} + k\sin\theta_i\sin\phi_i\hat{y} - k_{iqz}\hat{z} \tag{3.2.7}$$

where the subscript '*i*' represents incident and is changed to *'s'* when representing scattered. $\bar{r}_j = x_j\hat{x} + y_j\hat{y} + z_j\hat{z}$ is the position of the *j*th scatterer. *k* is the wavenumber in free space. $f_{pq,j}$ is the scattering amplitude for the *j*th scatterer. Cylinders and disks are used to model the vegetation scatterers [11]. For example, grass, wheat and the stalks of the canola plants are modeled as cylinders while canola leaves are modeled as disks as shown in Figure III.2, Figure III.3, Figure III.4, and Figure II.4 (a). The scattering amplitudes $f_{pq,j}$ for cylinders and disks are calculated using the Infinite Cylinder Approximation (ICA) and Generalized Rayleigh-Gans Approximation [4], respectively.

The boundary condition, which is also called the phase matching condition, states that the tangential component of the total electric field is continuous across the boundary when there are no sources at the boundary [2]. With the application of the phase matching condition [2] at the boundary between the air and vegetation layer, we obtain

$$k_{iqz} = \sqrt{k_q^2 - k^2\sin^2\theta_i} \tag{3.2.8}$$

where k_q is the effective propagation constant in the vegetation layer for polarization 'q'. k_q is calculated by Foldy's approximation where the scatterers are treated as embedded in the equivalent homogenous media [4],

$$k_q = k + \frac{2\pi n_0}{k}\left\langle f_{qq}\left(\pi-\theta_i, 0; \pi-\theta_i, 0\right)\right\rangle \tag{3.2.9}$$

where n_0 is the number of scatterers per m^3.

k_{spz} is obtained in the same way. Using equation (3.2.6) and assuming independent scattering,

$$\left\langle S_{pq}^{vol} S_{pq}^{vol*}\right\rangle = \sum_{j=1}^{N}\left\{\begin{array}{l}\left\langle \exp\left(-i\left(\bar{k}_{sp}-\overline{K}_{iq}\right)\bullet\bar{r}_j\right)\exp\left(i\left(\bar{k}_{sp}^{*}-\overline{K}_{iq}^{*}\right)\bullet\bar{r}_j\right)\right\rangle \\ \times\left\langle f_{pq,j}\left(\theta_s,\phi_s;\pi-\theta_i,\phi_i\right) f_{pq,j}^{*}\left(\theta_s,\phi_s;\pi-\theta_i,\phi_i\right)\right\rangle\end{array}\right\} \tag{3.2.10}$$

Assuming that the scatterers are statistically identical and uniformly distributed in the vegetation layer [4], we can rewrite equation (3.2.10) as:

$$\left\langle S_{pq}^{vol} S_{pq}^{vol*}\right\rangle = \frac{N}{V}\int d\bar{r}_j \exp\left(2\,\mathrm{Im}\left(\bar{k}_{sp}-\overline{K}_{iq}\right)\bullet\bar{r}_j\right)\left\langle\left| f_{pq}\left(\theta_s,\phi_s;\pi-\theta_i,\phi_i\right)\right|^2\right\rangle \tag{3.2.11}$$

where V is the volume of the vegetation layer, and Im() indicates that only the imaginary part is used. According to the phase matching condition [2], the x and y components of $\bar{k}_{sp}$ and $\overline{K}_{iq}$ are real and only the z component has an imaginary part. $\frac{N}{V} = n_0$. Let the thickness of the vegetation layer be d, and then it follows that:

$$\left\langle S_{pq}^{vol} S_{pq}^{vol*}\right\rangle = n_0 A\int_{-d}^{0}\exp\left(2\,\mathrm{Im}\left(k_{spz}-K_{iqz}\right)z_j\right)\left\langle\left| f_{pq}\left(\theta_s,\phi_s;\pi-\theta_i,\phi_i\right)\right|^2\right\rangle dz_j \tag{3.2.12}$$

where z_j is the z coordinate of the jth scatterer. The limits of the integration is $-d$ and 0 since the vegetation layer is within the range of $-d$ to 0 as illustrated in Figure III.1.

And finally, by substituting equation (3.2.12) into (3.2.5),

$$\gamma_{pq}^{vol} = \frac{4\pi n_0}{\cos\theta_i}\frac{1-\exp\left(-2\left(\mathrm{Im}\left(k_{spz}\right)+\mathrm{Im}\left(k_{iqz}\right)\right)d\right)}{2\left(\mathrm{Im}\left(k_{spz}\right)+\mathrm{Im}\left(k_{iqz}\right)\right)}\left\langle\left| f_{pq}\left(\theta_s,\phi_s;\pi-\theta_i,\phi_i\right)\right|^2\right\rangle \tag{3.2.13}$$

Next, for double-bounce scattering, there are two terms: (i) scattering from a scatterer that is then reflected by the surface, and (ii) scattering of the reflected wave by a scatterer, as shown in Figure

III.1 (b). The bistatic scattering coefficient for double-bounce scattering is thus the sum of the bistatic scattering coefficient of these two scattering terms:

$$\gamma_{qp}^{db} = \gamma_{qp}^{db,\mathrm{sr}} + \gamma_{qp}^{db,\mathrm{rs}} \tag{3.2.14}$$

where the superscripts 'sr' and 'rs' stand for term (i) and term (ii) of the double-bounce scattering, respectively.

For $\gamma_{qp}^{db,\mathrm{sr}}$ (scattered by the scatterer and then reflected), we have

$$S_{pq}^{db,sr} = \sum_{j=1}^{N} \mathrm{R}_p\left(\theta_s\right) \exp\left(2ik_{spz}d\right) \exp\left(-i\left(\overline{K}_{sp} - \overline{K}_{iq}\right)\bullet\bar{r}_j\right) f_{pq}\left(\pi-\theta_s,\phi_s;\pi-\theta_i,\phi_i\right) \tag{3.2.15}$$

where R_p is the coherent reflectivity of the rough surface for *p* polarization calculated from NMM3D [43] and *d* is the thickness of the vegetation layer.

Similarly, the assumption that the scatterers are statistically identical, mutually independent and uniformly distributed in the vegetation layer [4] leads to

$$\left\langle S_{pq}^{db,sr} S_{pq}^{db,sr*} \right\rangle = \mathrm{n}_0 A \int_{-d}^{0} dz_j \left\{ \begin{array}{l} \exp\left(2\,\mathrm{Im}\left(-k_{spz}+k_{iqz}\right)z_j\right)\left|\mathrm{R}_p\left(\theta_s\right)\right|^2 \times \\ \exp\left(-4\,\mathrm{Im}\left(k_{spz}\right)d\right)\left\langle\left|f_{pq}\left(\pi-\theta_s,\phi_s;\pi-\theta_i,\phi_i\right)\right|^2\right\rangle \end{array} \right\} \tag{3.2.16}$$

After simplification and substituting into equation (3.2.5), we obtain

$$\gamma_{pq}^{db,sr} = \left\{ \begin{array}{ll} \left[\begin{array}{l} \dfrac{4\pi n_0}{\cos\theta_i} \dfrac{1-\exp\left(2\left(\mathrm{Im}\left(k_{spz}\right)-\mathrm{Im}\left(k_{iqz}\right)\right)d\right)}{2\left(-\mathrm{Im}\left(k_{spz}\right)+\mathrm{Im}\left(k_{iqz}\right)\right)} \times \\ \left|\mathrm{R}_p\left(\theta_s\right)\right|^2 \exp\left(-4\,\mathrm{Im}\left(k_{spz}\right)d\right)\left\langle\left|f_{pq}\left(\pi-\theta_s,\phi_s;\pi-\theta_i,\phi_i\right)\right|^2\right\rangle \end{array} \right] & \text{if } \mathrm{Im}\left(k_{spz}\right) \neq \mathrm{Im}\left(k_{iqz}\right) \\ \dfrac{4\pi n_0 d}{\cos\theta_i}\left|\mathrm{R}_p\left(\theta_s\right)\right|^2 \exp\left(-4\,\mathrm{Im}\left(k_{spz}\right)d\right)\left\langle\left|f_{pq}\left(\pi-\theta_s,\phi_s;\pi-\theta_i,\phi_i\right)\right|^2\right\rangle & \text{if } \mathrm{Im}\left(k_{spz}\right) = \mathrm{Im}\left(k_{iqz}\right) \end{array} \right. \tag{3.2.17}$$

For the other term in the double-bounce scattering, $\gamma_{qp}^{db,\mathrm{sr}}$ (reflected by the rough surface and then scattered by the scatterer),

$$S_{pq}^{db,rs} = \sum_{j=1}^{N} \mathrm{R}_q\left(\theta_i\right) \exp\left(2ik_{iqz}d\right) \exp\left(-i\left(\bar{k}_{sp} - \bar{k}_{iq}\right)\bullet\bar{r}_j\right) f_{pq}\left(\theta_s,\phi_s;\theta_i,\phi_i\right) \tag{3.2.18}$$

Similarly, assuming independent scattering and that the scatterers are statistically identical and uniformly distributed in the vegetation layer [4],

$$\left\langle S_{pq}^{db,\mathrm{rs}} S_{pq}^{db,\mathrm{rs}*} \right\rangle = \mathrm{n}_0 A \int_{-d}^{0} dz_j \begin{Bmatrix} \exp\left(2\,\mathrm{Im}\left(k_{spz} - k_{iqz}\right) z_j\right) \left|\mathrm{R}_q\left(\theta_i\right)\right|^2 \times \\ \exp\left(-4\,\mathrm{Im}\left(k_{iqz}\right) d\right) \left\langle \left| f_{pq}\left(\theta_s,\phi_s;\theta_i,\phi_i\right)\right|^2 \right\rangle \end{Bmatrix} \tag{3.2.19}$$

Finally, $\gamma_{pq}^{db,sr}$ can be expressed as:

$$\gamma_{pq}^{db,sr} = \begin{cases} \left[\begin{array}{l} \dfrac{4\pi n_0}{\cos\theta_i} \dfrac{1-\exp\left(-2\left(\mathrm{Im}\left(k_{spz}\right) - \mathrm{Im}\left(k_{iqz}\right)\right)d\right)}{2\left(\mathrm{Im}\left(k_{spz}\right) - \mathrm{Im}\left(k_{iqz}\right)\right)} \times \\ \left|\mathrm{R}_q\left(\theta_i\right)\right|^2 \exp\left(-4\,\mathrm{Im}\left(k_{iqz}\right)d\right) \left\langle \left| f_{pq}\left(\theta_s,\phi_s;\theta_i,\phi_i\right)\right|^2 \right\rangle \end{array} \right] & \text{if } \mathrm{Im}\left(k_{spz}\right) \neq \mathrm{Im}\left(k_{iqz}\right) \\ \dfrac{4\pi n_0 d}{\cos\theta_i} \left|\mathrm{R}_q\left(\theta_i\right)\right|^2 \exp\left(-4\,\mathrm{Im}\left(k_{iqz}\right)d\right) \left\langle \left| f_{pq}\left(\theta_s,\phi_s;\theta_i,\phi_i\right)\right|^2 \right\rangle & \text{if } \mathrm{Im}\left(k_{spz}\right) = \mathrm{Im}\left(k_{iqz}\right) \end{cases} \tag{3.2.20}$$

Finally, for surface scattering, the bistatic scattering can be expressed as [6, 32]:

$$S_{pq}^{surf} = \exp\left(ik_{spz}d\right) \exp\left(ik_{iqz}d\right) S_{pq}^{R} \tag{3.2.21}$$

where S_{pq}^{R} is the surface scattering by bare soil calculated from NMM3D [32] and the exponential parts account for the attenuation through the vegetation layer.

In NMM3D, Maxwell's equations are solved numerically based on MoM and RWG basis functions, which is an intensive computational problem [43]. Tapered incidence fields are used since the simulated random rough surface is of finite extent, and the results for infinite surfaces are extracted from the simulations of the finite surfaces [43]. The soil surfaces are assumed to be

Gaussian random rough surfaces with exponential correlation functions, which appear to provide the best fit to the natural surfaces among the correlation functions reported in literature [2]. For L-band in this chapter, the surface area used for simulations in NMM3D is 16 by 16 square wavelengths. In this case, the RMS heights that can be simulated are within the range of 0 ~ 5 cm (0.21 wavelengths) which covers the RMS heights for all the fields studied in this chapter and captures the wide range of the natural conditions [6]. If an RMS height larger than 0.21 wavelengths is required, a larger surface area has to be simulated, which requires more computation resources and time.

Then, γ_{pq}^{surf} can be calculated by substituting the following expression into equation (3.2.17).

$$\left\langle S_{pq}^{surf} S_{pq}^{\text{surf}*} \right\rangle = \exp\left(-2\,\text{Im}\left(k_{spz}\right)d\right)\exp\left(-2\,\text{Im}\left(k_{iqz}\right)d\right)\left\langle S_{pq}^{R} S_{pq}^{\text{R}*} \right\rangle \tag{3.2.22}$$

After calculating the bistatic scattering coefficients γ, the emissivity is obtained by the integration of γ over the hemispherical solid angle as shown in equation (3.2.1). Finally, multiplying the emissivity by the physical temperature yields the brightness temperature of the vegetation fields.

For active microwave remote sensing, the backscattering coefficients are needed. We used the same vegetation model and formulations as illustrated above to calculate the backscattering coefficients and substitute $\theta_s = \theta_i,$ and $\phi_s = \phi_i + \pi$ which indicates the backscattering direction into the equations. In this way, the active and passive models are founded on the same theoretical basis and the same physical parameters as will be explained in section III are used.

3.3 Model Validation for Different Vegetation Types

In this section, the unified combined active and passive model is applied to calculate the backscattering coefficient and brightness temperature for different vegetation types. The results are compared with the data.

3.3.1 Physical Parameters for Different Vegetation Types

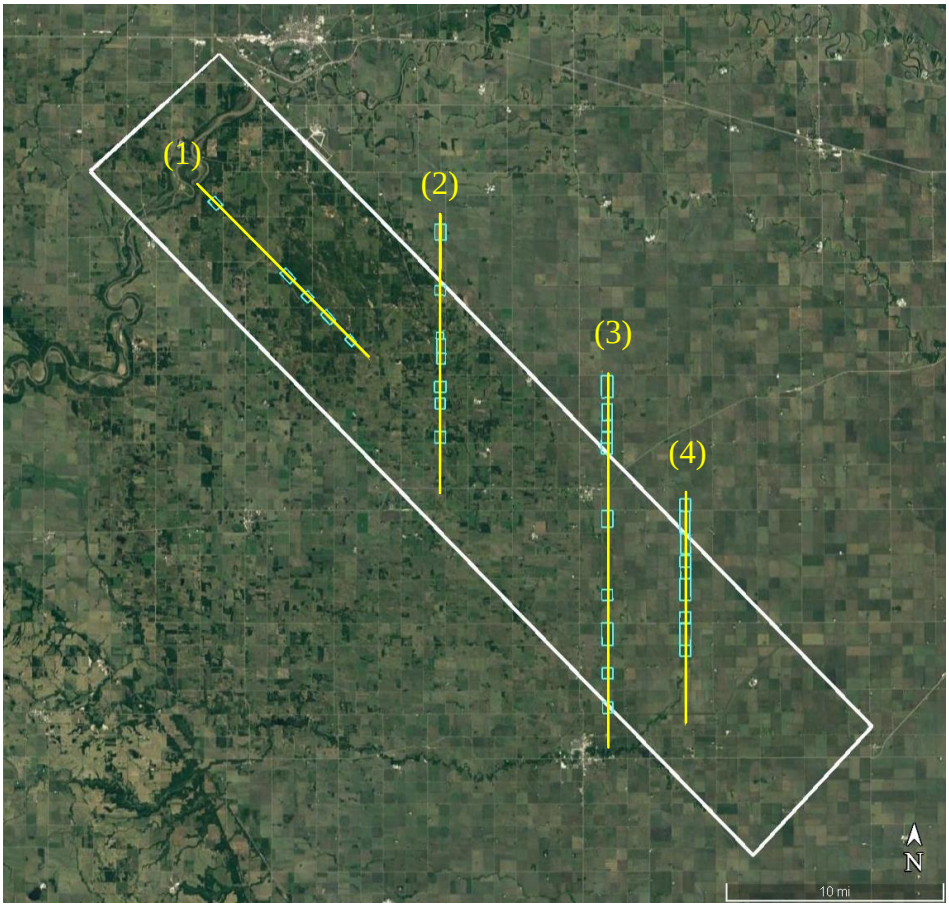

Figure III.5 SMAPVEX12 study area (white box), sampling fields (cyan boxes) and low altitude PALS flight lines (yellow lines).

To validate the consistent combined active and passive model NMM3D-DBA, we used the data from the SMAPVEX12 campaign. The SMAPVEX12 campaign is briefly summarized in this section and its details are available in [34]. Since SMAPVEX12 was described in chapter II. Here,

complementary information related to this chapter about SMPAVEX is described. The study area of SMAPVEX12 is shown in Figure III.5, where the dominant vegetation types are cereals (including wheat, winter wheat and oat), soybeans, canola, corn and pasture. The number of soybean fields is largest among all the sampling fields, as compared to the other vegetation types. The SMAPVEX12 campaign provided vegetation data, soil moisture data and coincident backscatterer and brightness temperature data which are of value in algorithm development for vegetation-covered surfaces.

Flights of the Uninhabited Aerial Vehicle Synthetic Aperture Radar (UAVSAR) [45], an aircraft-based fully polarimetric L-band radar, provided backscatter data of high-quality from its stable platform with high spatial resolution and reliable calibration. For UAVSAR, the noise floor was -45 dB and the relative calibration error was 0.3 dB. Flights of the Passive Active L-band System (PALS) provided both brightness temperature and radar backscatter data. For the passive sensor of PALS, the noise level for the field averages was less than 0.1 K and the calibration accuracy was 0.2 K. The UAVSAR was flown on a G-III aircraft while the PALS was flown on a Twin Otter. The flight lines of low altitude PALS are shown in Figure III.5 where the lines (3) and (4) were also flown by UAVSAR. Both aircrafts were flown several times per week providing coverage with a temporal frequency similar to that of the SMAP satellite. The operating frequencies were 1.413 GHz and 1.26 GHz for PALS and UAVSAR, respectively. Data within the UAVSAR swath were collected over a wide range of incidence angles. These values were normalized to an incidence angle of 40 degrees using the histogram-matching method [46], in order to be comparable to the SMAP data. The residual error in the normalization is smaller than 1 dB standard deviation. Speckle noise was significantly removed by averaging single-look data at ~7 m resolution over each field (~800 m×800 m). PALS was designed to measure data at a 40

degrees incidence angle, therefore already matching the observation angle of SMAP. PALS data were acquired at both low and high aircraft altitudes. The low-altitude flights provided an effective resolution of 600 m, which is smaller than the typical field size of 800 m×800 m. The PALS low-altitude data are hence more suitable for NMM3D-DBA model validation, which assumes homogeneous vegetation conditions. The PALS radiometer operates using a two-reference switching scheme with a matched load and a noise diode as the two references to remove internal gain fluctuations [34]. The calibration utilizes three measurements: the noise diode level, a lake and 45 degrees polarization rotation angle over the lake and land surface as detailed in [34]. The measured backscatter and brightness temperature data are compared with computed outputs from the model which will be illustrated in following sections.

Other measured model inputs were *VWC*, *RMS* rough-surface height, soil moisture, and soil and vegetation temperatures. The measurements of *VWC*, *RMS* rough-surface height, soil moisture, were described in chapter II. Subsurface soil, surface soil and vegetation temperatures were also measured on flight days at four sites in each field. Subsurface soil temperatures were measured at 5 cm and 10 cm using a digital thermometer. The temperatures for sunlit and shaded vegetation and surface soil were recorded using a thermal infrared thermometer. Vegetation attributes including crop density, plant height, stem diameter, stalk height, stalk angle, leaf thickness and leaf width were also measured. These observations provided a basis for choosing the parameters for the combined active and passive model. For the SMAPVEX12 wheat and winter wheat fields, most of the data were taken during the stem elongation, booting, heading, and ripened stages. The pasture fields varied little throughout the campaign. The growth stages of the SMAPVEX12 canola crops progressed from leaf development to stem elongation and finally entering ripening.

To validate the combined active and passive model using SMAPVEX12 data, the measured RMS height, VWC and in-situ soil moisture are input to the model to compute backscatter and brightness temperature; these are then compared with the UAVSAR and PALS low-altitude radiometer measurements. Other physical parameters needed in the model including crop density, plant height, stalk orientation and leaf radii are derived from the ground measurements which are explained in detail for each vegetation type as below. In general, the measured data directly ingested into the model are the RMS height, VWC and in-situ soil moisture. (The measured soil and vegetation temperatures are also directly given to the model to convert the emissivity to brightness temperature.) The other inputs are either constants estimated from field measurements or values calculated from the VWC, depending on how much the parameters changed during the SMAPVEX12 campaign. The goal when developing the forward models is to retrieve information about the vegetation-covered surfaces, such as the soil moisture and VWC, from the radar and radiometer data. In the future, we plan to implement a data-cube retrieval algorithm as detailed in [6], where lookup-tables are computed using the forward model. It is noted that the parameters used for wheat and canola plants listed below are a little different from those listed in chapter II. This is the DBA model has approximations and the results are based on fine tuning to match the data. In chapter II, only active data (i.e., backscattering coefficients) need to be matched. In this chapter, both active and passive (i.e., brightness temperature) data need to be matched, using the same sets of parameters. Thus, the parameters tuning is a little different in these two chapters. But all the parameters are tune within the reasonable ranges in nature. In the latter two chapters, new vegetation models which are accurate and solve Maxwell's equations for vegetation will be developed.

(i) Wheat and Winter Wheat

Wheat is modeled as a layer of uniformly distributed cylinders with different orientations. For simplicity, the wheat leaves and ears are ignored since the wheat plants during SMPAVEX 12 were dominated by the stalks, as shown in Figure III.3. The model parameters (diameter, density and orientations of the cylinders) for the wheat and winter wheat fields are presented in Table III-1.. The length of the cylinders is calculated from VWC using:

$$l = \frac{VWC}{\pi a^2 \rho_{water} n_a Mveg_{wheat}} \tag{3.3.1}$$

where l, a, ρ_{water}, n_a and M_{veg} stand for the length, radius, water density, number of cylinders per m^2 and volumetric water content of vegetation, respectively. The measured length is not used because it was not measured on flight days; instead, *VWC* was synchronized with the UAVSAR and PALS data. *VWC* measures the weight of the water contained in the vegetation in an area of 1 m^2 which has the unit kg/m^2. M_{veg} is defined as the volume of the water in plant divided by the total volume of the plant. M_{veg} is estimated from the gravimetric water content (M_g) measured during SMAPVEX12, which determines the dielectric constant [49] of leaves and stalks and subsequently affects the scattering by the vegetation.

Table III-1. Physical parameters for the wheat fields.
M_{veg} is the volumetric water content of the wheat. n_a is the number of wheat plants in 1 m^2. β and α which define the orientation of the scatterer are the elevation angle and the azimuth angle, respectively, as shown in Figure III.2. The probability function for the scatterer elevation angle is chosen to be $p(\beta)=C\sin^8(\beta)\cos^2(\beta)$ to achieve a good agreement between the data-cube and measurements. The coefficient C is determined so that the integration of p(β) over $5^\circ \sim 30^\circ$ is 1. The distribution of the scatterer azimuth angle is uniform over all the angles. For winter wheat, M_{veg} is 70% and n_a is 450 m^{-2}.

Diameter (mm)	M_{veg}	n_a (m^{-2})	β	α
2.6	80%	400	$5^\circ \sim 30^\circ$	$0 \sim 360^\circ$

(ii) Pasture

Pasture vegetation is modeled as a layer of uniformly distributed cylinders. The physical parameters (diameter, length and orientations of the cylinders) for the pasture field are presented in Table III-2.. The number of cylinders per unit volume is related to *VWC*:

$$n_0 = \frac{VWC}{\pi a^2 l^2 \rho_{water} Mveg_{wheat}} \tag{3.3.2}$$

Table III-2. Physical parameters for the pasture field.

M_{veg} is the volumetric water content of the pasture. The probability function for the scatterer elevation angle (β, measured from vertical, as shown in Figure III.2) is chosen to be $p(\beta)=C\sin^6(\beta)\cos(\beta)$ to achieve good agreement between the data-cube and measurements. The coefficient C is determined so that the integration of p(β) over $10 \sim 90^\circ$ is 1. The distribution of the scatterer azimuth angle (α as shown in Figure III.2) is uniform over all the angles.

Diameter (mm)	M_{veg}	Length (cm)	β	α
3.0	80%	60	$10^\circ \sim 90^\circ$	$0 \sim 360^\circ$

(iii) Canola

For canola, two different kinds of cylinders with different radii and lengths are used to model its main stem and branches while circular disks are used to model its leaves, as shown in Figure II.4 (a). The leaf thickness is much smaller than the wavelength at L-band, and thus the total area of the leave is more important than its shape [5]. Similar to the pasture and wheat case, these elements are assumed to be uniformly distributed in the canola layer with different orientations. It can be seen from Figure II.4 (b) and (c) that the geometry of the canola plant in June was different from that in July. There were more leaves with larger radii in June than July. Thus, two sets of physical parameters were used for canola to represent the geometry of the canola plants at the respective growth stages. The parameters are listed in Table III-3. The M_{veg} and leaf radius are adjusted to smaller values for the July data-cube based on the ground data. It can be seen from Figure II.4 (b) and (c) that the canola in July appears to be withered compared to conditions

in June. From the in-situ measurements, the average number of canola plants per m^2 (n_a) is about 60 and the number of leaves per plant (N_l) is about b (b = 2 for June and 1 for July, respectively) multiplied by the number of branches per plant (N_s). The main stem diameter (d), which increases with *VWC*, is calculated from the allometric relationship with *VWC* obtained from the data through curve fitting: $d = -0.03135VWC^2 + 0.938VWC + 4.87$ in mm, as in chapter II. Similarly, the main stem length (l) is obtained as: $l = -121.4VWC^{-1.186} + 130.2$ in cm, as in chapter II. N_s can be calculated from *VWC* using the following formula:

$$N_s = \frac{VWC - \rho_{water} n_a Vol_{stem} Mveg_{stem}}{n_a \rho_{water} (Vol_{branch} Mveg_{branch} + b Vol_{leaf} Mveg_{leaf})} \tag{3.3.3}$$

where Vol_{stem}, Vol_{branch} and Vol_{leaf} are the volume of stem, branch and leaf, respectively.

Table III-3. Physical parameters for the canola fields.
The values in parentheses are used starting from July 10th according to the data. The volumetric water content M_{veg} is estimated from the measured M_g in the same way as for the wheat [49]. *VWC* is measured in-situ. d and l are derived from *VWC* based on the empirical allometric relationships. β is the scatterer elevation angle. The distribution of the azimuthal angle (α as shown in Figure II.4 (a)) is uniform over $0 \sim 360^\circ$ for the stem, branch and leaves.

	Diameter (mm)	Length (cm)	M_{veg}	Distribution of β
Stem	d	l	60% (*40%*)	Uniform over $0 \sim 5^\circ$
Branch	$d/2$	$l/3$	60% (*40%*)	Uniform over $0 \sim 50^\circ$
Leaf	140 (*80*)	0.03	60% (*40%*)	Uniform over $70^\circ \sim 90^\circ$

3.3.2 Validation with SMAPVEX UAVSAR and PALS Data

The measured *RMS* height, *VWC*, in-situ soil moisture, and soil and vegetation temperature, as well as the physical parameters presented in section 3.3.1 are used as inputs to the combined active and passive model, as summarized in Table III-4. The calculated backscatter coefficients and brightness temperatures are validated using concurrent airborne PALS low-altitude radiometer

data and UAVSAR data for each day of flights during the SMAPVEX12 field campaign. The radar measurements from UAVSAR are used because they provide higher spatial resolution than PALS. Only fields that have PALS low-altitude radiometer data are considered here because the focus in this chapter is on the joint validation for emissivity and backscatter calculated from the combined active and passive model.

Table III-4. Input parameters for the combined active and passive model.
The parameters indicated with '*' are estimated from measurements whose values are listed in Table III-1 ~ Table III-3. The parameters indicated with '**' are calculated from measured *VWC*, where the formulas are presented in section 3.3. The remaining parameters without any indicators are directly ingested in the model with their measured values. The orientation is defined by the probability function of the two orientation angles α and β.

Land Cover	Input Parameters for the Combined Active and Passive Model
wheat / winter wheat	*VWC*, *RMS* rough-surface height, soil moisture, soil and vegetation temperatures, diameter*, M_{veg}*, length**, n_a*, orientation*
pasture	*VWC*, *RMS* rough-surface height, soil moisture, soil and vegetation temperatures, diameter*, M_{veg}*, length*, n_0**, orientation*
canola	*VWC*, *RMS* rough-surface height, soil moisture, soil and vegetation temperatures, n_a*, stem diameter**, stem M_{veg}*, stem length**, stem orientation*, stalk diameter**, stalk M_{veg}*, stalk length**, stalk orientation*, leaf diameter*, leaf M_{veg}*, leaf thickness*, leaf orientation*

The time-series forward comparison between the model results and data for the wheat fields is presented in Figure III.6 and Figure III.7 (a) and (b), and Figure III.8 (a), where (a) shows brightness temperature while (b) shows backscatter. Since there are no UAVSAR data to compare for field 931, therefore only brightness temperature comparisons are presented in Figure III.8 (a). In these figures, "CORR" stands for "correlation coefficient". "TBV_{mea}" and "TBH_{mea}" indicate measured brightness temperature at vertical polarization and horizontal polarization from the PALS radiometer. "TBV_{mod}" and "TBH_{mod}" represent the modeled brightness temperature at vertical polarization and horizontal polarization. "*Mv*" stands for soil moisture. "VV model" and "HH model" indicate modeled backscatter. "VV_{mea}" and "HH_{mea}" are measured backscatter from the UAVSAR. Soil moisture (*Mv*) and *VWC* are scaled as *Mv*/0.5 and *VWC**0.8 for plotting,

respectively. The x-axis presents the campaign date. For example, "120615" represents June 15th, 2012. The same notations apply for the other figures in this chapter.

For the three wheat fields the same set of vegetation parameters (such as the radius, orientation and crop density) are used to characterize the vegetation but the measured *RMS* height, *VWC*, in-situ soil moisture, and soil and vegetation temperature are different for the different fields. This is useful for the data-cube based soil moisture retrieval [5, 6] where a lookup-table is inverted. This lookup-table is computed using the forward model with the same set of parameters for each group of vegetation. It is worth mentioning that the input parameters and the allometric relationships from curve fitting based on the SMAPVEX12 ground measurements will put a burden on a future data-cube based inversion methodology where only three variables (*RMS* height, *VWC* and soil moisture) can be retrieved.

The root mean squared error (RMSE) between the modeled and measured backscatter is calculated using: $RMSE = \sqrt{\frac{1}{N}\sum_{i=1}^{N}\left(\sigma_{data,\mathrm{i}} - \sigma_{\mathrm{model,i}}\right)^2}$, where N is the number of samples, σ_{data} is the measured backscattering coefficient and σ_{model} is the predicted backscattering coefficient from the model. The RMSE between the modeled and measured brightness temperature is calculated in the same way. In terms of the RMSE and correlation coefficients, the consistent combined and passive model NMM3D-DBA provides a good prediction for the wheat fields for both active and passive for both polarizations under various soil and vegetation conditions.

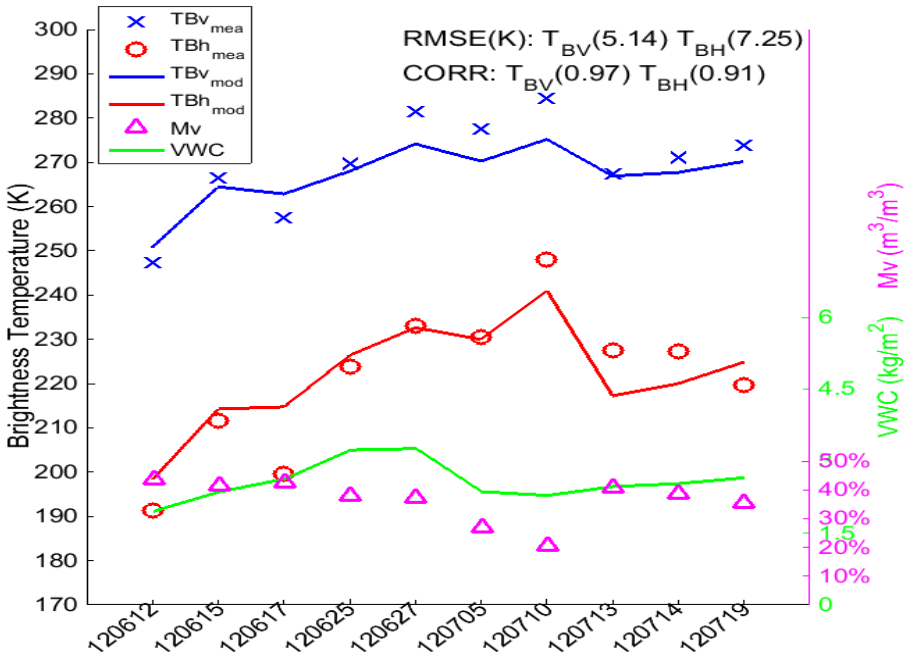
TBv mea
TBh mea
TBv mod
TBh mod
Mv
VWC
RMSE(K): T BV(5.14) T BH(7.25)
CORR: T BV(0.97) T BH(0.91)
Brightness Temperature (K)
Mv (m3/m3)
VWC (kg/m2)
120612
120615
120617
120625
120627
120705
120710
120713
120714
120719

(a)

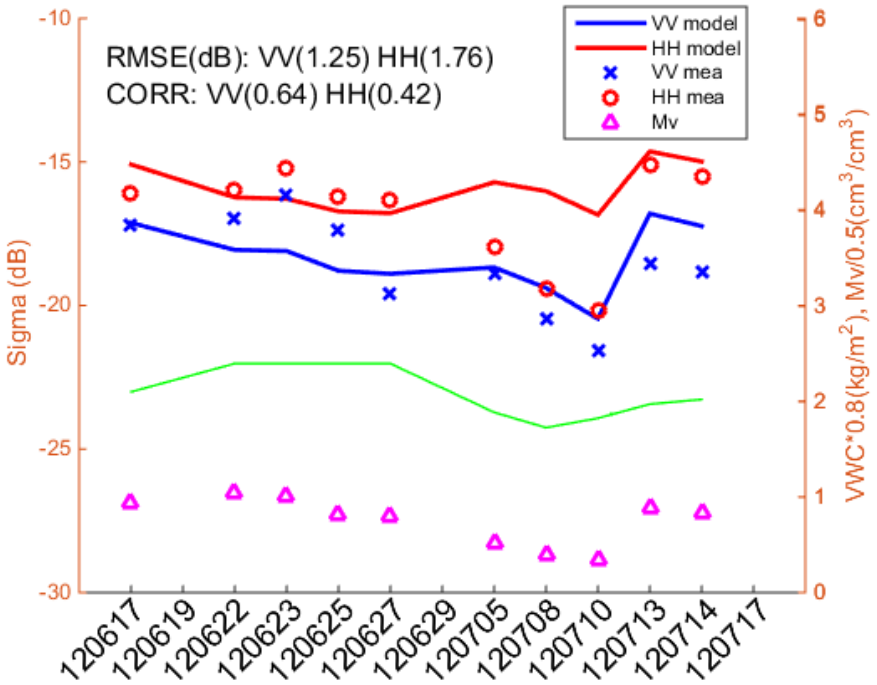
VV model
HH model
VV mea
HH mea
Mv
RMSE(dB): VV(1.25) HH(1.76)
CORR: VV(0.64) HH(0.42)
Sigma (dB)
VWC*0.8(kg/m2), Mv/0.5(cm3/cm3)
120617
120619
120622
120623
120625
120627
120629
120705
120708
120710
120713
120714
120717

(b)

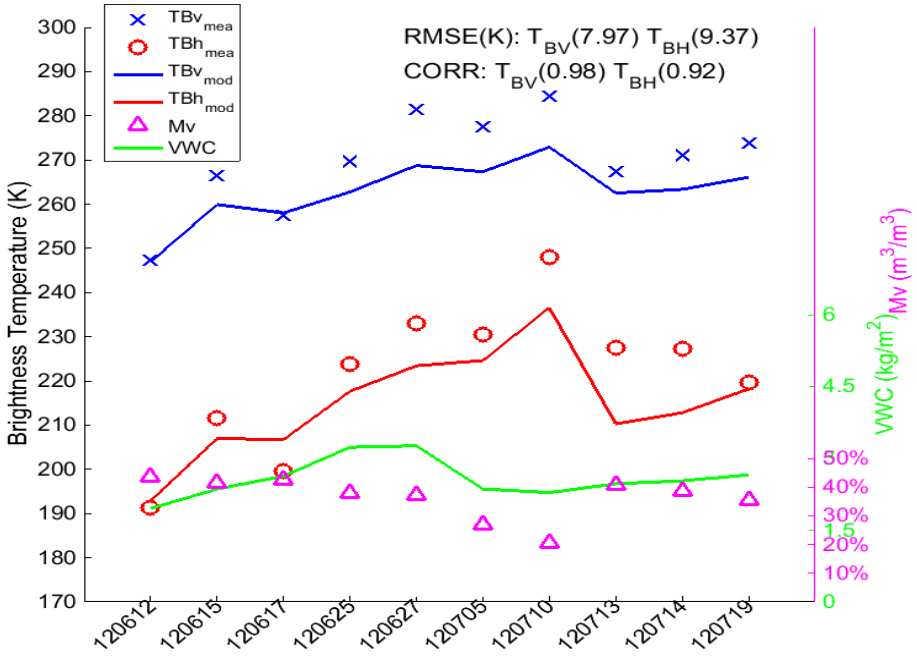

(c)

Figure III.6. Model and measurement comparison of wheat field 31 for (a) brightness temperature using NMM3D-DBA, (b) backscatter using NMM3D-DBA, (c) brightness temperature using the tau-omega model. Soil surface RMS height is 0.81 cm.

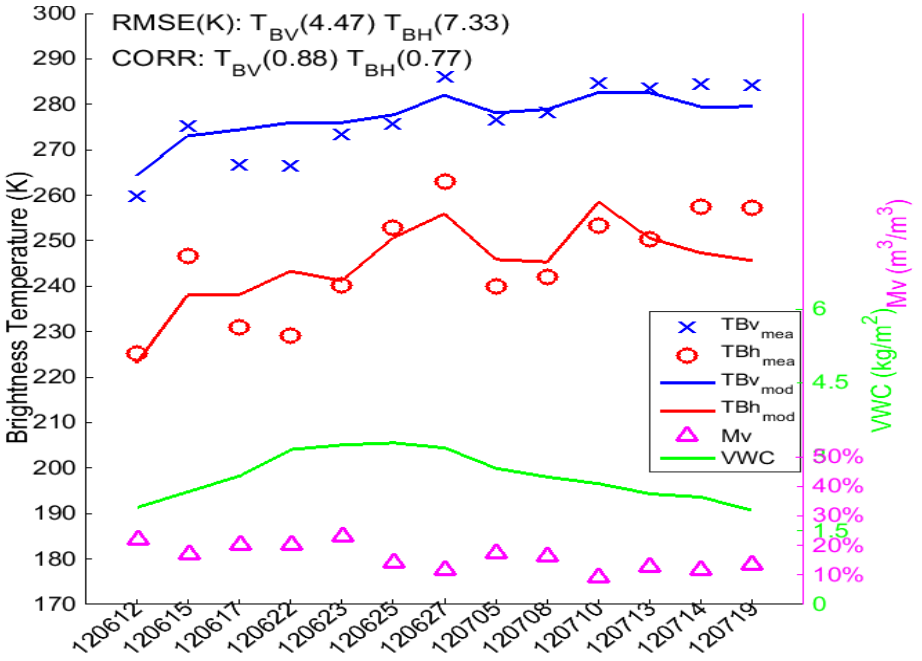

(a)

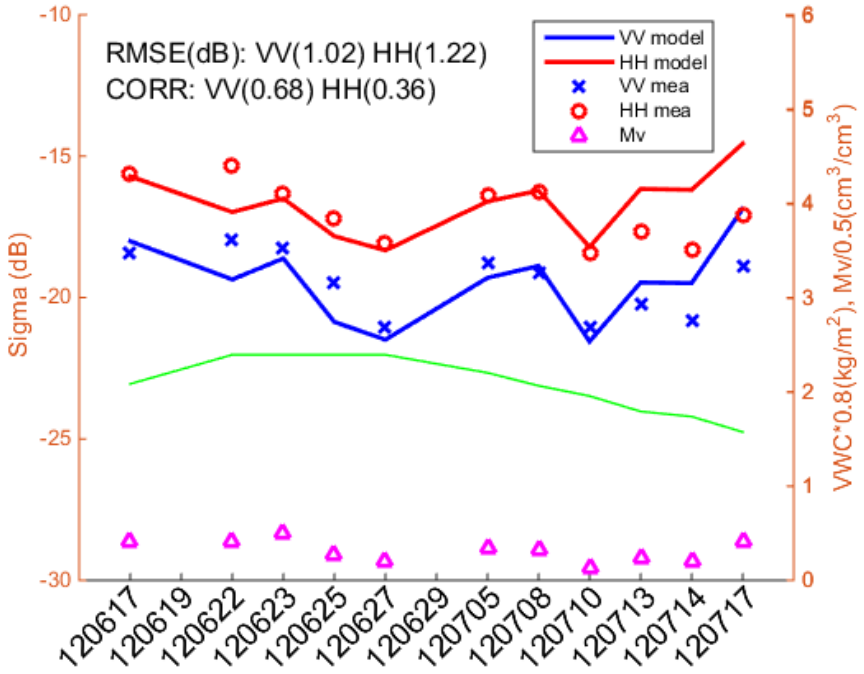

(b)

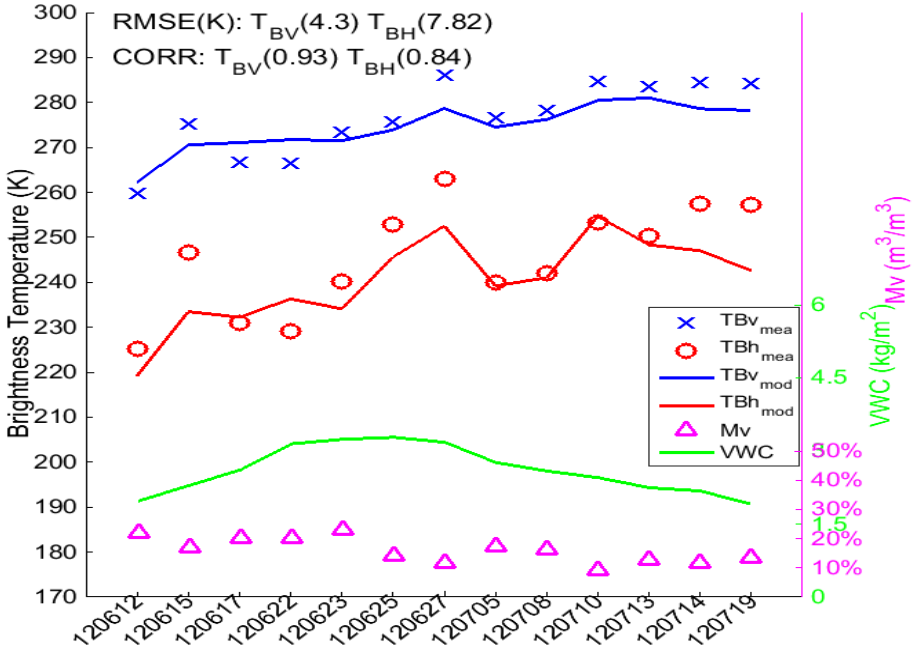

(c)

Figure III.7. Model and measurement comparison of wheat field 91 for (a) brightness temperature using NMM3D-DBA, (b) backscatter using NMM3D-DBA, (c) brightness temperature using tau-omega model. Soil surface RMS height is 0.91 cm.

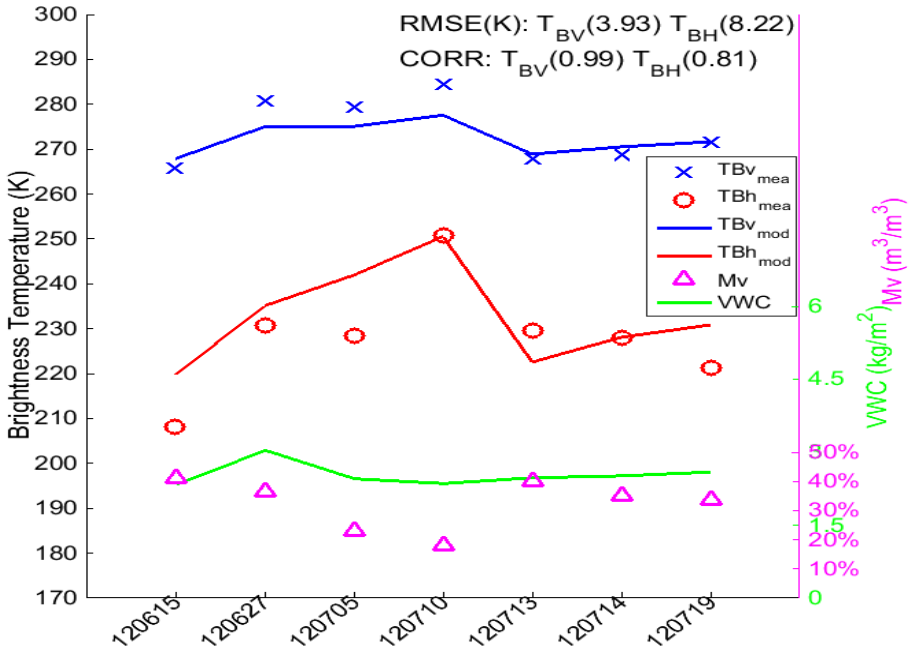

(a)

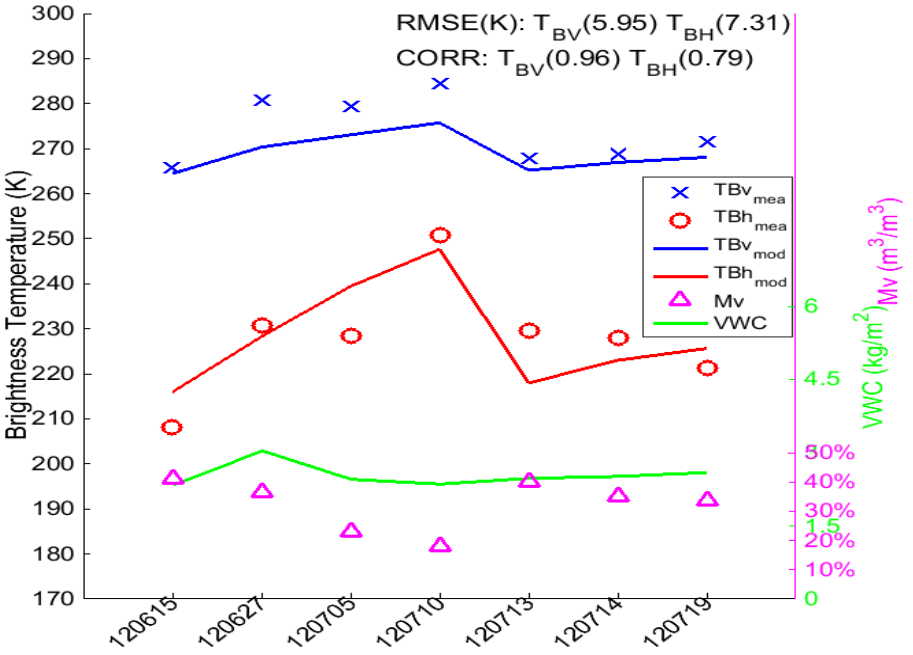

(b)

Figure III.8. Model and measurement comparison of wheat field 931 for brightness temperature using (a) NMM3D-DBA, (b) tau-omega model. Soil surface RMS height is 1.00 cm.

It is observed that the model results agree better with the measurements for V-pol than H-pol for both backscatters and brightness temperatures. This may be caused by that we modeled the wheat canopy as a layer of cylinders where the wheat leaves were ignored, resulting in more errors in H-pol than V-pol. The wheat leaves were oriented nearly parallel to the ground, as shown in Figure III.3, so that the horizontally polarized incident waves (H-pol) coupled more into the wheat leaves than the vertically polarized ones (V-pol). It is also observed that towards the end of the campaign, the NMM3D-DBA model generally overestimates the backscatter. This may be explained by the use of a fixed M_{veg} value for the whole period for simplicity and feasibility [5, 6]. As the wheat ripened, its M_{veg} generally decreased. Thus, during the end of the campaign, a higher M_{veg} value is used in the model, resulting in larger vegetation permittivity and larger scattering than expected. This general overestimation or underestimation in the last few campaign days is not observed in the brightness temperature comparisons. Similarly, the time-series forward comparisons for the winter wheat fields are presented in Figure III.9 and Figure III.10 (a) and (b), and Figure III.11 (a). There is no UAVSAR data to compare for field 941. It can be seen that the comparisons are similar to those of the wheat fields. The wheat and winter wheat were based on the same vegetation model and similar physical parameters were used.

For the pasture field, the comparison results are presented as time-series in Figure III.12 (a) and (b). The VWC of the pasture fields stays almost constant during the whole campaign period. It is observed from both the model results and measured radiometer and radar data that when the soil moisture increases with a fixed *VWC*, the brightness temperature generally decreases while the backscatter increases; and vice versa. This can be explained from the combined active and passive model as follows: when soil moisture increases, the soil permittivity increases. Then, the scattering from the soil surface and the soil surface reflectivity increase. For a fixed *VWC*, the

attenuation through the vegetation layer and the vegetation scattering stay unchanged. Thus, the total scattering from the vegetation-covered surface composed of surface scattering, double-bounce scattering and volume scattering increases. Therefore, the backscatter increases while the brightness temperature proportional to the emissivity, which is one minus the integration of bistatic scattering, decreases. The changes of the VV and HH backscattering coefficients ratio, as well the TBv (brightness temperature for V-pol) and TBh (brightness temperature for H-pol) ratio, with the soil moisture are also observed in both the model results and measurements. It is also noticed in Figure III.12 (b) that there are some mismatches for polarization ratio of VV and HH backscattering coefficients between model and measurements. This may be caused by the reason that a constant pasture orientation is used in the model but the pasture orientation could be changed by the wind and rain. The pasture orientation is hard to measure and the data of orientation for different dates is not available. The general polarization mismatch is not observed in the brightness temperature comparisons.

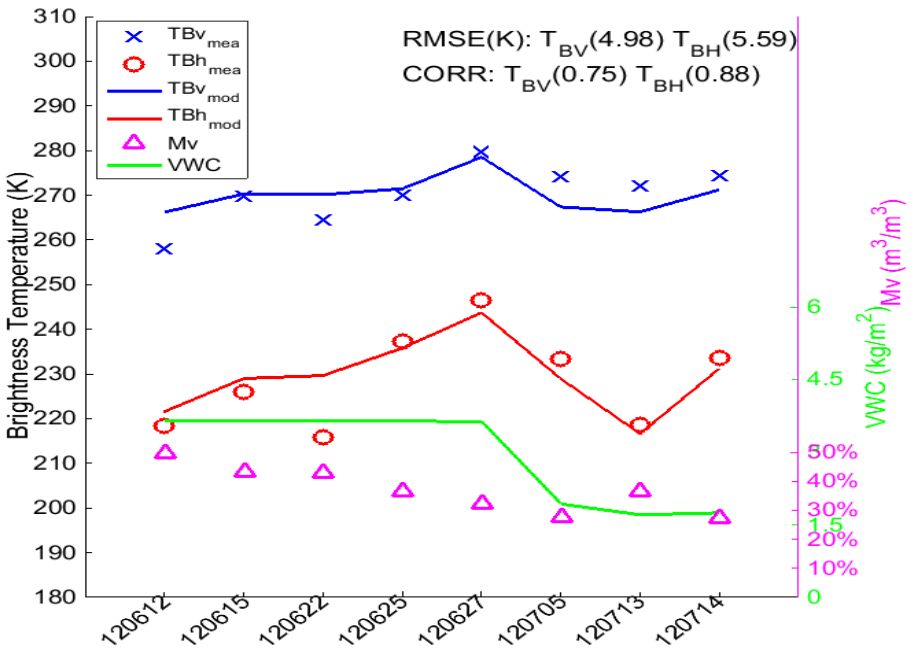

(a)

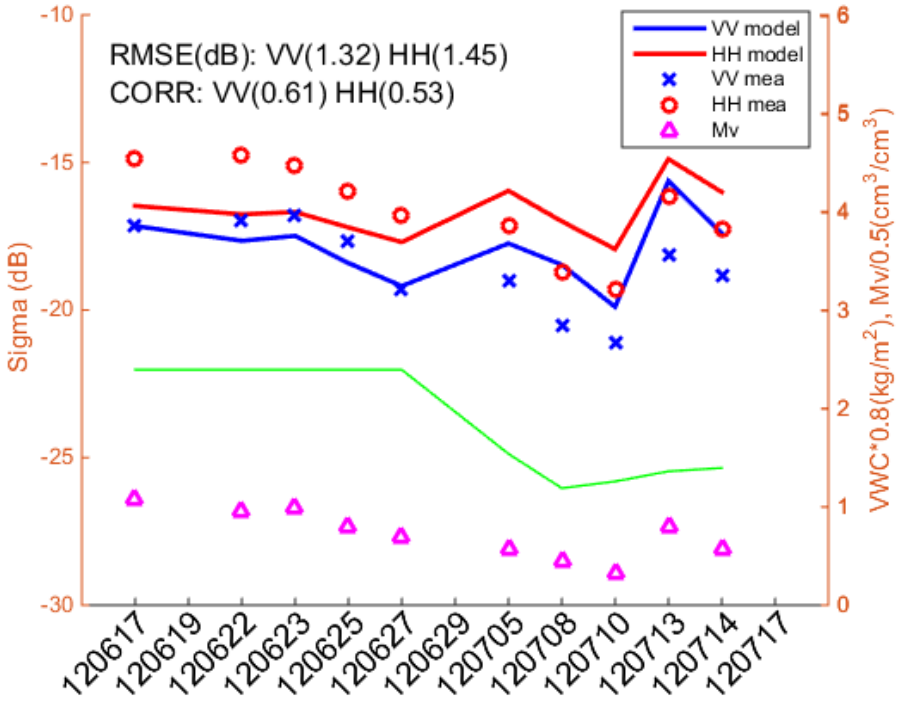

(b)

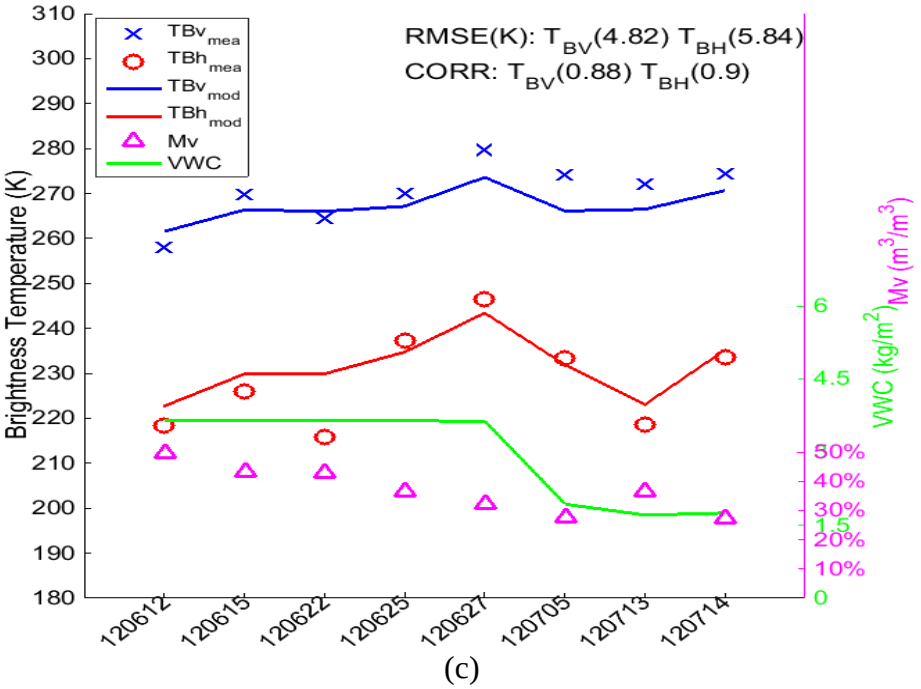

(c)

Figure III.9. Model and measurement comparison of winter wheat field 41 for (a) brightness temperature using NMM3D-DBA, (b) backscatter using NMM3D-DBA, (c) brightness temperature using tau-omega model. Soil surface RMS height is 1.15 cm.

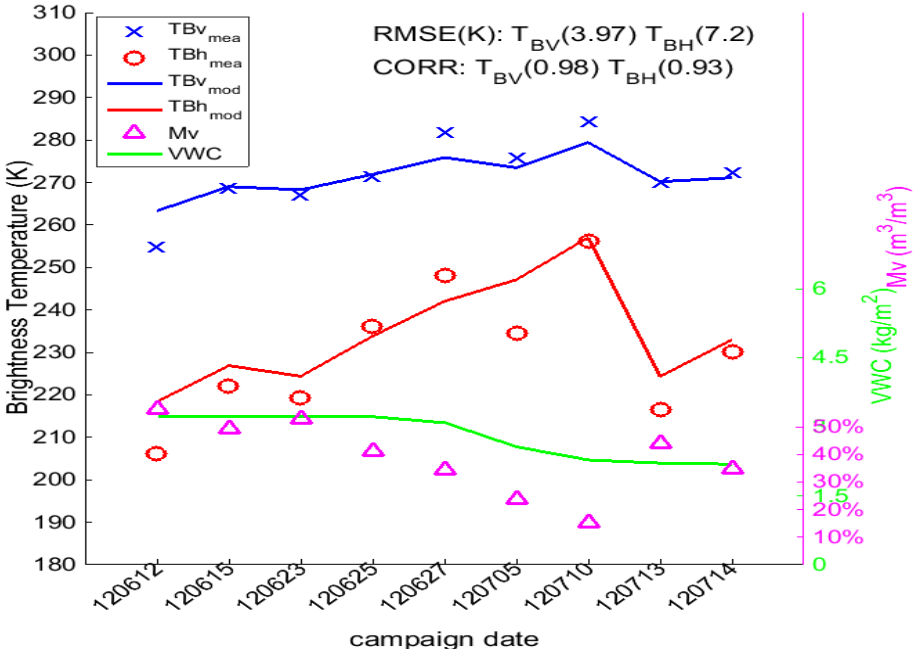
RMSE(K): T_BV(3.97) T_BH(7.2)
CORR: T_BV(0.98) T_BH(0.93)
TBv_mea
TBh_mea
TBv_mod
TBh_mod
Mv
VWC
Brightness Temperature (K)
VWC (kg/m^2)
Mv (m^3/m^3)
campaign date
120612
120615
120623
120625
120627
120705
120710
120713
120714

(a)

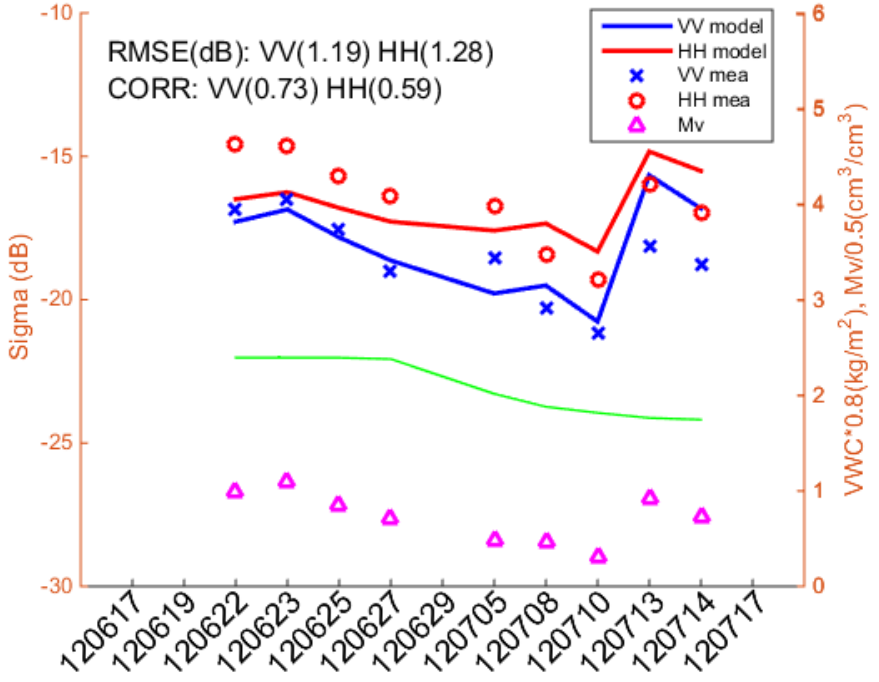
RMSE(dB): VV(1.19) HH(1.28)
CORR: VV(0.73) HH(0.59)
VV model
HH model
VV mea
HH mea
Mv
Sigma (dB)
VWC*0.8(kg/m^2), Mv/0.5(cm^3/cm^3)
120617
120619
120622
120623
120625
120627
120629
120705
120708
120710
120713
120714
120717

(b)

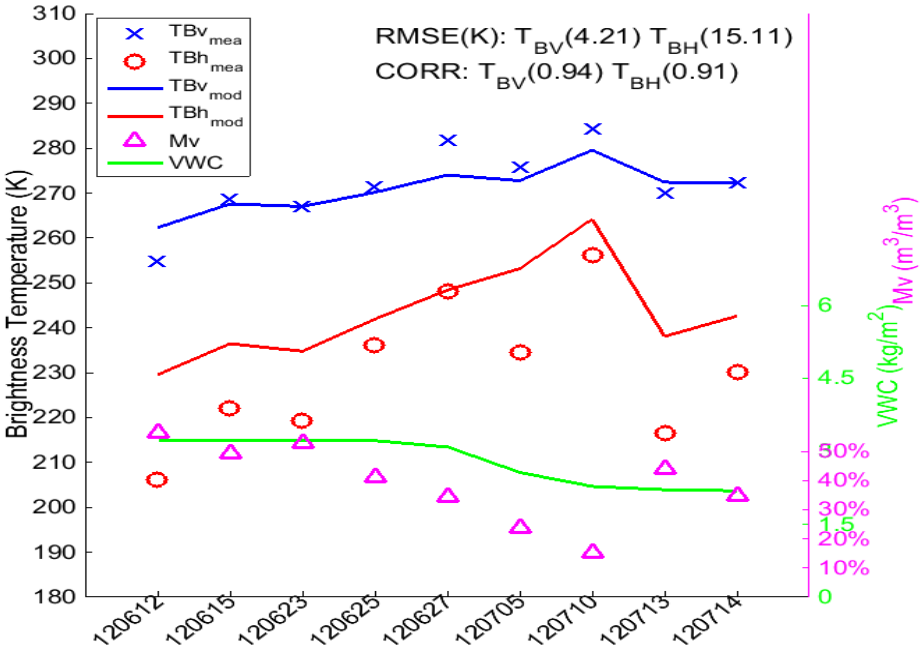

(c)

Figure III.10. Model and measurement comparison of winter wheat field 42 for (a) brightness temperature using NMM3D-DBA, (b) backscatter using NMM3D-DBA, (c) brightness temperature using tau-omega model. Soil surface RMS height is 1.61 cm.

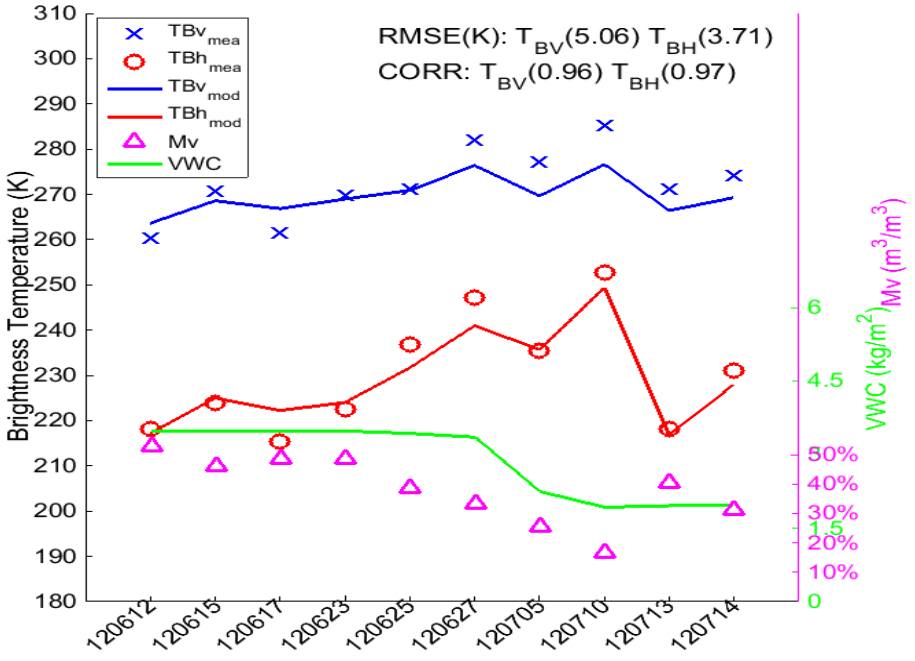

(a)

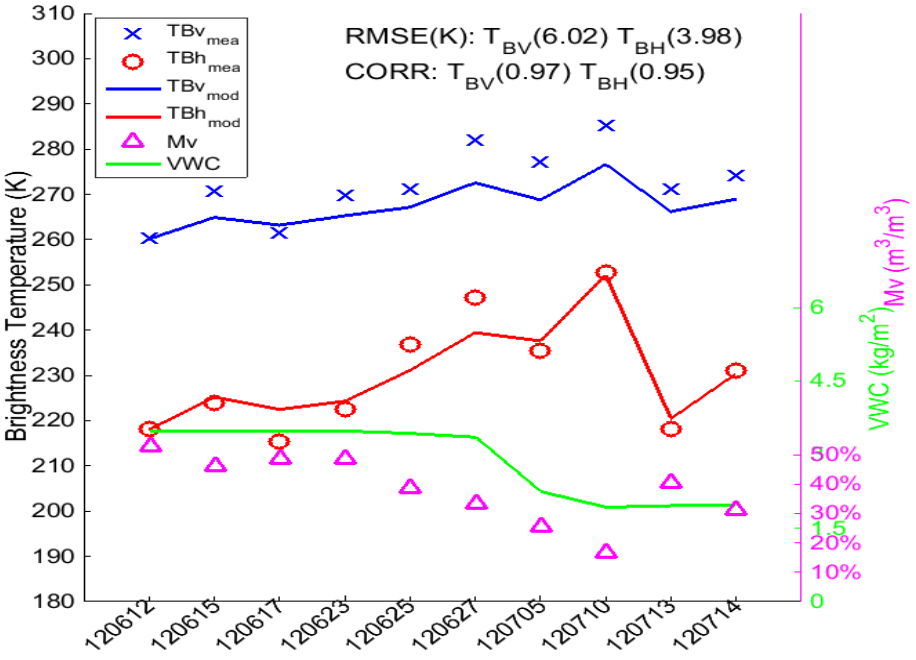

(b)

Figure III.11. Model and measurement comparison of winter wheat field 941 for brightness temperature using (a) NMM3D-DBA, (b) tau-omega model. Soil surface RMS height is 1.10 cm.

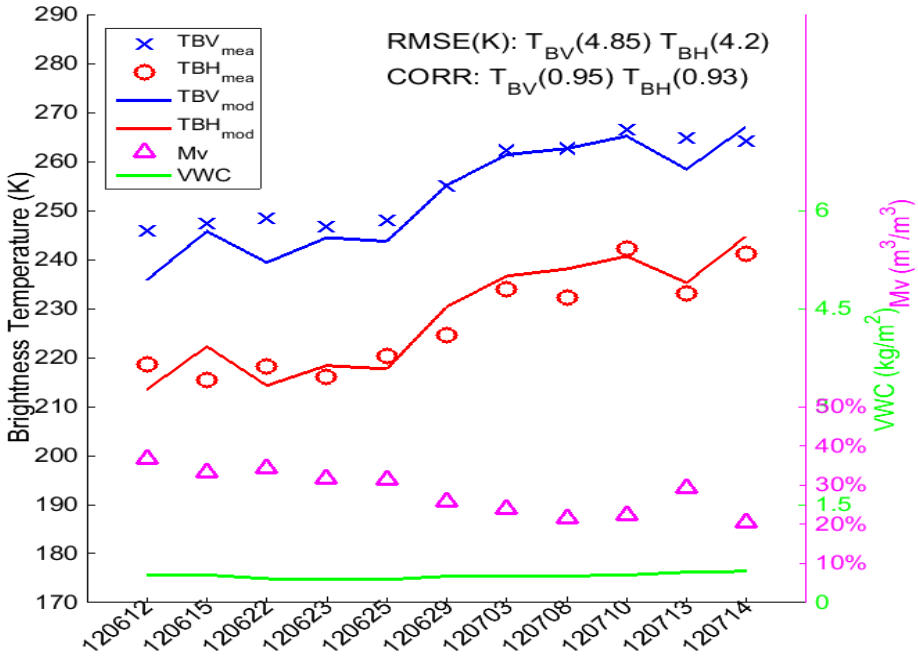

(a)

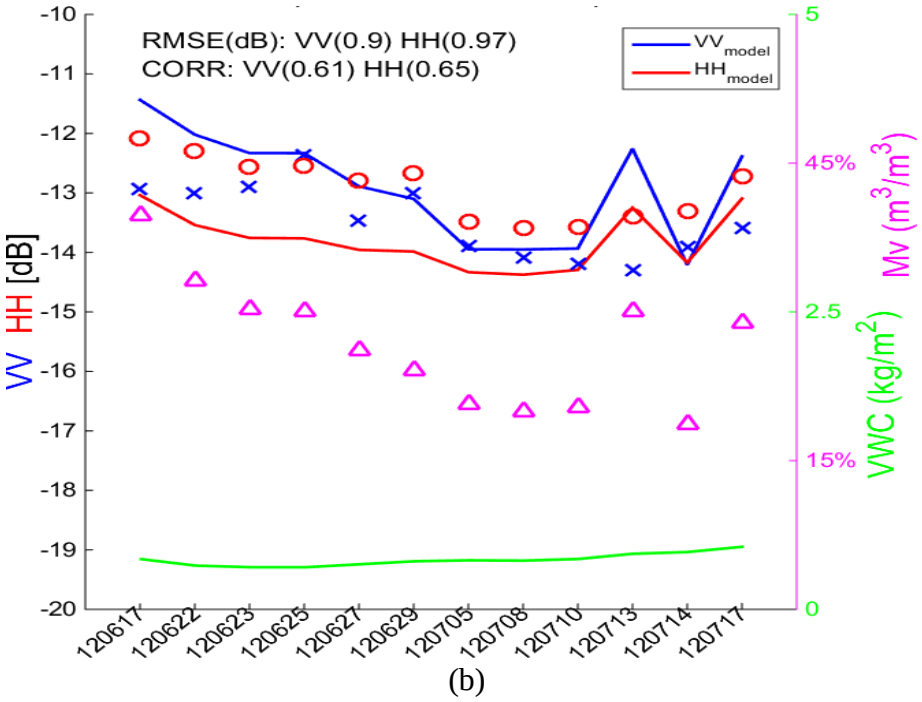

(b)

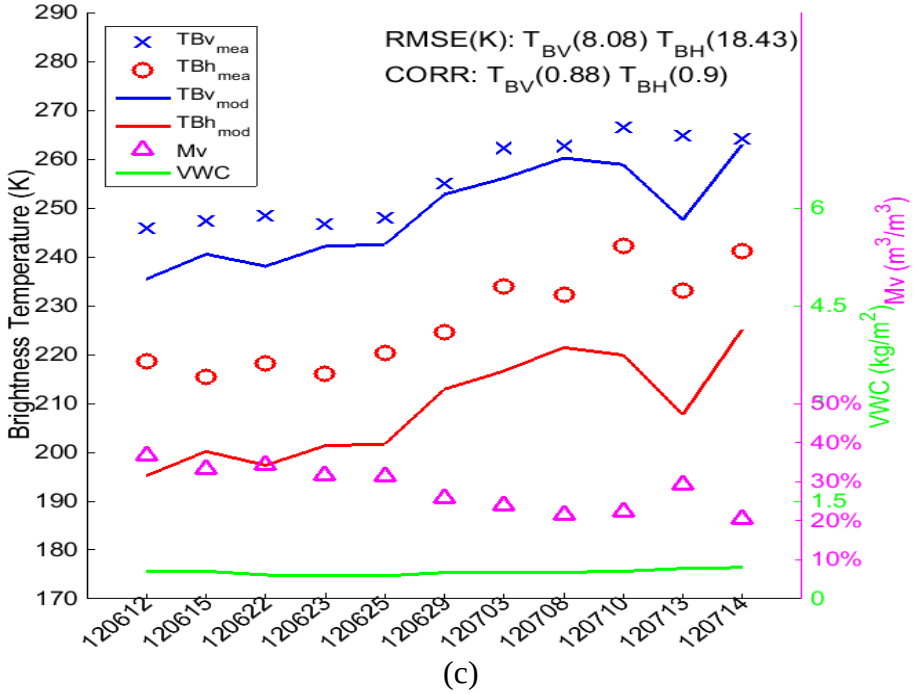

(c)

Figure III.12. Model and measurement comparison of pasture field 21 for (a) brightness temperature using NMM3D-DBA, (b) backscatter using NMM3D-DBA, (c) brightness temperature using tau-omega model. Soil surface RMS height is 0.90 cm.

For the canola field, the comparison results are presented as time-series in Figure III.13 (a) and (b). From June 25th to June 27th, the soil moisture increased, but the measured brightness temperature increased and the backscatters decreased. This may be caused by the decrease of the *VWC* between these two days, which resulted in less attenuation for the surface scattering and less vegetation scattering. Mismatches between the model and measurements for brightness temperature are observed from June 25th to June 29th, which are larger than the other dates, especially for H-pol. However, this is not observed in the backscatter comparisons. This could be caused by the constant *RMS* height used during the whole period. The soil moisture was relatively low from June 25th to June 29th, and thus the surface scattering is relatively small compared with the volume scattering and double-bounce scattering in the backscattering direction. Therefore, the error caused by *RMS* height which has the most influence on surface scattering does not affect the total backscatter much. On the other hand, the integration of surface scattering over the bistatic directions including the specular direction is also important compared with the integration of volume scattering and double-bounce scattering. Thus, the constant *RMS* height assumption in the model has a larger influence on the brightness temperature than the backscatter.

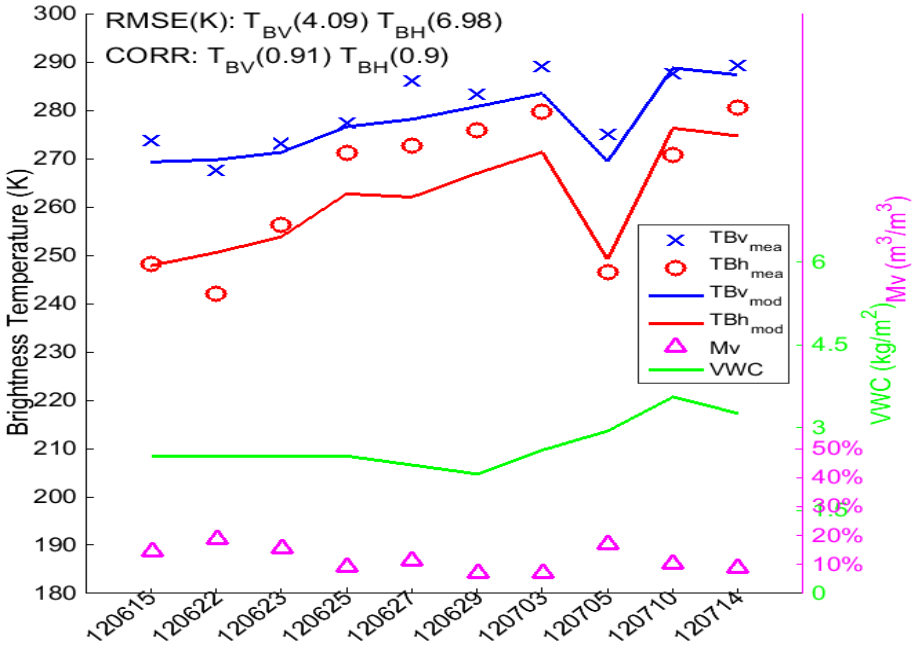
RMSE(K): T_BV(4.09) T_BH(6.98)
CORR: T_BV(0.91) T_BH(0.9)
Brightness Temperature (K)
VWC (kg/m^2)
Mv (m^3/m^3)
TBv_mea
TBh_mea
TBv_mod
TBh_mod
Mv
VWC
120615
120622
120623
120625
120627
120629
120703
120705
120710
120714

(a)

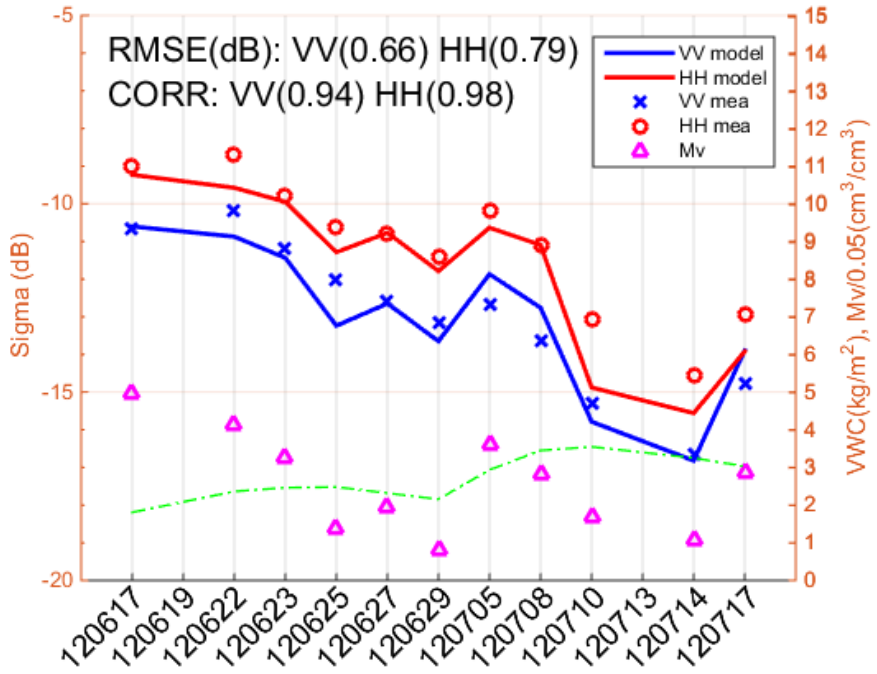
RMSE(dB): VV(0.66) HH(0.79)
CORR: VV(0.94) HH(0.98)
Sigma (dB)
VWC(kg/m^2), Mv/0.05(cm^3/cm^3)
VV model
HH model
VV mea
HH mea
Mv
120617
120619
120622
120623
120625
120627
120629
120705
120708
120710
120713
120714
120717

(b)

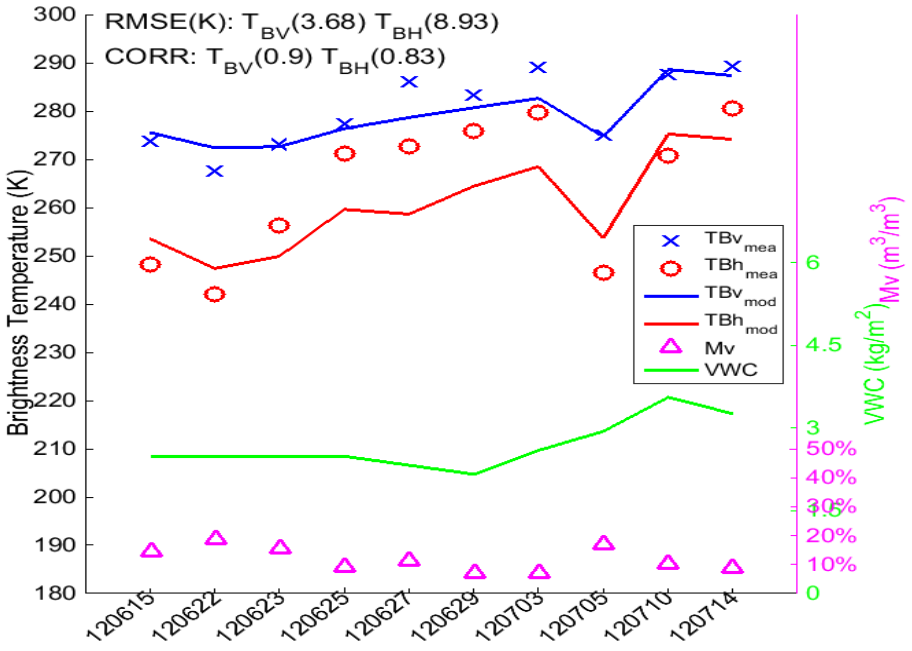

(c)

Figure III.13. Model and measurement comparison of canola field 61 for (a) brightness temperature using NMM3D-DBA, (b) backscatter using NMM3D-DBA, (c) brightness temperature using tau-omega model. Soil surface RMS height is 1.00 cm.

In the NMM3D-DBA model the same input parameters are used to compute both brightness temperature and backscatter. In terms of the RMSE and correlation coefficient between the model and measurement, the modeled backscatters are in good agreement with the UAVSAR data, while the modeled brightness temperatures are in good agreement with the PALS low-altitude radiometer data. For vertical polarization, the averaged RMSE and correlation coefficient over all the fields are 4.65 K and 0.91 for brightness temperature and 1.04 dB and 0.95 for backscatter at VV, as shown in the scatter plots in Figure III.14. For horizontal polarization, the average RMSE and correlation coefficient are 6.44 K and 0.94 for brightness temperature and 1.21 dB and 0.90 for backscatter at HH, as shown in Figure III.15. According to the analysis above, the defects in the vegetation modelling such as ignoring the wheat leaves generally have more influence on the backscatter than the brightness temperature while the defects in the rough surface modelling such

as using a constant *RMS* height generally have more influence on the brightness temperature than the backscatter, for the vegetation fields studied in this chapter. The RMSE and correlation coefficient for each field is summarized in Table III-5. Values in columns 3-6 are the backscatter while columns 7-10 show values for brightness temperature. The values in the last four columns are the results from the tau-omega model, which will be explained in the following section.

The sources of error, when comparing the backscatters from NMM3D-DBA and the data, are detailed in [6]. Thus, we focus on analyzing the sources of error between the brightness temperature computed from NMM3D-DBA and the measured values from the low altitude PALS. One of the main sources of error is expected to come from the measurement error in *RMS* rough-surface height. The contribution from the bistatic surface scattering generally dominates among the three scattering mechanisms for the wheat, winter wheat, pasture and canola fields studied in this chapter. The surface scattering strongly depends on the *RMS* height. Thus, the emissivity and brightness temperature also strongly depend on the *RMS* height. Furthermore, there is considerable uncertainty in the roughness measurements [21]. The *RMS* height was measured only once and thus a constant *RMS* height was used for the whole study period for each field [34]. The *RMS* height could have been influenced by rain, which would flatten the soil surface. Furthermore, the *RMS* height was measured at only two locations in each field, assuming the roughness variations are small over the same field [34] which may not be true. The change of brightness temperature with the *RMS* height for the bare soil surface computed from NMM3D-DBA is plotted in Figure III.16 where a volumetric soil moisture of 25% m^3/m^3 and soil physical temperature of 25℃ are used; these are around the average measured values of all the fields. The range of the *RMS* height in the figure covers the typical values for the vegetation-covered surfaces at L-band. It can be seen from the figure that 0.1 cm change in *RMS* height results in brightness temperature change of about

1 K and 2 K for V-pol and H-pol, respectively. Some other sources of error to be considered when interpreting the results are: (1) the spatial variations of the soil moisture and VWC are not considered; (2) UAVSAR data, more specifically the normalization error when transforming the raw data to 40º (RMSE is about 1 dB [34]); (3) PALS data and the associated calibration error as detailed in [34]; (4) the physical temperature used to calculate brightness temperature from emissivity. The physical temperature of the soil-vegetation continuum is necessary to precisely calculate the brightness temperature from the emissivity [69]. Since it is not available, an averaged measured soil and vegetation temperature is used instead; (5) model parameters. The plant geometry such as the radius and length vary for different plants and average values are used; (6) NMM3D-DBA model. The scatterers are assumed to be uniformly distributed in the vegetation layer, which is not strictly true for the crop fields; and (7) the resolution/scaling gap between model and observations. The model assumes vegetation-covered field is homogeneous which is better applicable to small scales than large scales.

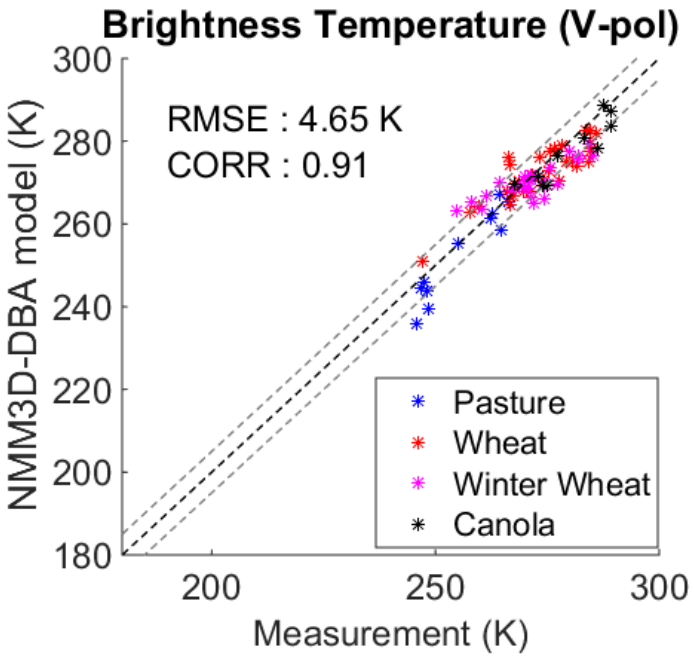

(a)

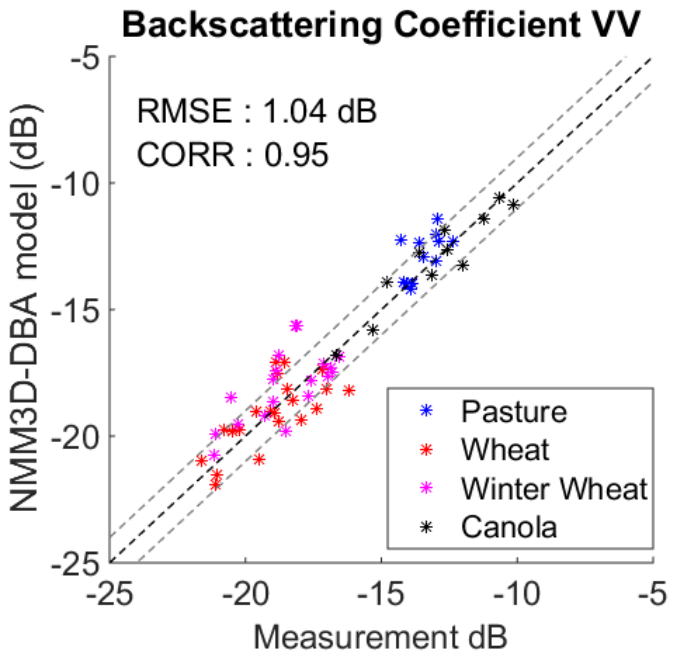

(b)

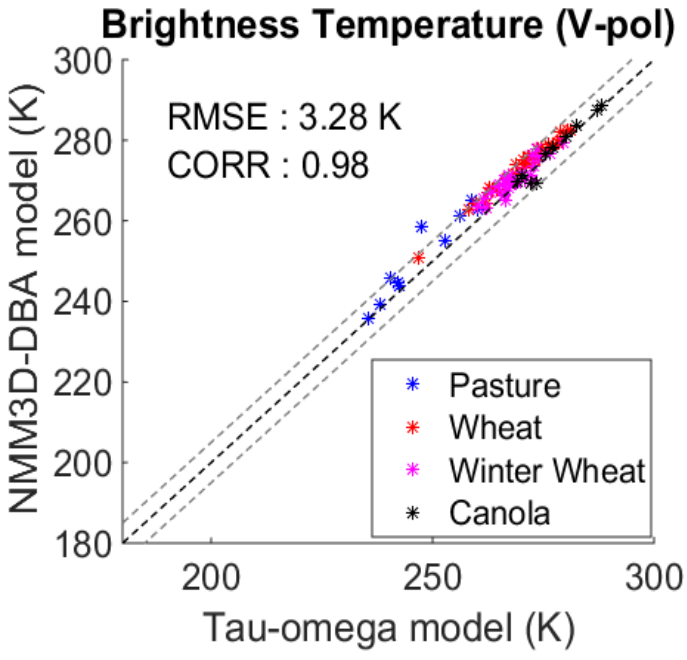

(c)

Figure III.14. NMM3D-DBA model and measurement comparison of all the fields at vertical polarization for (a) brightness temperature T_B (V-pol), (b) backscatter VV. (c) NMM3D-DBA model and tau-omega model comparison for brightness temperature T_B (V-pol). The two grey dashed auxiliary lines in each plot are for +/- 5K or +/- 1dB.

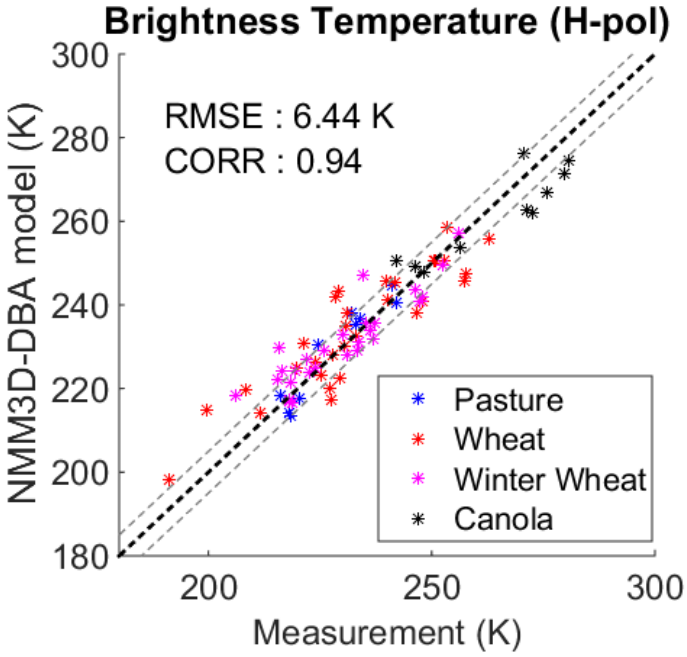
Brightness Temperature (H-pol)
RMSE : 6.44 K
CORR : 0.94
NMM3D-DBA model (K)
Measurement (K)
Pasture
Wheat
Winter Wheat
Canola

(a)

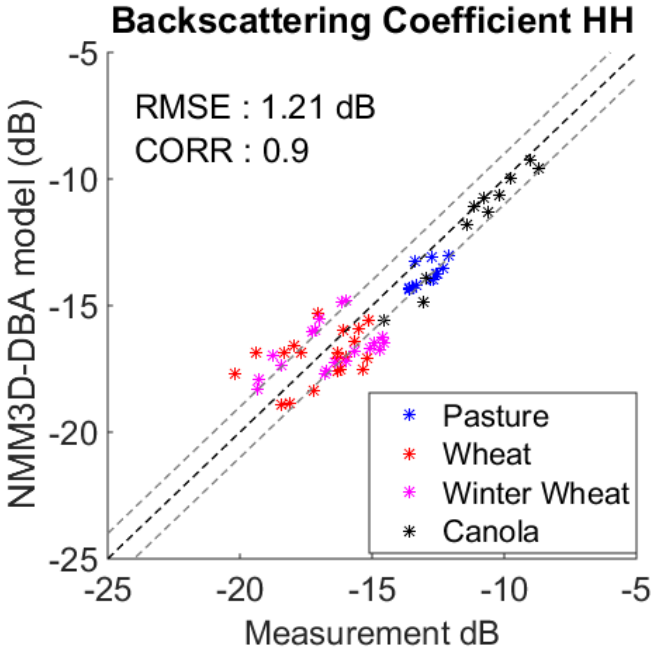
Backscattering Coefficient HH
RMSE : 1.21 dB
CORR : 0.9
NMM3D-DBA model (dB)
Measurement dB
Pasture
Wheat
Winter Wheat
Canola

(b)

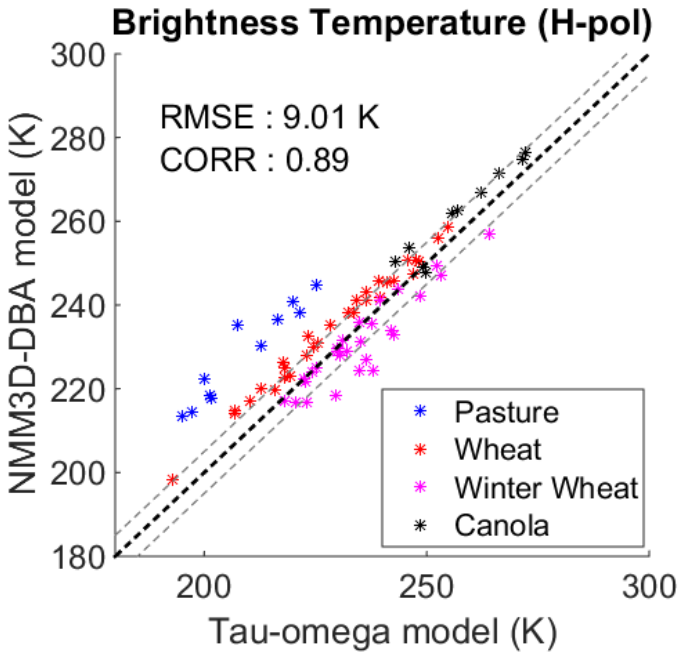

(c)

Figure III.15. NMM3D-DBA model and measurement comparison of all the fields at horizontal polarization for (a) brightness temperature T_B (H-pol), (b) backscatter HH. (c) NMM3D-DBA model and tau-omega model comparison for brightness temperature T_B (H-pol). The two grey dashed auxiliary lines in each plot are for +/- 5K or +/- 1dB.

Table III-5. RMSE and correlation coefficient (CORR) of backscatter and brightness temperatures (T_B) between model results and UAVSAR and PALS low-altitude radiometer observations.

There is no UAVSAR data available for field 931 and 941 to compare with the modeled backscatter.

Field No.	Land Cover	Backscatter (NMM3D-DBA)				T_B (NMM3D-DBA)				T_B (Tau-omega)			
		RMSE (dB)		CORR		RMSE (K)		CORR		RMSE (K)		CORR	
		VV	HH	VV	HH	V	H	V	H	V	H	V	H
31	wheat	1.25	1.76	0.64	0.42	5.14	7.25	0.97	0.91	7.79	9.37	0.98	0.92
91		1.02	1.22	0.68	0.36	4.47	7.33	0.88	0.77	4.30	7.82	0.93	0.84
931		-	-	-	-	3.93	8.22	0.99	0.81	5.95	7.31	0.96	0.79
41	winter wheat	1.32	1.45	0.61	0.53	4.98	5.59	0.75	0.88	4.82	5.84	0.88	0.90
42		1.19	1.28	0.73	0.59	3.97	7.20	0.98	0.93	4.21	15.1	0.94	0.91
941		-	-	-	-	5.06	3.71	0.96	0.97	6.02	3.98	0.97	0.95
21	pasture	0.90	0.97	0.61	0.65	4.85	4.20	0.95	0.93	8.08	18.4	0.88	0.90
61	canola	0.66	0.79	0.94	0.98	4.09	6.98	0.91	0.90	3.68	8.93	0.90	0.83

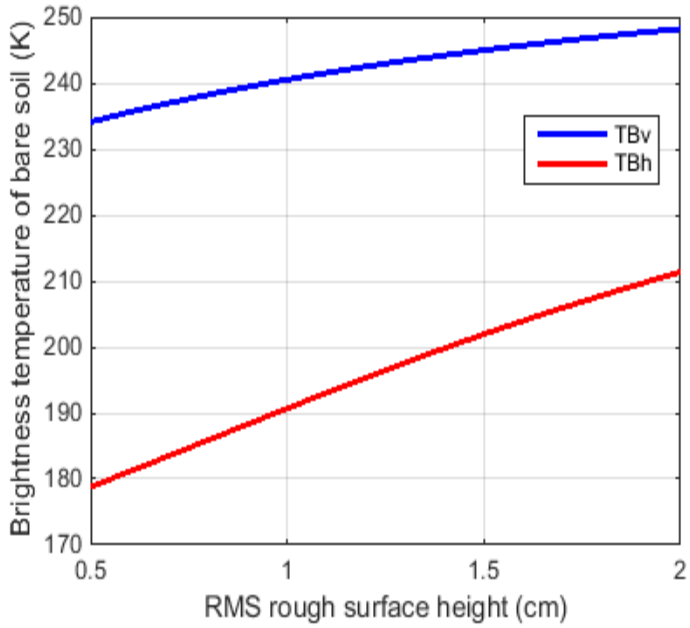

Figure III.16. Brightness temperature change with *RMS* rough-surface height for bare surface based on NMM3D

3.4 Comparisons with the Tau-Omega Model

In comparison, the formulas for the tau-omega model which only computes the brightness temperature instead of the backscattering coefficient is also presented here. In the tau-omega model [8], the brightness temperature T_B of the vegetation-covered surface is calculated as:

$$\begin{aligned} T_B(\theta) = {} & T_{soil}\left(1-r(\theta)\right)\exp\left(-\tau\bullet\sec(\theta)\right)+ \\ & T_{veg}\left(1-\omega\right)\left(1-\exp\left(-\tau\bullet\sec(\theta)\right)\right)\left(1+r(\theta)\bullet\exp\left(-\tau\bullet\sec(\theta)\right)\right) \end{aligned} \tag{3.4.1}$$

where θ is the observation angle of 40 degrees for SMAP and PALS in SMAPVEX12, T_{soil} is the physical temperature of the soil, T_{veg} is the physical temperature of the vegetation, ω is the scattering albedo of the vegetation, $\tau = b \times VWC$ is the vegetation optical thickness and $r(\theta)$ is the reflectivity of the soil surface defined as [8, 70]:

$$r_p(\theta) = \left(\left(1-Q\right)r_{0,p} + Qr_{0,q}\right)\exp\left(-h\cos^2(\theta)\right) \tag{3.4.2}$$

where the subscripts '*p*' and '*q*' denote polarization, r_0 is the reflectivity of the smooth surface calculated from the Fresnel equations, Q is the polarization mixing coefficient, and h is the effective roughness parameter defined as [70]:

$$h = \left(2\sigma k_0\right)^2 \tag{3.4.3}$$

where σ is the *RMS* height of the soil surface and k_0 is the wave number in free space.

The tau-omega model for passive microwaves uses empirical parameters instead of physical parameters and is totally different from the NMM3D-DBA model used for active microwaves. On the other hand, the combined active and passive model derived in the chapter uses the same model NMM3D-DBA and the same input physical parameters for both active and passive microwaves.

Table III-6. Comparison of vegetation scattering parameter ω and vegetation parameter b used in the tau-omega model for SMAPVEX12 [70] and calculated (cal.) from the NMM3D-DBA model.

Land Cover	Tau-omega				NMM3D-DBA			
	ω_V	ω_H	b_V	b_H	cal. ω_V	cal. ω_H	cal. b_V	cal. b_H
wheat	0.05	0.05	0.20	0.08	0.33	0.27	0.24	0.08
w. wheat	0.05	0.05	0.20	0.08	0.27	0.21	0.21	0.07
pasture	0.05	0.05	0.10	0.10	0.41	0.41	0.25	0.23
canola	0.05	0.05	0.21	0.12	0.15	0.15	0.26	0.24

* "w. wheat" is short for "winter wheat"

The tau-omega model is derived from the zeroth order solution of the radiative transfer equation. Since the zeroth order solution ignores the phase matrix term, it is only valid when ω is small. However, typical calculated values of ω at L-band are in the range of 0.15 to 0.41 using the physical scattering model of branches and leaves as shown in Table III-6. The value of ω used to fit the tau-omega model to observations is thus an empirically-determined effective parameter rather than a physical parameter. The value of ω used in the tau-omega model for SMAPVEX12

was empirically set to 0.05 to best match the SMAPVEX12 PALS low-altitude radiometer data [70] to the tau-omega model and is much smaller than the physically calculated ω as shown in Table III-6. The physically-based ω is defined as $\omega = \langle \kappa_s \rangle / \langle \kappa_e \rangle$ [4], where $\langle \kappa_s \rangle$ and $\langle \kappa_e \rangle$ are the scattering coefficient and extinction coefficient, respectively. $\langle \kappa_s \rangle$ and $\langle \kappa_e \rangle$ are calculated using the physical parameters as illustrated above. It is worth noting that the calculations of ω are not needed in the NMM3D-DBA model as shown in the derivations in section 3.3 and ω is calculated here for comparison with the empirically chosen ω. The physically calculated ω depends on the size of the scatterers such as the radius and length. As explained in section 3.3, for wheat, winter wheat and canola the size of the vegetation components (stalks, main stem and leaves) depends on *VWC*, thus ω also depends on *VWC*. The ω values for the wheat, winter wheat and canola fields in Table III-6 are calculated at *VWC* equal to 2 kg/m^2, which is a typical *VWC* value for these vegetation types.

For the τ parameter, if the physical ω is small, then attenuation is dominated by absorption, and the optical thickness τ of the vegetation layer is determined by the *VWC* and the *b* parameter, which is the proportionality constant between τ and *VWC*. However, if the physical ω is not small, then the *b* parameter also becomes non-physical. The physically calculated *b* and empirically adjusted *b* for SMAPVEX12 [70] are different and listed in Table III-6. Physically, the optical thickness is defined as $\tau = \langle \kappa_e \rangle d$ [4] where *d* is the thickness of the vegetation layer. Then, the physically-based *b* is calculated as $b = \langle \kappa_e \rangle d / VWC$ using the physical parameters. It is worth noting that the calculations of *b* are not needed in the NMM3D-DBA model and *b* is calculated here for comparison with the empirically chosen *b*.

The tau-omega model rough surface parameters *Q* and *h* are also empirically tuned to fit the data. According to previous studies it is commonly assumed that *Q*=0 at L-band [70]. In this case, h is

adjusted based on soil moisture, precipitation events and soil texture [70] to best fit the PALS observations. In this chapter, equations (3.4.2) and (3.4.3) with Q=0 are used for the tau-omega model for simplicity. When $r_p(\theta)$ for the tau-omega model is compared with the integration of $\left\langle S_{pq}^{R} S_{pq}^{R*} \right\rangle$ calculated from NMM3D, the results from NMM3D are generally larger than $r_p(\theta)$. This is because $r_p(\theta)$ only includes the coherent wave specular reflection [61] while ignoring the bistatic scattering. One example of a comparison between the result from NMM3D and the $r_p(\theta)$ used in the tau-omega model, under various soil moisture conditions and for an *RMS* height of 0.91cm (field 91), is shown in Figure III.17. It can be seen that regardless of the polarization, the results from NMM3D are larger than $r_p(\theta)$. It is also noticed that the results from the tau-omega model follow the same trend as those from the NMM3D which has several degrees more of complexity. This is because the coherent component along the specular direction dominates for rough surface with *ks* (product of the wavenumber and the *RMS* height which is around 0.2 in this case) on the order of 0.1 [2] and the error from the neglection of non-coherent components along the bistatic directions in the tau-omega model is small in this case.

The tau-omega model brightness temperatures calculated using the empirical parameters for SMAPVEX12 [70] are compared with the PALS low-altitude radiometer data for each of the fields as shown in Figure III.6 ~ Figure III.13. The results from tau-omega and NMM3D-DBA models for all the fields are also presented in the scatter plots in Figure III.14 (c) and Figure III.15 (c). The RMSE and correlation coefficient between the tau-omega model results and PALS observations are listed in Table III-5 for comparison with the NMM3D-DBA. It can be seen that the results from the tau-omega and NMM3D-DBA are comparable to each other even though empirical parameters are used in the tau-omega model, while physical parameters are used in NMM3D-DBA. The RMSE is generally lower and the correlation coefficient (CORR) higher for the NMM3D-

DBA than for the tau-omega model, indicating better agreement between measurement and model using the NMM3D-DBA, but this is not the case for all fields.

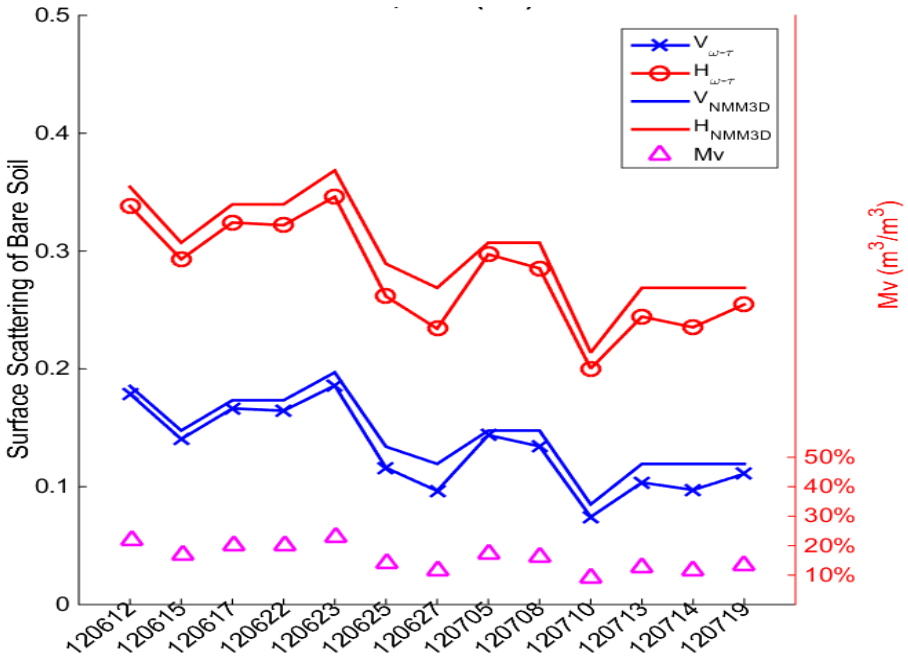

Figure III.17. Comparison of (1-emissivity) for bare soil surface contribution between the tau-omega model and NMM3D-DBA for field 91 at *RMS* height 0.91cm.

3.5 Conclusions

A consistent model for combined active and passive microwave remote sensing is formulated in which the same physical model NMM3D-DBA is used to calculate both backscatter and brightness temperature. The novel feature of this combined active and passive approach is its use of the same model NMM3D-DBA and physical parameters (such as the crop density, plant height, stalk orientation, leaf radius, surface roughness, amongst others) for both active and passive for vegetation-covered surfaces to achieve a consistent modeling framework. The NMM3D-DBA model allows the understanding that the defects in the vegetation modelling have more influence on the backscatter than the brightness temperature while the defects in the rough surface modelling

have more influence on the brightness temperature than the backscatter, for the vegetation fields studied in this chapter. In comparison, current approaches generally use different models and different parameters for active and passive with the tau-omega model most frequently used as the passive model with empirical input parameters. The physical model combines the distorted Born approximation (DBA) with the NMM3D, including three scattering mechanisms: volume scattering, double-bounce scattering and surface scattering. The distorted Born approximation is derived from the Foldy-Lax equation with first-order iteration using the half-space Green's function and the T matrix. NMM3D is used for the soil surface, which includes both the coherent wave specular reflection and the bistatic scattering of the rough surface. The emissivity is obtained by integration of the bistatic scattering over the hemispherical solid angle. The NMM3D-DBA model results are validated using coincident airborne PALS low-altitude radiometer data and UAVSAR data taken during the SMAPVEX12 field campaign. For vertical polarization the averaged RMSE and correlation coefficient over all the fields are 4.65 K and 0.91 K for brightness temperature and 1.04 dB and 0.95 dB for VV backscatter, while for horizontal polarization the average RMSE and correlation coefficient are 6.44 K and 0.94 K for brightness temperature and 1.21 dB and 0.90 dB for HH backscatter. The uncertainty in the *RMS* height measurements can be one of the main sources of error for the modeled brightness temperature which strongly depends on the *RMS* height for the vegetation-covered fields studied in this chapter. The NMM3D-DBA model assumes the vegetation scatterers are uniformly distributed which is not strictly true for the crop fields. This assumption can also cause errors in the model. Overall, on comparisons with the passive data, the results from NMM3D-DBA are comparable or better than those from the tau-omega model. The tau-omega model uses empirically adjusted parameters though the empirical parameters, such as ω, which are different from the physically calculated values.

In the future, the vegetation structure will be modeled more accurately by taking into account the leaves and grains for wheat and using elliptical disks for canola leaves. The consistent combined active and passive model based on NMM3D-DBA adopts a single scattering model for vegetation; it has been shown to be able to provide good estimations for backscatter and brightness temperature at L-band for wheat, winter wheat, pasture, and canola fields. As the frequency increases, multiple scattering effects in vegetation become more important [5]. Thus, at frequencies much higher than L-band, a multiple scattering approach should be used for vegetation instead of the distorted Born approximation. We can use the same concept as presented in this chapter to develop a consistent model for both active and passive at higher frequencies by using NMM3D for the soil surface together with a multiple scattering model for vegetation where the brightness temperature is calculated by integration of bistatic scattering coefficients. There are other vegetation types, such as soybean and corn, whose results are not presented here because the distorted Born approximation is not suitable for modeling them. Collective scattering effects of the vegetation scatterers are important for the soybean [5], thus a more accurate coherent model must be used for this vegetation type. For the corn field, multiple scattering effects [5] must be included because of the large scattering albedo and optical thickness. These two vegetation types and more accurate scattering models for higher frequencies will be studied in the future. Recently we have started the NMM3D full-wave simulations of vegetation scattering [31]. Future work will consist of using NMM3D to replace the DBA part of the methodology of combined active and passive.

CHAPTER IV

NMM3D Full-wave Simulations of a Layer of Dielectric Cylinders Using Fold-Lax Equations and Body of Revolution

Transmission, scattering and absorption by a layer of dielectric cylinders are studied in the context of microwave propagation through vegetation. The electromagnetic fields are calculated by Numerical Solutions of 3D Maxwell's equations (NMM3D) using the method of Foldy-Lax multiple scattering equations combined with method of the body of revolution (BOR). Using the calculated transmission, we derive, the "tau", the optical thickness, which describes the magnitude of the transmission. Two cases are considered: the short cylinders case and the extended-cylinders case. The case of short cylinders is that the lengths of cylinders are much smaller than the layer thickness, while the case of extended cylinders is that the lengths of the cylinders are the same as or comparable to the layer thickness. Numerical results are illustrated for plane vertical polarized waves obliquely incident on the layer of cylinders. The NMM3D results for the extended-cylinders case show large differences of transmission from the results of approaches such as effective permittivity (EP), the distorted Born approximation (DBA), and the radiative transfer equation (RTE). For the case of short cylinders, the NMM3D results are in close agreement with those from EP, DBA and RTE.

4.1 Introduction

Propagation, scattering and transmission of waves through a layer of finite-length dielectric cylinders have many applications including airborne and satellite microwave remote sensing over vegetation and forests, wireless communications in forests, radar foliage penetration (FoPen) and metamaterials of wires, etc [7, 30, 71-76]. In vegetation-covered surfaces, the finite length dielectric cylinders have been used to model grass, wheat, corn, rice, tree trunks of forests etc. [5, 6, 11, 27, 28, 77, 78]. A key calculation is the transmission of microwaves through such a canopy. The fraction of power transmitted for a plane wave at normal incidence is represented by $exp(-\tau)$. The quantity τ, "tau" has been extensively used in active and passive microwave remote sensing [1, 60, 74]. The phase shifts have been used in SAR interferometry [2, 79-81].

The existing methods used in the calculation of transmission are the effective permittivity (EP) [82], the distorted Born approximation (DBA) [11], and the vector radiative transfer equation (RTE) [4]. These three approaches make an assumption that the positions of the scatterers are statistically homogeneous in 3D. This means that the scatterers are uniformly distributed. The formulas of transmission utilize the scattering and absorption cross sections of a single scatterer which are averaged over distributions of sizes and orientations. A consequence is that there exists a per unit distance effective propagation constant k_{eff}. In the approach of effective permittivity [82], the effective permittivity ε_{eff} is used to calculate the effective propagation constant by the relation $k_{eff}^2 = k^2 \varepsilon_{eff}/\varepsilon$, where k and ε are the propagation constant and permittivity of the background medium, respectively. The per unit distance attenuation rate κ_e (extinction coefficient) is twice the imaginary part of the effective propagation constant [2, 4]. The product of κ_e and the layer thickness d gives τ. The product of the real part of the effective propagation constant k_{eff} and the layer thickness d gives the phase shift of transmission.

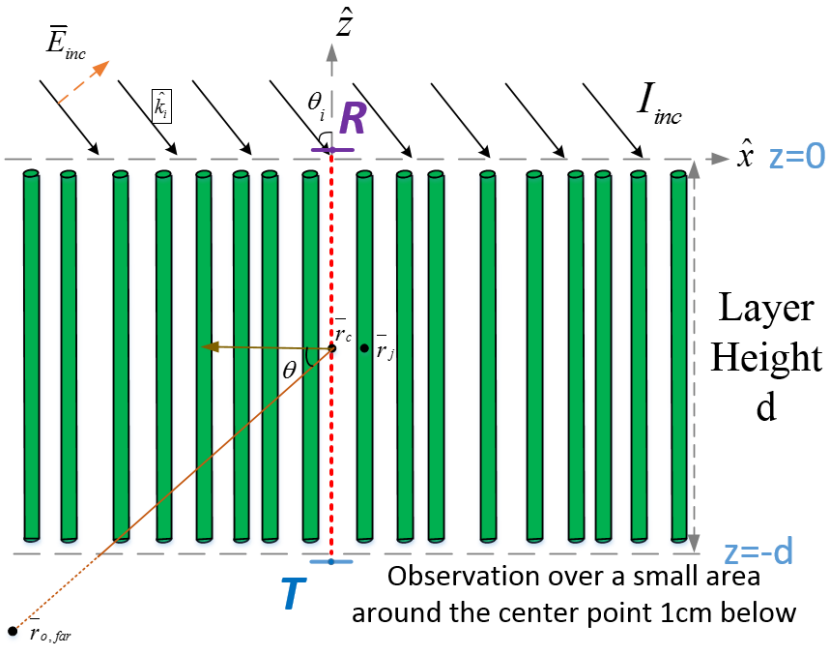

Figure IV.1. Extended cylinders with length comparable to layer thickness. Incident Plane wave. The area marked *T* is the transmission reception area at 1 cm below the layer. The area marked *R* is the reflection reception area at 1 cm above the layer. $\bar{r}_j$ is the center of jth cylinder. $\bar{r}_c$ is the center of the vegetation canopy. $\bar{r}_{o,far}$ is the far field observation point which is far away from the vegetation fields with $|\bar{r}_{o,far} - \bar{r}_c| = 500\lambda$. θ is the far fields observation angle used in FL-BOR and FL-ICA comparison.

Full-wave simulations by Numerical Solutions of 3D Maxwell's equations (NMM3D) of random rough surfaces have been performed for more than a decade [43]. NMM3D simulations for dense random media such as terrestrial snow [83, 84] began several years ago. Multiple scattering of vegetataion canopy upto second order was derived in [85, 86]. We started NMM3D simulations of vegetation recently, where all the multiple scatterings among the vegetation scatterers are considered. In this section, we study the scattering by a vegetation canopy consisting of thin dielectric cylindrical scatterers. The full-wave approach for solving Maxwell's equations is based on the Foldy-Lax multiple scattering equations (FL) [4, 30] combined with the Body of revolution (BOR) [12] (FL-BOR). The transmission is calculated using Monte Carlo simulation where the cylinders, as many as 500, are generated in each realization. The purpose of Monte Carlo

procedure is to simulate randomly placed receivers that are in the vegetation. Instead of randomly placing the receiver, we fix the receiver location and randomly shuffling the cylinders to create the many realizations. A merit of FL-BOR is the much smaller number of surface unknowns using only 1-dimensional discretization of the surface of the cylinder combined with Fourier expansions in the azimuthal direction. In usual 3D MoM codes, such as FEKO, the Rao-Wilton-Glisson (RWG) 2- dimensional basis functions are used. The results of transmission for C-band V-polarized (TM) incident wave are compared with those of EP, DBA and RTE. Two cases are studied: extended cylinders (Figure IV.1) and short cylinders (Figure IV.2). Extended cylinders mean that the cylinder lengths are the same as or comparable to the thickness of the vegetation layer.

This chapter is organized as follows. In Section 4.2, the approaches and the results of the effective permittivity (EP), the distorted Born approximation (DBA) and the radiative transfer equation (RTE) are reviewed. The derivation of the RTE equation using elemental cylindrical volumes is illustrated. Such elemental cylindrical volumes can be constructed for the case of short cylinders, but are improbable for extended cylinders. After that, the approach of Foldy-Lax equations combined with BOR (FL-BOR) is described. In section 4.3, the approach of FL-BOR is validated by comparing with the results from the commercial software HFSS as well as the method of combining Foldy-Lax equations with Infinite Cylinder Approximation (FL-ICA). In section 4.4, the procedures of Monte Carlo simulations of NMM3D for transmission, reflection, absorption, emission and the profiles of the electric field in the vegetation canopy are described. Next, the numerical results of short cylinders and extended cylinders are illustrated. The simulations are performed at C band (5.4GHz) with a plane vertically polarized incident wave at 40 degrees incident angle.

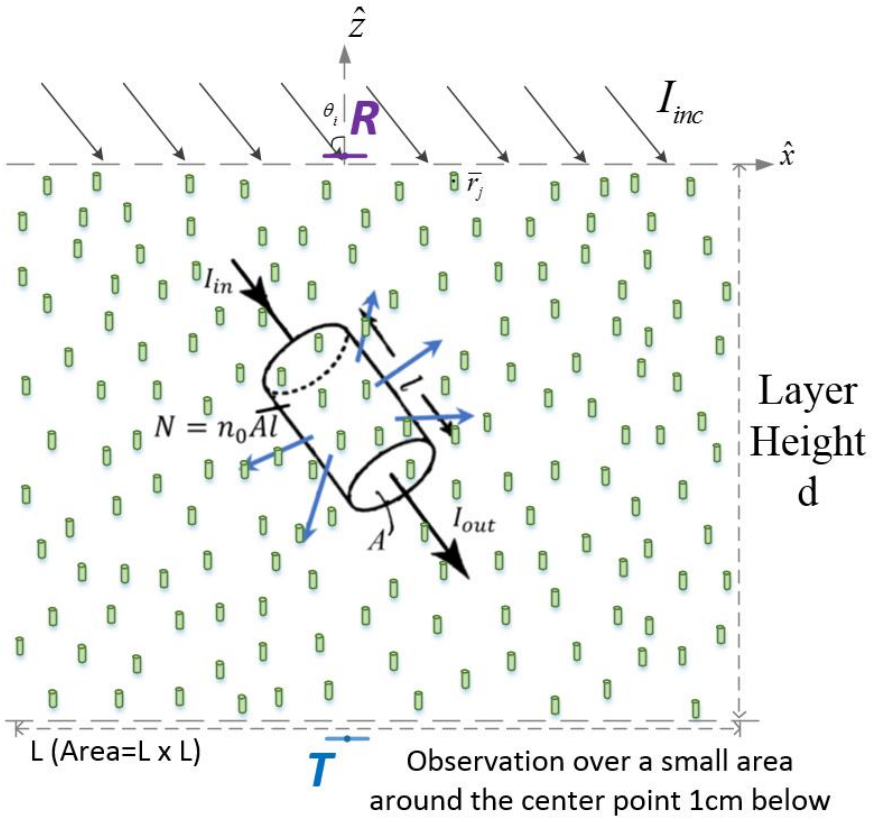

Figure IV.2. Short cylinders statistically homogeneous in 3D and a RTE elemental volume. A RTE cylindrical elemental volume with cross-sectional area *A* and length *l* containing *N* scatterers [36] is drawn in black. n_0 is the number of scatterers per m^3. The input and output intensities are I_{in} and I_{out} which are comparable with $\Delta I = I_{out} - I_{in}$. Each scatterer has σ_a and σ_s, the absorption and scattering cross section respectively. The area marked *T* is the transmission reception area at 1 cm below the layer. The area marked *R* is the reflection reception area at 1 cm above the layer.

4.2 Foldy-Lax Equation Combined with Body of Revolution (FL-BOR)

4.2.1 Review of RTE Derivation, DBA and EP

We first review the derivation of the radiative transfer equation [2, 43, 87, 88] for a random medium of discrete scatterers (Figure IV.2). Consider an RTE cylindrical elemental volume containing *N* scatterers. The elemental volume is defined by cross-sectional area *A* and length *l* as

shown in Figure IV.2.The change of power as the wave passes through the cylindrical elemental volume is

$$\Delta P = (I_{out} - I_{in})A \tag{4.2.1}$$

The power change is caused by absorption and scattering by the scatterers inside the cylindrical elemental volume. Let σ_a and σ_s represent the absorption and scattering cross section of a scatterer, respectively. Then

$$\Delta P = -N(\sigma_a + \sigma_s)I \tag{4.2.2}$$

Let the scatterers per unit volume be n_0. Then $N = n_0 Al$. Substituting into equation (2) and comparing with (1), we get $\Delta P = (I_{out} - I_{in})A = -n_0 Al(\sigma_a + \sigma_s)I$. Then

$$\frac{\Delta I}{l} = -n_0(\sigma_a + \sigma_s)I \tag{4.2.3}$$

where $\Delta I = (I_{out} - I_{in})$, and $I = (I_{out} + I_{in})/2$ is the "average I".

The extinction coefficient κ_e which calculates the power attenuation rate per unit distance through the vegetation layer is defined as

$$\kappa_e = n_0\sigma_a + n_0\sigma_s \tag{4.2.4}$$

By taking the small length limit of *l*, a differential equation is obtained

$$\frac{dI}{ds} = -\kappa_e I \tag{4.2.5}$$

The assumed properties of the elemental cylindrical volume [2, 43, 87, 88] include the following: 1) The number of scatterers inside RTE cylindrical elemental volume must not be small. 2) The entire scatterer must be inside the elemental volume because σ_a and σ_s are calculated for an entire scatterer and not part of a scatterer. 3) The I on the right-hand-side of equation (5) is the average of I_{out} and I_{in} so that I_{out} and I_{in} are not much different.

To complete RTE derivation, a similar argument accounts for coupling through the scattering phase function $p(\hat{s}, \hat{s}')$ which is the scattering from direction $\hat{s}'$ into direction $\hat{s}$. The phase function is caused by the scatterers inside the cylindrical volume. Then [4, 43, 88]

$$\frac{dI}{ds} = -\kappa_e I + \int d\hat{s}'\, p(\hat{s}, \hat{s}') I(\hat{s}') \tag{4.2.6}$$

The transmitted intensity, I_t of RTE for an incident wave with intensity I_{inc} is, ignoring the contribution of the phase function,

$$I_t = I_{inc} exp\big(-\kappa_e d(sec\theta_i)\big) \tag{4.2.7}$$

where θ_i is the incident angle and *d* is the thickness of the vegetation layer.

The optical thickness τ, in the radiative transfer approach, is $\tau = \kappa_e d$ [4]. Then the transmission can be calculated as

$$t = exp(-\tau sec\theta_i) \tag{4.2.8}$$

Another common approach is using the distorted Born approximation [11]. The distorted Born approximation follows from the lowest order of the mass operator in the Dyson equation [89], in which the mean field E is obtained for the vegetation layer as an equivalent medium with an effective permittivity ε_{eff} [82]. This means $\bar{D} = \varepsilon_{eff}\bar{E}$. The effective propagation constant is $k_{eff} = \omega\sqrt{\mu\varepsilon_{eff}}$. Since the intensity is the square of absolute value of the electric field, the transmission is

$$t = \exp\left[-2Im\big(k_{eff}\big)dsec\theta_i\right] \tag{4.2.9}$$

where $Im\big(k_{eff}\big)$ indicates the imaginary part of k_{eff}.

Using Foldy's approximation [4, 11], which assumes a sparse concentration of scatterers, the effective propagation constant is

$$k_{eff} = k + \frac{2\pi n_0}{k} f(\hat{k}_i, \hat{k}_i) \tag{4.2.10}$$

where k is the propagation constant of the background medium and $f(\hat{k}_i, \hat{k}_i)$ is the forward scattering amplitude of a single scatterer.

Then, $2Im(k_{eff}) = \frac{4\pi n_0}{k} Im\left(f(\hat{k}_i, \hat{k}_i)\right)$. From forward scattering theorem [4],

$$\frac{4\pi}{k} Im\left(f(\hat{k}_i, \hat{k}_i)\right) = \sigma_a + \sigma_s \tag{4.2.11}$$

Substituting equation (4.2.11) into equation (4.2.9) and using equation (4.2.6) for κ_e, the transmission for DBA is obtained as $t = exp(-\kappa_e d sec\theta_i)$. Thus, RTE and DBA have the same formula of the attenuation rate per unit distance κ_e. The Dyson's equation is a result of using Feymann diagrams. In the book chapter of Frisch [89] the lowest order approximation (equation (6.40) in [89]) of the mass operator is

$$\otimes = \sum_{a=1}^{N} \int p(\bar{r}_a) S(\bar{r} - \bar{r}_a, \bar{r}' - \bar{r}_a)\, d\bar{r}_a \tag{4.2.12}$$

where $p(\bar{r}_a)$ is the probability density function of scatterers' positions, S is the scattering matrix and N is the total number of scatterers.

In Frisch [89], the probability density function $p(\bar{r}_a)$, for the position of a scatterer is

$$p(\bar{r}_a) = \frac{1}{V} \tag{4.2.13}$$

This means that the scatterers are statistically homogeneously distributed in the 3D space. Then $\sum_{a=1}^{N} \frac{1}{V} = \frac{N}{V} = n_0$ and the mass operator becomes

$$\otimes = n_0 \int S(\bar{r} - \bar{r}_a, \bar{r}' - \bar{r}_a) d\bar{r}_a \tag{4.2.14}$$

The vegetation layer of short cylinders are illustrated in Figure IV.2. The figure shows that the RTE elemental cylindrical volume can be constructed for such a medium. The figure also shows that the pdf of equation (4.2.13) of 3D statistical homogeneity also applies. However, for the extended cylinders of Figure IV.1, it is improbable to construct the RTE elemental cylindrical

volume since the length of the extended cylinder is the same or comparable to the layer thickness. Figure IV.1 shows that the cylinders can be translated horizontally but vertical translation would move the cylinders out of the bounds of the layer. The case of extended cylinders represents several vegetation types such as grass, wheat, canola, corn and the understory of forests.

Three other observations of the formula are: 1) n_0 is clearly defined for the short cylinder case. Strictly speaking, n_0 is not defined for the extended cylinder case. It has been customary to use $n_a = n_0 d$ where n_a is the number of cylinders per unit area [5, 6, 28]. 2) In the calculations of σ_a and σ_s, the entire cylinder of length L is used which means the entire cylinder from top to bottom receives the same incident electric fields. This does not apply to the extended-cylinders case since attenuation and scattering in the vegetation canopy will change the wave significantly before the wave hits the lower part of the cylinder. 3) In the calculations of scattering phase function $p(\hat{s}, \hat{s}')$, far field approximation is used, which means each two cylinders much be in the far field region of each other. Far field distance is larger than L^2/λ where L is the length of the cylinder and λ is the wavelength. For example, the far field distance for 30cm tall grass at C-band is around 1.8m. But the adjacent two grass cannot be so far from each other.

To summarize, firstly, the geometries and positions of extended cylinders do not satisfy the assumption of elemental cylindrical volume used in the derivation of RTE. Secondly, RTE assumes uniform distributions of scatterers while in vegetation and forest canopies, the positions of scatterers are not uniform. The scatterers can be in dense clusters and in the other extreme, there can be large gaps between scatterers. Thirdly, RTE uses far field approximation but the adjacent vegetation scatterers are generally not in the far field region of each other. Thus, in this chapter, we use numerical solutions of Maxwell's equations which can take into accounts these factors that are not addressed by RTE.

4.2.2 Formulations of FL-BOR

In this section, the formulation of FL-BOR is presented in subsection (a). The derivations of Foldy-Lax equations and the Body of Revolution method is also presented in subsection (b).

(a) FL-BOR

Consider the case of N_L scatterers illuminated by an incident plane wave. The Foldy-Lax multiple scattering equations are [4, 90]

$$\bar{E}_m^{ex} = \bar{E}_m^{inc} + \sum_{\substack{n=1 \\ n\neq m}}^{N_L} \bar{E}_n^{scat} \tag{4.2.15}$$

where $\bar{E}_m^{ex}$ is the excitation field on scatterer m, $\bar{E}_m^{inc}$ is the incident field on scatterer *m*, and $\bar{E}_n^{scat}$ is the scattered field from scatterer *n* to scatterer *m*. The Foldy-Lax multiple scattering equations are derived from Maxwell's equations and are exact relations without approximations. The derivation can be found in sections 1 and 2 of chapter 5 in [30] and a brief derivation is also presented in section 4.2.2 (b). The Foldy-Lax multiple scattering equations state that the final exciting field on scatterer *m* is the sum of incident wave and the scattered waves from all other scatterers except *m* itself.

Using the T matrix of an isolated scatterer that $\bar{E}_n^{scat} = \bar{\bar{G}}_0 \bar{\bar{T}}_n \bar{E}_n^{ex}$. Previously, the numerical implementations of Foldy-Lax equations are using the spherical wave expansions for both the Green's function $\bar{\bar{G}}_0$ and the T matrix $\bar{\bar{T}}_n$ [4, 90, 91]. However, spherical wave expansions are not suitable for cylinders which have large aspect ratios of length to radius. We use BOR which are for rotationally symmetric objects such as cylinders and disks. In this section, we use the Z matrix from BOR instead of the T matrix. In this case, wave expansions are not needed. Huygen's principles are used to calculate scattering from the cylinder to another cylinder [4].

$$\bar{E}_n^{scat} = \int_{dS_n} dS' \left[\bar{\bar{G}}_0 \cdot i\omega\mu_0 \bar{J}(\bar{r}') - \nabla \times \bar{\bar{G}}_0 \cdot \bar{M}(\bar{r}')\right] \tag{4.2.16}$$

where $\bar{\bar{G}}_0$ is the dyadic Green's function, and $\bar{J}(\bar{r}')$ and $\bar{M}(\bar{r}')$ are the equivalent surface electric and magnetic currents, respectively.

Substituting equation (4.2.16) into the Foldy-Lax equations, we obtain

$$\bar{E}_m^{ex} = \bar{E}_m^{inc} + \sum_{\substack{n=1 \\ n\neq m}}^{N_L} \int_{dS_n} dS' \begin{bmatrix} \bar{\bar{G}}_0 \cdot i\omega\mu_0 \bar{J}(\bar{r}') - \\ \nabla \times \bar{\bar{G}}_0 \cdot \bar{M}(\bar{r}') \end{bmatrix} \tag{4.2.17}$$

Similarly, for magnetic fields, we have

$$\bar{H}_m^{ex} = \bar{H}_m^{inc} + \sum_{\substack{n=1 \\ n\neq m}}^{N_L} \int_{dS_n} dS' \begin{bmatrix} \bar{\bar{G}}_0 \cdot i\omega\varepsilon_0 \bar{M}(\bar{r}') + \\ \nabla \times \bar{\bar{G}}_0 \cdot \bar{J}(\bar{r}') \end{bmatrix} \tag{4.2.18}$$

To solve equations (4.2.17) and (4.2.18) numerically, each cylinder is divided into N_S sections. The total number of sections of all the cylinders are $N_{tot} = N_L \times N_S$. Equations (4.2.17) and (4.2.18) are put together in matrix form as,

$$\begin{bmatrix} \bar{E}^{ex} \\ \bar{H}^{ex} \end{bmatrix} = \begin{bmatrix} \bar{E}^{inc} \\ \bar{H}^{inc} \end{bmatrix} + \bar{\bar{P}} \begin{bmatrix} \bar{J} \\ \bar{M} \end{bmatrix} \tag{4.2.19}$$

$\bar{E}$ and $\bar{H}$ are expressed in $\hat{x}$, $\hat{y}$ and $\hat{z}$ directions. For each section, the surface currents $\bar{J}$ and $\bar{M}$ are decomposed into vector components of two directions $\hat{t}$ and $\hat{\phi}$ which are the body directions of the cylinder in the longitudinal and azimuthal directions, respectively. Thus $\begin{bmatrix} \bar{E}^{ex} \\ \bar{H}^{ex} \end{bmatrix}$ and $\begin{bmatrix} \bar{E}^{inc} \\ \bar{H}^{inc} \end{bmatrix}$ are both $6N_{tot} \times 1$ matrices, $\begin{bmatrix} \bar{J} \\ \bar{M} \end{bmatrix}$ is a $4N_{tot} \times 1$ matrix and $\bar{\bar{P}}$ is a $6N_{tot} \times 4N_{tot}$ matrix. The orders for the matrix elements section by section are as follows:

$$\begin{bmatrix} \bar{E}^{ex} \\ \bar{H}^{ex} \end{bmatrix} = [E_{x,1}^{ex}; E_{y,1}^{ex}; E_{z,1}^{ex}; H_{x,1}^{ex}; H_{y,1}^{ex}; H_{z,1}^{ex}; \ldots$$

$$E_{x,N_{tot}}^{ex}; E_{y,N_{tot}}^{ex}; E_{z,N_{tot}t}^{ex}; H_{x,N_{tot}}^{ex}; H_{y,N_{tot}}^{ex}; H_{z,N_{tot}}^{ex}],$$

where the semicolon indicates that it is a column vector instead of a row vector. Similarly,

$$\begin{bmatrix}\bar{E}^{inc}\\ \bar{H}^{inc}\end{bmatrix} = [E_{x,1}^{inc}; E_{y,1}^{inc}; E_{z,1}^{inc}; H_{x,1}^{inc}; H_{y,1}^{inc}; H_{z,1}^{inc}; \ldots$$

$$E_{x,N_{tot}}^{inc}; E_{y,N_{tot}}^{inc}; E_{z,N_{tot}}^{inc}; H_{x,N_{tot}}^{inc}; H_{y,N_{tot}}^{inc}; H_{z,N_{tot}}^{inc}],$$

and

$$\begin{bmatrix}\bar{J}\\ \bar{M}\end{bmatrix} = [J_{t,1}; J_{\phi,1}; M_{t,1}; M_{\phi,1}; \ldots$$

$$J_{t,N_{tot}}; J_{\phi,N_{tot}}; M_{t,N_{tot}}; M_{\phi,N_{tot}}].$$

Matrix $\bar{\bar{P}}$ is defined as

$$\bar{\bar{P}} = \begin{bmatrix} \bar{\bar{p}}_{1,1} & \cdots & \bar{\bar{p}}_{1,N_{tot}} \\ \vdots & \ddots & \vdots \\ \bar{\bar{p}}_{N_{tot},1} & \cdots & \bar{\bar{p}}_{N_{tot},N_{tot}} \end{bmatrix}$$

with each $\bar{\bar{p}}_{i,j}$ BEING A 6×4 MATRIX. $\bar{\bar{p}}_{i,j}$ calculates the scattered fields from section *j* to the section *i* caused by the equivalent surface currents on section *j*.

In the derivations below, the radius of the cylinder is assumed to be much less than the wavelength. The assumption is valid for many vegetation types at L- and C- band such as grass and wheat. We assume here that the cylinders are vertically oriented. There is no conceptual difficulty in extending the formulation to cylinders with an orientation distribution and to cylinders with larger radii. In the vertically oriented case, $\hat{t}$ equals $\hat{z}$ for all cylinders. As explained above, the scattered field from the cylinder itself is excluded in the Foldy-Lax equations. Thus, $\bar{\bar{p}}_{i,j}$ is $\bar{\bar{0}}$ if *j* and *i* sections are on the same cylinder. For example, $\bar{\bar{p}}_{1,2} = \bar{\bar{0}}$ since both section 1 and section 2 are on cylinder 1. In mathematical notations,

$$\bar{\bar{p}}_{i,j} = \bar{\bar{0}} \begin{cases} i = (k-1)N_S + 1 : kN_S \\ j = (k-1)N_S + 1 : kN_S \end{cases},$$

where $k = 1,2,\dots,NL$. Otherwise, the thin cylinder approximation is used to calculate $\bar{\bar{p}}_{i,j}$ as follows. According to equation (4.2.16), the scattered fields from section *j* to the center of section *i* is calculated as

$$\bar{E}_j^{scat}(\bar{r}_i) = \int_{dS_j} dS' \begin{bmatrix} \bar{\bar{G}}_0(\bar{r}_i, \bar{r}') \cdot i\omega\mu_0 \bar{J}(\bar{r}') - \\ \nabla \times \bar{\bar{G}}_0(\bar{r}_i, \bar{r}') \cdot \bar{M}(\bar{r}') \end{bmatrix} \tag{4.2.20}$$

where $\bar{r}_i = x_i\hat{x} + y_i\hat{y} + z_i\hat{z}$ is center of section *i*.

Since the radius of the cylinder is much less than wavelength (thin cylinder) and the section length Δz is chosen to be small, $\bar{J}(\bar{r}')$ and $\bar{M}(\bar{r}')$ are approximately constant within each section. Let the surface currents on section *j* be $\bar{J}(\bar{r}_j)$ and $\bar{M}(\bar{r}_j)$, which are decomposed into the two directions $\hat{t}'$ and $\hat{\phi}'$. For vertically oriented cylinders, $\hat{t}' = \hat{z}$ and $\hat{\phi}' = -sin\phi'\hat{x} + cos\phi'\hat{y}$. Thus

$$\bar{J}(\bar{r}_j) = J_{t,j}\hat{t}' + J_{\phi,j}\hat{\phi}' = -J_{\phi,j}sin\phi'\hat{x} + J_{\phi,j}cos\phi'\hat{y} + J_{t,j}\hat{z},$$

and

$$\bar{M}(\bar{r}_j) = M_{t,j}\hat{t}' + M_{\phi,j}\hat{\phi}' = -M_{\phi,j}sin\phi'\hat{x} + M_{\phi,j}cos\phi'\hat{y} + M_{t,j}\hat{z}.$$

Under the thin cylinder assumption, Green's function $\bar{\bar{G}}_0(\bar{r}_i, \bar{r}')$ can also be approximated by $\bar{\bar{G}}_0(\bar{r}_i, \bar{r}_j)$ where $\bar{r}_j$ is the center of section *j*. The expression for the dyadic Green's function is

$$\bar{\bar{G}}_0(\bar{r}_i, \bar{r}_j) = G_1(R)\bar{\bar{I}} + G_2(R)\hat{R}\hat{R} \tag{4.2.21}$$

with $\bar{\bar{I}} = \hat{x}\hat{x} + \hat{y}\hat{y} + \hat{z}\hat{z}$,

$$R = \sqrt{(x_i - x_j)^2 + (y_i - y_j)^2 + (z_i - z_j)^2},$$

$$G_1(R) = \frac{\exp(ikR)}{4\pi k^2 R^3}(-1 + ikR + k^2R^2)$$

$$G_2(R) = \frac{\exp(ikR)}{4\pi k^2 R^3}(3 - 3ikR - k^2R^2),$$

$$\hat{R} = \left[(x_i - x_j)\hat{x} + (y_i - y_j)\hat{y} + (z_i - z_j)\hat{z}\right]/R.$$

From equation (4.2.21), $\bar{\bar{G}}_0(\bar{r}_i, \bar{r}_j)$ can be written in the form $\bar{\bar{G}}_0(\bar{r}_i, \bar{r}_j) = \bar{G}_{x,ij}\hat{x} + \bar{G}_{y,ij}\hat{y} + \bar{G}_{z,ij}\hat{z}$. Next, the expression for the curl of the dyadic Green's function is

$$\nabla \times \bar{\bar{G}}_0(\bar{r}_i, \bar{r}_j) =$$

$$\frac{\exp(ikR)}{4\pi R^2}\left(ik - \frac{1}{R}\right)\left[(x_i - x_j)(\hat{z}\hat{y} - \hat{y}\hat{z}) + (y_i - y_j)(\hat{x}\hat{z} - \hat{z}\hat{x}) + (z_i - z_j)(\hat{y}\hat{x} - \hat{x}\hat{y})\right] \tag{4.2.22}$$

Let $\bar{\bar{F}}_0(\bar{r}_i, \bar{r}_j) = \nabla \times \bar{\bar{G}}_0(\bar{r}_i, \bar{r}_j)$. Similarly, from equation (4.2.22), $\bar{\bar{F}}_0(\bar{r}_i, \bar{r}_j)$ can be written in the form $\bar{\bar{F}}_0(\bar{r}_i, \bar{r}_j) = \bar{F}_{x,ij}\hat{x} + \bar{F}_{y,ij}\hat{y} + \bar{F}_{z,ij}\hat{z}$.

The surface integration can be expressed as $\int_{dS_j} dS' = a_j \int_0^{2\pi} d\phi' \int_{z_j - \Delta z_j/2}^{z_j + \Delta z_j/2} dz'$ with a_j, z_j and Δz_j being the radius, z component of the center position and the length of section *j*, respectively. Substituting these into equation (20), then

$$a_j \int_0^{2\pi} d\phi' \int_{z_j - \frac{\Delta z_j}{2}}^{z_j + \frac{\Delta z_j}{2}} dz' \left(\bar{\bar{G}}_0(\bar{r}_i, \bar{r}_j) \cdot \bar{J}(\bar{r}_j)\right) = a_j \Delta z_j \begin{bmatrix} -J_{\phi,j}\bar{G}_{x,ij}\int_0^{2\pi} d\phi' sin\phi' \\ +J_{\phi,j}\bar{G}_{y,ij}\int_0^{2\pi} d\phi' cos\phi' \\ +J_{t,j}\bar{G}_{z,ij}\int_0^{2\pi} d\phi' \end{bmatrix} = 2\pi a_j \Delta z_j J_{t,j}\bar{G}_{z,ij} \tag{4.2.23}$$

Similarly,

$$a_j \int_0^{2\pi} d\phi' \int_{z_j - \Delta z_j/2}^{z_j + \Delta z_j/2} dz' \left(\nabla \times \bar{\bar{G}}_0(\bar{r}_i, \bar{r}_j) \cdot \bar{M}(\bar{r}_j)\right) = 2\pi a_j \Delta z_j M_{t,j}\bar{F}_{z,ij} \tag{4.2.24}$$

Thus equation (4.2.20) becomes

$$\bar{E}_j^{scat}(\bar{r}_i) = 2\pi a_j \Delta z_j [i\omega\mu_0 \bar{G}_{z,ij} J_{t,j} - \bar{F}_{z,ij} M_{t,j}] \tag{4.2.25}$$

Similarly, for magnetic fields,

$$\bar{H}_j^{scat}(\bar{r}_i) = 2\pi a_j \Delta z_j [i\omega\varepsilon_0 \bar{G}_{z,ij} M_{t,j} + \bar{F}_{z,ij} J_{t,j}] \tag{4.2.26}$$

Substituting equation (4.2.25) and (4.2.26) into equation (4.2.19), the expression for the non-zeros $\bar{\bar{p}}_{i,j}$ is obtained as

$$\bar{\bar{p}}_{i,j} = 2\pi a_j \Delta z_j \begin{bmatrix} i\omega\mu_0 \bar{G}_{z,ij} & \bar{0} & -\bar{F}_{z,ij} & \bar{0} \\ \bar{F}_{z,ij} & \bar{0} & i\omega\varepsilon_0 \bar{G}_{z,ij} & \bar{0} \end{bmatrix} \tag{4.2.27}$$

where a_j is the radius and Δz_j is the length of section j. $\bar{G}_{z,ij} = [G_{xz,ij};\quad G_{yz,ij};\quad G_{zz,ij}]$ which is obtained from the expression for the dyadic Green's function $\bar{\bar{G}}_0(\bar{r}_i, \bar{r}_j)$ in equation (4.2.21). Similarly,$\bar{F}_{z,ij} = [F_{xz,ij};\quad F_{yz,ij};\quad F_{zz,ij}]$ is obtained from equation (4.2.22).

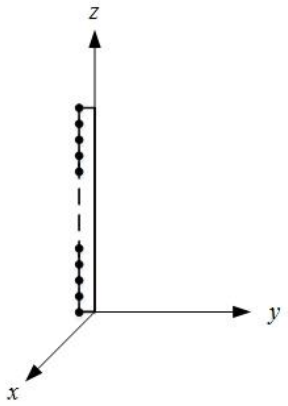

Figure IV.3. One dimensional discretization of the cylinder in the BOR.

The expressions for the matrix $\bar{\bar{P}}$ which relates the surface currents to the scattered fields are obtained. The next step is to relate the surface currents to the exciting fields, and for this the BOR formulation [12] is used. In BOR, the surface currents $\bar{J}_s(\bar{r}')$ and $\bar{M}_s(\bar{r}')$ are represented by locally oriented basis functions ($\hat{t}'$ and $\hat{\phi}'$), which are expanded in Fourier series in the $\hat{\phi}'$ dimension making use of the rotational symmetry [12, 92]. Therefore only 1-dimensional discretization is used in MoM, as shown in Figure IV.3. This is different from the usual surface integral equation where the Rao-Wilton-Glisson (RWG) 2- dimensional vector basis functions are used to represent tangential surface fields on curved surfaces. The electric surface currents are solved as:

$$\bar{J}_s(\bar{r}') = \sum_{\alpha=-\infty}^{\infty} \sum_{s=1}^{N_S} \begin{bmatrix} I_{\alpha,s}^{J,t'} f_s^{J,t'} e^{-i\alpha\phi'} \hat{t}' + \\ I_{\alpha,s}^{J,\phi'} f_s^{J,\phi'} e^{-i\alpha\phi'} \hat{\phi}' \end{bmatrix} \tag{4.2.28}$$

where α is the Fourier harmonic order, $I_{\alpha,s}^{J,t'}$ and $I_{\alpha,s}^{J,\phi'}$ are the unknown coefficients, and $f_s^{J,t'}$ and $f_s^{J,\phi'}$ are the one-dimensional basis functions for electric surface current in the $\hat{t}'$ and $\hat{\phi}'$ direction, respectively.

Since the radius of the cylinder is much smaller than the wavelength, only the zeroth Fourier harmonic ($\alpha = 0$) is important. Thus, equation (4.2.28) becomes

$$\bar{J}_s(\bar{r}') = \sum_{s=1}^{N_S} [I_{0,s}^{J,t'} f_s^{J,t'} \hat{t}' + I_{0,s}^{J,\phi'} f_s^{J,\phi'} \hat{\phi}'] \tag{4.2.29}$$

Similarly, for $\bar{M}_s(\bar{r}')$,

$$\bar{M}_s(\bar{r}') = \sum_{s=1}^{N_S} [I_{0,s}^{M,t'} f_s^{M,t'} \hat{t}' + I_{0,s}^{M,\phi'} f_s^{M,\phi'} \hat{\phi}'] \tag{4.2.30}$$

where $I_{\alpha,s}^{M,t'}$ and $I_{\alpha,s}^{M,\phi'}$ are the unknown coefficients, and $f_s^{M,t'}$ and $f_s^{M,\phi'}$ are the one-dimensional basis functions for the magnetic surface current in the $\hat{t}'$ and $\hat{\phi}'$ direction, respectively.

In this section, the basis functions are chosen to be pulse functions with amplitude one for currents in $\hat{\phi}'$ direction currents and amplitude $\frac{1}{2\pi a}$ for currents in $\hat{t}'$ direction where a is the radius of the cylinder. Thus,

$$\begin{bmatrix} \bar{J} \\ \bar{M} \end{bmatrix} = \bar{\bar{C}} \begin{bmatrix} \bar{I}^J \\ \bar{I}^M \end{bmatrix} \tag{4.2.31}$$

where $\begin{bmatrix} \bar{I}^J \\ \bar{I}^M \end{bmatrix}$ is the matrix for the unknown coefficients $I_{0,s}^{J,t'}$ and $I_{0,s}^{M,t'}$, and

$$\bar{\bar{C}} = \begin{bmatrix} \bar{\bar{c}}_1 & & \bar{\bar{0}} \\ & \ddots & \\ \bar{\bar{0}} & & \bar{\bar{c}}_{N_S} \end{bmatrix}, \text{ with } \bar{\bar{c}}_s = \begin{bmatrix} \frac{1}{2\pi a} & 0 & 0 & 0 \\ 0 & 0 & 0 & 0 \\ 0 & 0 & \frac{1}{2\pi a} & 0 \\ 0 & 0 & 0 & 0 \end{bmatrix}.$$

Using both the Electric Field Integral Equation (EFIE) and the Magnetic Field Integral Equation (MFIE), we have for the cylinder *n* that [12]

$$\left[\begin{matrix}\bar{I}^J\\ \bar{I}^M\end{matrix}\right]_n = \bar{\bar{\beta}}_n^{-1}\left[\begin{matrix}\bar{V}^E\\ \bar{V}^H\end{matrix}\right]_n \tag{4.2.32}$$

where the subscript *n* denotes cylinder *n*. The details of the formulations are available in [12] and the matrix elements of $\bar{\bar{\beta}}_n$ are available on pages 23-28 in [12] The testing functions are pulse functions with amplitude one. The column vector on the right-hand side is related to the excitation field.

Substituting equation (4.2.32) to equation (4.2.31), we obtain

$$\left[\begin{matrix}\bar{J}\\ \bar{M}\end{matrix}\right]_n = \bar{\bar{z}}_n^{-1}\left[\begin{matrix}\bar{V}^E\\ \bar{V}^H\end{matrix}\right]_n \tag{4.2.33}$$

where $\bar{\bar{z}}_n^{-1} = \bar{\bar{C}}\bar{\bar{\beta}}_n^{-1}$ is the modified inverse of the MoM system matrix for cylinder *n* which relates the excitation to the surface current.

The BOR code, developed by Glisson and Wilton [12], provides $\bar{\bar{z}}_n^{-1}$. But the code [12] only calculates solutions for incident plane waves. For the present case, we study multiple scattering from one cylinder to another. Thus, we compute scattering field from one point on the cylinder to another point as the exciting field and then convert the exciting fields to harmonics. $\bar{V}^E$ and $\bar{V}^H$ are results from integration of testing function with the excitation fields. $\bar{J}$, $\bar{M}$, $\bar{V}^E$ and $\bar{V}^H$ have both $\hat{t}'$ and $\hat{\phi}'$ components and there are N_S sections in total; therefore, $\bar{\bar{z}}_n^{-1}$ is of size $4N_S \times 4N_S$. Consider section j on the cylinder n. Then [12],

$$V_{t'}^E = a_j \int_0^{2\pi} d\phi' \int_{z_j-\frac{\Delta z_j}{2}}^{z_j+\frac{\Delta z_j}{2}} dz'\, E_{t'}^{ex}(\bar{r}') \tag{4.2.34}$$

$$V_{\phi'}^E = a_j \int_0^{2\pi} d\phi' \int_{z_j-\frac{\Delta z_j}{2}}^{z_j+\frac{\Delta z_j}{2}} dz'\, E_{\phi'}^{ex}(\bar{r}') \tag{4.2.35}$$

where the subscripts t' and ϕ' denote the $\hat{t}'$ and $\hat{\phi}'$ components, respectively. Pulse testing functions are used to obtain equations (4.2.34) and (4.2.35) as in [12].

Since the cylinders are vertically oriented, $E_{t'}^{ex}(\bar{r}') = E_z^{ex}(\bar{r}')$, and $E_{\phi'}^{ex}(\bar{r}') = -sin\phi' E_x^{ex}(\bar{r}') + cos\phi' E_y^{ex}(\bar{r}')$. As discussed before, the excitation fields $\bar{E}^{ex}(\bar{r}')$ on each section can be approximated by a constant value for the thin cylinders. As before, we use the excitation fields at the center of each section. Then, equations (4.2.34) and (4.2.35) become

$$V_{j,t'}^{E} = a_j \int_0^{2\pi} d\phi' \int_{z_j-\frac{\Delta z_j}{2}}^{z_j+\frac{\Delta z_j}{2}} dz'\, E_z^{ex}(\bar{r}_j) = 2\pi a_j \Delta z_j E_z^{ex}(\bar{r}_j) \tag{4.2.36}$$

$$V_{j,\phi'}^{E} = a_j \int_0^{2\pi} d\phi' \int_{z_j-\frac{\Delta z_j}{2}}^{z_j+\frac{\Delta z_j}{2}} dz' \begin{bmatrix} -sin\phi' E_x^{ex}(\bar{r}_j) \\ +cos\phi' E_y^{ex}(\bar{r}_j) \end{bmatrix} = 0 \tag{4.2.37}$$

Similarly, $V_{j,t'}^{H} = 2\pi a_j \Delta z_j H_z^{ex}(\bar{r}_j)$, and $V_{j,\phi'}^{H} = 0$. Thus for section *j*,

$$\begin{bmatrix} \bar{V}_j^E \\ \bar{V}_j^H \end{bmatrix} = \begin{bmatrix} \bar{\bar{w}}_j^E & \bar{\bar{0}} \\ \bar{\bar{0}} & \bar{\bar{w}}_j^H \end{bmatrix} \begin{bmatrix} \bar{E}_j^{ex} \\ \bar{H}_j^{ex} \end{bmatrix} \tag{4.2.38}$$

where $\bar{\bar{w}}_j^E = \bar{\bar{w}}_j^H = \begin{bmatrix} 0 & 0 & 2\pi a_j \Delta z_j \\ 0 & 0 & 0 \end{bmatrix}$.

The equations for all the cylinders are put in matrix form,

$$\begin{bmatrix} \bar{J} \\ \bar{M} \end{bmatrix} = \bar{\bar{Z}}^{-1} \begin{bmatrix} \bar{V}^E \\ \bar{V}^H \end{bmatrix} = \bar{\bar{Z}}^{-1}\, \bar{\bar{W}} \begin{bmatrix} \bar{E}^{ex} \\ \bar{H}^{ex} \end{bmatrix} \tag{4.2.39}$$

where

$$\bar{\bar{Z}}^{-1} = \begin{bmatrix} \bar{\bar{z}}_1^{-1} & & \bar{\bar{0}} \\ & \ddots & \\ \bar{\bar{0}} & & \bar{\bar{z}}_{NL}^{-1} \end{bmatrix}.$$

$\bar{\bar{z}}_n^{-1}$ is the modified inverse of the MoM system matrix for the cylinder *n* as in equation (4.2.33). The exciting fields are related to $\bar{V}$ by the matrix

$$\bar{\bar{W}} = \begin{bmatrix} \bar{\bar{w}}_1 & & \bar{\bar{0}} \\ & \ddots & \\ \bar{\bar{0}} & & \bar{\bar{w}}_{N_{tot}} \end{bmatrix}, \text{ where } \bar{\bar{w}}_j = \begin{bmatrix} \bar{\bar{w}}_j^E & \bar{\bar{0}} \\ \bar{\bar{0}} & \bar{\bar{w}}_j^H \end{bmatrix} \text{ as in equation (4.2.38).}$$

Letting $\bar{\bar{Q}} = \bar{\bar{Z}}^{-1}\,\bar{\bar{W}}$ and substituting Equation (4.2.39) into (4.2.19), we have

$$\begin{bmatrix} \bar{E}^{ex} \\ \bar{H}^{ex} \end{bmatrix} = \left[\bar{\bar{I}} - \bar{\bar{P}}\bar{\bar{Q}}\right]^{-1} \begin{bmatrix} \bar{E}^{inc} \\ \bar{H}^{inc} \end{bmatrix} \tag{4.2.40}$$

Equation (4.2.40) is the final form of the Foldy-Lax multiple scatter equations derived from Maxwell's equations where the matrix $\bar{\bar{P}}$ is calculated using Huygen's principle and $\bar{\bar{Q}}$ is calculated using the BOR technique.

After the final exciting fields are solved, they are substituted into Equation (4.2.39) to find the equivalent surface currents from which the absorption can be calculated.

Using Huygen's principle, the scattered fields from the vegetation canopy are obtained from the surface currents by superposition of the scattered fields from all the cylinders. Let the observation point be at $\bar{r}_o$. Following the derivations for $\bar{\bar{P}}$ above, the same equations as (4.2.25) and (4.2.26) for scattered fields are obtained except replacing $\bar{r}_j$ by $\bar{r}_o$. In matrix form, the final scattered fields at $\bar{r}_o$ from all the cylinders are

$$\bar{E}^s(\bar{r}_o) = \bar{\bar{S}}^E(\bar{r}_o)\begin{bmatrix} \bar{J} \\ \bar{M} \end{bmatrix} \tag{4.2.41a}$$

$$\bar{H}^s(\bar{r}_o) = \bar{\bar{S}}^H(\bar{r}_o)\begin{bmatrix} \bar{J} \\ \bar{M} \end{bmatrix} \tag{4.2.41b}$$

where $\bar{\bar{S}}^E(\bar{r}_o) = [\bar{\bar{s}}^E_{o,1}, \ldots, \bar{\bar{s}}^E_{o,Ntot}]$ with each $\bar{\bar{s}}^E_{o,j} = 2\pi a_j \Delta z_j \begin{bmatrix} i\omega\mu_0 \bar{G}_{z,oj} & \bar{0} & -\bar{F}_{z,oj} & \bar{0} \end{bmatrix}$ being a 3×4 matrix and $\bar{\bar{S}}^H(\bar{r}_o) = [\bar{\bar{s}}^H_{o,1}, \ldots, \bar{\bar{s}}^H_{o,Ntot}]$ with each $\bar{\bar{s}}^H_{o,j} = 2\pi a_j \Delta z_j \begin{bmatrix} \bar{F}_{z,oj} & \bar{0} & i\omega\varepsilon_0 \bar{G}_{z,oj} & \bar{0} \end{bmatrix}$ being a 3×4 matrix. The expressions for $\bar{G}_{z,oj}$ and $\bar{F}_{z,oj}$ are the same as those for $\bar{G}_{z,ij}$ and $\bar{F}_{z,ij}$ except replacing $\bar{r}_j$ by $\bar{r}_o$.

(b) Review of Key Derivations of Foldy-Lax Equations and BOR

Foldy-Lax Equations

The detail derivations can be found in sections 1 and 2 of chapter 5 in [30] and a brief derivation using operator notation following the methods in [30] is presented here.

Considering N_L scatterers, the Maxwell's equations give [4, 30]

$$\bar{\bar{G}} = \bar{\bar{G}}_0 + \sum_{n=1}^{N_L} \bar{\bar{G}}_0 \bar{\bar{U}}_n \bar{\bar{G}} \tag{4.2.42}$$

where $\bar{\bar{G}}$ is the exact Green's function for the problem, $\bar{\bar{G}}_0$ is the unperturbed Green's function and $\bar{\bar{U}}_n$ is the scattering potential for scatterer *n*.

Then,

$$\bar{\bar{G}} = \bar{\bar{G}}_0 + \sum_{\substack{n=1 \\ n\neq m}}^{N_L} \bar{\bar{G}}_0 \bar{\bar{U}}_n \bar{\bar{G}} + \bar{\bar{G}}_0 \bar{\bar{U}}_m \bar{\bar{G}} \tag{4.2.43}$$

Next, define

$$\bar{\bar{G}}_m = \bar{\bar{G}}_0 + \sum_{\substack{n=1 \\ n\neq m}}^{N_L} \bar{\bar{G}}_0 \bar{\bar{U}}_n \bar{\bar{G}} \tag{4.2.44}$$

Then equation (4.2.43) becomes

$$\bar{\bar{G}} = \bar{\bar{G}}_m + \bar{\bar{G}}_0 \bar{\bar{U}}_m \bar{\bar{G}} \tag{4.2.45}$$

Multiply both sides of equation (4.2.45) by $\bar{\bar{U}}_m$,

$$\bar{\bar{U}}_m \bar{\bar{G}} = \bar{\bar{U}}_m \bar{\bar{G}}_m + \bar{\bar{U}}_m \bar{\bar{G}}_0 \bar{\bar{U}}_m \bar{\bar{G}} \tag{4.2.46}$$

Then,

$$\left(\bar{\bar{I}} - \bar{\bar{U}}_m \bar{\bar{G}}_0\right) \bar{\bar{U}}_m \bar{\bar{G}} = \bar{\bar{U}}_m \bar{\bar{G}}_m \tag{4.2.47}$$

Thus,

$$\bar{\bar{U}}_m \bar{\bar{G}} = \left(\bar{\bar{I}} - \bar{\bar{U}}_m \bar{\bar{G}}_0\right)^{-1} \bar{\bar{U}}_m \bar{\bar{G}}_m \tag{4.2.48}$$

Since the transition operator for scatterer *m* [4, 30] is

$$\bar{\bar{T}}_m = \left(\bar{\bar{I}} - \bar{\bar{U}}_m \bar{\bar{G}}_0\right)^{-1} \bar{\bar{U}}_m \tag{4.2.49}$$

Substituting equation (4.2.49) to (4.2.48) leads to

$$\bar{\bar{U}}_m \bar{\bar{G}} = \bar{\bar{T}}_m \bar{\bar{G}}_m \tag{4.2.50}$$

Substituting it into equation (4.2.44), then

$$\bar{\bar{G}}_m = \bar{\bar{G}}_0 + \sum_{\substack{n=1 \\ n\neq m}}^{N_L} \bar{\bar{G}}_0 \bar{\bar{T}}_n \bar{\bar{G}}_n \tag{4.2.51}$$

Applying source state to equation (4.2.51) [4, 30]

$$\bar{E}_m^{ex} = \bar{\bar{G}}_m |\bar{J}\rangle \tag{4.2.52a}$$

$$\bar{E}^{inc} = \bar{\bar{G}}_0 |\bar{J}\rangle \tag{4.2.52a}$$

We obtain

$$\bar{E}_m^{ex} = \bar{E}_m^{inc} + \sum_{\substack{n=1 \\ n\neq m}}^{N_L} \bar{\bar{G}}_0 \bar{\bar{T}}_n \bar{E}_n^{ex} \tag{4.2.53}$$

Since $\bar{\bar{G}}_0 \bar{\bar{T}}_n \bar{E}_n^{ex} = \bar{E}_n^{scat}$ is the scattered field from scatterer *n*, equation (4.2.53) becomes

$$\bar{E}_m^{ex} = \bar{E}_m^{inc} + \sum_{\substack{n=1 \\ n\neq m}}^{N_L} \bar{E}_n^{scat} \tag{4.2.54}$$

Equation (4.2.54) is the Foldy-Lax multiple scattering equations which states that the final exciting field on scatterer *m* is the sum of incident wave and the scattered waves from all other scatterers except *m* itself. It is to be noted that in the derivations of (4.2.54) above, no approximations were made.

Body of Revolution (BOR) Method

The detail derivations can be found in [12, 92],and brief derivation is summarized here.

EFIE:

$$\begin{aligned} -\hat{n}\times\bar{E}^{inc}(\bar{r}) &= i\omega\hat{n}\times\int dS'\left[\mu_1 g_1\left(\bar{r},\bar{r}'\right)+\mu_2 g_2\left(\bar{r},\bar{r}'\right)\right]\bar{J}_S\left(\bar{r}'\right) \\ &+\frac{i}{\omega}\hat{n}\times\int_P dS'\nabla\left[\frac{g_1\left(\bar{r},\bar{r}'\right)}{\varepsilon_1}+\frac{g_2\left(\bar{r},\bar{r}'\right)}{\varepsilon_2}\right]\nabla'_S\cdot\bar{J}_S\left(\bar{r}'\right) \\ &-\hat{n}\times\left[\int_P dS'\nabla\left[g_1\left(\bar{r},\bar{r}'\right)+g_2\left(\bar{r},\bar{r}'\right)\right]\times\bar{M}_S\left(\bar{r}'\right)\right] \end{aligned} \tag{4.2.55}$$

MFIE:

$$
\begin{aligned}
-\hat{n}\times\bar{H}^{inc}(\bar{r}) &= i\omega\hat{n}\times\int dS'\left[\varepsilon_1 g_1\left(\bar{r},\bar{r}'\right)+\varepsilon_2 g_2\left(\bar{r},\bar{r}'\right)\right]\bar{M}_S\left(\bar{r}'\right)\\
&+\frac{i}{\omega}\hat{n}\times\int_P dS'\nabla\left[\frac{g_1\left(\bar{r},\bar{r}'\right)}{\mu_1}+\frac{g_2\left(\bar{r},\bar{r}'\right)}{\mu_2}\right]\nabla'_S\cdot\bar{M}_S\left(\bar{r}'\right)\\
&+\hat{n}\times\int_P dS'\nabla\left[g_1\left(\bar{r},\bar{r}'\right)+g_2\left(\bar{r},\bar{r}'\right)\right]\times\bar{J}_S\left(\bar{r}'\right)
\end{aligned}
\tag{4.2.56}
$$

The surface electric and magnetic currents are expanded using the basis function as blow,

$$
\bar{J}_S(\bar{r})=\sum_{\alpha=-\infty}^{\infty}\sum_{n=1}^{N}\left(I_{\alpha n}^{Jt}f_n(t)e^{-i\alpha\phi}\hat{t}(\bar{r})-I_{an}^{J\phi}f_n(t)e^{-i\alpha\phi}\hat{\phi}(\bar{r})\right) \tag{4.2.57}
$$

$$
\bar{M}_S(\bar{r})=\sum_{\alpha=-\infty}^{\infty}\sum_{n=1}^{N}\left(I_{\alpha n}^{Mt}g_n(t)e^{-i\alpha\phi}\hat{t}(\bar{r})-I_{an}^{M\phi}g_n(t)e^{-i\alpha\phi}\hat{\phi}(\bar{r})\right) \tag{4.2.58}
$$

where $I_{\alpha n}^{Jt}$, $I_{an}^{J\phi}$, $I_{\alpha n}^{Mt}$ and $I_{an}^{M\phi}$ are the unknown coefficients for n[th] basis function and order α. $f_n(t)$ and $g_n(t)$ are the basis functions. It is noted that $f_n(t)$ and $g_n(t)$ are 1-D basis function with discretization only in the $\hat{t}$ direction. Because of rotational symmetry of the object, the function of ϕ is expanded into Fourier series. In this chapter, we let $f_n(t)=g_n(t)=\dfrac{T_n(t)}{\rho(t)}$.

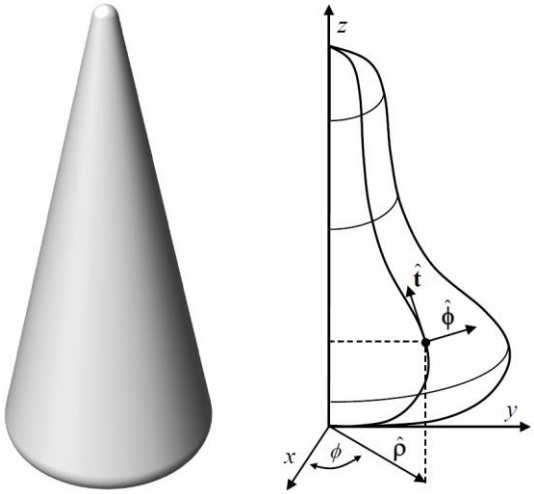

Figure IV.4. Definition of $\hat{t}$ and $\hat{\phi}$ in BOR (picture from [12, 92]).

The unit vectors in the t and ϕ directions are

$$\hat{t} = \sin\gamma\cos\phi\hat{x} + \sin\gamma\sin\phi\hat{y} + \cos\gamma\hat{z} \tag{4.2.59}$$

$$\hat{\phi} = -\sin\phi\hat{x} + \cos\phi\hat{y} \tag{4.2.60}$$

where $\sin\gamma = \dfrac{\dfrac{d\rho}{dz}}{\sqrt{1+\left(\dfrac{d\rho}{dz}\right)^2}}$ and $\cos\gamma = \dfrac{1}{\sqrt{1+\left(\dfrac{d\rho}{dz}\right)^2}}$.

Then, the following properties can be derived,

$$\begin{aligned}
&\hat{\phi}\cdot\hat{t}' = \sin\gamma'\sin\left(\phi'-\phi\right)\\
&\hat{t}\cdot\hat{\phi}' = -\sin\gamma\sin\left(\phi'-\phi\right)\\
&\hat{t}\cdot\hat{t}' = \sin\gamma\sin\gamma'\cos\left(\phi'-\phi\right)+\cos\gamma\cos\gamma'\\
&\hat{\phi}\cdot\hat{\phi}' = \cos\left(\phi'-\phi\right)
\end{aligned} \tag{4.2.61}$$

Also, the derivatives can be derived,

$$\begin{aligned}
&\frac{\partial\hat{\phi}}{\partial t} = 0\\
&\frac{\partial\hat{t}}{\partial t} = \frac{\dfrac{d^2\rho}{dz^2}}{\left[1+\left(\dfrac{d\rho}{dz}\right)^2\right]^2}\left[-\frac{d\rho}{dz}\hat{z}+\hat{\rho}\right]\\
&\frac{\partial\hat{\phi}}{\partial\phi} = -\cos\phi\hat{x}-\sin\phi\hat{y} = -\hat{\rho}\\
&\frac{\partial\hat{t}}{\partial\phi} = \frac{1}{\sqrt{1+\left(\dfrac{d\rho}{dz}\right)^2}}\left[\frac{d\rho}{dz}\right]\hat{\phi}
\end{aligned} \tag{4.2.62}$$

Using these properties, the following manipulations on the Green's function are calculated as

$$\hat{\phi}\cdot\nabla g = -\rho'\sin\left(\phi'-\phi\right)\frac{dg}{dR}\frac{1}{R} \tag{4.2.63}$$

$$\hat{t}\cdot\nabla g=\left[\left(\rho-\rho'\cos\left(\phi'-\phi\right)\right)\sin\gamma+\left(z-z'\right)\cos\gamma\right]\frac{dg}{dR}\frac{1}{R} \tag{4.2.64}$$

$$\hat{n}\cdot\nabla g=\frac{1}{R}\frac{dg}{dR}\left[\rho\cos\gamma-\rho'\cos\gamma\cos\left(\phi'-\phi\right)-\sin\gamma\left(z-z'\right)\right] \tag{4.2.65}$$

where $R=\sqrt{\left(x-x'\right)^2+\left(y-y'\right)^2+\left(z-z'\right)^2}$, and $g\left(\bar{r},\bar{r}'\right)=g(R)$.

Next, let

$$\bar{J}_S\left(\bar{r}'\right)=\hat{\phi}'J_{S\phi}\left(\bar{r}'\right)+\hat{t}'J_{St}\left(\bar{r}'\right) \tag{4.2.59}$$

$$\bar{M}_S\left(\bar{r}'\right)=\hat{\phi}'M_{S\phi}\left(\bar{r}'\right)+\hat{t}'M_{St}\left(\bar{r}'\right) \tag{4.2.60}$$

where the subscript 'ϕ' means the current in the ϕ direction while the subscript 't' means the current in the *t* direction.

The *t* component of the EFIE can be calculated as

$$E_t^{inc}(\bar{r})=\beta_{11}\left(J_{St}\right)+\beta_{12}\left(J_{S\phi}\right)+\beta_{13}\left(M_{St}\right)+\beta_{14}\left(M_{S\phi}\right) \tag{4.2.61}$$

where,

$$\begin{aligned}\beta_{11}\left(J_{St}\right)=&-i\omega\int dS'\left[\mu g\left(\bar{r},\bar{r}'\right)+\mu_1 g_1\left(\bar{r},\bar{r}'\right)\right]\left[\left(\sin\gamma\sin\gamma'\cos\left(\phi'-\phi\right)+\cos\gamma\cos\gamma'\right)J_{St}\left(\bar{r}'\right)\right]\\&-\frac{i}{\omega}\int dS'\left[\left[\frac{1}{\varepsilon}\hat{t}\cdot\nabla g\left(\bar{r},\bar{r}'\right)+\frac{1}{\varepsilon_1}\hat{t}\cdot\nabla g_1\left(\bar{r},\bar{r}'\right)\right]\right]\left[\frac{1}{\rho'}\frac{\partial}{\partial t'}\left(\rho'J_{St}\left(\bar{r}'\right)\right)\right]\end{aligned} \tag{4.2.62}$$

$$\begin{aligned}\beta_{12}\left(J_{S\phi}\right)=&\,i\omega\int dS'\left[\mu g\left(\bar{r},\bar{r}'\right)+\mu_1 g_1\left(\bar{r},\bar{r}'\right)\right]\left[\sin\gamma\sin\left(\phi'-\phi\right)J_{S\phi}\left(\bar{r}'\right)\right]\\&-\frac{i}{\omega}\int dS'\left[\frac{1}{\varepsilon}\hat{t}\cdot\nabla g\left(\bar{r},\bar{r}'\right)+\frac{1}{\varepsilon_1}\hat{t}\cdot\nabla g_1\left(\bar{r},\bar{r}'\right)\right]\frac{1}{\rho'}\left(\frac{\partial}{\partial\phi'}J_{S\phi}\left(\bar{r}'\right)\right)\end{aligned} \tag{4.2.63}$$

$$\beta_{13}\left(M_{St}\right)=\int dS'\begin{bmatrix}\rho\cos\gamma\sin\gamma'\sin\left(\phi'-\phi\right)\\-\rho'\sin\gamma\cos\gamma'\sin\left(\phi'-\phi\right)\\-\left(z-z'\right)\sin\gamma'\sin\gamma\sin\left(\phi'-\phi\right)\end{bmatrix}\frac{1}{R}\frac{d\left(g(R)+g_1(R)\right)}{dR}M_{St}\left(\bar{r}'\right) \tag{4.2.64}$$

$$\beta_{14}\left(M_{S\phi}\right)=\int dS'\left\{\cos\gamma\left[\rho\cos\left(\phi'-\phi\right)-\rho'\right]-\left(z-z'\right)\sin\gamma\cos\left(\phi'-\phi\right)\right\}\times\frac{1}{R}\frac{d\left[g(R)+g_1(R)\right]}{dR}M_{S\phi}\left(\bar{r}'\right) \tag{4.2.65}$$

The ϕ component of EFIE is calculated as

$$E_{\phi}^{inc}(\bar{r})=\beta_{21}\left(J_{St}\right)+\beta_{22}\left(J_{S\phi}\right)+\beta_{23}\left(M_{St}\right)+\beta_{24}\left(M_{S\phi}\right) \tag{4.2.66}$$

where,

$$\beta_{21}\left(J_{St}\right)=-i\omega\int dS'\left[\mu g\left(\bar{r},\bar{r}'\right)+\mu_1 g_1\left(\bar{r},\bar{r}'\right)\right]\left(\hat{\phi}\cdot\hat{t}'\right)J_{St}\left(\bar{r}'\right)-\frac{i}{\omega}\int dS'\left[\frac{1}{\varepsilon}\hat{\phi}\cdot\nabla g\left(\bar{r},\bar{r}'\right)+\frac{1}{\varepsilon_1}\hat{\phi}\cdot\nabla g_1\left(\bar{r},\bar{r}'\right)\right]\frac{1}{\rho'}\frac{\partial}{\partial t'}\left(\rho' J_{St}\left(\bar{r}'\right)\right) \tag{4.2.67}$$

$$\beta_{22}\left(J_{S\phi}\right)=-i\omega\int dS'\left[\mu g\left(\bar{r},\bar{r}'\right)+\mu_1 g_1\left(\bar{r},\bar{r}'\right)\right]\left(\hat{\phi}\cdot\hat{\phi}'\right)J_{S\phi}\left(\bar{r}'\right)-\frac{i}{\omega}\int dS'\left[\frac{1}{\varepsilon}\hat{\phi}\cdot\nabla g\left(\bar{r},\bar{r}'\right)+\frac{1}{\varepsilon_1}\hat{\phi}\cdot\nabla g_1\left(\bar{r},\bar{r}'\right)\right]\frac{1}{\rho'}\left(\frac{\partial}{\partial\phi'}J_{S\phi}\left(\bar{r}'\right)\right) \tag{4.2.68}$$

$$\beta_{23}\left(M_{St}\right)=\int dS'\left[\frac{1}{R}\frac{dg(R)}{dR}+\frac{1}{R}\frac{dg_1(R)}{dR}\right]\begin{bmatrix}\left(-\rho+\rho'\cos\left(\phi'-\phi\right)\right)\cos\gamma'\\+\left(z-z'\right)\sin\gamma'\cos\left(\phi'-\phi\right)\end{bmatrix}M_{St}\left(\bar{r}'\right) \tag{4.2.69}$$

$$\beta_{24}\left(M_{S\phi}\right)=\int dS'\left[\frac{1}{R}\frac{dg(R)}{dR}+\frac{1}{R}\frac{dg_1(R)}{dR}\right]\left[-\sin\left(\phi'-\phi\right)\left(z-z'\right)\right]M_{S\phi}\left(\bar{r}'\right) \tag{4.2.70}$$

Next, let the testing function be

$$f_{\beta m}^{t}(\bar{r})=f_n(t)e^{i\beta\phi}\hat{t}(\bar{r}) \tag{4.2.71}$$

$$\bar{f}_{\beta m}^{\phi}(\bar{r})=f_n(t)e^{i\beta\phi}\hat{\phi}(\bar{r}) \tag{4.2.72}$$

Substituting the basis function and the testing function leads to

$$\int dS f_m(t)e^{i\beta\phi}\beta_{11}\left(J_{St}\right)=\sum_{\alpha=-\infty}^{\infty}\sum_{n=1}^{N}L_{mn}^{tt(E)}I_{\alpha n}^{Jt} \tag{4.2.73a}$$

$$\int dSf_m(t)e^{i\beta\phi}\beta_{12}\left(J_{St}\right)=\sum_{\alpha=-\infty}^{\infty}\sum_{n=1}^{N}L_{mn}^{t\phi(E)}I_{\alpha n}^{I\phi} \tag{4.2.73b}$$

$$\int dSf_m(t)e^{i\beta\phi}\beta_{13}\left(M_{St}\right)=\sum_{\alpha=-\infty}^{\infty}\sum_{n=1}^{N}K_{mn}^{tt(E)}I_{\alpha n}^{Mt} \tag{4.2.73c}$$

$$\int dSf_m(t)e^{i\beta\phi}\beta_{14}\left(M_{S\phi}\right)=\sum_{\alpha=-\infty}^{\infty}\sum_{n=1}^{N}K_{mn}^{t\phi(E)}I_{\alpha n}^{M\phi} \tag{4.2.73d}$$

where,

$$L_{mn}^{tt(E)}=\int dt\int dt'\int_0^{2\pi}d\phi\int_0^{2\pi}d\phi'\begin{bmatrix}-i\omega\left[\mu g\left(\bar{r},\bar{r}'\right)+\mu_1 g_1\left(\bar{r},\bar{r}'\right)\right]T_m(t)T_n\left(t'\right)\hat{t}\cdot\hat{t}'\\+\dfrac{i}{\omega}\left(\dfrac{1}{\varepsilon}g+\dfrac{1}{\varepsilon_1}g_1\right)T_m'(t)T_n'\left(t'\right)\end{bmatrix}e^{i\beta\phi}e^{-i\alpha\phi'} \tag{4.2.74}$$

$$L_{mn}^{t\phi(E)}=\int dt\int dt'\int_0^{2\pi}d\phi\int_0^{2\pi}d\phi'\begin{bmatrix}i\omega T_m(t)T_n\left(t'\right)\left(\mu g+\mu_1 g_1\right)\hat{t}\cdot\hat{\phi}'\\-\dfrac{\alpha}{\omega\rho\left(t'\right)}T_m'(t)T_n\left(t'\right)\left(\dfrac{g}{\varepsilon}+\dfrac{g_1}{\varepsilon_1}\right)\end{bmatrix}e^{i\beta\phi}e^{-i\alpha\phi'} \tag{4.2.75}$$

$$K_{mn}^{tt(E)}=\int dt\int dt'\int_0^{2\pi}d\phi\int_0^{2\pi}d\phi'\begin{bmatrix}\rho\cos\gamma\sin\gamma'\sin\left(\phi'-\phi\right)\\-\rho'\sin\gamma\cos\gamma'\sin\left(\phi'-\phi\right)\\-\left(z-z'\right)\sin\gamma'\sin\gamma\sin\left(\phi'-\phi\right)\end{bmatrix}\frac{1}{R}\frac{d\left(g(R)+g_1(R)\right)}{dR}T_m(t)T_n\left(t'\right)e^{i\beta\phi}e^{-i\alpha\phi'} \tag{4.2.76}$$

$$K_{mn}^{t\phi(E)}=-\int dt\int dt'\int_0^{2\pi}d\phi\int_0^{2\pi}d\phi'\left\{\cos\gamma\left[\rho\cos\left(\phi'-\phi\right)-\rho'\right]-\left(z-z'\right)\sin\gamma\cos\left(\phi'-\phi\right)\right\}\frac{1}{R}\frac{d\left[g(R)+g_1(R)\right]}{dR}\left[T_m(t)T_n\left(t'\right)\right]e^{i\beta\phi}e^{-i\alpha\phi'} \tag{4.2.77}$$

The integrations can be calculated following [12, 92].

Thus,

$$\sum_{\alpha=-\infty}^{\infty}\sum_{n=1}^{N}\left(L_{mn}^{tt(E)}I_{\alpha n}^{Jt}+L_{mn}^{t\phi(E)}I_{\alpha n}^{J\phi}+K_{mn}^{tt(E)}I_{\alpha n}^{Mt}+K_{mn}^{t\phi(E)}I_{\alpha n}^{M\phi}\right)=\int dSf_m(t)e^{i\beta\phi}E_t^{inc}(\bar{r}) \tag{4.2.78}$$

Similar manipulations are performed for the ϕ component of EFIE.

$$\sum_{\alpha=-\infty}^{\infty}\sum_{n=1}^{N}\left(L_{mn}^{\phi t(E)}I_{\alpha n}^{Jt}+L_{mn}^{\phi\phi(E)}I_{\alpha n}^{J\phi}+K_{mn}^{\phi t(E)}I_{\alpha n}^{Mt}+K_{mn}^{\phi\phi(E)}I_{\alpha n}^{M\phi}\right)=\int dSf_m(t)e^{i\beta\phi}E_{\phi}^{inc}(\bar{r}) \tag{4.2.79}$$

Using duality property, the equations for MFIE are obtained.

The integrations of $\int_0^{2\pi} d\phi' e^{i\beta\phi}e^{-i\alpha\phi'}$ gives $\delta_{\alpha\beta}$ which results in $\alpha=\beta$.

Finally, in matrix form,

$$\begin{bmatrix} \overline{\overline{L}}_{\alpha}^{tt(E)} & \overline{\overline{L}}_{\alpha}^{t\phi(E)} & \overline{\overline{K}}_{\alpha}^{tt(E)} & \overline{\overline{K}}_{\alpha}^{t\phi(E)} \\ \overline{\overline{L}}_{\alpha}^{\phi t(E)} & \overline{\overline{L}}_{\alpha}^{\phi\phi(E)} & \overline{\overline{K}}_{\alpha}^{\phi t(E)} & \overline{\overline{K}}_{\alpha}^{\phi\phi(E)} \\ -\overline{\overline{K}}_{\alpha}^{tt(M)} & -\overline{\overline{K}}_{\alpha}^{t\phi(M)} & \overline{\overline{L}}_{\alpha}^{tt(M)} & \overline{\overline{L}}_{\alpha}^{t\phi(M)} \\ -\overline{\overline{K}}_{\alpha}^{\phi t(M)} & -\overline{\overline{K}}_{\alpha}^{\phi\phi(M)} & \overline{\overline{L}}_{\alpha}^{\phi t(M)} & \overline{\overline{L}}_{\alpha}^{\phi\phi(M)} \end{bmatrix} \begin{bmatrix} \overline{I}_{\alpha}^{Jt} \\ \overline{I}_{\alpha}^{J\phi} \\ \overline{I}_{\alpha}^{Mt} \\ \overline{I}_{\alpha}^{M\phi} \end{bmatrix} = \begin{bmatrix} \int dt\int_0^{2\pi} d\phi T_m(t)e^{i\alpha\phi}E_t^{inc}(\bar{r}) \\ \int dt\int_0^{2\pi} d\phi T_m(t)e^{i\alpha\phi}\ E_{\phi}^{inc}(\bar{r}) \\ \int dt\int_0^{2\pi} d\phi T_m(t)e^{i\alpha\phi}H_t^{inc}(\bar{r}) \\ \int dt\int_0^{2\pi} d\phi T_m(t)e^{i\alpha\phi}H_{\phi}^{inc}(\bar{r}) \end{bmatrix} \tag{4.2.80}$$

where the superscript '*(E)*' stands for EFIE while '*(M)*' stands for MFIE.

The formulas for the matrix components are available in [12, 92]. The square matrix in equation (4.2.80) is the *Z* matrix using in the FL-BOR calculations.

4.3 FL-BOR Compared with HFSS and FL-ICA

First, we calculate the absorption of two and five cylinders in clusters at C-band (5.4 GHz) as shown in Figure IV.5 (a) and (b), respectively.

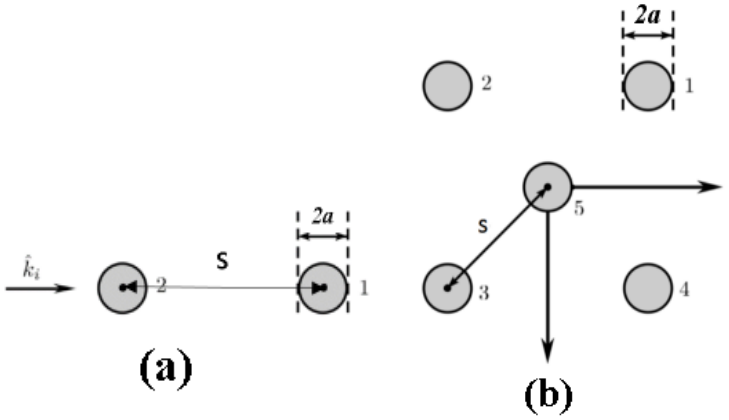

Figure IV.5. Top view of the Cylinders.

Typical parameters for grass are used with 1mm radius, 30cm length and permittivity of 30.7+5.5i. The incident angle is 90^o. The averaged absorption cross section of each cylinder for different spacing between the cylinders (s) is presented in Table IV-1. The absorption cross section for a single isolated cylinder without the existence of other cylinders is $1.1 \times 10^{-3}\ m^2$. According to the results from FL-BOR, when the spacing between the cylinders is 0.5 cm (~0.09λ), the averaged absorption cross section is about 35% and 63% less than that of a single isolated cylinder. This means that the internal fields of the cylinder changes when there are other cylinders close by. HFSS is also used to simulate the two cases for comparison. The results for the two cylinders' cluster are also presented in Table IV-1, which compare well with the FL-BOR results with no more than $10^{-4}\ m^2$ error. For the five cylinders' cluster, only the case of s=1cm is simulated on HFSS for the sake of time saving. The result is $0.88 \times 10^{-3}\ m^2$ which compares well with the result of $0.83 \times 10^{-3}\ m^2$ from FL-BOR. The ratio between the averaged absorption cross section of two cylinders and the absorption cross section of a single cylinder without the other cylinder is plotted in Figure IV.6. Three methods are used: FL-BOR, MoM and HFSS. It is observed that the results of the three methods compared where. It also can be seen that the absorption cross section of the cylinder changes significantly when there is another cylinder close by. Thus, the assumption in RTE/DBA that the absorption cross section of a cylinder is unchanged with the existence of the other cylinders is inaccurate.

In terms of the computation time, our FL-BOR code is much faster than HFSS. The FL-BOR codes used 266s and 267s while HFSS used 1080s and 4942s CPU time for the two cylinders' cluster and five cylinders' cluster, respectively. The CPU time required by HFSS increases significantly when the number of cylinders increases. This means HFSS is not suitable for simulations of vegetation layer which contains a large number of cylinders.

Table IV-1. Averaged absorption cross section (m^2) of each cylinder for different spacing s for two cases: (a) two cylinders and (b) five cylinders in a cluster.

	s(cm)	0.5	1	2	4	5
(a)	FL-BOR (10^{-3})	0.72	1.0	1.4	1.1	1.2
	HFSS (10^{-3})	0.82	1.1	1.5	1.1	1.3
(b)	FL-BOR (10^{-3})	0.41	0.83	1.0	0.70	0.75

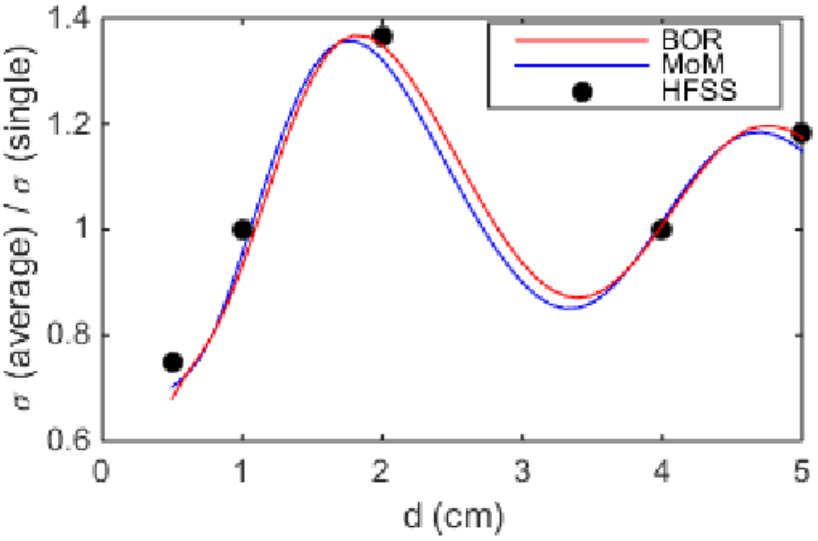

Figure IV.6. Comparisons of the ratio between the averaged absorption cross section of two cylinders and the absorption cross section when only one cylinder exists using three methods: FL-BOR, MoM and HFSS.

The Foldy-Lax multiple scattering equations and infinite cylinder approximation (ICA) were combined (FL-ICA) previously for scattering by vertical cylinders [93, 94]. The approach was later applied to scattering by a rice canopy [71, 72]. In the approach [93, 94], the dyadic Green's function and the fields including incident, exciting, internal and scattered fields are expanded in terms of vector cylindrical waves. The ICA is used to calculate the scattering by each cylinder. An iterative method is used to solve the unknown coefficients of the internal fields. An integration over dk_z is used to represent the fields in various oblique directions. In the integration of dk_z from minus infinity to infinity, evanescent waves in ρ are also included. Here, the results

from the first-order FL-ICA and FL-BOR are compared. The interactions between different cylinders are not taken into account in the first-order solutions.

Following the methods in [93, 94], the first-order solution for FL-ICA is briefly derived here.

The scattered fields of the vegetation at the observation points is the sum of all the scattered fields from all the *NL* cylinders modelling the vegetation particles.

$$\overline{E}^{s}\left(\overline{r}_{o}\right)=\sum_{j=1}^{NL}\overline{E}_{j}^{s}\left(\overline{r}_{o}\right) \tag{4.3.1}$$

where $\bar{r}_o$ is the location of the observation point.

Let the center of the *jth* cylinder be $\bar{r}_j=\left(x_j,y_j,z_j\right)$. Using Huygen's principle [4], the scattered fields from the *jth* cylinder are

$$\overline{E}_{j}^{s}\left(\overline{r}_{o}\right)=\int_{-L/2+z_j}^{L/2+z_j}dz\int_{0}^{2\pi}d\phi_{\rho\rho_j}a\begin{Bmatrix}i\omega\mu\hat{\rho}_{\rho\rho_j}\times\bar{H}_{j}^{p}\left(\overline{r}\right)\bullet\bar{\bar{G}}_{o}\left(\overline{r},\overline{r}_{o}\right)+\\ \hat{\rho}_{\rho\rho_j}\times\bar{E}_{j}^{p}\left(\overline{r}\right)\bullet\nabla\times\bar{\bar{G}}_{o}\left(\overline{r},\overline{r}_{o}\right)\end{Bmatrix} \tag{4.3.2}$$

where $\phi_{\rho\rho_j}$ and $\rho_{\rho\rho_j}$ are polar coordinates with center at $\bar{\rho}_j=x_j\hat{x}+y_j\hat{y}$. L and a are the length and radius of the cylinder, respectively. $\bar{\bar{G}}_0$ is the free space Green's function. $\bar{H}_j^p(\bar{r})$ and $\bar{E}_j^p(\bar{r})$ are the internal magnetic and electric fields of the *jth* cylinder.

Using the infinite cylinder approximation (ICA) [4], the internal fields are expressed in terms of vector cylindrical waves:

$$\bar{E}_j^p(\bar{r})=\sum_{n'=-\infty}^{\infty}\int_{-\infty}^{\infty}dk_z'\begin{bmatrix}c_{n',j}^{(M)}(k_z')\cdot Rg\bar{M}_{n'}\left(k_{p\rho}',k_z',\bar{r}-\bar{r}_j\right)\\ +c_{n',j}^{(N)}(k_z')\cdot Rg\bar{N}_{n'}\left(k_{p\rho}',k_z',\bar{r}-\bar{r}_j\right)\end{bmatrix} \tag{4.3.3}$$

$$i\omega\mu\bar{H}_j^p(\bar{r})=\sum_{n'=-\infty}^{\infty}k_p\int_{-\infty}^{\infty}dk_z'\begin{bmatrix}c_{n',j}^{(M)}(k_z')\cdot Rg\bar{N}_{n'}\left(k_{p\rho}',k_z',\bar{r}-\bar{r}_j\right)\\ +c_{n',j}^{(N)}(k_z')\cdot Rg\bar{M}_{n'}\left(k_{p\rho}',k_z',\bar{r}-\bar{r}_j\right)\end{bmatrix} \tag{4.3.4}$$

where k_p is the wavenumber inside the cylinder and $k'_{p\rho} = \sqrt{k_p^2 - k_z'^2}$. $c_{n',j}^{(M)}(k'_z)$ and $c_{n',j}^{(N)}$ are the unknown coefficients and will be calculated later. $Rg\bar{M}_{n'}$ and $Rg\bar{N}_{n'}$ are vector cylindrical waves calculated as [4]

$$Rg\bar{M}_n(k_\rho, k_z, \bar{r}) = Rg\bar{m}_n(k_\rho, k_z, \bar{\rho})e^{ik_z z + in\phi} \tag{4.3.5}$$

$$Rg\bar{N}_n(k_\rho, k_z, \bar{r}) = Rg\bar{n}_n(k_\rho, k_z, \bar{\rho})e^{ik_z z + in\phi} \tag{4.3.6}$$

with

$$Rg\bar{m}_n(k_\rho, k_z, \bar{\rho}) = \hat{\rho}\frac{in}{\rho}J_n(k_\rho\rho) - \hat{\phi}k_\rho J_n'(k_\rho\rho) \tag{4.3.7}$$

$$Rg\bar{n}_n(k_\rho, k_z, \bar{\rho}) = \hat{\rho}\frac{ik_\rho k_z}{k}J_n'(k_\rho\rho) - \hat{\phi}\frac{nk_z}{k\rho}J_n(k_\rho\rho) + \hat{z}\frac{k_\rho^2}{k}J_n(k_\rho\rho) \tag{4.3.8}$$

The vector cylindrical waves have the relation that

$$\nabla \times Rg\bar{M}_n(k_\rho, k_z, \bar{r}) = kRg\bar{N}_n(k_\rho, k_z, \bar{r}) \tag{4.3.9}$$

$$\nabla \times Rg\bar{N}_n(k_\rho, k_z, \bar{r}) = kRg\bar{M}_n(k_\rho, k_z, \bar{r}) \tag{4.3.10}$$

where $k = \sqrt{k_\rho^2 + k_z^2}$.

The free space Green's function $\bar{\bar{G}}_0$ can also be expanded using vector cylindrical waves centered at $\bar{r}_j$ as [4]

$$\bar{\bar{G}}_0(\bar{r}, \bar{r}') = -\frac{\hat{z}\hat{z}}{k_o^2}\delta(\bar{r} - \bar{r}') + \frac{i}{4\pi}\int_0^\infty dk_\rho \frac{1}{k_z k_\rho}\sum_{n=-\infty}^{\infty}(-1)^n \cdot$$

$$\begin{cases} Rg\bar{M}_n(k_\rho, k_z, \bar{r})Rg\bar{M}_{-n}(k_\rho, -k_z, \bar{r}') + \\ \quad Rg\bar{N}_n(k_\rho, k_z, \bar{r})Rg\bar{N}_{-n}(k_\rho, -k_z, \bar{r}') \end{cases} for\ z > z'$$

$$\begin{cases} Rg\bar{M}_n(k_\rho, -k_z, \bar{r})Rg\bar{M}_{-n}(k_\rho, k_z, \bar{r}') + \\ \quad Rg\bar{N}_n(k_\rho, -k_z, \bar{r})Rg\bar{N}_{-n}(k_\rho, k_z, \bar{r}') \end{cases} for\ z < z' \tag{4.3.11}$$

Next, equations (4.3.3), (4.3.4) and (4.3.11) are substituted into equation (4.3.2). Since we calculate the scattered fields below the vegetation canopy, we choose the Green's function expansion for $\bar{\bar{G}}_0(\bar{r},\bar{r}_o)$ which satisfies $z_o > z$. The final scattered fields are

$$\bar{E}_j^s(\bar{r}_o) = \sum_{n'=-\infty}^{\infty}\left(-\frac{L_j}{\pi}\right)\int_{-\infty}^{\infty}dk_z'\int_0^{\infty}dk_\rho\,\frac{k_\rho}{k_z}e^{\left(i(k_z'+k_z)(z_j+d)\right)}sinc\left((k_z'+k_z)\frac{L_j}{2}\right)\cdot$$

$$\left\{\begin{array}{l} Rg\bar{M}_{n'}\left(k_\rho,k_z,\bar{r}_o-\bar{r}_j\right)\left[\begin{array}{l} c_{n',j}^{(M)}(k_z')RgA_{n'}^{MM}\left(k_\rho,k_z,k_{p\rho}',k_z',a_j\right) \\ +c_{n',j}^{(N)}(k_z')RgA_{n'}^{MN}\left(k_\rho,k_z,k_{p\rho}',k_z',a_j\right)\end{array}\right] \\ +Rg\bar{N}_{n'}\left(k_\rho,k_z,\bar{r}_o-\bar{r}_j\right)\left[\begin{array}{l} c_{n',j}^{(M)}(k_z')RgA_{n'}^{NM}\left(k_\rho,k_z,k_{p\rho}',k_z',a_j\right) \\ +c_{n',j}^{(N)}(k_z')RgA_{n'}^{NN}\left(k_\rho,k_z,k_{p\rho}',k_z',a_j\right)\end{array}\right]\end{array}\right\} \tag{4.3.12}$$

where

$$RgA_{n'}^{MM}\left(k_\rho,k_z,k_{p\rho}',k_z',a\right) = -\frac{ia\pi}{2k_\rho^2}\left[k_{p\rho}'^2k_\rho J_n\left(k_{p\rho}'a\right)J_n'\left(k_\rho a\right) - k_{p\rho}'k_\rho^2J_n'\left(k_{p\rho}'a\right)J_n\left(k_\rho a\right)\right]$$

$$RgA_{n'}^{MN}\left(k_\rho,k_z,k_{p\rho}',k_z',a\right) = -\frac{ia\pi}{2k_\rho^2}\left[\frac{n}{k_\rho a}\left(k_{p\rho}'^2k_z - k_z'k_\rho^2\right)J_n\left(k_{p\rho}'a\right)J_n\left(k_\rho a\right)\right]$$

$$RgA_{n'}^{NM}\left(k_\rho,k_z,k_{p\rho}',k_z',a\right) = -\frac{ia\pi}{2k_\rho^2}\left[\frac{n}{ka}\left(k_{p\rho}'^2k_z - k_z'k_\rho^2\right)J_n\left(k_{p\rho}'a\right)J_n\left(k_\rho a\right)\right]$$

$$RgA_{n'}^{NN}\left(k_\rho,k_z,k_{p\rho}',k_z',a\right) = -\frac{ia\pi}{2k_\rho^2}\left[\frac{kk_\rho}{k_\rho}k_{p\rho}'^2J_n\left(k_{p\rho}'a\right)J_n'\left(k_\rho a\right) - \frac{k_\rho k_{p\rho}'}{k}k_\rho^2J_n'\left(k_{p\rho}'a\right)J_n\left(k_\rho a\right)\right]$$

For the first-order solution [94],

$$c_{n',j}^{(M)}(k_z') = c_{n',j}^{(M)}(-k_{iz})\delta(k_z'+k_{iz}) \tag{4.3.13}$$

$$c_{n',j}^{(N)}(k_z') = c_{n',j}^{(N)}(-k_{iz})\delta(k_z'+k_{iz}) \tag{4.3.14}$$

where $c_{n',j}^{(M)}(-k_{iz})$ and $c_{n',j}^{(N)}(-k_{iz})$ are obtained using ICA for a single cylinder [39]. After substituting equations (4.3.13) and (4.3.14) to (4.3.12), the first-order scattered fields from cylinder *j* are

$$\bar{E}_j^s(\bar{r}_o) = \sum_{n'=-\infty}^{\infty}\left(-\frac{L_j}{\pi}\right)\int_0^{\infty} dk_\rho \frac{k_\rho}{k_z} e^{\left(i(-k_{iz}+k_z)(z_j+d)\right)} sinc\left((-k_{iz}+k_z)\frac{L_j}{2}\right)$$

$$\cdot\left\{ Rg\bar{M}_{n'}\left(k_\rho, k_z, \bar{r}_o - \bar{r}_j\right)\begin{bmatrix} c_{n',j}^{(M)}(-k_{iz}) RgA_{n'}^{MM}\left(k_\rho, k_z, k'_{p\rho}, -k_{iz}, a_j\right) \\ +c_{n',j}^{(N)}(-k_{iz}) RgA_{n'}^{MN}\left(k_\rho, k_z, k'_{p\rho}, -k_{iz}, a_j\right)\end{bmatrix}\right.$$

$$\left. + Rg\bar{N}_{n'}\left(k_\rho, k_z, \bar{r}_o - \bar{r}_j\right)\begin{bmatrix} c_{n',j}^{(M)}(-k_{iz}) RgA_{n'}^{NM}\left(k_\rho, k_z, k'_{p\rho}, -k_{iz}, a_j\right) \\ +c_{n',j}^{(N)}(-k_{iz}) RgA_{n'}^{NN}\left(k_\rho, k_z, k'_{p\rho}, -k_{iz}, a_j\right)\end{bmatrix}\right\} \tag{4.3.15}$$

Finally, the first-order scattered fields from all the cylinders are obtained by substituting equation (4.3.15) to (4.3.1).

For the first-order FL-BOR, equation (4.2.15) becomes

$$\bar{E}_m^{ex,1st} = \bar{E}_m^{inc} \tag{4.3.16}$$

The first-order exciting fields are substituted into equation (4.2.39) to find the surface currents without the calculations of $\bar{\bar{P}}$. The final scattered electric fields are obtained from equation (4.2.41a). We compute the scattered fields form the vegetation canopy consisting of extended cylinders randomly and uniformly distributed 1 m^2 area, as shown inFigure IV.1.. Typical parameters for grass are used with 1mm radius, 30cm length and permittivity of 30.7+5.5i. All the cylinders are vertically oriented. The center of the lower boundary of the vegetation layer is $\bar{r}_{c,bottom} = [0.5\ m, 0.5\ m, -d]$ where *d* is the layer thickness and is the same as the cylinder length in this case. First, we compare the scattered near fields computed from FL-BOR and FL-ICA. 64 cylinders are used. The observation point is chosen to be 4 cm below the vegetation layer (i.e., the z component of the observation point $z_o = -d - 0.04\ m$) and $y_o = 0.5\ m$. The scattered field $|\bar{E}^s|/|\bar{E}^{inc}|$ at different x_o (x component of the observation point) computed from first-order FL-

BOR and FL-ICA are presented in Figure IV.7. The results are in good agreement. Next, the scattered fields in the far field, f_{vv} are calculated from $\bar{E}^s$

$$f_{vv} = \lim_{|\bar{r}_o|\to\infty} [\bar{E}^s(\bar{r}_o) \cdot \hat{v}(\bar{r}_o)]/[\exp(ik|\bar{r}_o|)/|\bar{r}_o|] \tag{4.3.17}$$

where the incident field is normalized to one.

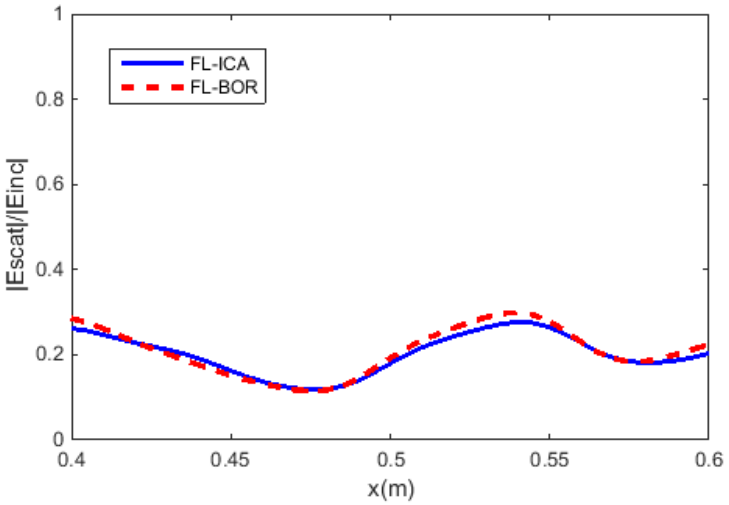

Figure IV.7. Near fields comparison between FL-ICA and FL-BOR with observation points at 4cm below the vegetation layer and the y component of the observation positions is 0.5 m.

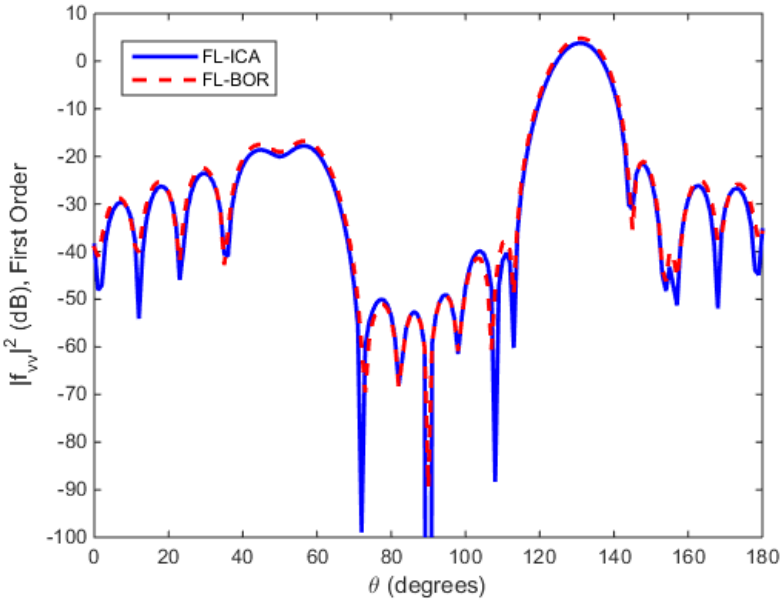

Figure IV.8. Far fields comparison between first-order FL-ICA and FL-BOR. The angle θ is shown in Figure IV.1.

The same parameters of the cylinders are used as before with 100 cylinders for simulation. The observation point is chosen to be far away so that $|\bar{r}_o - \bar{r}_c| = 500\lambda$, with $\bar{r}_c = [0.5\,m, 0.5\,m, -d/2]$ being the center of the vegetation layer. $\bar{r}_o$ is also chosen to be below the vegetation layer and in the x-z plane. The results for $|f_{vv}|^2$ from both FL-ICA and FL-BOR are plotted in Figure IV.8. The scattering angle θ is the angle between $\bar{r}_o - \bar{r}_c$ and $-\hat{x}$, as shown in Figure IV.1. It can be seen that the first-order FL-ICA results are in agreement with those from the first-order FL-BOR.

4.4 Simulation of Transmission, Reflection, Absorption and Field Profile

4.4.1 Simulation Procedures

We use Monte Carlo simulations to calculate the transmission, reflection and absorption of a vegetation canopy composed of dielectric cylinders. For each realization, a large number of cylinders, such as 500, are generated. For each realization, the solutions of electromagnetic fields and equivalent surface currents on the cylinders are calculated by using FL-BOR. The FL-BOR calculations are repeated for each realization. For the calculations of transmission and reflection (Figure IV.1 and Figure IV.2), we use a receiver of area of one square wavelength to calculate the power received in reflection and transmission. In numerical simulations in this section, we simulate this scenario by fixing the position of the receiver and shuffling the positions of the cylinders from realization to realization. The receiver is fixed at the center below the layer for transmission and at the center above the layer for reflection (Figure IV.1 and Figure IV.2).

(a) Transmission through the Vegetation Canopy

We first calculate the power received by the receiver of one square wavelength in size. The "receiver" is put at 1cm below the center of the bottom boundary of the vegetation canopy. Thus,

the center of the "receiver" is at $\bar{r}_{cb} = [L/2, L/2, -d - 0.01]$ where $L \times L$ is the area occupied by the cylinders. The intensity transmitted downward at the observation point $\bar{r}_o$ is

$$I_t(\bar{r}_o) = \frac{1}{2} Re[\bar{E}^{tot}(\bar{r}_o) \times \left(\bar{H}^{tot}(\bar{r}_o)\right)^*] \cdot (-\hat{z}) \tag{4.4.1}$$

$$\text{with, } \bar{E}^{tot}(\bar{r}_o) = \bar{E}^{inc}(\bar{r}_o) + \sum_{n=1}^{N_L} \bar{E}_n^{scat}(\bar{r}_o) \tag{4.4.2a}$$

$$\bar{H}^{tot}(\bar{r}_o) = \bar{H}^{inc}(\bar{r}_o) + \sum_{n=1}^{N_L} \bar{H}_n^{scat}(\bar{r}_o) \tag{4.4.2b}$$

where the superscript 'tot' denotes the total field, which is the sum of the incident and the scattered fields from all the cylinders. The scattered fields are calculated from FL-BOR using equations (4.2.41a) and (4.2.41b).

The transmitted Poynting vector at the observation point $\bar{r}_o$ is defined as

$$T_{s,p} = \frac{I_t(\bar{r}_o)}{I_{inc}(\bar{r}_o)} = \frac{\bar{S}^{tot}(\bar{r}_o) \cdot (-\hat{z})}{\bar{S}^{inc}(\bar{r}_o) \cdot (-\hat{z})} \tag{4.4.3}$$

where $\bar{S}^{tot}(\bar{r}_o)$ and $\bar{S}^{inc}(\bar{r}_o)$ are the total and incident Poynting vector, respectively.

We next consider an area of $\lambda \times \lambda$ to define transmission as follows.

$$T_s = \iint_{\lambda^2} I_t \Big/ \iint_{\lambda^2} I_{inc} \tag{4.4.4}$$

T_s is the normalized transmitted power received by a $\lambda \times \lambda$ "receiver" put right below the center of the vegetation layer (Figure IV.1 and Figure IV.2) which is normalized by the incident intensity. The transmission t for the vegetation canopy is obtained after averaging over all N_r realizations:

$$t_\beta(\theta_i) = \langle T_s \rangle = \left(\sum_{N_r} T_s\right)/N_r \tag{4.4.5}$$

where β is the incident polarization and θ_i is the incident angle. T_s is the normalized transmitted power at each realization. The number of realizations N_r is chosen to be large enough so that t converges. It is to be noted that the transmission is calculated by solving the Foldy-Lax equations without the need of defining nor calculating the attenuation rate per unit distance κ_e.

(b) Optical Thickness τ from NMM3D Simulations

Since NMM3D only calculates transmission, we define τ in NMM3D as

$$\tau_{NMM3D} = -cos\theta_i \ln(t) \tag{4.4.6}$$

where θ_i is the incident angle.

(c) Electric Field Profile inside the Vegetation Canopy

Using FL-BOR, we can calculate the total fields anywhere including inside the vegetation canopy. The electric field profile inside the vegetation canopy is the absolute value of the total electric field of the vegetation canopy. Because the vegetation layer is horizontally statistical invariant, we choose the center line as indicated by the red dashed line in Figure IV.1. From the profile, we can observe the change of the total electric field as the wave propagates through the vegetation canopy. The magnitude of the electric field $\langle|\bar{E}^{tot}(z)|\rangle$ is averaged over N_r realizations

$$\langle|\bar{E}^{tot}(z)|\rangle = \left(\sum_{N_r}|\bar{E}^{tot}(z)|\right)/N_r \tag{4.4.7}$$

where z is from $z = 0$ to $z = -d$ since the observation point is inside the vegetation canopy. The x and y component of the observation point are both at $L/2$. The electric field is that of outside the cylinder.

The realizations where there is a cylinder located on the center axis are discarded because this corresponds to fields inside the cylinder and not outside the cylinder. The probability for the point to fall inside the cylinder is low since the volume fraction of the scatterers in the vegetation fields is low (0.20% for the extended-cylinders case). Thus only a few realizations are discarded.

(d) Reflection from the Vegetation Canopy

The $\lambda \times \lambda$ "receiver"is placed 1cm above the center of the upper boundary of the vegetation layer, as shown in Figure IV.1 and Figure IV.2 highlighted using purple. (i.e., the $\lambda \times \lambda$

"receiver" is centered at $\bar{r}_{cu} = [L/2, L/2, 0.01]$). Using the idea of shuffling the cylinders instead of moving the "receiver", the reflection *r* is averaged over realizations

$$r_\beta(\theta_i) = \langle R_s \rangle \tag{4.4.8}$$

$$\text{where, } R_s = \frac{\iint_{\lambda^2} \bar{S}_s(\bar{r}_o)\cdot(\hat{z})}{\iint_{\lambda^2} \bar{S}_{inc}(\bar{r}_o)\cdot(-\hat{z})} \tag{4.4.9}$$

$\bar{S}_s(\bar{r}_o)$ is the Poynting vector of the scattered energy, defined as $\frac{1}{2}Re[\bar{E}^{scat}(\bar{r}_o) \times \left(\bar{H}^{scat}(\bar{r}_o)\right)^*]$ where $\bar{E}^{scat}$ and $\bar{H}^{scat}$ are the scattered electric and magnetic fields which are the sum of the scattered fields from all the cylinders as calculated in equation (4.2.41). It is noticed that the scattered fields are used instead of the total fields since the reflection comes from the scattering by the scatters inside the vegetation canopy. $\bar{S}_s(\bar{r}_o) \cdot (\hat{z})$ calculates the intensity going up at $\bar{r}_o$ which is the reflected intensity.

(e) Absorption by the Vegetation Cano

Absorption is the power absorbed by all the cylinders in the vegetation canopy. The power absorbed by a cylinder is [39]

$$P_a = \frac{1}{2}\omega\varepsilon_c'' \iiint dv \left|\bar{E}^{int}\right|^2 \tag{4.4.10}$$

where ε_c'' is the imaginary part of the permittivity of the cylinder and $\bar{E}^{int}$ is the internal electric field. Since the radius of the cylinder is small, we approximate the internal electric field by the surface electric field whose magnitude is the same as that of the surface magnetic current. Then,

$$P_a = \frac{1}{2}\omega\varepsilon_c'' \sum_{j=1}^{N_S} \pi a_j^2 \Delta z_j \left|\bar{M}_j\right|^2 \tag{4.4.11}$$

where $\pi a_j^2 \Delta z_j$ is the volume of section *j* and $\bar{M}_j$ is the surface magnetic current of section *j* calculated in FL-BOR.

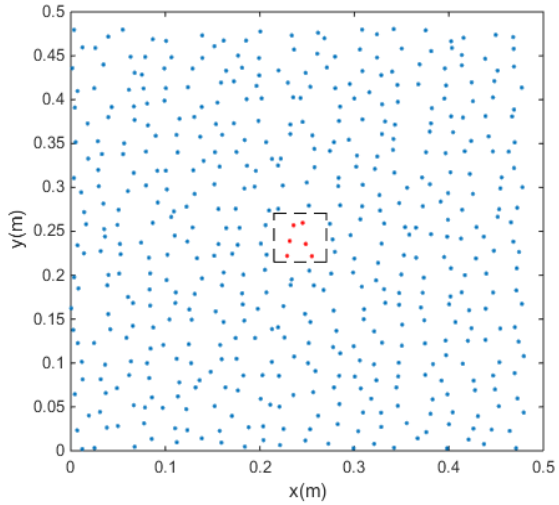

Figure IV.9. Cylinders inside the center $\lambda \times \lambda$ area (red).

Next, the averaged absorption for each cylinder inside the center $\lambda \times \lambda$ area (Figure IV.9) in the vegetation canopy is obtained by averaging over many realizations. Finally, the absorption by the vegetation canopy ($a_\beta(\theta_i)$) is the total number of cylinders multiplied by the averaged absorption for each cylinder, and then normalized by the incident power,

$$a_\beta(\theta_i) = \frac{N_L \langle P_a \rangle}{\iint_S \bar{S}_{inc}(\bar{r}_o)\cdot(-\hat{z})} \tag{4.4.12}$$

where N_L is the total number of cylinders simulated, $\langle P_a \rangle$ is the averaged absorption for each cylinder over many realizations, and S is the simulated area.

(f) Emissivity of the Vegetation Canopy

In passive microwave remote sensing, the brightness temperature T_B at angle θ_i for polarization β is [2]

$$T_{B,\beta}(\theta_i) = e_\beta(\theta_i)T \tag{4.4.13}$$

where $e_\beta(\theta_i)$ is the emissivity at angle θ_i for polarization β. T is the physical temperature.

The emissivity is equal to one minus the integration of bistatic scattering and transmission of the vegetation canopy over hemispherical solid angles. In the NMM3D simulations of transmission and reflection described previously, the transmission and reflection "receivers" capture all the bistatic transmission and scattering. Thus, the present simulation procedure does not require angular integrations. Then the emissivity of the vegetation canopy is

$$e_\beta(\theta_i) = 1 - t_\beta(\theta_i) - r_\beta(\theta_i) = a_\beta(\theta_i) \tag{4.4.14}$$

where the transmissivity $t_\beta(\theta_i)$ is given by equation (4.4.5), reflectivity $r_\beta(\theta_i)$ is given by equation (4.4.8) and absorption $a_\beta(\theta_i)$ is given by equation (4.4.12).

4.4.2 Simulation Results

In this section, the NMM3D simulation results for the cases of extended cylinders and short cylinders are presented. The simulations are at C-band (5.4 GHz) with V-polarized incident wave, that is $\beta = V$ and incidence angle θ_i is 40 degrees.

(a) NMM3D Simulation Results of Transmission and Comparison with EP/DBA/RTE

The extended-cylinders case

The density of the cylinders in the vegetation canopy is set at 2122 per m^2, corresponding to vegetation water content (VWC) 1kg/m^2 which is a typical value for grass fields. Note that for such cases the average spacing between cylinders is less than half a wavelength. We compute results for 100 and 500 cylinders (N_L). They occupy an area (S) of 0.217×0.217 m^2 and 0.485×0.485 m^2, respectively. The side length of the area needed for simulation should be at least $2dtan\theta_i$, where d is the height of the vegetation layer, as illustrated in Figure IV.10.

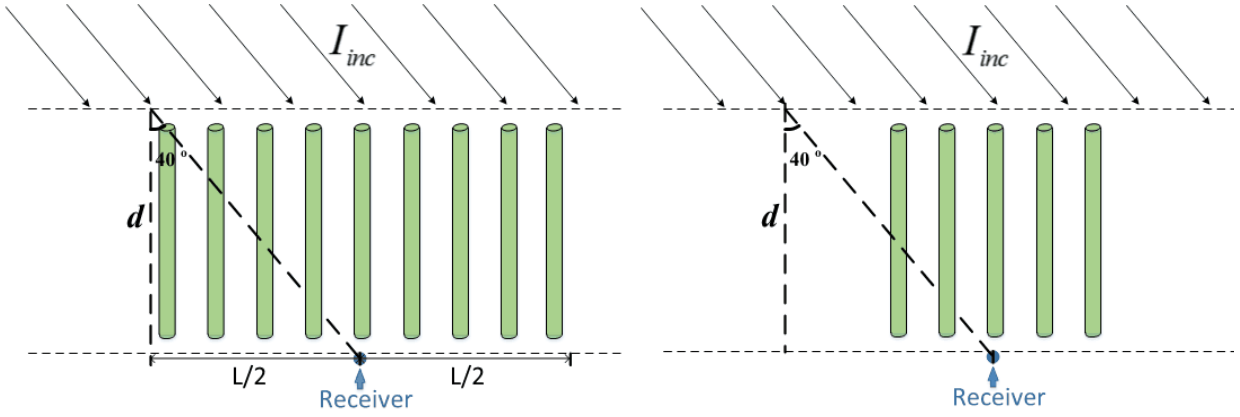

(a) (b)

Figure IV.10. Illustration of simulation area needed for NMM3D, $\theta_i = 40^o$ in this case.

The parameters for the cylinders are the same as those used in section 4.3. The layer thickness d is 0.3 m which is the same as the cylinders' lengths. Two distributions are simulated: one is uniformly distributed and the other is distributed in clusters with five cylinders per cluster, as shown in Figure IV.11 (a) and (b), respectively. Figure IV.11 (c) shows the top view of a cylinder cluster for the clustered case.

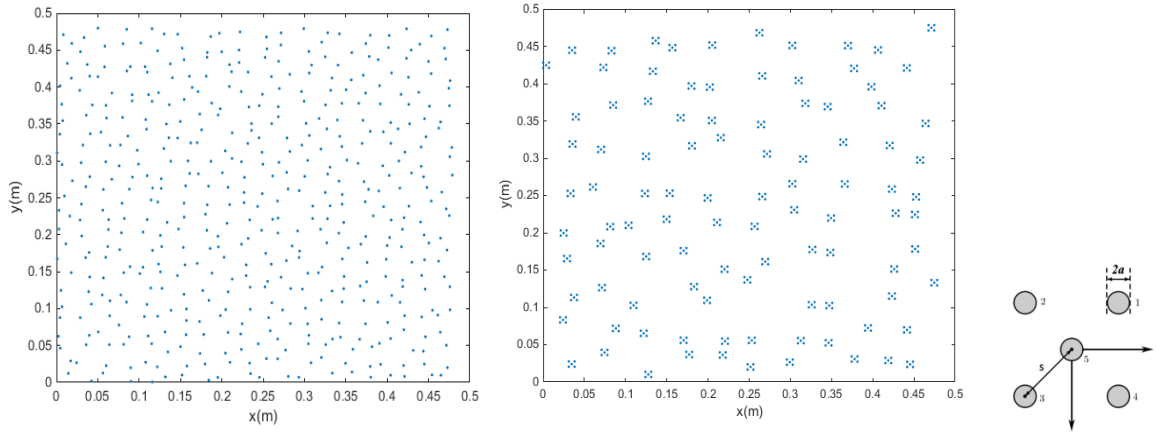

(a) (b) (c)

Figure IV.11. Positions of the 500 cylinders on the x-y plane in one realization for (a) uniformly distributed case, (b) clustered case. The scale of both axes is meter. (c) Top view of a cylinder cluster composed of five cylinders with radius a. The separation s is 0.5 cm for each cluster.

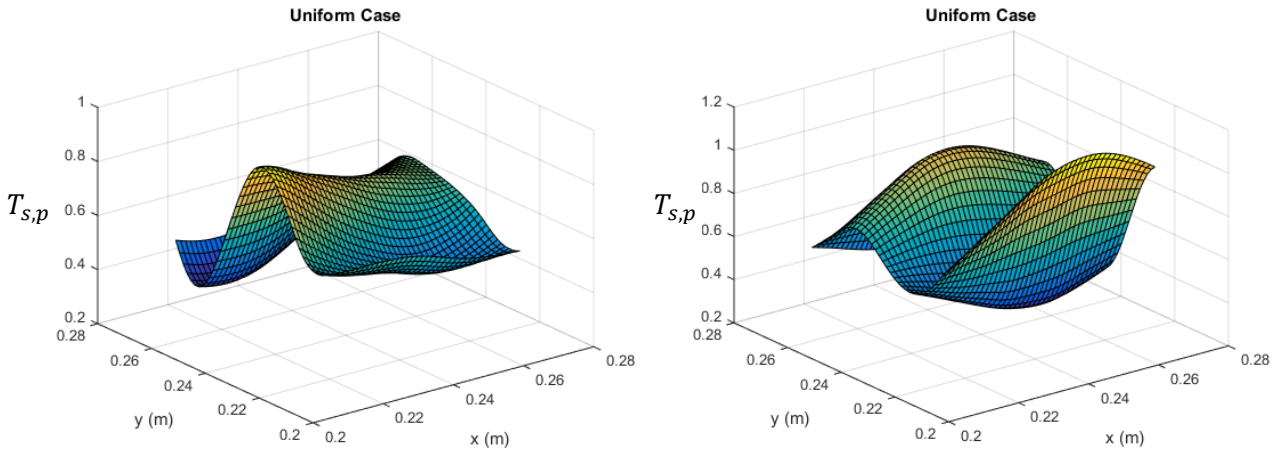

(a) (b)

Figure IV.12. Transmitted Poynting vector at different observation points within an area $\lambda \times \lambda$ centered at $\bar{r}_{cb}$ for two realizations of the uniformly distributed 500 cylinders.

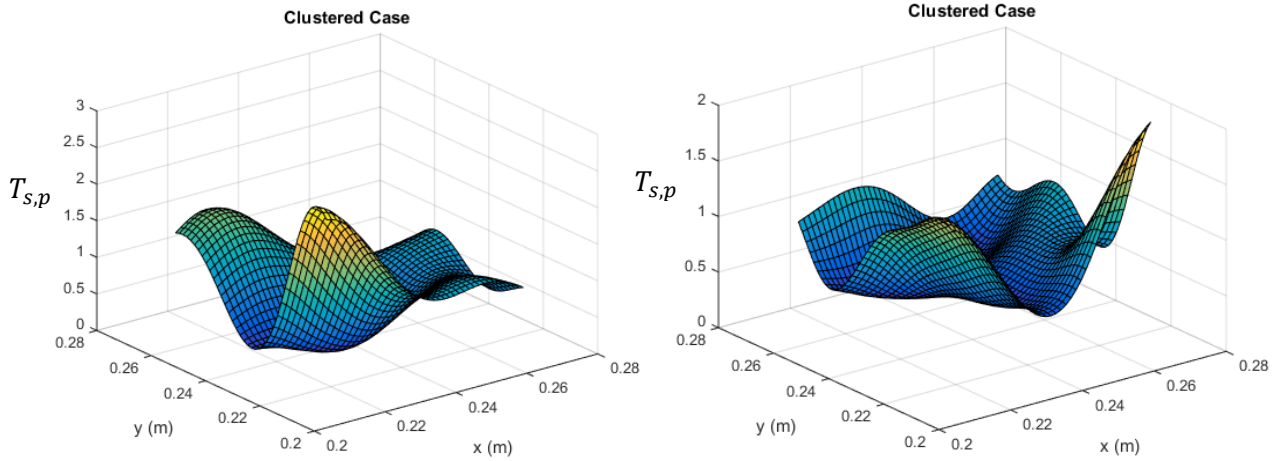

(a) (b)

Figure IV.13. Transmitted Poynting vector at different observation points within an area $\lambda \times \lambda$ centered at $\bar{r}_{cb}$ for two realizations of the clustered distributed 500 cylinders.

The transmitted Poynting vector $T_{s,p}$ defined in equation (4.4.3) at different observation points within an area $\lambda \times \lambda$ centered at $\bar{r}_{cb}$ for two realizations using 500 cylinders are shown in Figure IV.12 and Figure IV.13 for the uniform distribution and clustered distribution, respectively. Note that the transmitted Poynting vector can be larger than unity, because of constructive or destructive interferences of the scattered waves from all the cylinders and the incident wave

(speckle fluctuations). It can be seen that the transmitted Poynting vector fluctuates significantly over the $\lambda \times \lambda$ area. The figure shows that the transmitted Poynting vector in the clustered case fluctuates more than that in the uniform case. This is because the scattered field at the point right below one cluster composed of five cylinders is significantly different from that at the point not below the cluster. In comparison, the fluctuations of the scattered field are less for the uniform case.

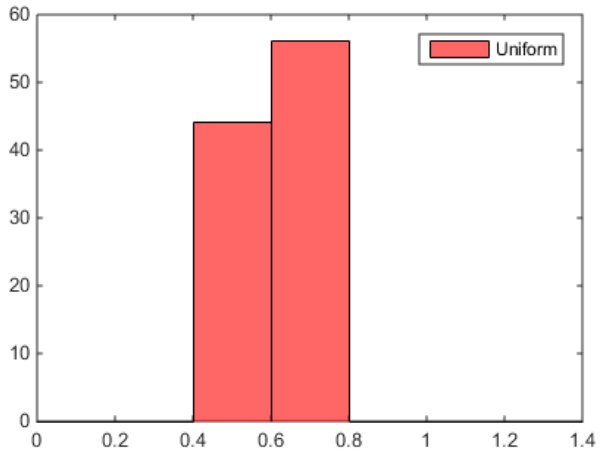

T_s

(a)

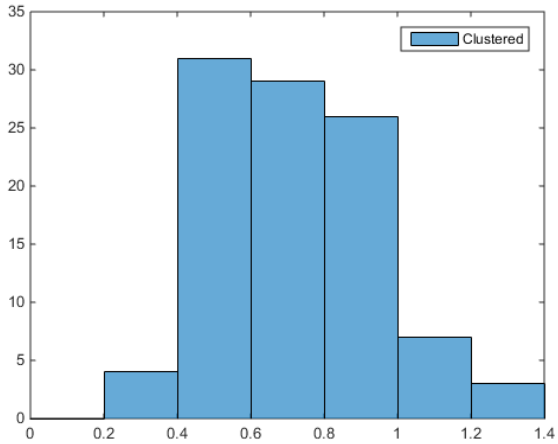

T_s

(b)

Figure IV.14. T_s (power received by the "receiver" below the vegetation canopy) for 100 realizations for the extended-cylinders case using 500 cylinders for simulation: (a) Histogram of T_s for the uniform distribution, (b) Histogram of T_s for the clustered distribution.

Figure IV.14 (a) and (b) show histograms of the, for 100 realizations. It is observed that for the clustered case, T_s has larger fluctuation between realizations than it has for the uniform case. For the simulation using 100 cylinders, the standard deviation of T_s is 0.2017 for the clustered case and 0.0591 for the uniform case. For the simulation using 500 cylinders, the standard deviation of T_s is 0.2144 for the clustered case and 0.0385 for the uniform case. The T_s for each realization is also plotted in Figure IV.15. It can be seen that the transmission for the clustered case has larger fluctuation between realizations than that for the uniform case, as expected. Results are convergent after 100 realizations. The results of transmission t using NMM3D simulations are listed in Table IV-2. For the uniform case, t is 0.6874 and 0.6124 for the 100-cylinders simulations and 500-cylinders simulations, respectively. For the clustered case, t is 0.7527 and 0.7044 for the 100-cylinders simulations and 500-cylinders simulations, respectively. Comparing the NMM3D results for the 100-cylinders and 500-cylinders simulations, there are small differences. A larger number of cylinders with a larger area will be studied in the future to study the sensitivity due to variations of the number of cylinders.

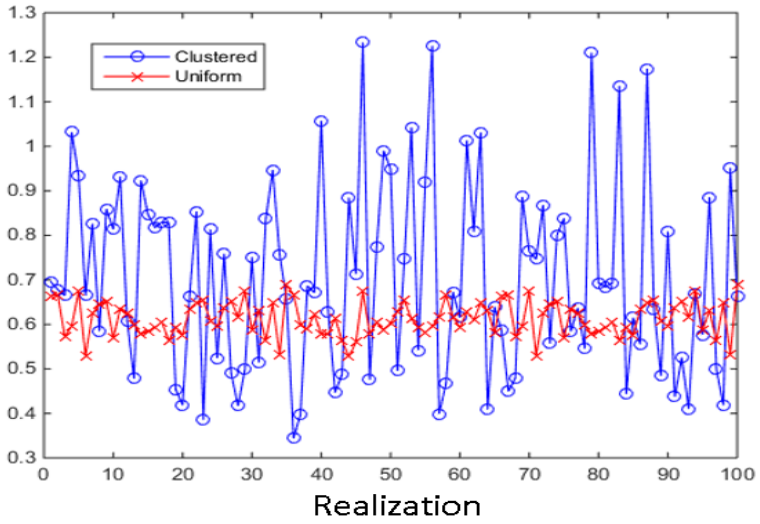

Figure IV.15. T_s for each realization for the clustered case (blue) and uniform case (red).

Table IV-2. Transmission through vegetation layer for the extended-cylinders case with uniform and clustered distributions computed from EP/DBA/RTE and NMM3D simulations. 100 cylinders and 500 cylinders are used in NMM3D simulations.

Cylinder No.	L (m) (Area=L^2)	EP/DBA/RTE	NMM3D Uniform	NMM3D Clustered
100	0.217	0.1722	0.6874	0.7527
500	0.485	0.1722	0.6124	0.7044

For comparison, the transmission through the vegetation canopy is also calculated using EP/DBA/RTE using equation (4.2.8). The extinction κ_e is calculated using equation (4.2.4) and the standard procedures are used to calculate n_0, and σ_a and σ_s for one cylinder [2, 39, 87, 88]. The κ_e is calculated to be 4.4914m^{-1} and thus the transmission computed from EP/DBA/RTE is 0.1722 which is also listed in Table IV-2. It can be seen that the transmissions from NMM3D simulations of the 500 cylinders are 3.56 times (5.51 dB) and 4.09 times (6.12 dB) larger than that from EP/DBA/RTE, for the uniform distribution and clustered distribution, respectively. Thus, the attenuation of EP/DBA/RTE is much larger than that of NMM3D for the case of extended cylinders.

In EP/DBA/RTE, $\tau = \kappa_e d$. The values for τ are tabulated in Table IV-3. The results for the extended-cylinders case show that τ_{NMM3D} from NMM3D 500-cylinders simulations are 3.6 and 5.0 times smaller than the τ from EP/DBA/RTE for the uniform distribution and clustered distribution, respectively.

Table IV-3. Values of the optical thickness τ from EP/DBA/RTE and NMM3D simulations for the extended-cylinders case.

Cylinder No.	EP/DBA/RTE	NMM3D Uniform	NMM3D Clustered
100	1.347	0.2871	0.2176
500	1.347	0.3756	0.2684

The short-cylinders case

NMM3D full-wave simulations are next applied to the short-cylinders case as shown in Figure IV.2 where the short thin cylinders are uniformly distributed in 3D in the vegetation layer. There are 720 cylinders in total. The average spacing between the cylinders is about 10cm (~1.8λ). The simulation area is $1\text{m} \times 1\text{m}$. The radius and length of the cylinders are 1mm and 3cm, respectively. The total vegetation canopy height is 60cm and the incident angle is 40^o. The histogram of the averaged transmitted Poynting T_s for 100 realizations is presented in Figure IV.16. The standard deviation of T_s is 0.0188. The computed transmission t through vegetation layer using NMM3D is 0.9097. In EP/DBA/RTE, κ_e is calculated to be 0.1368m^{-1} and thus the transmission is 0.8984 as calculated using equation (4.2.9). The results for transmission from NMM3D simulations and EP/DBA/RTE agree with each other for the case of short cylinders.

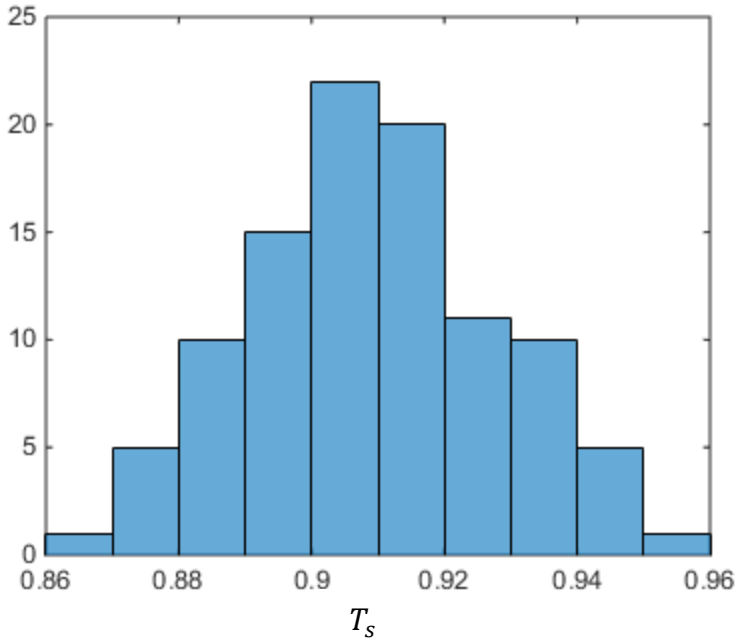

Figure IV.16. The histogram of T_s (power received by the "receiver" below the vegetation canopy) for 100 realizations for the short-cylinders case.

The optical thickness τ_{NMM3D} from NMM3D simulations is 0.0725. In comparison τ from EP/DBA/RTE is 0.0821, which is close to that from NMM3D.

(b) Electric Field Profile Simulations

The profiles for the extended-cylinders case from NMM3D simulations and EP/DBA/RTE are plotted in Figure IV.17. For EP/DBA/RTE, the absolute values of the total effective electric fields inside the vegetation canopy is

$$\left|\bar{E}_{eff}^{tot}(\bar{r}_o)\right| = exp\left(-\frac{1}{2}\kappa_e|z_o|sec\theta_i\right) \tag{4.4.15}$$

where z_o is the z component of the observation point $\bar{r}_o$.

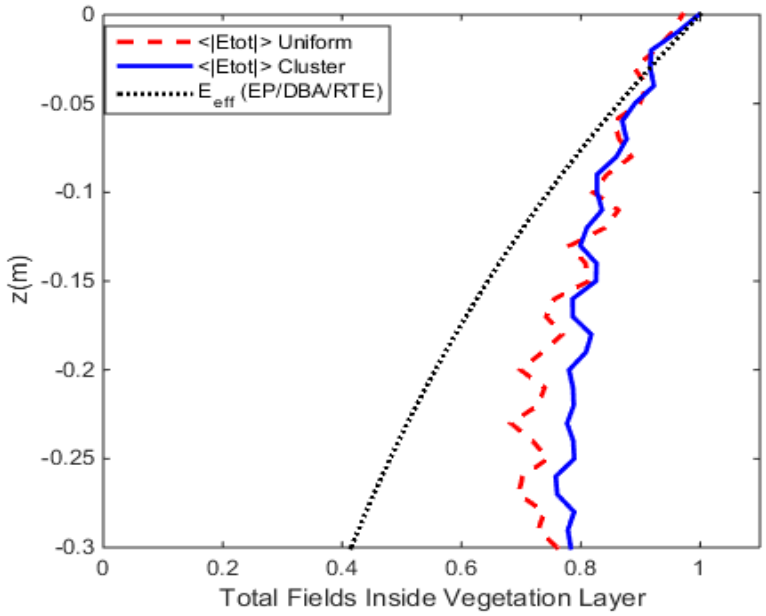

Figure IV.17. Profile of the averaged total field inside the vegetation canopy composed of extended cylinders. The red-dash line is for NMM3D simulations using uniform distribution, blue line is for NMM3D simulations using clustered distribution, and the black-dot line is for EP/DBA/RTE.

It can be seen that the electric fields computed from EP/DBA/RTE are attenuated more in the vegetation canopy than those from NMM3D simulations. At the bottom of the vegetation canopy (i.e., z = -0.3m), the averaged total electric field from NMM3D simulations is about twice larger than that from EP/DBA/RTE. Since power is electric field squared, it is about four times larger from NMM3D simulations, compared with EP/DBA/RTE. Figure IV.17 shows that the electric field profiles from NMM3D simulations show approximately exponential decay merely at the top 5cm of the vegetation layer (i.e., z = 0 to z = 0.05m). EP/DBA/RTE gives exponential decay for the entire profile. The fluctuations of the total electric fields from NMM3D simulations is due to the interference of the incident field and the scattered fields from all the cylinders.

The profiles for the short-cylinders case from NMM3D simulations and EP/DBA/RTE are plotted in Figure IV.18. It can be seen that the two profiles agree with each other except that there are fluctuations in the NMM3D simulation results.

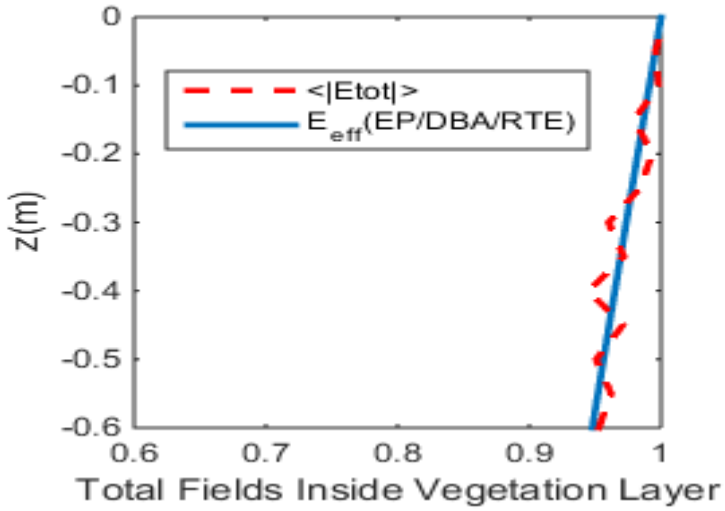

Figure IV.18. Profile of the averaged total field inside the vegetation canopy composed of short cylinders. The red-dash line is for NMM3D simulations and the blue line is for EP/DBA/RTE.

(c) Simulation Results of Reflection and Absorption, and Energy Conservation Check for both Extended-cylinders and Short-cylinders Cases

The reflection from NMM3D simulations using 500 cylinders for the extended-cylinders case is 0.0020 and 0.0045 for the uniform distribution and clustered distribution, respectively. The absorption from NMM3D simulations is 0.4030 for the uniform distribution. For the clustered distribution, there are 100 five-cylinder clusters and the clusters are uniformly randomly distributed in the vegetation area. We calculate the averaged absorption of the four clusters closest to the center of the vegetation fields in each realization.

The absorption is also calculated by equation (4.4.12) after replacing N_L by the number of clusters and $\langle P_a \rangle$ by the averaged absorption for each cluster over many realizations. The absorption from NMM3D simulations is 0.3249 for the clustered distribution.

For the short-cylinders case, the reflection and absorption from NMM3D simulations are 0.0023 and 0.0920, respectively.

For energy conservation, the sum of transmission, reflection and absorption should be unity. The sums of the transmission, reflection and absorption from NMM3D simulations for the different cases are listed in Table IV-4, which shows 1.0174, 1.0338 and 1.0040 for the extended-cylinders case with uniform distribution, the extended-cylinders case with clustered distribution, and the short-cylinders case, respectively. It can be seen that the results for all of them are close to one.

Table IV-4. Energy conservation check for the extend-cylinders and short-cylinders cases.

The transmission (t_V), reflection (r_V) and absorption (a_V) are normalized to the incident power. The subscript "*V*" stands for V-polarization.

Case	Transmission (t_V)	Reflection (r_V)	Absorption (a_V)	$t_V + r_V + a_V$
Extended-cylinders Uniform	0.6124	0.0020	0.4030	1.0174
Extended-cylinders Clustered	0.7044	0.0045	0.3249	1.0338
Short-cylinders	0.9097	0.0023	0.0920	1.0040

(d) NMM3D Simulations of Transmission and Tau of Vegetation for Different VWC and Frequency

We also applied the NMM3D to simulated grass canopies composed of cylinders for different VWC. Figure IV.19 shows the microwave transmission t from the NMM3D simulations for the grass canopy with uniform distribution of cylinders at C-band (5.4 GHz) with 40^o incident angle

as a function of VWC. The transmission generally decreases with VWC. The transmission from NMM3D is much larger than that from RTE/DBA, especially when the VWC is high. The transmission from RTE/DBA decreases exponentially with the increase of VWC while the transmission from NMM3D decrease much slower. For example, at VWC = 1.5 kg/m^2, the transmission from NMM3D is 0.5372 while it is only 0.0715 from RTE/DBA. In this case, the transmission from NMM3D is 7.5 times larger than that from RTE/DBA. The tau from NMM3D is 0.4760, which is 4.2 times smaller than that of RTE.

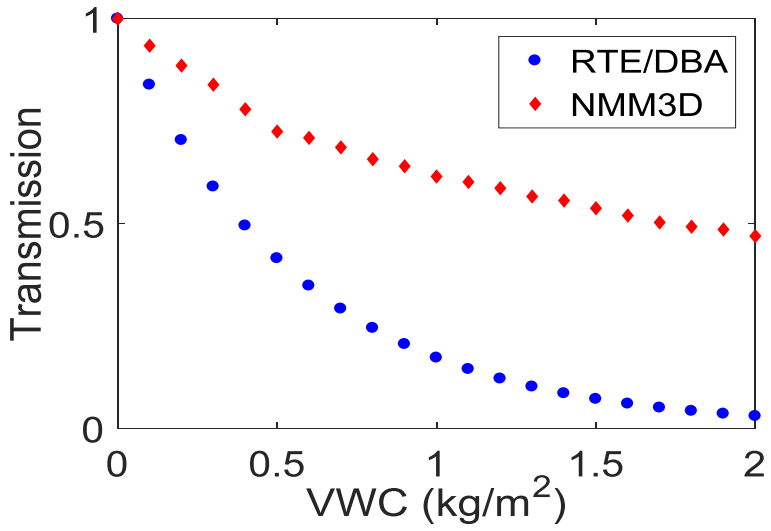

Figure IV.19. Transmission from RTE/DBA and NMM3D vs VWC.

The FL-BOR is also applied for NMM3D simulations of small tree trunks at P-band (370 MHz). The incident angle is 40 degrees. Tree height is 4m with diameter of 6cm. The VWC is 8.14 kg/m^2 with tree density of 4 per m^2. The results are listed in Table IV-5, which shows that transmission from NMM3D is 4.2 times larger than that from RTE/DBA.

Table IV-5. P-band: The transmission t and optical thickness τ from RTE/DBA and NMM3D for tree trunks.

	NMM3D	RTE/DBA
Transmissivity (t)	0.1559	0.0371
Optical Thickness (τ)	2.5232	1.4237

4.5 Conclusion

In the past, the common approaches of studying propagation of microwaves through vegetation are using the Radiative transfer equation and the distorted Born approximation. We showed that the derivation of RTE is based on the assumption of cylindrical elemental volumes. The concept of cylindrical elemental volumes is applicable to short cylinders and small particles, but is difficult to apply to extended cylinders. We noted that the attenuation constant κ_e used in EP/DBA/RTE is based on the assumption of 3D statistically homogenous distribution of the scatterers. The attenuation rate κ_e is not a result from Maxwell's equations. In the calculation of attenuation constants in RTE and DBA, the scattering and the absorption cross sections of entire cylinders are used. The cross sections of such extended cylinders are large, making the attenuation constant a large number. Thus, in this section, we use a new approach of NMM3D full-wave simulations which are used to calculate transmission, reflection and absorption of the vegetation canopy composed of many vertically oriented dielectric thin cylinders. The results are significantly different from past approaches for the case of extended cylinders. The correctness of the FL-BOR simulation method is validated by comparing with FL-ICA and checking the energy conservation. The NMM3D simulations are performed at C-band for vertical polarization and applied to the extended-cylinders case and the short-cylinders case. The results are compared with those from EP/DBA/RTE. The results from the NMM3D and EP/DBA/RTE agree for the short-cylinders case. For the examples of extended-cylinders case, the transmission from the NMM3D

is 6.12 dB larger than that from EP/DBA/RTE while the optical thickness τ from the NMM3D is 5.0 times smaller than that from EP/DBA/RTE.

The NMM3D method and results, presented in this section, are studied in the context of airborne and satellite active and passive microwave remote sensing of vegetation-covered surfaces. The significant differences in results from those of RTE and DBA suggest that there is a need to make theoretical predictions using NMM3D simulations to re-evaluate the ability of microwaves to penetrate vegetation canopy of extended cylinders which are characteristic of many vegetation and forest types. The physical process of radiative transfer at microwave frequencies are governed exactly by Maxwell's equations. The radiative transfer equation (RTE) make assumptions on radiative transfer and such assumptions can be invalid. The NMM3D methodology described in this section can also be used for wireless communications through vegetation canopy, foliage penetration radar, and waves in wire-like metamaterials.

This section presents first results based on a new approach to vegetation effects in microwave propagation, scattering and emission in vegetation. For future studies, other polarizations such as H polarization and cross polarizations should be considered. Orientation distributions should also be considered. The phase shifts of the transmitted wave relative to the incident wave will be calculated.

CHAPTER V

NMM3D Full-wave Simulations of Vegetation/Forest Using Hybrid Method in Fold-Lax Equations with Vector Spherical/Spheroidal/Cylindrical Wave Expansions

In this chapter, a hybrid method is developed for Numerical Maxwell Model of 3D (NMM3D) full-wave simulations of vegetation/trees. The hybrid method combines off-the-shelf techniques for single object and our developed techniques of Foldy-Lax method that include extracting the T matrix for single object, vector translation addition theorem and solving Foldy-Lax multiple scattering equations (FL). Vector spherical, spheroidal and cylindrical waves are used. For vector spherical and spheroidal waves, the commercial software HFSS is utilized to extract the T matrix of a single object. HFSS enables us to perform full-wave simulations of single objects with complicated structures. From the numerical integration of the scattered fields from HFSS with the vector spherical/spheroidal waves, the T matrix is obtained. To perform wave transformations (i.e., addition theorem) for vector spherical/spheroidal waves, we develop robust numerical methods. In solving FL, the coherent wave interactions among the objects are considered and the multiple scattering of all the objects is calculated. For cylindrical scatterers such as tree trunks, the T matrix in vector 3D cylindrical waves are extracted from Infinite Cylinder Approximation (ICA). The extracted T matrices have been verified. The results of the hybrid method have also been verified by the HFSS brute force method for the cases feasible to be run on HFSS. In comparison, the hybrid method is much more efficient than HFSS for vegetation

scattering and applicable to large problems such as full-wave simulations of trees. The hybrid method has been applied to calculate the propagation of microwaves in randomly distributed dielectric cylinders representing tree trunks. In solving FL to calculate statistical moments, we iterate one order of multiple scattering at a time, with averaging over realizations performed after each order. This physically based iterative method of calculating averaged solution converges faster than the traditional iterative method of calculating the exact solution for each realization. Numerical results are illustrated for a large number of cylinders of up to 196 and cylinder lengths of up 94 wavelengths which are typical of forests at L-band. Results of the simulations of the hybrid method show that the transmission coefficient of waves are several times larger than that of the commonly used models of the radiative transfer equation (RTE) and the distorted Born approximation (DBA). The material covered in this Chapter has been partially published in [31].

5.1 Introduction

A large fraction of the soil is covered by vegetation/trees. Thus, understanding the effects of vegetation/trees on microwaves is important for remote sensing of soil moisture: in particular, how much electromagnetic energy can penetrate through the vegetation/trees to reach the soil underneath. In radar remote sensing, understanding the effects of vegetation/forests on microwave propagation, is important for retrieval of soil moisture and snow-wate-equivalent (SWE) below the trees [95, 96]. For passive remote sensing, the transmission coefficient determines the amount of surface emission which can pass through vegetation/forests to reach the radiometer above the vegetation/forest canopy [8] [97]. In terms of wireless communications, transmission through forest can help to model how well the electronic devices such as cell phones and GPS receivers can receive wireless signals under the forest [98].

For three decades, computations of wave propagation coefficient in randomly distributed cylinders have been based on radiative transfer equations (RTE) [4, 28] and the distorted Born approximation (DBA) [6, 11]. In both DBA and RTE, a key parameter is the attenuation rate per unit distance κ_e. κ_e is calculated using $\kappa_e = n_0(\sigma_a + \sigma_s)$, where n_0 is the number of scatterers per m^3, and σ_a and σ_s are the scattering cross section and the absorption cross section of a single scatterer, respectively. RTE originates from the applications in clouds and rainfalls where the water droplets have 3D statistical homogeneity [2, 4]. Thus, RTE is regarded commonly as a 'cloud/droplets' model to represent the scatterers. There are several assumptions in RTE and DBA that are difficult to justify for modelling a layer of randomly distributed cylinders. Three of the most significant ones are listed as follows: (i) The derivation of the RTE and DBA equations assume that the scatterers were uniformly distributed in 3D. The gaps between tree trunks are ignored. The free propagation of microwaves through the gaps results in an effect that the uniform scattering layer is not able to capture. (ii) The absorption and scattering cross section of the entire objects based on plane wave illuminations are included in the attenuation coefficients and phase matrix. These cannot be justified in tall cylinder environments such as tree trunks because the waves scattered by cylinders affect each other. (iii) RTE/DBA uses the far field approximation in the scattering phase matrix. The far field means distance larger than $length^2 / wavelength$. The far field approximation is not valid for the cases of trees at L-band where the far field distance is tens to hundreds of meters. In addition to RTE and DBA, another model is the coherent/branching model [5, 36]. The coherent/branching model is a single scattering approach and the attenuation was not calculated correctly.

In an earlier paper, second order theory was used for Monte Carlo simulations of scattering by vertical dielectric cylinders [94]. Full-wave simulations of dielectric cylinders with random

orientations was also studied using the Method of Moment (MoM) [99]. In chapter IV, a full-wave simulation method combining Foldy-Lax full multiple scattering equations and the impedance matrix of the body of resolution (BOR) was developed for a layer of dielectric cylinders of small radii.

To perform NMM3D full-wave simulations of vegetation and trees, a hybrid method is developed in this chapter. This method is a hybrid of the off-the-shelf technique (e.g.HFSS) and newly developed techniques. The newly developed techniques are the three key steps of the hybrid method: (1) calculating the T matrix of each single object using vector waves, (2) vector wave transformations, and (3) solving Foldy-Lax multiple scattering equations (FL) for all the objects. Vector spherical, spheroidal and cylindrical waves are used. The T matrix relates the incident fields to the scattered fields for an arbitrary-shape scatterer [4]. Previously, vector spherical wave expansions were used for the T matrix for a sphere, where a circumscribing sphere is defined [4]. In this chapter, we extract the T matrix for an arbitrarily-shaped object. When the objects are closely packed, it is impractical to enclose each object by a spherical surface without overlap. In general, spheroidal surfaces are more compact to enclose closely packed objects. Thus, vector spheroidal wave expansions are also used, which are more complicated than the spherical waves. To extract the T matrix for an arbitrary-shape object, the off-the-shelf technique HFSS is used. HFSS enables us to perform full-wave simulations of single objects with complicated structures. To extract the T matrix of the single object from HFSS, we first define a spherical/spheroidal surface (∂S) which encloses the object. Then, we excite the object using incident plane waves at different incident angles and polarizations in HFSS. Using the scattered field values on ∂S from HFSS, the spherical/spheroidal wave expansion coefficients of the scattered waves are obtained. Since the expansion coefficients of the incident plane waves are known, the T matrix is extracted.

The accuracy of the extracted T matrix from HFSS is verified by comparison with the analytical solution for the sphere. It is noted that the T matrix extraction method works for arbitrary-shaped objects. It is noted that the T matrix extraction method also works for those requiring a spheroidal surface with a large aspect ratio (e.g. branches with leaves). Next, we develop robust numerical methods to perform wave transformations for vector spherical and spheroidal waves, which is also called addition theorem. Finally, the extracted T matrices for the single objects are substituted to FL, and the FL is solved with the use of the numerical wave transformations. In solving FL, the multiple scattering of all the objects is calculated. The hybrid method for full-wave solutions of multiple scattering is illustrated using several complicated objects. For three objects, it is feasible to simulate them with the HFSS brute force method to provide validation. However, the HFSS brute force method is impractical computationally for large problems including lots of objects or empty space, while the hybrid method can still operate with available computation resources. The hybrid method is feasible to perform full-wave simulations of vegetation/trees, which has applications in microwave remote sensing of vegetation, vegetation-covered surfaces, and forest.

For trees/tree trunks, the hybrid method with 3D vector cylindrical wave expansions is used. It is because trees/tree trunks can be compactly enclosed by infinite cylindrical surfaces. The vegetation/forest components such as trunks, branches, main stems, stalks, etc. are modeled by dielectric cylinders [9, 77, 100, 101]. We use ICA to extract the T matrix for the cylinder and the analytical expressions for the T matrix are derived. The main purpose is to simulate tall tree trunks at L-band and ICA is of sufficient accuracies. The accuracy of the T matrix is also verified. For 3D vector cylindrical waves, the scattered field formulation of FL is used instead of the usual exciting field formulation. In traditional method of solving such matrix equations of FL, the equations are solved iteratively using conjugate gradient or similar algorithms for each realization

until the root mean squared error (RMSE) for the coefficients reaches a threshold. Then the averaged solutions of scattering and transmission coefficient are calculated by taking averages over many realizations such as 10 to 40 realizations. For simulating large problems of many tree trunks, we use a physically based iterative method to calculate the averaged solution which is based on the observation that the averaged multiple scattering solutions have a much faster convergence because of inherent averaging. We have implemented the hybrid method on parallel computing. Using the hybrid method, we calculate the transmission of microwaves through the forest canopy, represented by a layer of randomly distributed cylinders. To model tree trunks at L-band, dielectric cylinders of up to 20 meters tall are simulated. The results of hybrid method show that the past models of RTE/DBA significantly overestimate attenuation for a layer of cylinders. The hybrid method predicts transmission coefficient several times larger and and the optical thickness τ several times smaller than that of the past models.

This chapter is organized as follows. Section 5.2 provides the derivations and formulas for vector spherical, spheroidal and cylindrical waves. Section 5.3 derives the three steps of the hybrid method in detail for all the three kinds of vector waves: (1) T matrix extraction, (2) vector wave transformations, and (3) solving the Foldy-Lax equations. Section 5.4 presents the intermediate results and final results of the hybrid method, as well as discussions.

5.2 Vector Spherical, Spheroidal and Cylindrical Waves

In the Fold-Lax equations, the fields are expanded in terms of vector waves [4]. The vector waves are complete basis functions outside the exclusion volume. As illustrated in Figure V.1: when the two branches are far apart, they can be enclosed by spherical surfaces without overlap. In this case, the exclusion volume is spherical and thus vector spherical wave expansions are used

for fields outside the spherical surfaces. When the two branches are close to each other, they can be enclosed by spheroidal surfaces without overlap. In this case, the exclusion volume is spheroidal and thus vector spheroidal wave expansions are used for fields outside the spheroidal surfaces. Figure V.2 illustrates the infinite cylindrical exclusion volume. The tree trunk (Figure V.2 left) and the whole tree (Figure V.2 right) can be enclosed by infinite cylindrical volume without overlap and thus 3D vector cylindrical wave expansions are used outside the cylindrical surfaces.

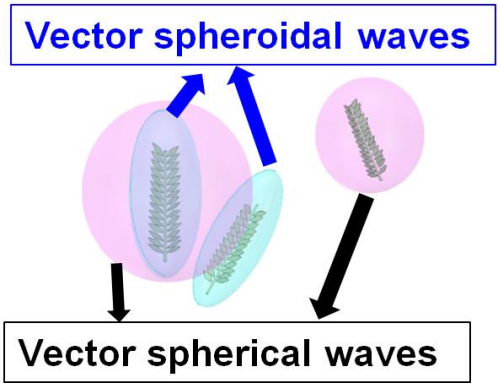

Figure V.1. Illustration of spherical and spheroidal exclusion volumes for vector spherical and spheroidal waves, respectively.

Figure V.2. Illustration of infinite cylindrical exclusion volumes for 3D vector cylindrical waves.

The scalar wave equation is

$$\left(\nabla^2 + k^2\right)\psi(\bar{r}) = 0 \tag{5.2.1}$$

The vector wave equation is

$$\nabla \times \nabla \times \bar{\bar{E}} - k^2 \bar{\bar{E}}(\bar{r}) = 0 \tag{5.2.2}$$

The vector spherical, spheroidal and cylindrical waves are the solutions to the vector wave equation in spherical, spheroidal and cylindrical coordinate systems, respectively

5.2.1 Vector Spherical Waves

The three parameters in the spherical coordinate system are (r, θ, ϕ). The outgoing scalar spherical wave is

$$\psi_{mn}(kr, \theta, \phi) = h_n^{(1)}(kr) P_n^m(\cos\theta) e^{im\phi} \tag{5.2.3}$$

where $h_n^{(1)}$ is the spherical Hankel function of the first kind and P_n^m is the associated Legendre function defined as

$$P_n^m(x) = \frac{(-1)^m}{2^n n!}\left(1 - x^2\right)^{m/2} \frac{d^{n+m}}{dx^{n+m}}\left(x^2 - 1\right)^n \tag{5.2.4}$$

where m = 0, ±1, ±2,… , ±n, and n starts with 0.

The regular scalar spherical wave is

$$Rg\psi_{mn}(kr, \theta, \phi) = j_n(kr) P_n^m(\cos\theta) e^{im\phi} \tag{5.2.5}$$

where the prefix *Rg* stands for regular and j_n is the spherical Bessel function.

The regular vector spherical waves are

$$\begin{aligned} Rg\bar{M}_{mn}(kr, \theta, \phi) &= \gamma_{mn} \nabla \times \left[\bar{r} Rg\psi_{mn}(kr, \theta, \phi)\right] \\ &= \gamma_{mn} j_n(kr) \bar{C}_{mn}(\theta, \phi) \end{aligned} \tag{5.2.6}$$

$$
\begin{aligned}
Rg\bar{N}_{mn}(kr,\theta,\phi) &= \frac{1}{k}\nabla \times Rg\bar{M}_{mn}(kr,\theta,\phi) \\
&= \gamma_{mn}\left\{\frac{n(n+1)\,j_n(kr)}{kr}\bar{P}_{mn}(\theta,\phi) + \frac{\left[krj_n(kr)\right]'}{kr}\bar{B}_{mn}(\theta,\phi)\right\}
\end{aligned}
\tag{5.2.7}
$$

The vector spherical waves $\bar{M}_{mn}$ and $\bar{N}_{mn}$ are obtained by changing the spherical Bessel function to Hankel function of the first kind. γ_{mn} is defined as

$$
\gamma_{mn} = \sqrt{\frac{(2n+1)(n-m)!}{4\pi n(n+1)(n+m)!}} \tag{5.2.8}
$$

The $\bar{C}_{mn}$, $\bar{P}_{mn}$ and $\bar{B}_{mn}$ are the vector spherical harmonics defined as follows.

$$
\bar{C}_{mn}(\theta,\phi) = \left[\hat{\theta}\frac{im}{\sin\theta}P_n^m(\cos\theta) - \hat{\phi}\frac{d}{d\theta}P_n^m(\cos\theta)\right]e^{im\phi} \tag{5.2.9}
$$

$$
\bar{P}_{mn}(\theta,\phi) = \hat{r}P_n^m(\cos\theta)e^{im\phi} \tag{5.2.10}
$$

$$
\bar{B}_{mn}(\theta,\phi) = \left[\hat{\theta}\frac{d}{d\theta}P_n^m(\cos\theta) + \hat{\phi}\frac{im}{\sin\theta}P_n^m(\cos\theta)\right]e^{im\phi} \tag{5.2.11}
$$

n starts with 0 for $\bar{P}_{mn}$ and starts with 1 for $\bar{C}_{mn}$ and $\bar{B}_{mn}$. The orthogonality relation for vector spherical harmonics is

$$
\int_0^{\pi} d\theta \sin\theta \int_0^{2\pi} d\phi \bar{V}_{mn}^{(\alpha)}(\theta,\phi)\cdot\bar{V}_{-m'n'}^{(\beta)}(\theta,\phi) = \delta_{\alpha\beta}\delta_{mm'}\delta_{nn'}z_{\alpha mn} \tag{5.2.12}
$$

where $\bar{V}_{mn}^{(1)}(\theta,\phi) = \bar{P}_{mn}(\theta,\phi), \bar{V}_{mn}^{(2)}(\theta,\phi) = \bar{B}_{mn}(\theta,\phi), \bar{V}_{mn}^{(3)}(\theta,\phi) = \bar{C}_{mn}(\theta,\phi)$, and

$$
z_{1mn} = (-1)^m\frac{4\pi}{2n+1} \tag{5.2.13}
$$

$$
z_{2mn} = z_{3mn} = (-1)^m\frac{4\pi n(n+1)}{2n+1} \tag{5.2.14}
$$

5.2.2 Vector Spheroidal Waves

The three parameters in the spheroidal coordinate system are (ξ, η, ϕ), with $-1 \leq \eta \leq 1, 1 \leq \xi < \infty, 0 \leq \phi \leq 2\pi$. The transformation between the Cartesian coordinate system and the spheroidal coordinate system is

$$\begin{aligned} x &= \frac{d}{2}\sqrt{\left(1-\eta^2\right)\left(\xi^2-1\right)}\cos\phi \\ y &= \frac{d}{2}\sqrt{\left(1-\eta^2\right)\left(\xi^2-1\right)}\sin\phi \\ z &= \frac{d}{2}\eta\xi \end{aligned} \tag{5.2.15}$$

Then, it can be deduced that

$$\frac{x^2+y^2}{\left(\xi^2-1\right)\frac{d^2}{4}} + \frac{z^2}{\frac{d^2}{4}\xi^2} = 1 \tag{5.2.16}$$

$$\frac{z^2}{\eta^2} - \frac{x^2+y^2}{1-\eta^2} = \frac{d^2}{4} \tag{5.2.17}$$

where d is the interfocal distance. For constant ϕ, the plot is a half plane (Figure V.3 (A)), the same as the spherical system. For constant ξ, the plot is a spheroidal surface (Figure V.3 (B)). The major axis length is $d\xi$ and the minor axis length is $\frac{d}{2}\sqrt{\xi^2-1}$. For constant η, the plot is a hyperboloid (Figure V.4).

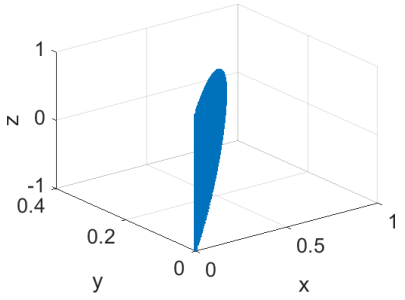

(A)

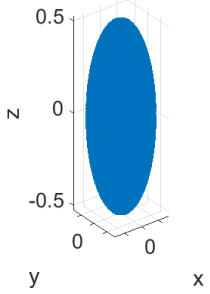

(B)

Figure V.3. (A) Constant $\phi = \pi/8$ and (B) constant $\xi = 1.05$ in the spheroidal coordinate system.

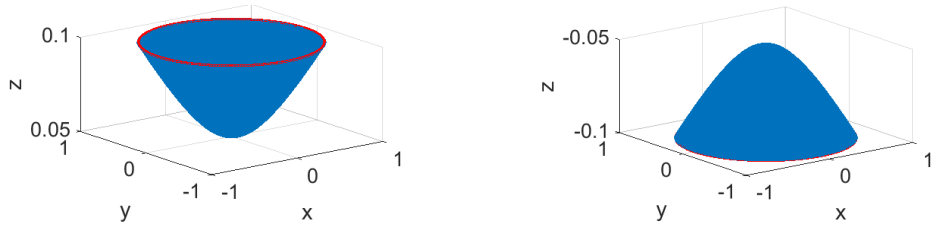

(A) (B)

Figure V.4. Constant η, (A) $\eta = 0.1$ and (B) $\eta = -0.1$.

The prolate spheroidal scalar wave function is

$$\psi_{mn} = S_{mn}(c,\eta)R_{mn}(c,\xi)\begin{matrix}\sin\\ \cos\end{matrix}(m\phi) \tag{5.2.18}$$

where $c = \frac{1}{2}kd$. $\sin(m\phi)$ are the odd modes while $\cos(m\phi)$ are the even modes, which are used instead of $\exp(im\phi)$ to follow the formulations in [102]. $S_{mn}(c,\eta)$ is the spheroidal angular function and $R_{mn}(c,\xi)$ is the spheroidal radial function.

The spheroidal angular function $S_{mn}(c,\eta)$ satisfy the following equation,

$$\frac{d}{d\eta}\left[\left(1-\eta^2\right)\frac{d}{d\eta}S_{mn}(c,\eta)\right]+\left[\lambda_{mn}-c^2\eta^2-\frac{m^2}{1-\eta^2}\right]S_{mn}(c,\eta)=0 \tag{5.2.19}$$

where λ_{mn} is the characteristic value.

There are two linearly independent solutions to this equation: spheroidal angular function of the first kind

$$S_{mn}^{(1)}(c,\eta) = \sum_{r=0,1}^{\infty}{}' d_r^{mn}(c)P_{m+r}^{m}(\eta) \tag{5.2.20}$$

and spheroidal angular function of the second kind

$$S_{mn}^{(2)}(c,\eta) = \sum_{r=-\infty}^{\infty}{}' d_r^{mn}(c) Q_{m+r}^m(\eta) \tag{5.2.21}$$

where $P_{m+r}^m(\eta)$ is the associated Legendre function of the first kind and $Q_{m+r}^m(\eta)$ is the Legendre function of the second kind. The prime on the summation means that the summation is over even *k* when *(n-m)* is even and over odd *k* when *(n-m)* is odd. In this section, only prolate spheroidal function is used and thus only $S_{mn}^{(1)}(c,\eta)$ is needed. For simplification, the superscript '*(1)*' is omitted later in this section.

The coefficient d_r^{mn} can be calculated using the following formula,

$$A_r^m(c) d_{r+2}^{mn}(c) + \left[B_r^m(c) - \lambda_{mn}(c) \right] d_r^{mn}(c) + C_r^m(c) d_{r-2}^{mn}(c) = 0 \tag{5.2.22}$$

The detailed steps of calculations can be found in [103, 104].

$S_{mn}(c,\eta)$ for m=0, c=5 and n=0,1,2,3 is plotted in Figure V.5 (a) and $S_{mn}(c,\eta)$ for m=1, c=5, and n=1,2,3,4 is plotted in Figure V.5 (b). The plots compare well with those in [103] which validates the correctness of the results.

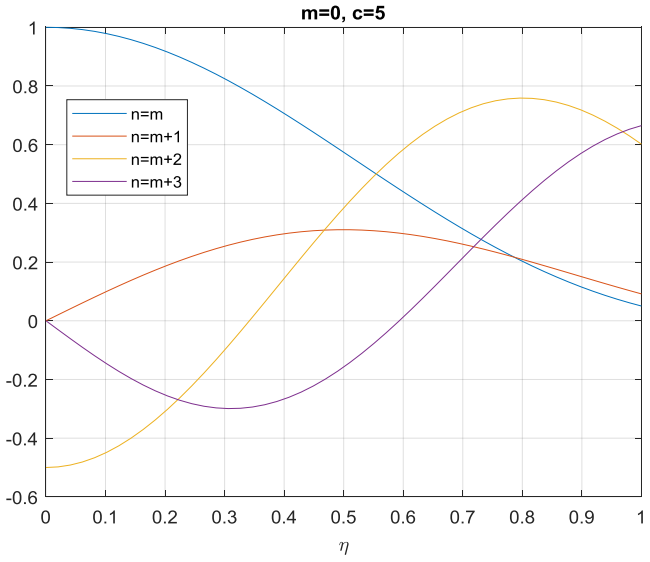

(a)

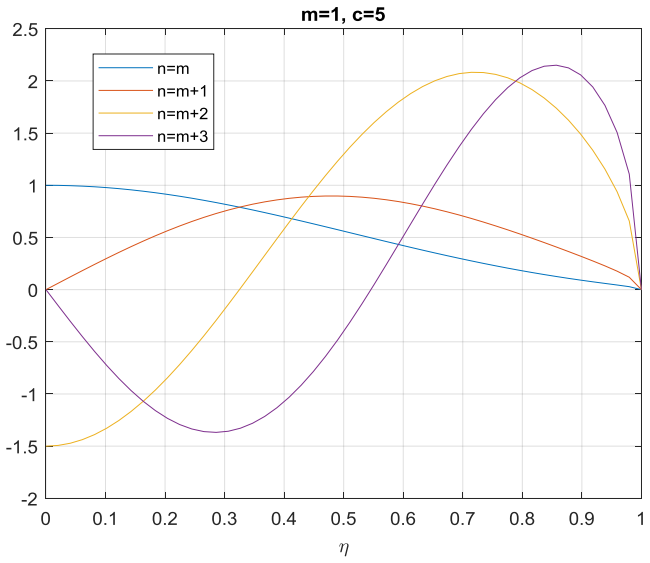

(b)

Figure V.5. $S_{mn}(c,\eta)$ for different n at (a) m=0, c=5 and (b) m=1, c=5.

For our application, the spheroidal surface is used to enclose vegetation scatterers such as a branch with leaves. In this case, the aspect ratio (i.e., the ratio between the major axis length and minor axis length) is large. In this case, ξ us close to 1. An example is shown in Figure V.6. For d=1m, c=14.76 at L-band of frequency 1.41 GHz.

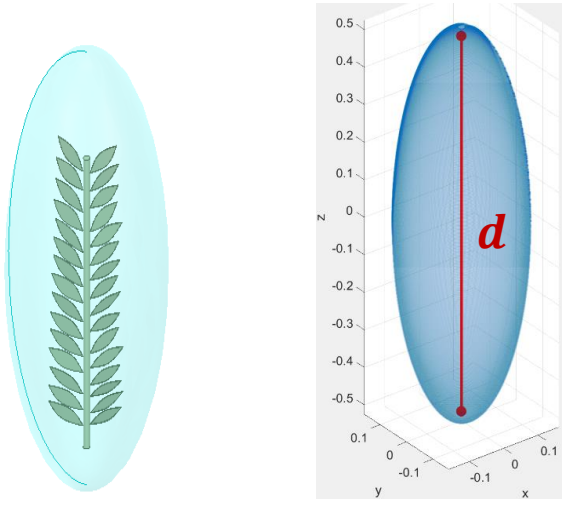

Figure V.6. A branch enclosed by a prolate spheroidal surface (left), spheroidal surface with $\xi = 1.05$.

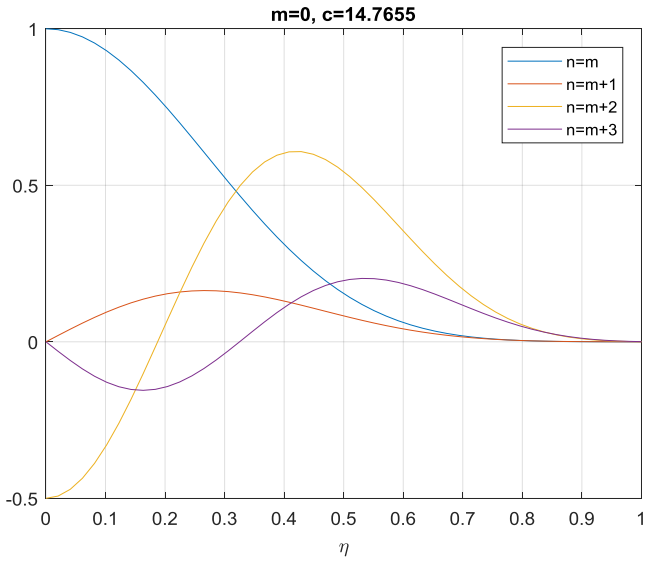

(a)

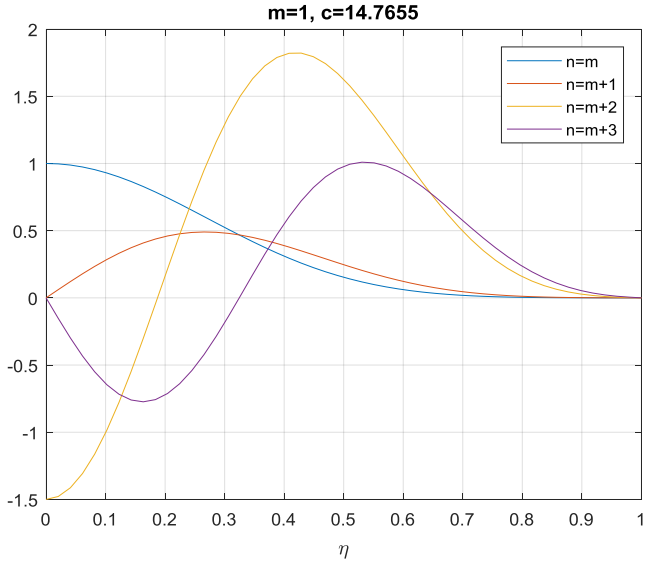

(b)

Figure V.7. $S_{mn}(c,\eta)$ for different n at (a) m=0, c=14.76 and (b) m=1, c=14.76.

$S_{mn}(c,\eta)$ for m=0, c=14.76 and n=0,1,2,3 is plotted in Figure V.7 (a) and $S_{mn}(c,\eta)$ for m=1, c=14.76, and n=1,2,3,4 is plotted in Figure V.7 (b). $S_{mn}(c,\eta)$ is also plotted for different c as shown in Figure V.8. It can be seen that $S_{mn}(c,\eta)$ decreases with c.

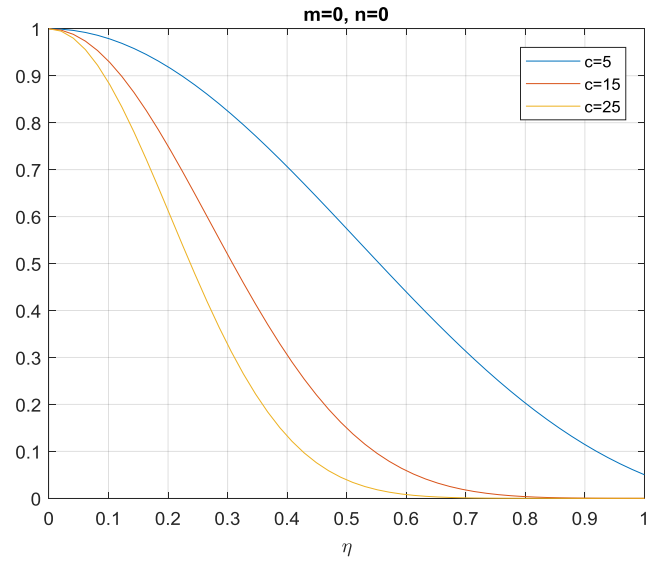

(a)

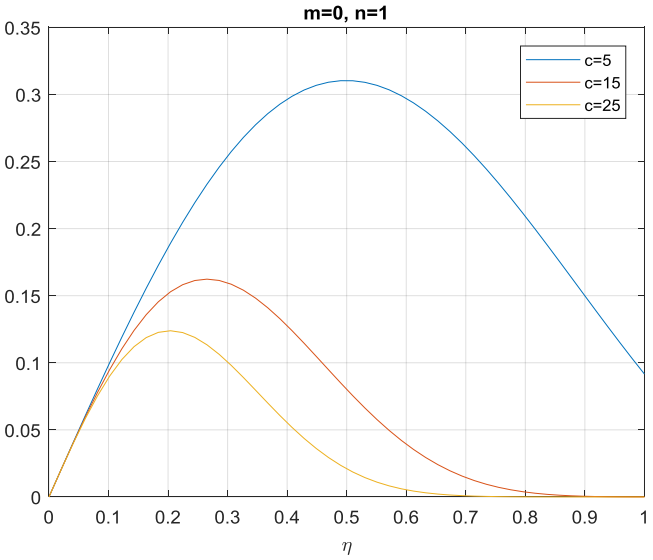

(b)

Figure V.8. $S_{mn}(c,\eta)$ for different c at (a) m=0, n=0 and (b) m=0, n=1.

The spheroidal radial function $R_{mn}(c,\xi)$ satisfies the following equation

$$\frac{d}{d\xi}\left[\left(\xi^2-1\right)\frac{d}{d\xi}R_{mn}(c,\xi)\right]-\left[\lambda_{mn}-c^2\xi^2+\frac{m^2}{\xi^2-1}\right]R_{mn}(c,\xi)=0 \tag{5.2.23}$$

The solution is as follows

$$R_{mn}^{(i)}(c,\xi) = \frac{1}{\sum_{r=0,1}^{\infty}{}' d_r^{mn}(c)\frac{(2m+r)!}{r!}}\left(\frac{\xi^2-1}{\xi^2}\right)^{m/2} \cdot \sum_{r=0,1}^{\infty}{}' i^{r+m-n} d_r^{mn}(c)\frac{(2m+r)!}{r!} z_{m+r}^{(i)}(c\xi) \tag{5.2.24}$$

where i = 1,2,3,4 with $z_n^{(1)}(x) = j_n(x)$, $z_n^{(2)}(x) = n(x)$, $z_n^3(x) = h_n^{(1)}(x)$, $z_n^{(4)}(x) = h_n^{(2)}(x)$.

Thus,

$$R_{mn}^{(3)}(c,\xi) = R_{mn}^{(1)}(c,\xi) + iR_{mn}^{(2)}(c,\xi) \tag{5.2.25}$$

$$R_{mn}^{(4)}(c,\xi) = R_{mn}^{(1)}(c,\xi) - iR_{mn}^{(2)}(c,\xi) \tag{5.2.26}$$

$R_{mn}^{(1)}(c,\xi)$ for m=0, c=5 and n=0,1,2,3 is plotted in Figure V.9 (a) and $R_{mn}^{(2)}(c,\xi)$ for m=1, c=5, and n=1,2,3,4 is plotted in Figure V.9 (b). The plots compare well with those in [103] which validates the correctness of the results.

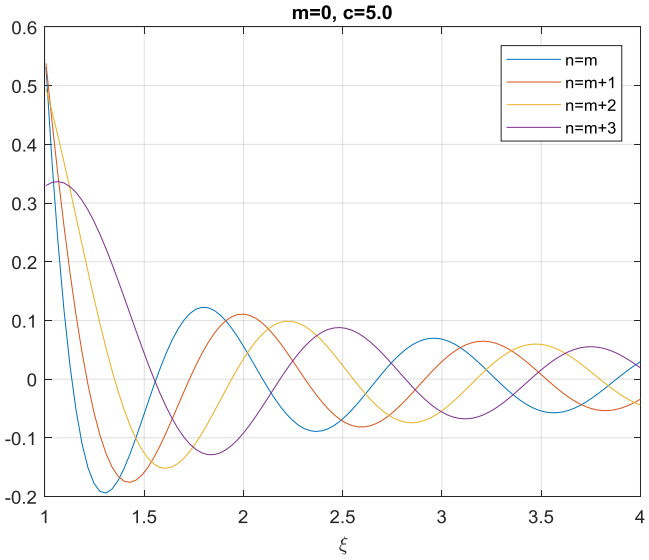

(a)

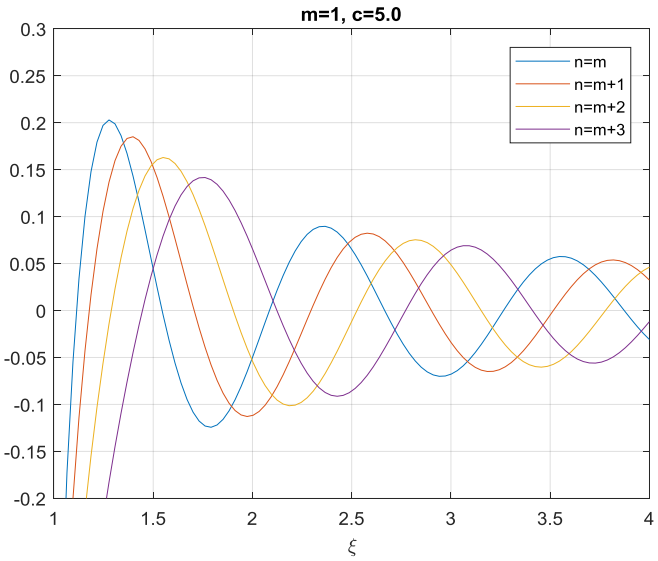

(b)

Figure V.9. (a) $R_{mn}^{(1)}(c,\xi)$ for m=0, c=5 and (b) $R_{mn}^{(2)}(c,\xi)$ for m=1, c=5, at different n.

$R_{mn}^{(1)}(c,\xi)$ for m=0, c=14.76 and n=0,1,2,3 is plotted in Figure V.10 (a) and $R_{mn}^{(2)}(c,\xi)$ for m=1, c=14.76, and n=1,2,3,4 is plotted in Figure V.10 (b). $R_{mn}^{(1)}(c,\xi)$ and $R_{mn}^{(2)}(c,\xi)$ is also plotted for different c as shown in Figure V.8. It can be seen that the oscillation frequency increase with c for both $R_{mn}^{(1)}(c,\xi)$ and $R_{mn}^{(2)}(c,\xi)$.

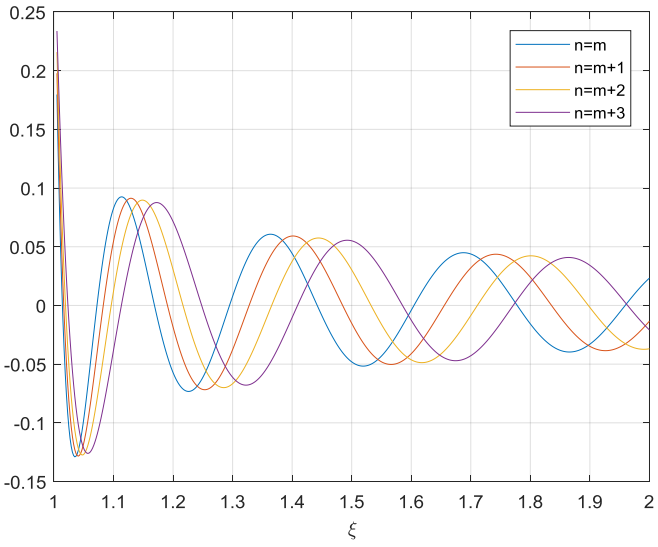

(a)

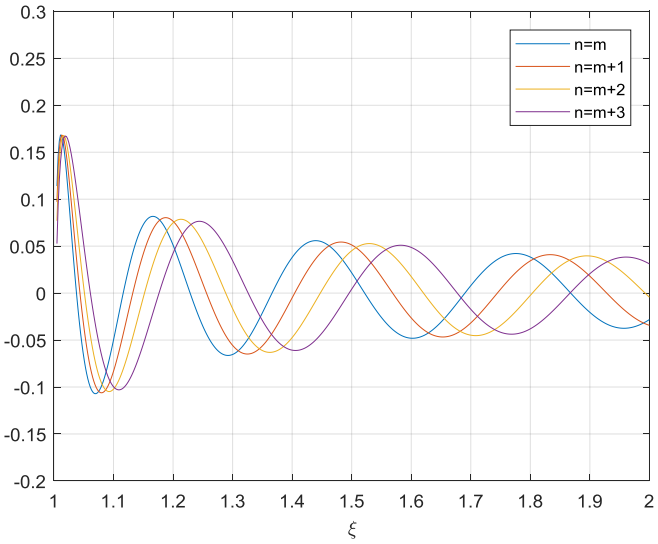

(b)

Figure V.10. (a) $R_{mn}^{(1)}(c,\xi)$ for m=0, c=14.76 and (b) $R_{mn}^{(2)}(c,\xi)$ for m=1, c=14.76, at different n.

The comparisons between the spherical wave function and spheroidal wave function are summarized in Table V-1. When $c \to 0$, or $\xi \to \infty$, the spheridal wave function approaches spherical wave functions. Both wave functions have the same ϕ dependence.

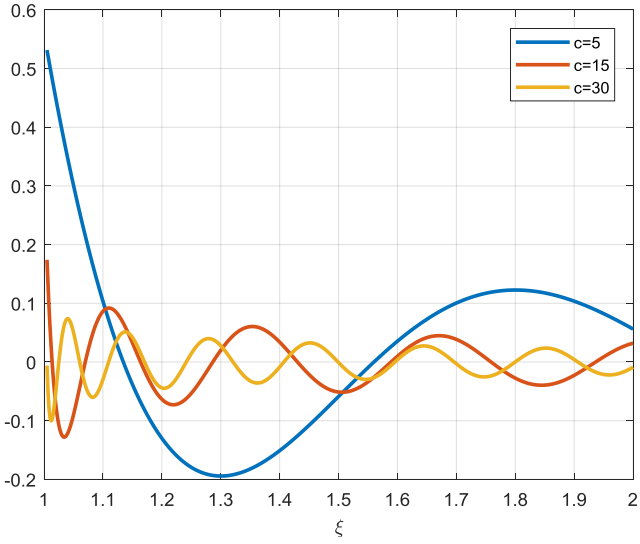

(a)

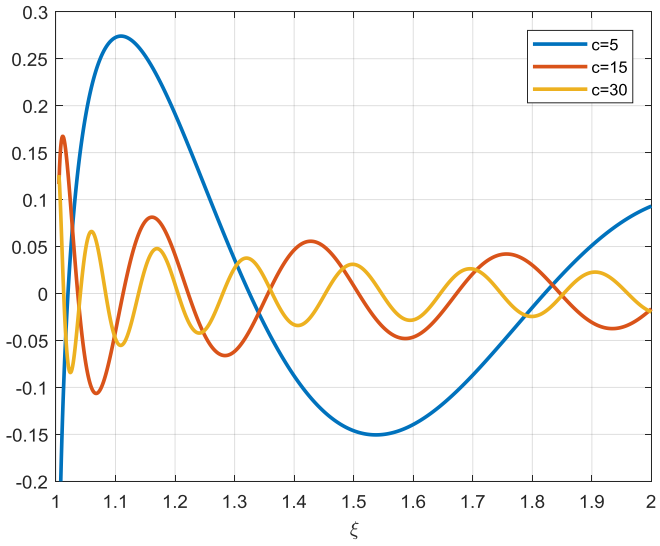

(b)

Figure V.11. (a) $R_{mn}^{(1)}(c,\xi)$ and (b) $R_{mn}^{(2)}(c,\xi)$ for m=0, n=0, at different n.

Table V-1. Comparisons between the spherical and spheroidal functions.

Spherical function (r,θ,ϕ)	Spheroidal function (ξ,η,ϕ) ($c \to 0$, or $\xi \to \infty$: spheroidal → spherical)
$exp(im\phi)$	$exp(im\phi)$
$P_n^m(cos\theta)$	$S_{mn}(c,\eta)$
$j_n(kr)$ $h_n^{(1)}(kr) = j_n(kr) + in_n(kr)$	$R_{mn}^{(1)}(c,\xi)$: expansion of $j_n(kr)$ $R_{mn}^{(2)}(c,\xi)$: expansion of $n_n(kr)$ $R_{mn}^{(3)}(c,\xi) = R_{mn}^{(1)}(c,\xi) + iR_{mn}^{(2)}(c,\xi)$
$Rg\psi_{mn} = P_n^m(cos\theta)j_n(kr)exp(im\phi)$ $\psi_{mn} = P_n^m(cos\theta)h_n^{(1)}(kr)exp(im\phi)$	$\psi_{mn}^{(1)} = S_{mn}(c,\eta)R_{mn}^{(1)}(c,\xi)exp(im\phi)$ $\psi_{mn}^{(3)} = S_{mn}(c,\eta)R_{mn}^{(3)}(c,\xi)exp(im\phi)$

The vector spheroidal wave functions are calculated from the scalar wave functions as below

$$\overline{M}_{(e,o)mn}^{a(i)}(c;\eta,\xi,\phi) = \nabla \times \left[\psi_{(e,o)mn}^{(i)}\hat{a}\right] \tag{5.2.27}$$

$$\overline{N}_{(e,o)mn}^{a(i)}(c;\eta,\xi,\phi) = \frac{1}{k}\nabla \times \nabla \times \left[\psi_{(e,o)mn}^{(i)}\hat{a}\right] \tag{5.2.28}$$

where $\hat{a}$ is $\hat{x},\hat{y},\hat{z}$ or $\hat{r}$.

In this section, we use $\hat{r}$. The expressions for the vector prolate spheroidal wave functions are as follows [104].

$$\bar{M}^{r(i)}_{(e,o)mn} = M^{r(i)}_{(e,o)m,n,\eta}\hat{\eta} + M^{r(i)}_{(e,o)m,n,\xi}\hat{\xi} + M^{r(i)}_{(e,o)m,n,\phi}\hat{\phi} \tag{5.2.29}$$

with $M^{r(i)}_{(e,o)m,n,\eta} = \dfrac{m\xi}{\left(\xi^2-\eta^2\right)^{\frac{1}{2}}\left(1-\eta^2\right)^{\frac{1}{2}}} S_{mn}R^{(i)}_{mn}\begin{bmatrix}\sin\\ -\cos\end{bmatrix}(m\phi)$

$$M^{r(i)}_{(e,o)m,n,\xi} = \frac{-m\eta}{\left(\xi^2-\eta^2\right)^{\frac{1}{2}}\left(\xi^2-1\right)^{\frac{1}{2}}} S_{mn}R^{(i)}_{mn}\begin{bmatrix}\sin\\ -\cos\end{bmatrix}(m\phi)$$

$$M^{r(i)}_{(e,o)m,n,\phi} = \frac{\left(\xi^2-1\right)^{\frac{1}{2}}\left(1-\eta^2\right)^{\frac{1}{2}}}{\xi^2-\eta^2}\left[\xi\frac{dS_{mn}}{d\eta}R^{(i)}_{mn} - \eta S_{mn}\frac{dR^{(i)}_{mn}}{d\xi}\right]\begin{bmatrix}\cos\\ \sin\end{bmatrix}(m\phi)$$

$$\bar{N}^{r(i)}_{(e,o)mn} = N^{r(i)}_{(e,o)m,n,\eta}\hat{\eta} + N^{r(i)}_{(e,o)m,n,\xi}\hat{\xi} + N^{r(i)}_{(e,o)m,n,\phi}\hat{\phi} \tag{5.2.30}$$

with $N^{r(i)}_{(e,o)m,n,\eta} = \dfrac{2\left(1-\eta^2\right)^{\frac{1}{2}}}{kd\left(\xi^2-\eta^2\right)^{\frac{1}{2}}}\left[\begin{array}{l}\dfrac{dS_{mn}}{d\eta}\dfrac{\partial}{\partial\xi}\left(\dfrac{\xi\left(\xi^2-1\right)}{\xi^2-\eta^2}R^{(i)}_{mn}\right) - \eta S_{mn}\dfrac{\partial}{\partial\xi}\left(\dfrac{\xi^2-1}{\xi^2-\eta^2}\dfrac{dR^{(i)}_{mn}}{d\xi}\right)\\ +\dfrac{m^2\eta}{\left(1-\eta^2\right)\left(\xi^2-1\right)}S_{mn}R^{(i)}_{mn}\end{array}\right]\begin{bmatrix}\cos\\ \sin\end{bmatrix}(m\phi)$

$$N^{r(i)}_{(e,o)m,n,\xi} = -\frac{2\left(\xi^2-1\right)^{\frac{1}{2}}}{kd\left(\xi^2-\eta^2\right)^{\frac{1}{2}}}\left[\begin{array}{l}-\dfrac{\partial}{\partial\eta}\left(\dfrac{\eta\left(1-\eta^2\right)}{\xi^2-\eta^2}S_{mn}\right)\dfrac{dR^{(i)}_{mn}}{d\xi} + \xi\dfrac{\partial}{\partial\eta}\left(\dfrac{1-\eta^2}{\xi^2-\eta^2}\dfrac{dS_{mn}}{d\eta}\right)R^{(i)}_{mn}\\ -\dfrac{m^2\xi}{\left(1-\eta^2\right)\left(\xi^2-1\right)}S_{mn}R^{(i)}_{mn}\end{array}\right]\begin{bmatrix}\cos\\ \sin\end{bmatrix}(m\phi)$$

$$N^{r(i)}_{(e,o)m,n,\phi} = \frac{2m\left(1-\eta^2\right)^{\frac{1}{2}}\left(\xi^2-1\right)^{\frac{1}{2}}}{kd\left(\xi^2-\eta^2\right)}\left[\frac{-1}{\xi^2-1}\frac{d}{d\eta}\left(\eta S_{mn}\right)R^{(i)}_{mn} - \frac{1}{1-\eta^2}S_{mn}\frac{d}{d\xi}\left(\xi R^{(i)}_{mn}\right)\right]\begin{bmatrix}\sin\\ -\cos\end{bmatrix}(m\phi)$$

where the upper function of $(m\phi)$ is for even function while the lower sign is for odd function. S_{mn} is function of η and $R^{(i)}_{mn}$ is function of ξ which are not written out explicitly for simplicity.

It can be seen that the first and second order derivatives are needed in calculating the spheroidal vector wave functions. The first-order derivative of the spheroidal angular function is

$$\frac{dS_{mn}(c,\eta)}{d\eta} = \sum_{r=0,1}^{\infty}{}' d_r^{mn}(c)\frac{dP_{m+r}^{m}(\eta)}{d\eta} \tag{5.2.31}$$

$dS_{mn}(c,\eta)/d\eta$ for c=14.76 and m=0 and m=1 is plotted in Figure V.12.

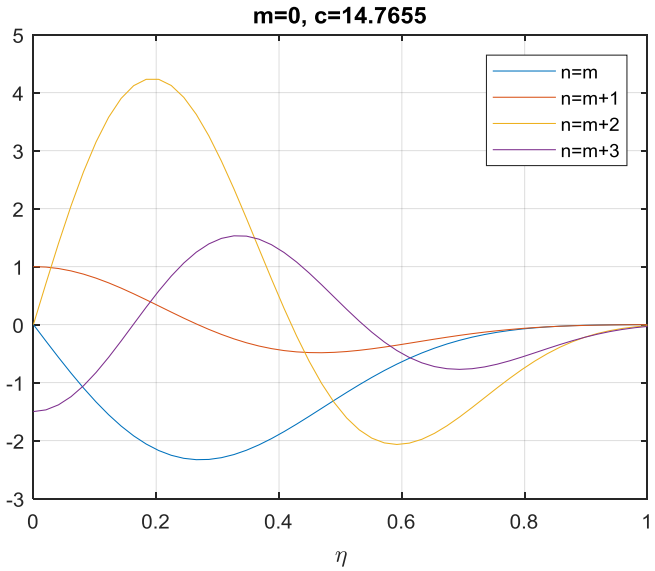

(a)

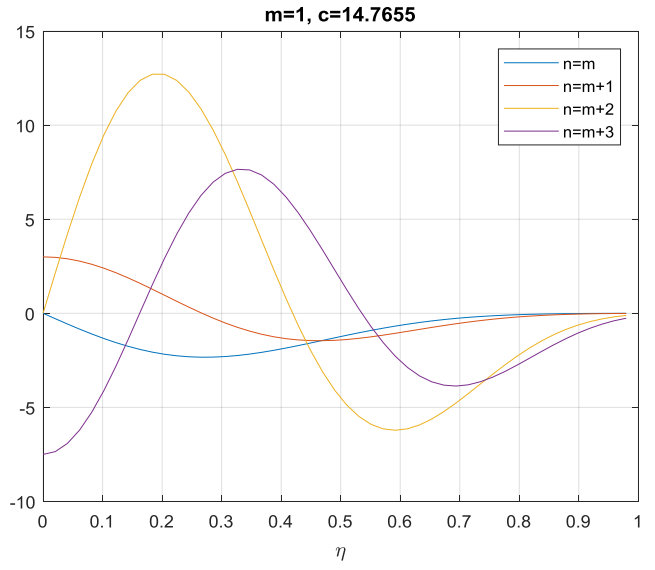

(b)

Figure V.12. $dS_{mn}(c,\eta)/d\eta$ for (a) m=0, c=14.76 and (b) m=1, c=14.76, at different n.

The second order derivative is calculated using equation (5.2.19),

$$\frac{d^2S_{mn}(c,\eta)}{d\eta^2}=\frac{1}{\left(1-\eta^2\right)}\left\{2\eta\frac{d}{d\eta}S_{mn}(c,\eta)-\left[\lambda_{mn}-c^2\eta^2-\frac{m^2}{1-\eta^2}\right]S_{mn}(c,\eta)\right\} \tag{5.2.32}$$

$d^2S_{mn}(c,\eta)/d\eta^2$ for c=14.76 and m=0 and m=1 is plotted in Figure V.13.

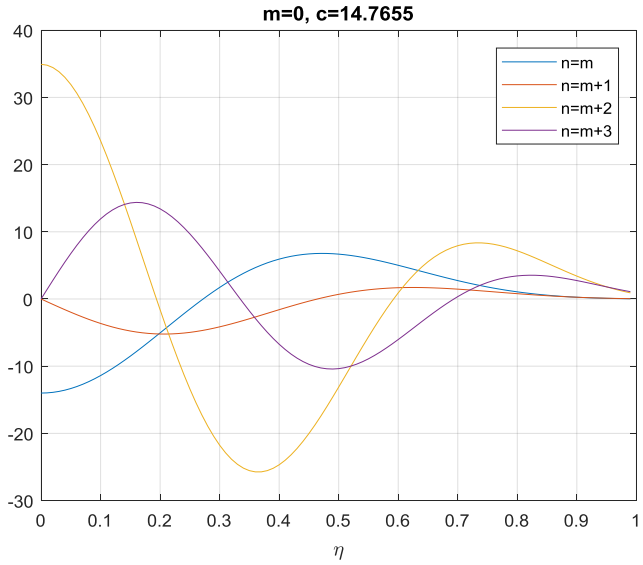

(a)

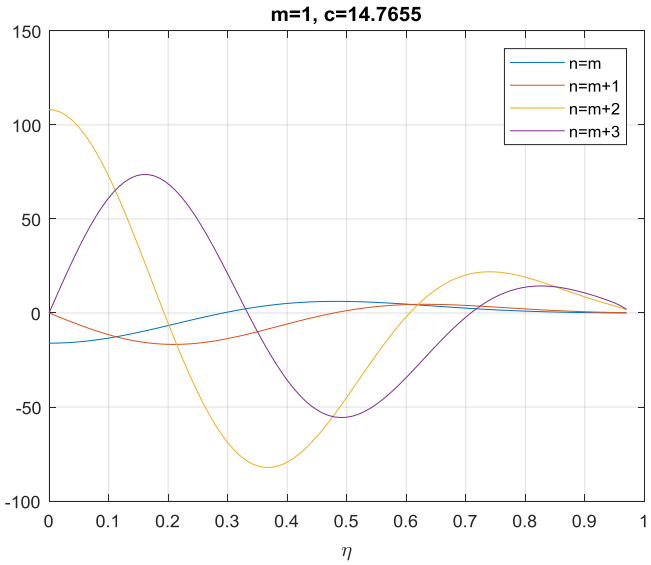

(b)

Figure V.13. $d^2S_{mn}(c,\eta)/d\eta^2$ for (a) m=0, c=14.76 and (b) m=1, c=14.76, at different n.

The first-order derivative of the spheroidal radial function is

$$\frac{dR_{mn}^{(i)}(c,\xi)}{d\xi} = \frac{1}{\sum_{r=0,1}^{\infty}{}' d_r^{mn}(c)\frac{(2m+r)!}{r!}}$$

$$\cdot \sum_{r=0,1}^{\infty}{}' i^{r+m-n} d_r^{mn}(c)\frac{(2m+r)!}{r!}\frac{d\left[\left(\frac{\xi^2-1}{\xi^2}\right)^{m/2} z_{m+r}^{(i)}(c\xi)\right]}{d\xi} \tag{5.2.33}$$

$dR_{mn}^{(1)}(c,\xi)/d\xi$ for c=14.76 and m=0 and m=1 is plotted in Figure V.14 and $dR_{mn}^{(2)}(c,\xi)/d\xi$ for c=14.76, and m=0 and m=1 is plotted in Figure V.15. It observed that the change of $dR_{mn}^{(1)}(c,\xi)/d\xi$ with ξ is very different for m=0 and m=1. In comparison, the change of $dR_{mn}^{(2)}(c,\xi)/d\xi$ with ξ is similar for m=0 and m=1.

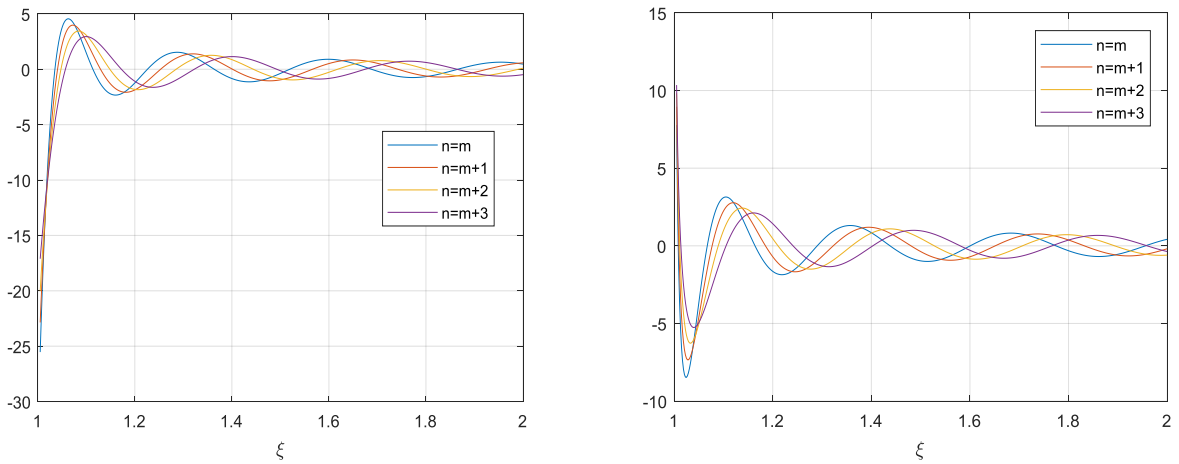

Figure V.14. $dR_{mn}^{(1)}(c,\xi)/d\xi$ for (a) m=0, c=14.76 and (b) m=1, c=14.76, at different n.

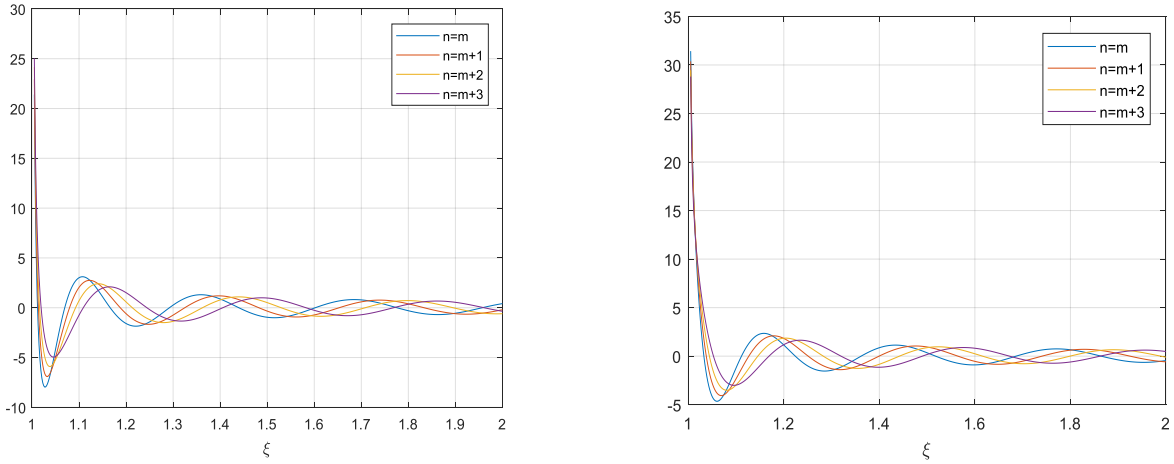

(a) (b)

Figure V.15. $dR_{mn}^{(2)}(c,\xi)/d\xi$ for (a) m=0, c=14.76 and (b) m=1, c=14.76, at different n.

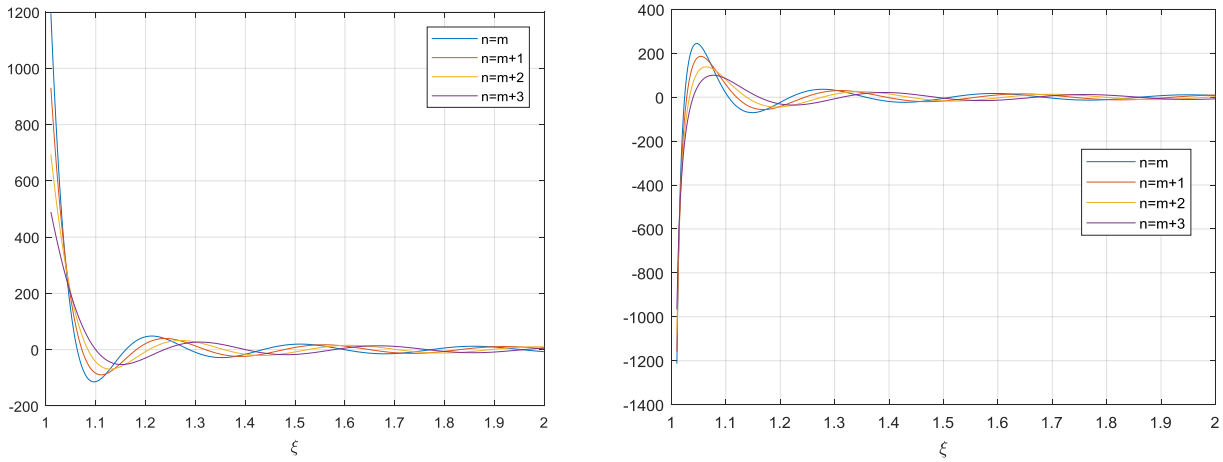

(a) (b)

Figure V.16. $d^2R_{mn}^{(1)}(c,\xi)/d\xi^2$ for (a) m=0, c=14.76 and (b) m=1, c=14.76, at different n.

The second order derivative of the spheroidal radial function is calculated as

$$\frac{d^2}{d\xi^2}R_{mn}(c,\xi)=\frac{1}{\left(\xi^2-1\right)}\left\{\left[\lambda_{mn}-c^2\xi^2+\frac{m^2}{\xi^2-1}\right]R_{mn}(c,\xi)-2\xi\frac{d}{d\xi}R_{mn}(c,\xi)\right\} \quad (5.2.34)$$

Thus, the second order derivative can be calculated using the first-order derivative.

$d^2R_{mn}^{(1)}(c,\xi)/d\xi^2$ for c=14.76 and m=0 and m=1 is plotted in Figure V.16 and $d^2R_{mn}^{(2)}(c,\xi)/d\xi^2$ for c=14.76, and m=0 and m=1 is plotted in Figure V.17. It observed that the change of $d^2R_{mn}^{(1)}(c,\xi)/d\xi^2$ with ξ is very different for m=0 and m=1. In comparison, the change of $dR_{mn}^{(2)}(c,\xi)/d\xi$ with ξ is similar for m=0 and m=1.

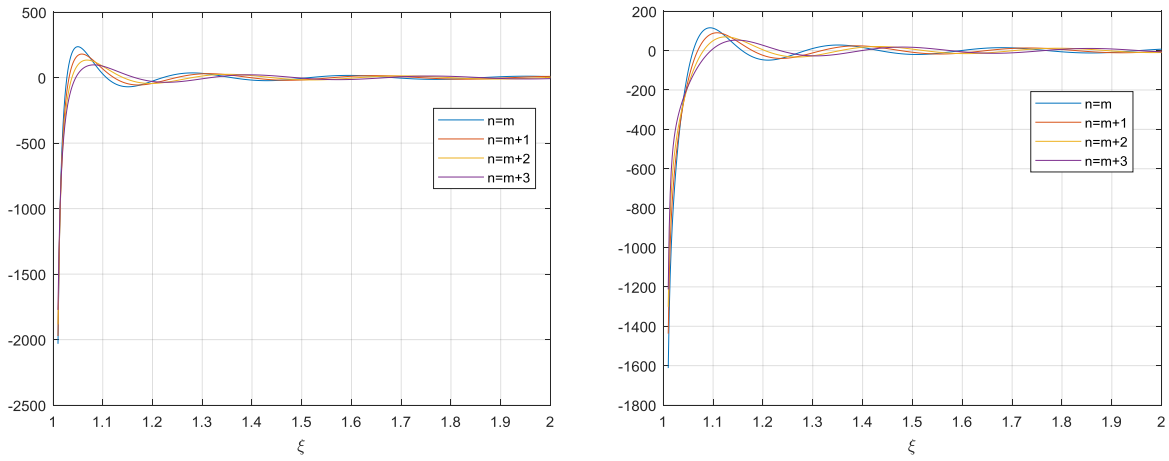

Figure V.17. $d^2R_{mn}^{(2)}(c,\xi)/d\xi^2$ for (a) m=0, c=14.76 and (b) m=1, c=14.76, at different n.

5.2.3 3D Vector Cylindrical Waves

As detailed in [39], the regular scalar 3D cylindrical wave function is

$$Rg\psi_n\left(k_\rho,k_z,\bar{r}\right)=J_n\left(k_\rho\rho\right)e^{ik_z z+in\phi} \tag{5.2.35}$$

This is called 3D cylindrical waves because it depends on k_z while there is no k_z dependence for 2D cylindrical waves. For outgoing waves, the Bessel function is changed to Hankel function:

$$\psi_n\left(k_\rho,k_z,\bar{r}\right)=H_n^{(1)}\left(k_\rho\rho\right)e^{ik_z z+in\phi} \tag{5.2.36}$$

The regular 3D vector cylindrical wave functions are

$$Rg\bar{M}_n\left(k_\rho,k_z,\bar{r}\right)=Rg\bar{m}_n\left(k_\rho,k_z,\bar{\rho}\right)e^{ik_z z+in\phi} \tag{5.2.37}$$

$$Rg\bar{N}_n\left(k_\rho,k_z,\bar{r}\right)=Rg\bar{n}_n\left(k_\rho,k_z,\bar{\rho}\right)e^{ik_z z+in\phi} \tag{5.2.38}$$

where

$$Rg\bar{m}_n\left(k_\rho,k_z,\bar{\rho}\right)=\hat{\rho}\frac{in}{\rho}J_n\left(k_\rho\rho\right)-\hat{\phi}k_\rho J_n'\left(k_\rho\rho\right)$$

$$Rg\bar{n}_n\left(k_\rho,k_z,\bar{\rho}\right)=\hat{\rho}\frac{ik_\rho k_z}{k}J_n'\left(k_\rho\rho\right)-\hat{\phi}\frac{nk_z}{k\rho}J_n\left(k_\rho\rho\right)+\hat{z}\frac{k_\rho^2}{k}J_n\left(k_\rho\rho\right).$$

For outgoing 3D vector cylindrical waves $\bar{M}_n\left(k_\rho,k_z,\bar{r}\right)$ and $\bar{N}_n\left(k_\rho,k_z,\bar{r}\right)$, the Bessel function is changed to Hankel function.

5.3 The Hybrid Method

The hybrid method for NMM3D full-wave simulations of vegetation combines

(iii) Off-the-shelf techniques for single objects. Off-the-shelf techniques, such as HFSS, BOR (Body of Revolution) [12], ICA (Infinite Cylinder approximation) [4], and FEKO are used to solve Maxwell's equations for a complicated single object of a moderate size, such as trunks and branches with leaves attached.

(iv) We developed techniques that (a) extract T matrices of single objects from (i), (b) perform translation addition theorem for vector cylindrical and spheroidal waves, and (c) utilize the Foldy-Lax multiple scattering equations to calculate multiple scattering among the single objects.

In NMM3D full-wave simulations, we use the Foldy-Lax multiple scattering equations (FL) with generalized T matrix. Consider an incident wave $\bar{E}_{inc}$ incident on *N* number of scatterers. In the Foldy-Lax equations, one uses $\bar{E}_{ex}^m$, the final exciting field of scatterer *m*. Let

there be N number of scatterers. The coupled equations of N final exciting fields, $\bar{E}_{ex}^{n}$, $n=1,2,3,...N$ are (Figure V.18) :

$$\bar{E}_{ex}^{m} = \bar{E}_{inc} + \sum_{\substack{n=1 \\ n\neq m}}^{N} \bar{\bar{G}}_{mn}\bar{\bar{T}}_{n}\bar{E}_{ex}^{n} \tag{5.3.1}$$

where $\bar{\bar{T}}^{n}$ is the generalized T matrix of scatterer n, $\bar{\bar{G}}_{mn}$ is the Green's function of propagation of wave from scatterer n to scatterer m, which can be in the near field, intermediate field or far field. Foldy-Lax equations were rigorously derived from Maxwell's equations [4].

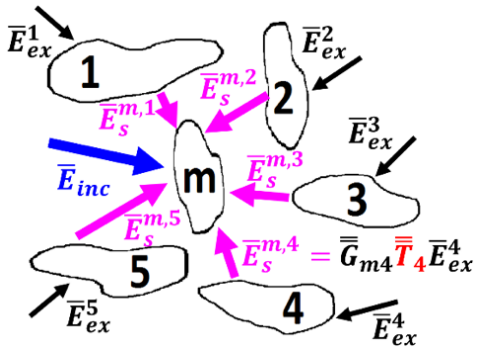

Figure V.18. Illustration of the Foldy-Lax equations with six objects.

In the Hybrid Method, we first use off-the-shelf softwares to solve Maxwell's equations for single objects. This is followed by three steps that we developed: (1) extracting the T matrix of vector cylindrical/spheroidal waves using robust numerical methods; (2) numerical/analytical vector wave transformations where scattered waves from one object are transformed to incident waves on another object; and (3) solving Foldy-Lax equations (FL) and using physical multiple scattering orders of iteration with averaging after each order. The three steps are explained below.

5.3.1 Numerical and Analytical T Matrix Extraction

The exciting fields are expanded in regular vector waves while the scattered waves outside the enclosing surface (∂S) are expressed with outgoing vector waves. Then, the T matrix describes the linear relation between scattering coefficients and the exciting field coefficients [4].

$$\begin{bmatrix} \bar{a}^{S(M)} \\ \bar{a}^{S(N)} \end{bmatrix} = \begin{bmatrix} \bar{\bar{T}}^{(11)} & \bar{\bar{T}}^{(12)} \\ \bar{\bar{T}}^{(21)} & \bar{\bar{T}}^{(22)} \end{bmatrix} \begin{bmatrix} \bar{a}^{E(M)} \\ \bar{a}^{E(N)} \end{bmatrix} = \bar{\bar{T}} \begin{bmatrix} \bar{a}^{E(M)} \\ \bar{a}^{E(N)} \end{bmatrix} \tag{5.3.2}$$

where the size of the T matrix ($\bar{\bar{T}}$) is $2L_{max} \times 2L_{max}$. L_{max} depends on the number of multipole (N_{max}) used. For example, for vector spherical waves, $L_{max} = N_{max}(N_{max} + 2)$ [4]. N_{max} is decided by the electrical size of the scatterer.

To find $\bar{\bar{T}}$ numerically, we excite the scatterer with $2L_{max}$ different incident waves (different incident angles and polarizations) and calculate the scatter fields using off-the-shelf techniques such as BOR, HFSS, FEKO, etc. After the expansion coefficients are calculated, $\bar{\bar{T}}$ is obtained by

$$\bar{\bar{T}} = \begin{bmatrix} \bar{a}_1^{S(M)} & \dots & \bar{a}_{2L_{max}}^{S(M)} \\ \bar{a}_1^{S(N)} & \dots & \bar{a}_{2L_{max}}^{S(N)} \end{bmatrix} \begin{bmatrix} \bar{a}_1^{E(M)} & \dots & \bar{a}_{2L_{max}}^{E(M)} \\ \bar{a}_1^{E(N)} & \dots & \bar{a}_{2L_{max}}^{E(N)} \end{bmatrix}^{-1} \tag{5.3.3}$$

where $\bar{a}_l^E$ and $\bar{a}_l^S$ are the coefficients of exciting field l and the resulting scattered field, respectively.

Thus, the key steps in extracting the T matrix numerically is calculating the expansion coefficients. Since different vector waves have different properties, different methods are used to find the expansion coefficients, as detailed below.

(a) The T Matrix Extraction for Vector Spherical Waves

The scattered fields are expanded using the outgoing vector spherical waves as

$$\bar{E}^S(\bar{r}) = \sum_{m,n}\left[a_{mn}^{S(M)}\bar{M}_{mn}(kr,\theta,\phi) + a_{mn}^{S(N)}\bar{N}_{mn}(kr,\theta,\phi)\right] \tag{5.3.4}$$

where the expansion coefficients $a_{mn}^{S(M)}$ and $a_{mn}^{S(N)}$ are needed to be obtained.

Next, applying dot product with $\bar{M}_{-m'n'}(kr,\theta,\phi)$ and integration over θ and ϕ to the equation,

$$\begin{aligned}&\int_0^{\pi} d\theta \sin\theta \int_0^{2\pi} d\phi \bar{E}^S(\bar{r}) \cdot \bar{M}_{-m'n'}(kr,\theta,\phi) \\ &= \int_0^{\pi} d\theta \sin\theta \int_0^{2\pi} d\phi \sum_{m,n}\left[a_{mn}^{S(M)}\bar{M}_{mn}(kr,\theta,\phi) + a_{mn}^{S(N)}\bar{N}_{mn}(kr,\theta,\phi)\right] \cdot \bar{M}_{-m'n'}(kr,\theta,\phi)\end{aligned} \tag{5.3.5}$$

To calculate the integration on the right hand side, we substitute the expressions for $\bar{M}_{mn}(kr,\theta,\phi)$ and $\bar{N}_{mn}(kr,\theta,\phi)$ as listed in section 5.2. Then,

$$\begin{aligned}&\int_0^{\pi} d\theta \sin\theta \int_0^{2\pi} d\phi \bar{M}_{mn}(kr,\theta,\phi) \cdot \bar{M}_{-m'n'}(kr,\theta,\phi) \\ &= \gamma_{-m'n'} h_{n'}(kr) \gamma_{mn} h_n(kr) \int_0^{\pi} d\theta \sin\theta \int_0^{2\pi} d\phi \bar{C}_{mn}(\theta,\phi) \cdot \bar{C}_{-m'n'}(\theta,\phi) \\ &= \gamma_{-m'n'} h_{n'}(kr) \gamma_{mn} h_n(kr) \delta_{mm'} \delta_{nn'} z_{3m'n'}\end{aligned} \tag{5.3.6}$$

where the orthogonality property is used and $z_{3m'n'} = (-1)^{m'} \dfrac{4\pi n'(n'+1)}{2n'+1}$. The expressions for γ are in section 5.2,

Next,

$$\begin{aligned}&\int_0^{\pi} d\theta \sin\theta \int_0^{2\pi} d\phi \bar{N}_{mn}(kr,\theta,\phi) \cdot \bar{M}_{-m'n'}(kr,\theta,\phi) \\ &= \int_0^{\pi} d\theta \sin\theta \int_0^{2\pi} d\phi \left\{ \gamma_{mn} \left[\frac{n(n+1)h_n(kr)}{kr} \bar{P}_{mn}(\theta,\phi) + \frac{[krh_n(kr)]'}{kr} \bar{B}_{mn}(\theta,\phi) \right] \cdot \left[\gamma_{-m'n'} h_{n'}(kr) \bar{C}_{-m'n'}(\theta,\phi) \right] \right\} \\ &= 0\end{aligned} \tag{5.3.7}$$

Substituting into equation (5.3.5) leads to

$$a_{m'n'}^{S(M)} = \frac{\int_0^{\pi} d\theta \sin\theta \int_0^{2\pi} d\phi \bar{E}^S(\bar{r}) \cdot \bar{M}_{-m'n'}(kr,\theta,\phi)}{\gamma_{m'n'} h_{n'}(kr) \gamma_{-m'n'} h_{n'}(kr) z_{3m'n'}} \tag{5.3.8}$$

Similarly, applying dot product with $\bar{N}_{-m'n'}(kr,\theta,\phi)$ and integration over θ and ϕ to the equation,

$$\begin{aligned}&\int_0^{\pi} d\theta \sin\theta \int_0^{2\pi} d\phi \bar{E}^S(\bar{r}) \cdot \bar{N}_{-m'n'}(kr,\theta,\phi) \\ &= \int_0^{\pi} d\theta \sin\theta \int_0^{2\pi} d\phi \sum_{m,n} \left[a_{mn}^{S(M)} \bar{M}_{mn}(kr,\theta,\phi) + a_{mn}^{S(N)} \bar{N}_{mn}(kr,\theta,\phi) \right] \cdot \bar{N}_{-m'n'}(kr,\theta,\phi)\end{aligned} \tag{5.3.9}$$

Since,

$$\int_0^{\pi} d\theta \sin\theta \int_0^{2\pi} d\phi \bar{M}_{mn}(kr,\theta,\phi) \cdot \bar{N}_{-m'n'}(kr,\theta,\phi) = 0 \tag{5.3.10}$$

and,

$$\begin{aligned}&\int_0^{\pi} d\theta \sin\theta \int_0^{2\pi} d\phi \bar{N}_{mn}(kr,\theta,\phi) \cdot \bar{N}_{-m'n'}(kr,\theta,\phi) \\ &= \gamma_{-m'n'}\gamma_{mn} \left\{ \begin{aligned} &\frac{n'(n'+1)h_{n'}(kr)}{kr} \frac{n(n+1)h_n(kr)}{kr} \int_0^{\pi} d\theta \sin\theta \int_0^{2\pi} d\phi \bar{P}_{-m'n'}(\theta,\phi) \cdot \bar{P}_{mn}(\theta,\phi) \\ &+ \frac{\left[krh_{n'}(kr)\right]'}{kr} \frac{\left[krh_n(kr)\right]'}{kr} \int_0^{\pi} d\theta \sin\theta \int_0^{2\pi} d\phi \bar{B}_{-m'n'}(\theta,\phi) \cdot \bar{B}_{mn}(\theta,\phi) \end{aligned} \right\} \\ &= \gamma_{-m'n'}\gamma_{mn}\delta_{mm'}\delta_{nn'} \left\{ \frac{n'(n'+1)h_{n'}(kr)}{kr} \frac{n(n+1)h_n(kr)}{kr} z_{1m'n'} + \frac{\left[krh_{n'}(kr)\right]'}{kr} \frac{\left[krh_n(kr)\right]'}{kr} z_{2m'n'} \right\}\end{aligned} \tag{5.3.11}$$

Then,

$$a_{m'n'}^{S(N)} = \frac{\int_0^{\pi} d\theta \sin\theta \int_0^{2\pi} d\phi E^S(\bar{r}) \cdot \bar{N}_{-m'n'}(kr,\theta,\phi)}{\gamma_{-m'n'}\gamma_{m'n'} \left[\left(\frac{n'(n'+1)h_{n'}(kr)}{kr} \right)^2 z_{1m'n'} + \left(\frac{\left[krh_{n'}(kr)\right]'}{kr} \right)^2 z_{2m'n'} \right]} \tag{5.3.12}$$

Since m' and n' are dummy variables, we can change them to m and n. Thus

$$a_{mn}^{S(M)} = \frac{\int_0^{\pi} d\theta \sin\theta \int_0^{2\pi} d\phi \bar{E}^S(\bar{r}) \cdot \bar{M}_{-mn}(kr,\theta,\phi)}{\gamma_{mn} h_n(kr) \gamma_{-mn} h_n(kr) z_{3mn}} \tag{5.3.13a}$$

$$a_{mn}^{S(N)} = \frac{\int_0^{\pi} d\theta \sin\theta \int_0^{2\pi} d\phi E^S(\bar{r}) \cdot \bar{N}_{-mn}(kr,\theta,\phi)}{\gamma_{-mn}\gamma_{mn}\left[\left(\frac{n(n+1)h_n(kr)}{kr}\right)^2 z_{1mn} + \left(\frac{[krh_n(kr)]'}{kr}\right)^2 z_{2mn}\right]} \quad (5.3.13b)$$

The scattered fields $E^S(\bar{r})$ is obtained using the off-the-shelf techniques for the single scatterer, such as ICA, BOR, commercial software HFSS, FEKO, etc. After that, the integration in the nominator is calculated numerically.

If the tangential scattered fields are used, the scattered field coefficients can also be obtained using

$$a_{mn}^{S(M)} = [\gamma_{mn} h_n(kR) z_{2mn}]^{-1} \int_0^{\pi} d\theta sin\theta \int_0^{2\pi} d\phi \hat{r} \times \bar{E}^s(r,\theta,\phi) \cdot \bar{B}_{-mn}(\theta,\phi) \quad (5.3.14a)$$

$$a_{mn}^{S(N)} = \left[\gamma_{mn} \frac{[kRh_n(kR)]'}{kR} z_{3mn}\right]^{-1} \int_0^{\pi} d\theta sin\theta \int_0^{2\pi} d\phi \hat{r} \times \bar{E}^s(r,\theta,\phi) \cdot \bar{C}_{-mn}(\theta,\phi) \quad (5.3.14b)$$

The derivations for the above equations are similar to those above.

After the scattered field coefficients are obtained, the next step is calculating the incident field coefficients. For incident plan waves $\bar{E}_i = E_{pi}\hat{p}_i e^{i\bar{k}_i \cdot \bar{r}}$, the vector spherical wave expansion coefficients are [4],

$$a_{mn}^{E(M)} = (-1)^m \frac{(2n+1)}{\gamma_{mn} n(n+1)} i^n \left[E_{pi}(\hat{p}_i \cdot \bar{C}_{-mn}(\theta_i,\phi_i))\right] \quad (5.3.15a)$$

$$a_{mn}^{E(N)} = (-1)^m \frac{(2n+1)}{\gamma_{mn} n(n+1)} i^n \left[E_{pi}\left(\hat{p}_i \cdot (-i\bar{B}_{-mn}(\theta_i,\phi_i))\right)\right] \quad (5.3.15b)$$

where the superscript '*E*' means exciting fields. $\hat{p}_i$ is the polarization (either $\hat{v}$ or $\hat{h}$).

The expressions for both the scattered fields and incident fields are obtained. the T matrix with vector spherical wave expansions for arbitrarily shaped objects is can be obtained. It is noted that this numerical method of extracting T matrix works for the object with arbitrary shape since the scattered fields from the object can be obtained using the commercial software such as HFSS and FEKO. Then, the scattered field coefficients are obtained, and the T matrix is extracted.

(b) The T Matrix Extraction for Vector Spheroidal Waves

For vector spheroidal waves, there is no orthogonality property as for the vector spherical waves; therefore, calculating the scattered field expansion coefficients are more complicated than that for the vector spherical waves.

Using the even and odd modes, the scattered field is expanded as

$$\bar{E}^s = \sum_{m,n}\left[a_{mn}^{S(M),e}\bar{M}_{e,mn}^{a(3)} + a_{mn}^{S(M),o}\bar{M}_{o,mn}^{a(3)} + a_{mn}^{S(N),e}\bar{N}_{e,mn}^{a(3)} + a_{mn}^{S(N),o}\bar{N}_{o,mn}^{a(3)}\right] \tag{5.3.16}$$

where 'e' stands for the even mode and 'o' stands for the odd mode. The superscript '(3)' means the vector spheroidal waves of the third kind, which is the outgoing vector spheroidal waves. The definition of 'a' is in section 5.2. In this section, $a = r$.

Next, finding the tangential fields and applying dot product and integration on both sides,

$$\begin{aligned}&\int_{\partial SO}\hat{\xi}\times\bar{E}^s\cdot\bar{V}_{\sigma',m'n'}^{a(3)}\\&=\sum_{m,n}\begin{bmatrix}a_{mn}^{S(M),e}\int_{\partial SO}\hat{\xi}\times\bar{M}_{e,mn}^{a(3)}\cdot\bar{V}_{\sigma',m'n'}^{a(3)} + a_{mn}^{S(M),o}\int_{\partial SO}\hat{\xi}\times\bar{M}_{o,mn}^{a(3)}\cdot\bar{V}_{\sigma',m'n'}^{a(3)}\\ +a_{mn}^{S(N),e}\int_{\partial SO}\hat{\xi}\times\bar{N}_{e,mn}^{a(3)}\cdot\bar{V}_{\sigma',m'n'}^{a(3)} + a_{mn}^{S(N),o}\int_{\partial SO}\hat{\xi}\times\bar{N}_{o,mn}^{a(3)}\cdot\bar{V}_{\sigma',m'n'}^{a(3)}\end{bmatrix}\end{aligned} \tag{5.3.17}$$

where $\sigma = e\ or\ v$, and $V = M\ or\ N$. The integration is performed over the spheroidal surface.

To simply the expression, let $\int_{\partial SO}\hat{\xi}\times\bar{E}^s\cdot\bar{V}_{\sigma',m'n'}^{a(3)} = b_{m'n'}^{V,\sigma}$, $\int_{\partial SO}\hat{\xi}\times\bar{M}_{e,mn}^{a(3)}\cdot\bar{V}_{\sigma',m'n'}^{a(3)} = C_{mnm'n'}^{V,\sigma,M,e}$, $\int_{\partial SO}\hat{\xi}\times\bar{M}_{o,mn}^{a(3)}\cdot\bar{V}_{\sigma',m'n'}^{a(3)} = C_{mnm'n'}^{V,\sigma,M,o}$, $\int_{\partial SO}\hat{\xi}\times\bar{N}_{e,mn}^{a(3)}\cdot\bar{V}_{\sigma',m'n'}^{a(3)} = C_{mnm'n'}^{V,\sigma,N,e}$, and $\int_{\partial SO}\hat{\xi}\times\bar{N}_{o,mn}^{a(3)}\cdot\bar{V}_{\sigma',m'n'}^{a(3)} = C_{mnm'n'}^{V,\sigma,N,o}$, then,

$$b_{m'n'}^{V,\sigma} = \sum_{m,n}\left[C_{mnm'n'}^{V,\sigma,M,e}a_{mn}^{S(M),e} + C_{mnm'n'}^{V,\sigma,M,o}a_{mn}^{S(M),o} + C_{mnm'n'}^{V,\sigma,N,e}a_{mn}^{S(N),e} + C_{mnm'n'}^{V,\sigma,N,o}a_{mn}^{S(N),o}\right] \tag{5.3.18}$$

In matrix form,

$$\bar{b} = \bar{\bar{C}}\bar{a}^S \tag{5.3.19}$$

Then, the scattered field coefficients are obtained as

$$\bar{a}^S = \bar{\bar{C}}^{-1}\bar{b} \tag{5.3.20}$$

Thus, the key points are to find the matrix $\bar{\bar{C}}$ and the column vector $\bar{b}$.

There are four combinations for $\bar{V}^{a(3)}_{\sigma',m'n'}$: $\bar{M}^{a(3)}_{e,m'n'}$, $\bar{M}^{a(3)}_{o,m'n'}$, $\bar{N}^{a(3)}_{e,m'n'}$, or $\bar{N}^{a(3)}_{o,m'n'}$. To simply the integration, a function of η is also multiplied. Thus, $\bar{V}^{a(3)}_{\sigma',m'n'}$ becomes $\bar{M}^{a(3)}_{e,m'n'}g^{Me}(\eta)$, $\bar{M}^{a(3)}_{o,m'n'}g^{Mo}(\eta)$, $\bar{N}^{a(3)}_{e,m'n'}g^{Ne}(\eta)$, or $\bar{N}^{a(3)}_{o,m'n'}g^{No}(\eta)$. The expression of the function will be decided later.

First, let $\bar{V}^{a(3)}_{\sigma',m'n'} = g^{Me}(\eta)\bar{M}^{a(3)}_{e,m'n'}$.

$$\begin{aligned}\hat{\xi}\times\bar{M}^{a(3)}_{e,mn} &= \hat{\xi}\times\left(M^{a(3)}_{e,mn\eta}\hat{\eta} + M^{a(3)}_{e,mn\xi}\hat{\xi} + M^{a(3)}_{e,mn\phi}\hat{\phi}\right)\\ &= -M^{a(3)}_{e,mn\eta}\hat{\phi} + M^{a(3)}_{e,mn\phi}\hat{\eta}\end{aligned} \tag{5.3.21}$$

where the expressions for different components of $\bar{M}^{a(3)}_{e,mn}$ are in section 5.2.

Then,

$$\begin{aligned}C^{M,e,M,e}_{m'n'mn} &= \int_{\partial SO}\hat{\xi}\times\bar{M}^{a(3)}_{e,mn}\cdot g^{Me}(\eta)\bar{M}^{a(3)}_{e,m'n'}\\ &= \int_{\partial SO} g^{Me}(\eta)\left(-M^{a(3)}_{e,mn\eta}\hat{\phi} + M^{a(3)}_{e,mn\phi}\hat{\eta}\right)\cdot\left(M^{a(3)}_{e,m'n'\eta}\hat{\eta}' + M^{a(3)}_{e,m'n'\xi}\hat{\xi} + M^{a(3)}_{e,m'n'\phi}\hat{\phi}\right)\\ &= \int_{\partial SO} g^{Me}(\eta)\left[-M^{a(3)}_{e,mn\eta}M^{a(3)}_{e,m'n'\phi} + M^{a(3)}_{e,mn\phi}M^{a(3)}_{e,m'n'\eta}\right]\\ &= f^2\left(\xi^2-1\right)^{\frac{1}{2}}\int_0^{2\pi}d\phi\int_{-1}^{1}d\eta\left(\xi^2-\eta^2\right)^{\frac{1}{2}} g^{Me}(\eta)\left[-M^{a(3)}_{e,mn\eta}M^{a(3)}_{e,m'n'\phi} + M^{a(3)}_{e,mn\phi}M^{a(3)}_{e,m'n'\eta}\right]\end{aligned} \tag{5.3.22}$$

where $f = d/2$ and d is the interfocal distance.

To simply the expression, let

$$\begin{aligned}M^{r(i)}_{e,mn\eta} &= f^{M\eta}_{mn}\sin(m\phi)\\ M^{r(i)}_{o,mn\eta} &= -f^{M\eta}_{mn}\cos(m\phi)\\ M^{r(i)}_{e,mn\phi} &= f^{M\phi}_{mn}\cos(m\phi)\\ M^{r(i)}_{o,mn\phi} &= f^{M\phi}_{mn}\sin(m\phi)\end{aligned} \tag{5.3.23}$$

By comparing the expressions in section 5.2, we obtain

$$f_{mn}^{M\eta} = \frac{m\xi}{\left(\xi^2-\eta^2\right)^{\frac{1}{2}}\left(1-\eta^2\right)^{\frac{1}{2}}} S_{mn} R_{mn}^{(3)} \tag{5.3.24}$$

$$f_{mn}^{M\phi} = \frac{\left(\xi^2-1\right)^{\frac{1}{2}}\left(1-\eta^2\right)^{\frac{1}{2}}}{\xi^2-\eta^2}\left[\xi\frac{dS_{mn}}{d\eta}R_{mn}^{(3)} - \eta S_{mn}\frac{dR_{mn}^{(3)}}{d\xi}\right] \tag{5.3.25}$$

Thus,

$$C_{m'n'mn}^{M,e,M,e} = f^2\left(\xi^2-1\right)^{\frac{1}{2}}\left\{\begin{array}{l}\left[\int_0^{2\pi} d\phi \sin(m\phi)\cos\left(m'\phi\right)\int_{-1}^{1} d\eta g^{Me}(\eta)\left(\xi^2-\eta^2\right)^{\frac{1}{2}}\left(-f_{mn}^{M\eta}(\eta)\, f_{m'n'}^{M\phi}(\eta)\right)\right] \\ +\left[\int_0^{2\pi} d\phi \cos(m\phi)\sin\left(m'\phi\right)\int_{-1}^{1} d\eta g^{Me}(\eta)\left(\xi^2-\eta^2\right)^{\frac{1}{2}} f_{mn}^{M\phi}(\eta)\, f_{m'n'}^{M\eta}(\eta)\right]\end{array}\right\} \tag{5.3.26}$$

It is noted that $f_{mn}^{M\eta}$ and $f_{mn}^{M\phi}$ are only functions of η, since the ξ is a constant for a defined spheroidal surface.

Using the property that

$$\int_0^{2\pi} \sin(m\phi)\cos\left(m'\phi\right)d\phi = 0 \tag{5.3.27}$$

We obtain

$$C_{mnm'n'}^{M,e,M,e} = 0 \tag{5.3.28}$$

Next,

$$\begin{aligned} C_{m'n'mn}^{M,e,M,o} &= \int_{\partial SO} \hat{\xi}\times \bar{M}_{o,mn}^{a(3)} \cdot \bar{M}_{e,m'n'}^{a(3)} g^{Me}(\eta) \\ &= f^2\left(\xi^2-1\right)^{\frac{1}{2}}\int_0^{2\pi} d\phi\int_{-1}^{1} d\eta\left(\xi^2-\eta^2\right)^{\frac{1}{2}} g^{Me}(\eta)\left[-M_{o,mn\eta}^{a(3)} M_{e,m'n'\phi}^{a(3)} + M_{o,mn\phi}^{a(3)} M_{e,m'n'\eta}^{a(3)}\right] \\ &= f^2\left(\xi^2-1\right)^{\frac{1}{2}}\int_0^{2\pi} d\phi\int_{-1}^{1} d\eta\left(\xi^2-\eta^2\right)^{\frac{1}{2}} g^{Me}(\eta)\left[\begin{array}{l} f_{mn}^{M\eta}(\eta)\cos(m\phi)\, f_{m'n'}^{M\phi}(\eta)\cos\left(m'\phi\right) \\ + f_{mn}^{M\phi}(\eta)\sin(m\phi)\, f_{m'n'}^{M\eta}(\eta)\sin\left(m'\phi\right)\end{array}\right] \end{aligned} \tag{5.3.29}$$

Using the property that

$$\int_0^{2\pi} \sin(m\phi)\sin\left(m'\phi\right)d\phi = \begin{Bmatrix} 0, \text{ if } m = m' = 0 \\ \pi\delta_{mm'}, \text{ otherwise} \end{Bmatrix} \tag{5.3.30}$$

$$\int_0^{2\pi} \cos(m\phi)\cos\left(m'\phi\right)d\phi = \begin{Bmatrix} 2\pi, \text{ if } m = m' = 0 \\ \pi\delta_{mm'}, \text{ otherwise} \end{Bmatrix} \tag{5.3.31}$$

Thus,

$$C_{m'n'mn}^{M,e,M,o} = \pi\delta_{mm'} f^2\left(\xi^2-1\right)^{\frac{1}{2}} \int_{-1}^{1} d\eta \left(\xi^2-\eta^2\right)^{\frac{1}{2}} g^{Me}(\eta)\left[f_{mn}^{M\eta}(\eta) f_{m'n'}^{M\phi}(\eta) + f_{mn}^{M\phi}(\eta) f_{m'n'}^{M\eta}(\eta)\right] \tag{5.3.32}$$

The integration will be examined later. It is noted that, the case that $m = m' = 0$ is excluded here.

Next,

$$\begin{aligned} C_{m'n'mn}^{M,e,N,e} &= \int_{\partial SO} \hat{\xi} \times \bar{N}_{e,mn}^{a(3)} \cdot \bar{M}_{e,m'n'}^{a(3)} g^{Me}(\eta) \\ &= f^2\left(\xi^2-1\right)^{\frac{1}{2}} \int_0^{2\pi} d\phi \int_{-1}^{1} d\eta \left(\xi^2-\eta^2\right)^{\frac{1}{2}} g^{Me}(\eta)\left[-N_{e,mn\eta}^{a(3)} M_{e,m'n'\phi}^{a(3)} + N_{e,mn\phi}^{a(3)} M_{e,m'n'\eta}^{a(3)}\right] \end{aligned} \tag{5.3.33}$$

To simplify the expressions, let

$$\begin{aligned} N_{e,mn\eta}^{r(i)} &= f_{mn}^{N\eta}\cos(m\phi) \\ N_{o,mn\eta}^{r(i)} &= f_{mn}^{N\eta}\sin(m\phi) \\ N_{e,mn\phi}^{r(i)} &= f_{mn}^{N\phi}\sin(m\phi) \\ N_{o,mn\phi}^{r(i)} &= -f_{mn}^{N\phi}\cos(m\phi) \end{aligned} \tag{5.3.34}$$

By comparing with the expressions in section 5.2, we obtain

$$f_{mn}^{N\eta} = \frac{2\left(1-\eta^2\right)^{\frac{1}{2}}}{kd\left(\xi^2-\eta^2\right)^{\frac{1}{2}}} \left[\begin{aligned} &\frac{dS_{mn}}{d\eta}\frac{\partial}{\partial\xi}\left(\frac{\xi\left(\xi^2-1\right)}{\xi^2-\eta^2}R_{mn}^{(i)}\right) - \eta S_{mn}\frac{\partial}{\partial\xi}\left(\frac{\xi^2-1}{\xi^2-\eta^2}\frac{dR_{mn}^{(i)}}{d\xi}\right) \\ &+ \frac{m^2\eta}{\left(1-\eta^2\right)\left(\xi^2-1\right)} S_{mn} R_{mn}^{(i)} \end{aligned} \right] \tag{5.3.35}$$

$$f_{mn}^{N\phi} = \frac{2m\left(1-\eta^2\right)^{\frac{1}{2}}\left(\xi^2-1\right)^{\frac{1}{2}}}{kd\left(\xi^2-\eta^2\right)} \left[\frac{-1}{\xi^2-1}\frac{d}{d\eta}\left(\eta S_{mn}\right)R_{mn}^{(i)} - \frac{1}{1-\eta^2} S_{mn}\frac{d}{d\xi}\left(\xi R_{mn}^{(i)}\right)\right] \left[\begin{matrix} \sin \\ -\cos \end{matrix} (m\phi)\right] \tag{5.3.36}$$

Then,

$$C_{m'n'mn}^{M,e,N,e} = f^2\left(\xi^2-1\right)^{\frac{1}{2}}\int_0^{2\pi}d\phi\int_{-1}^{1}d\eta\left(\xi^2-\eta^2\right)^{\frac{1}{2}}g^{Me}(\eta)\begin{bmatrix}-f_{mn}^{N\eta}(\eta)\cos(m\phi)\,f_{m'n'}^{M\phi}(\eta)\cos\left(m'\phi\right)\\+f_{mn}^{N\phi}(\eta)\sin(m\phi)\,f_{m'n'}^{M\eta}(\eta)\sin\left(m'\phi\right)\end{bmatrix} \quad (5.3.37)$$

$$C_{m'n'mn}^{M,e,N,e} = \pi\delta_{mm'}f^2\left(\xi^2-1\right)^{\frac{1}{2}}\int_{-1}^{1}d\eta\left(\xi^2-\eta^2\right)^{\frac{1}{2}}g^{Me}(\eta)\left[-f_{mn}^{N\eta}(\eta)\,f_{m'n'}^{M\phi}(\eta)+f_{mn}^{N\phi}(\eta)\,f_{m'n'}^{M\eta}(\eta)\right] \quad (5.3.38)$$

Next,

$$\begin{aligned}C_{m'n'mn}^{M,e,N,o} &= \int_{\partial SO}\hat{\xi}\times\bar{N}_{o,mn}^{a(3)}\cdot\bar{M}_{e,m'n'}^{a(3)}g^{Me}(\eta)\\ &= f^2\left(\xi^2-1\right)^{\frac{1}{2}}\int_0^{2\pi}d\phi\int_{-1}^{1}d\eta\left(\xi^2-\eta^2\right)^{\frac{1}{2}}g^{Me}(\eta)\left[-N_{o,mn\eta}^{a(3)}M_{e,m'n'\phi}^{a(3)}+N_{o,mn\phi}^{a(3)}M_{e,m'n'\eta}^{a(3)}\right] \quad (5.3.39)\\ &= f^2\left(\xi^2-1\right)^{\frac{1}{2}}\int_0^{2\pi}d\phi\int_{-1}^{1}d\eta\left(\xi^2-\eta^2\right)^{\frac{1}{2}}g^{Me}(\eta)\begin{bmatrix}-f_{mn}^{N\eta}(\eta)\sin(m\phi)\,f_{m'n'}^{M\phi}(\eta)\cos\left(m'\phi\right)\\-f_{mn}^{N\phi}(\eta)\cos(m\phi)\,f_{m'n'}^{M\eta}(\eta)\sin\left(m'\phi\right)\end{bmatrix}\end{aligned}$$

Thus,

$$C_{mnm'n'}^{N,o,M,e} = 0 \quad (5.3.40)$$

Secondly, let $\bar{V}_{\sigma',m'n'}^{a(3)} = g^{Mo}(\eta)\bar{M}_{o,m'n'}^{a(3)}$. Using similar derivations as (5.3.21) to (5.3.40), we obtain

$$\begin{aligned}C_{m'n'mn}^{M,o,M,e} &= \int_{\partial SO}\hat{\xi}\times\bar{M}_{e,mn}^{a(3)}\cdot\bar{M}_{o,m'n'}^{a(3)}g^{Mo}(\eta)\\ &= \pi\delta_{mm'}f^2\left(\xi^2-1\right)^{\frac{1}{2}}\int_{-1}^{1}d\eta\left(\xi^2-\eta^2\right)^{\frac{1}{2}}g^{Mo}(\eta)\left[-f_{mn}^{M\eta}(\eta)\,f_{m'n'}^{M\phi}(\eta)-f_{mn}^{M\phi}(\eta)\,f_{m'n'}^{M\eta}(\eta)\right]\end{aligned} \quad (5.3.41)$$

$$C_{m'n'mn}^{M,o,M,o} = \int_{\partial SO}\hat{\xi}\times\bar{M}_{o,mn}^{a(3)}\cdot\bar{M}_{o,m'n'}^{a(3)}g^{Mo}(\eta) = 0 \quad (5.3.42)$$

$$C_{m'n'mn}^{M,o,N,e} = \int_{\partial SO}\hat{\xi}\times\bar{N}_{e,mn}^{a(3)}\cdot\bar{M}_{o,m'n'}^{a(3)}g^{Mo}(\eta) = 0 \quad (5.3.43)$$

$$\begin{aligned}C_{m'n'mn}^{M,o,N,o} &= \int_{\partial SO}\hat{\xi}\times\bar{N}_{o,mn}^{a(3)}\cdot\bar{M}_{o,m'n'}^{a(3)}g^{Mo}(\eta)\\ &= \pi\delta_{mm'}f^2\left(\xi^2-1\right)^{\frac{1}{2}}\int_{-1}^{1}d\eta\left(\xi^2-\eta^2\right)^{\frac{1}{2}}g^{Mo}(\eta)\left[-f_{mn}^{N\eta}(\eta)\,f_{m'n'}^{M\phi}(\eta)+f_{mn}^{N\phi}(\eta)\,f_{m'n'}^{M\eta}(\eta)\right]\end{aligned} \quad (5.3.44)$$

Thirdly, let $\bar{V}_{\sigma',m'n'}^{a(3)} = g^{Ne}(\eta)\bar{N}_{e,m'n'}^{a(3)}$. Similarly, we obtain

$$
\begin{aligned}
C_{m'n'mn}^{N,e,M,e} &= \int_{\partial SO} \hat{\xi} \times \bar{M}_{e,mn}^{a(3)} \cdot \bar{N}_{e,m'n'}^{a(3)} g^{Ne}(\eta) \\
&= \pi \delta_{mm'} f^2 \left(\xi^2 - 1\right)^{\frac{1}{2}} \int_{-1}^{1} d\eta \left(\xi^2 - \eta^2\right)^{\frac{1}{2}} g^{Ne}(\eta) \left[- f_{mn}^{M\eta}(\eta) f_{m'n'}^{N\phi}(\eta) + f_{mn}^{M\phi}(\eta) f_{m'n'}^{N\eta}(\eta) \right]
\end{aligned} \tag{5.3.45}
$$

$$
C_{m'n'mn}^{N,e,M,o} = \int_{\partial SO} \hat{\xi} \times \bar{M}_{o,mn}^{a(3)} \cdot \bar{N}_{e,m'n'}^{a(3)} g^{Ne}(\eta) = 0 \tag{5.3.46}
$$

$$
C_{m'n'mn}^{N,e,N,e} = \int_{\partial SO} \hat{\xi} \times \bar{N}_{e,mn}^{a(3)} \cdot \bar{N}_{e,m'n'}^{a(3)} g^{Ne}(\eta) = 0 \tag{5.3.47}
$$

$$
\begin{aligned}
C_{m'n'mn}^{N,e,N,o} &= \int_{\partial SO} \hat{\xi} \times \bar{N}_{o,mn}^{a(3)} \cdot \bar{N}_{e,m'n'}^{a(3)} g^{Ne}(\eta) \\
&= \pi \delta_{mm'} f^2 \left(\xi^2 - 1\right)^{\frac{1}{2}} \int_{-1}^{1} d\eta \left(\xi^2 - \eta^2\right)^{\frac{1}{2}} g^{Ne}(\eta) \left[- f_{mn}^{N\eta}(\eta) f_{m'n'}^{N\phi}(\eta) - f_{mn}^{N\phi}(\eta) f_{m'n'}^{N\eta}(\eta) \right]
\end{aligned} \tag{5.3.48}
$$

Fourthly, let $\bar{V}_{\sigma',m'n'}^{a(3)} = g^{No}(\eta) \bar{N}_{o,m'n'}^{a(3)}$. Similarly, we obtain

$$
C_{m'n'mn}^{N,o,M,e} = \int_{\partial SO} \hat{\xi} \times \bar{M}_{e,mn}^{a(3)} \cdot \bar{N}_{o,m'n'}^{a(3)} g^{No}(\eta) = 0 \tag{5.3.49}
$$

$$
\begin{aligned}
C_{m'n'mn}^{N,o,M,o} &= \int_{\partial SO} \hat{\xi} \times \bar{M}_{o,mn}^{a(3)} \cdot \bar{N}_{o,m'n'}^{a(3)} g^{No}(\eta) \\
&= \pi \delta_{mm'} f^2 \left(\xi^2 - 1\right)^{\frac{1}{2}} \int_{-1}^{1} d\eta \left(\xi^2 - \eta^2\right)^{\frac{1}{2}} g^{No}(\eta) \left[- f_{mn}^{M\eta}(\eta) f_{m'n'}^{N\phi}(\eta) + f_{mn}^{M\phi}(\eta) f_{m'n'}^{N\eta}(\eta) \right]
\end{aligned} \tag{5.3.50}
$$

$$
\begin{aligned}
C_{m'n'mn}^{N,o,N,e} &= \int_{\partial SO} \hat{\xi} \times \bar{N}_{e,mn}^{a(3)} \cdot \bar{N}_{o,m'n'}^{a(3)} g^{No}(\eta) \\
&= \pi \delta_{mm'} f^2 \left(\xi^2 - 1\right)^{\frac{1}{2}} \int_{-1}^{1} d\eta \left(\xi^2 - \eta^2\right)^{\frac{1}{2}} g^{No}(\eta) \left[f_{mn}^{N\eta}(\eta) f_{m'n'}^{N\phi}(\eta) + f_{mn}^{N\phi}(\eta) f_{m'n'}^{N\eta}(\eta) \right]
\end{aligned} \tag{5.3.51}
$$

$$
C_{m'n'mn}^{N,o,N,o} = \int_{\partial SO} \hat{\xi} \times \bar{N}_{o,mn}^{a(3)} \cdot \bar{N}_{o,m'n'}^{a(3)} g^{No}(\eta) = 0 \tag{5.3.52}
$$

In matrix form,

$$
\begin{bmatrix} \bar{b}^{M,e} \\ \bar{b}^{M,o} \\ \bar{b}^{N,e} \\ \bar{b}^{N,o} \end{bmatrix} = \begin{bmatrix} \bar{\bar{C}}^{M,e,M,e} & \bar{\bar{C}}^{M,e,M,o} & \bar{\bar{C}}^{M,e,N,e} & \bar{\bar{C}}^{M,e,N,o} \\ \bar{\bar{C}}^{M,e,M,o} & \bar{\bar{C}}^{M,o,M,o} & \bar{\bar{C}}^{N,e,M,o} & \bar{\bar{C}}^{N,o,M,o} \\ \bar{\bar{C}}^{M,e,N,e} & \bar{\bar{C}}^{M,o,N,e} & \bar{\bar{C}}^{N,e,N,e} & \bar{\bar{C}}^{N,o,N,e} \\ \bar{\bar{C}}^{M,e,N,o} & \bar{\bar{C}}^{M,o,N,o} & \bar{\bar{C}}^{N,e,N,o} & \bar{\bar{C}}^{N,o,N,o} \end{bmatrix} \begin{bmatrix} \bar{a}^{S(M),e} \\ \bar{a}^{S(M),o} \\ \bar{a}^{S(N),e} \\ \bar{a}^{S(N),o} \end{bmatrix} \tag{5.3.53}
$$

where $\bar{\bar{C}}^{V',\sigma',V,\sigma} = \begin{bmatrix} C_{1,1}^{V',\sigma',V,\sigma} & C_{1,2}^{V',\sigma',V,\sigma} & \cdots & C_{1,L\max}^{V',\sigma',V,\sigma} \\ C_{2,1}^{V',\sigma',V,\sigma} & C_{2,2}^{V',\sigma',V,\sigma} & \cdots & C_{2,L\max}^{V',\sigma',V,\sigma} \\ \vdots & \vdots & \ddots & \vdots \\ C_{L\max,1}^{V',\sigma',V,\sigma} & C_{L\max,2}^{V',\sigma',V,\sigma} & \cdots & C_{L\max,L\max}^{V',\sigma',V,\sigma} \end{bmatrix}$.

The combined index is used that $(m,n) \to l$, where $l = (n+2)(n-1)/2 + m + 1$. Following is the example of using combined index to map (m,n) to l

m	0	1	0	1	2	0	1	2	…
n	1	1	2	2	2	3	3	3	…
l	1	2	3	4	5	6	7	8	…

Then, $\bar{\bar{C}}_{l',l}^{V',\sigma',V,\sigma} = C_{m'n'mn}^{V',\sigma',V,\sigma}$. The size of the T matrix is decided by $N_{\max}$. For example, when $N_{\max} = 2,\ L_{\max} = \dfrac{N_{\max}(N_{\max}+3)}{2} = 6.$ The size of the T matrix is 24 by 24.

To calculate $C_{m'n'mn}^{V',\sigma',V,\sigma}$, the next step is to calculate the integrations over η. Following is a summary of the integration needed to be computed.

$$\begin{aligned} &\int_{-1}^{1} d\eta \left(\xi^2 - \eta^2\right)^{\frac{1}{2}} f_{mn}^{M\eta}(\eta)\, f_{m'n'}^{M\phi}(\eta)\, g(\eta) \\ &\int_{-1}^{1} d\eta \left(\xi^2 - \eta^2\right)^{\frac{1}{2}} f_{mn}^{N\eta}(\eta)\, f_{m'n'}^{M\phi}(\eta)\, g(\eta) \\ &\int_{-1}^{1} d\eta \left(\xi^2 - \eta^2\right)^{\frac{1}{2}} f_{mn}^{N\phi}(\eta)\, f_{m'n'}^{M\eta}(\eta)\, g(\eta) \\ &\int_{-1}^{1} d\eta \left(\xi^2 - \eta^2\right)^{\frac{1}{2}} f_{mn}^{N\phi}(\eta)\, f_{m'n'}^{N\eta}(\eta)\, g(\eta) \end{aligned} \tag{5.3.54}$$

where $g^{Me}(\eta) = g^{Mo}(\eta) = g^{Ne}(\eta) = g^{No}(\eta) = g(\eta)$.

The analytical solutions of the integrations are not available. Thus, we use numerical integration. The values for the values of $S_{mn}(c,\eta)$, $R_{mn}^{(3)}(c,\xi)$ and their first and second derivatives have been computed in section 5.2. Then, $f_{mn}^{M\eta}(\eta)$ and $f_{mn}^{M\phi}(\eta)$ are ready to be computed. For

$f_{mn}^{N\eta}(\eta)$ and $f_{mn}^{N\phi}(\eta)$, further computations are conducted (e.g. computations of $\frac{\partial}{\partial\xi}\left(\frac{\xi\left(\xi^2-1\right)}{\xi^2-\eta^2}R_{mn}^{(i)}\right)$) so that their expressions contains $S_{mn}(c,\eta)$, $R_{mn}^{(3)}(c,\xi)$ and their first and second derivatives explicitly. The final expression to be computed is as below.

$$f_{mn}^{N\eta}(\eta)=\frac{2\left(1-\eta^2\right)^{\frac{1}{2}}}{kd\left(\xi^2-\eta^2\right)^{\frac{1}{2}}}\left[\begin{array}{l}\frac{dS_{mn}}{d\eta}\left(\left(\frac{\xi\left(\xi^2-1\right)}{\xi^2-\eta^2}\right)\frac{dR_{mn}^{(i)}}{d\xi}+\left(\frac{\left(\xi^4+\xi^2\right)-\left(3\xi^2-1\right)\eta^2}{\left(\xi^2-\eta^2\right)^2}\right)R_{mn}^{(i)}\right)\\ -\eta S_{mn}\left(\left(\frac{\xi^2-1}{\xi^2-\eta^2}\right)\frac{d^2R_{mn}^{(i)}}{d\xi^2}+\left(\frac{2\xi\left(1-\eta^2\right)}{\left(\xi^2-\eta^2\right)^2}\right)\frac{dR_{mn}^{(i)}}{d\xi}\right)\\ +\frac{m^2\eta}{\left(1-\eta^2\right)\left(\xi^2-1\right)}S_{mn}R_{mn}^{(i)}\end{array}\right] \tag{5.3.55}$$

$$f_{mn}^{N\phi}=\frac{2m\left(1-\eta^2\right)^{\frac{1}{2}}\left(\xi^2-1\right)^{\frac{1}{2}}}{kd\left(\xi^2-\eta^2\right)}\left[\begin{array}{l}\frac{-1}{\xi^2-1}\left(S_{mn}+\eta\frac{dS_{mn}}{d\eta}\right)R_{mn}^{(i)}\\ -\frac{1}{1-\eta^2}S_{mn}\left(R_{mn}^{(i)}+\xi\frac{dR_{mn}^{(i)}}{d\xi}\right)\end{array}\right] \tag{5.3.56}$$

To avoid singularity, let $g^{Me}(\eta)=g^{Mo}(\eta)=g^{Ne}(\eta)=g^{No}(\eta)=\left(1-\eta^2\right)\left(\xi^2-\eta^2\right)^3$. Thus,

$$f_{mn}^{M\eta}(\eta)\left(1-\eta^2\right)^{1/2}\left(\xi^2-\eta^2\right)^{3/2}=m\xi\left(\xi^2-\eta^2\right)S_{mn}R_{mn}^{(i)} \tag{5.3.57}$$

$$f_{mn}^{M\phi}(\eta)\left(1-\eta^2\right)^{1/2}\left(\xi^2-\eta^2\right)^{3/2}=\left(\xi^2-1\right)^{\frac{1}{2}}\left(1-\eta^2\right)\left(\xi^2-\eta^2\right)^{\frac{1}{2}}\left[\xi\frac{dS_{mn}}{d\eta}R_{mn}^{(i)}-\eta S_{mn}\frac{dR_{mn}^{(i)}}{d\xi}\right] \tag{5.3.58}$$

$$\begin{aligned}&f_{mn}^{N\eta}(\eta)\left(1-\eta^2\right)^{1/2}\left(\xi^2-\eta^2\right)^{5/2}\\&=\frac{2}{kd}\left[\begin{array}{c}\frac{dS_{mn}}{d\eta}\left(\left(\xi\left(\xi^2-1\right)\left(\xi^2-\eta^2\right)\left(1-\eta^2\right)\right)\frac{dR_{mn}^{(i)}}{d\xi}+\left(\left(\xi^4+\xi^2-\left(3\xi^2-1\right)\eta^2\right)\left(1-\eta^2\right)\right)R_{mn}^{(i)}\right)\\ -\eta S_{mn}\left(\left(\left(\xi^2-1\right)\left(\xi^2-\eta^2\right)\left(1-\eta^2\right)\right)\frac{d^2R_{mn}^{(i)}}{d\xi^2}+\left(2\xi\left(1-\eta^2\right)^2\right)\frac{dR_{mn}^{(i)}}{d\xi}\right)\\ +\frac{m^2\eta\left(\xi^2-\eta^2\right)^2}{\left(\xi^2-1\right)}S_{mn}R_{mn}^{(i)}\end{array}\right]\end{aligned} \tag{5.3.59}$$

$$f_{mn}^{N\phi}(\eta)\left(1-\eta^2\right)^{1/2}\left(\xi^2-\eta^2\right)^{3/2}=\frac{2m\left(\xi^2-1\right)^{\frac{1}{2}}\left(\xi^2-\eta^2\right)^{1/2}}{kd}\begin{bmatrix}\dfrac{-\left(1-\eta^2\right)}{\xi^2-1}\left(S_{mn}+\eta\dfrac{dS_{mn}}{d\eta}\right)R_{mn}^{(i)}\\ -S_{mn}\left(R_{mn}^{(i)}+\xi\dfrac{dR_{mn}^{(i)}}{d\xi}\right)\end{bmatrix} \quad (5.3.60)$$

It is observed that there is no singularity in the equations (5.3.57) – (5.3.60). These functions are also plotted blow. $f_{mn}^{M\phi}(\eta)\left(1-\eta^2\right)^{1/2}\left(\xi^2-\eta^2\right)^{3/2}$ is plotted in Figure V.19.

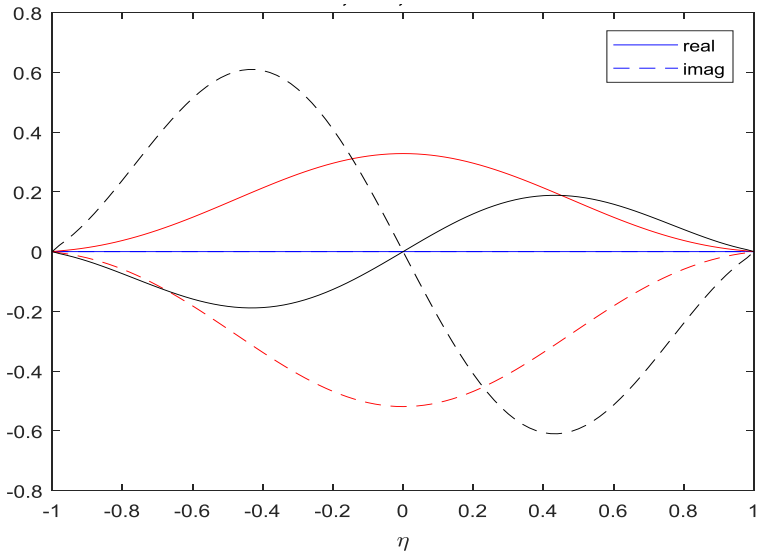

(a) Plot of $f_{mn}^{M\eta}(\eta)\left(1-\eta^2\right)^{1/2}\left(\xi^2-\eta^2\right)^{3/2}$

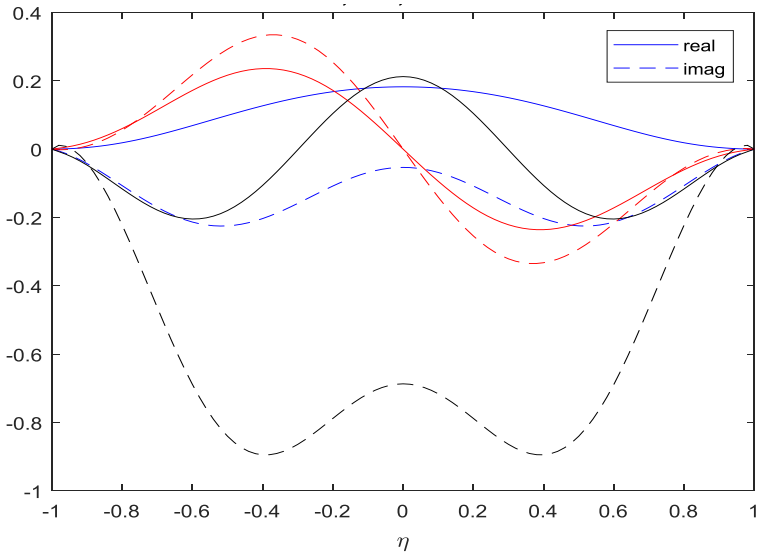

(b) $f_{mn}^{M\phi}(\eta)\left(1-\eta^2\right)^{1/2}\left(\xi^2-\eta^2\right)^{3/2}$

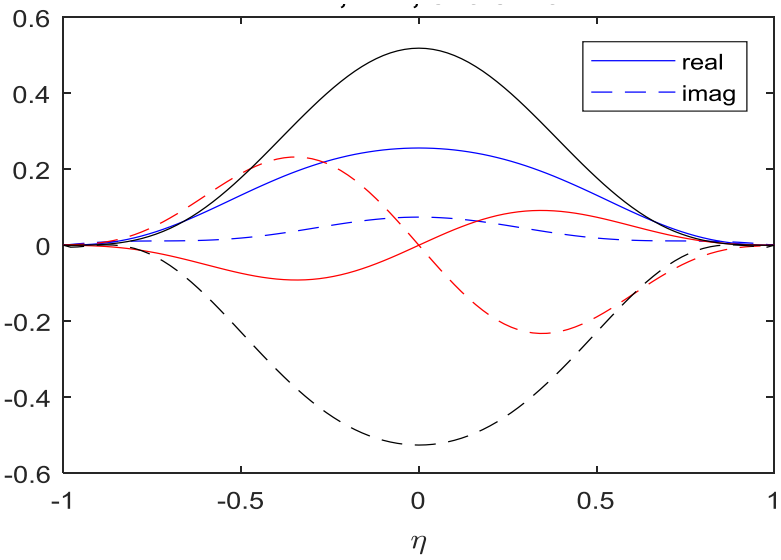

(c) $f_{mn}^{N\eta}(\eta)\left(1-\eta^2\right)^{1/2}\left(\xi^2-\eta^2\right)^{5/2}$

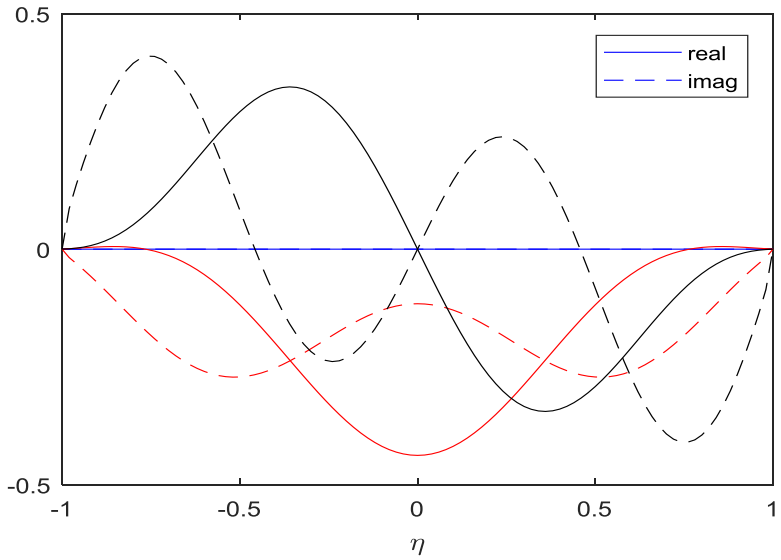

(d) $f_{mn}^{N\phi}(\eta)\left(1-\eta^2\right)^{1/2}\left(\xi^2-\eta^2\right)^{3/2}$

Figure V.19. Plot of functions (5.3.57) – (5.3.60), at c=3.8773, ξ = 1.05: blue: (m, n) = (0, 1), red: (m, n) = (1, 1), and black (m, n) = (1,2).

It is noted that $f_{mn}^{N\eta}(\eta)\left(1-\eta^2\right)^{1/2}\left(\xi^2-\eta^2\right)^{5/2}$ is plotted instead of $f_{mn}^{N\eta}(\eta)\left(1-\eta^2\right)^{1/2}\left(\xi^2-\eta^2\right)^{3/2}$, because $f_{mn}^{N\eta}(\eta)\left(1-\eta^2\right)^{1/2}\left(\xi^2-\eta^2\right)^{3/2}$ has singularity. However, in the integration as listed in

(5.3.54), $f_{mn}^{N\eta}(\eta)$ is multiplied with the other functions which gives another $(\xi^2-\eta^2)$ to $f_{mn}^{N\eta}(\eta)$ and makes the resulted functions has no singularity over the whole range of η. For example, the integrand $(\xi^2-\eta^2)^{\frac{1}{2}} f_{mn}^{N\phi}(\eta) f_{m'n'}^{N\eta}(\eta) g(\eta)$ is also plotted in Figure V.20, which shows no singularity over the range of η.

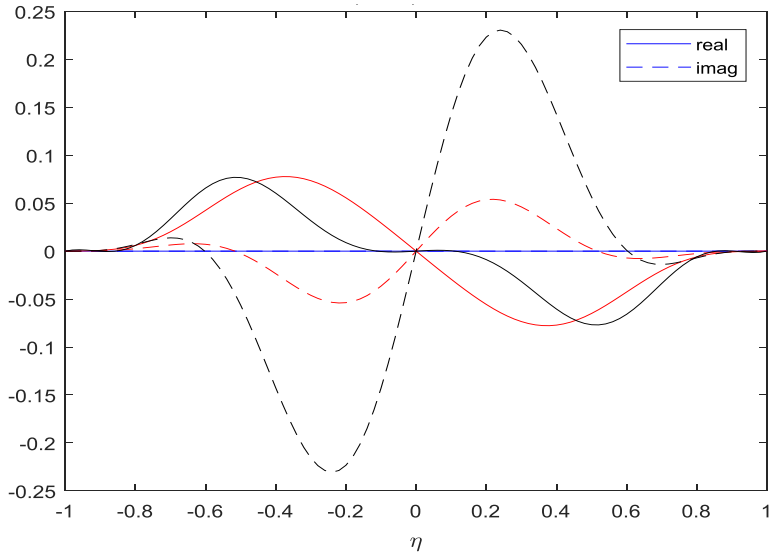

Figure V.20. Plot of the integrand in (5.3.54) at c=3.8773, ξ = 1.05, (m', n') = (m, n) : blue: (m, n) = (0, 1), red: (m, n) = (1, 1), and black (m, n) = (1,2).

Then, these functions are ready to be integrated numerically to find the matrix $\bar{\bar{C}}$. To find the scattered fields coefficients, the next step is to find the column vector $\bar{b}$. The element of $\bar{b}$ is defined as $b_{m'n'}^{V,\sigma'} = \int_{\partial SO} \hat{\xi} \times \bar{E}^s \cdot \bar{V}_{\sigma',m'n'}^{a(3)} g(\eta)$, the integration of the dot product of the tangential components of the scattered fields and the vector spheroidal harmonics. This integration is also performed numerically. The calculations of $\bar{V}_{\sigma',m'n'}^{a(3)} g(\eta)$ have been discussed above. The scattered fields $\bar{E}^s$ are obtained from the off-the-shelf techniques. For example, a method applied to generally objects is using the commercial software HFSS. In HFSS, the output scattered fields are

usually defined in the rectangular coordinates $\bar{E} = E_x\hat{x} + E_y\hat{y} + E_z\hat{z}$. Thus, the output scattered fields need to be transformed into spheroidal coordinates $\bar{E} = E_\eta\hat{\eta} + E_\xi\hat{\xi} + E_\phi\hat{\phi}$. The transformations between the rectangular coordinate so prolate spheroidal coordinate are,

$$\begin{aligned}
\hat{\eta} &= -\eta\frac{\left(\xi^2-1\right)^{\frac{1}{2}}}{\left(\xi^2-\eta^2\right)^{\frac{1}{2}}}\left(\hat{x}\cos\phi + \hat{y}\sin\phi\right) + \xi\frac{\left(1-\eta^2\right)^{\frac{1}{2}}}{\left(\xi^2-\eta^2\right)^{\frac{1}{2}}}\hat{z} \\
\hat{\xi} &= \xi\frac{\left(1-\eta^2\right)^{\frac{1}{2}}}{\left(\xi^2-\eta^2\right)^{\frac{1}{2}}}\left(\hat{x}\cos\phi + \hat{y}\sin\phi\right) + \eta\frac{\left(\xi^2-1\right)^{\frac{1}{2}}}{\left(\xi^2-\eta^2\right)^{\frac{1}{2}}}\hat{z} \\
\hat{\phi} &= -\hat{x}\sin\phi + \hat{y}\cos\phi
\end{aligned} \tag{5.3.61}$$

Thus,

$$E_\eta = \bar{E}\cdot\hat{\eta} = E_x\hat{x}\cdot\hat{\eta} + E_y\hat{y}\cdot\hat{\eta} + E_z\hat{z}\cdot\hat{\eta} \tag{5.3.62}$$

$$E_\eta = -\eta\frac{\left(\xi^2-1\right)^{\frac{1}{2}}}{\left(\xi^2-\eta^2\right)^{\frac{1}{2}}}\left(E_x\cos\phi + E_y\sin\phi\right) + \xi\frac{\left(1-\eta^2\right)^{\frac{1}{2}}}{\left(\xi^2-\eta^2\right)^{\frac{1}{2}}}E_z \tag{5.3.63}$$

Similarly,

$$E_\xi = \xi\frac{\left(1-\eta^2\right)^{\frac{1}{2}}}{\left(\xi^2-\eta^2\right)^{\frac{1}{2}}}\left(E_x\cos\phi + E_y\sin\phi\right) + E_z\frac{\left(\xi^2-1\right)^{\frac{1}{2}}}{\left(\xi^2-\eta^2\right)^{\frac{1}{2}}}\hat{z} \tag{5.3.64}$$

$$E_\phi = -E_x\sin\phi + E_y\cos\phi \tag{5.3.65}$$

After the $\bar{b}$ and $\bar{\bar{C}}$ are obtained, the expansion coefficients for the scattered fields are obtained as $\bar{a}^S = \bar{\bar{C}}^{-1}\bar{b}$. To find the T matrix, the expansion coefficients for the incident fields are also needed. The incident plane waves are expanded in terms of incoming prolate spheroidal waves [102]. For TE plane wave,

$$\bar{E}^{plane,TE} = \sum_{n=1}^{N_{max}} \sum_{m=0}^{n} i^n \left[f_{mn}^{(2)} \bar{M}_{e,mn}^{r(1)} + i f_{mn}^{(1)} \bar{N}_{o,mn}^{r(1)} \right] \tag{5.3.66}$$

For TM plane wave,

$$\bar{E}^{plane,TM} = \sum_{n=1}^{N_{max}} \sum_{m=0}^{n} i^n \left[f_{mn}^{(1)} \bar{M}_{o,mn}^{r(1)} - i f_{mn}^{(2)} \bar{N}_{e,mn}^{r(1)} \right] \tag{5.3.67}$$

where

$$f_{mn}^{(1)}(\theta_i) = \frac{4m}{\Lambda_{mn}} \sum_{r=0,1}^{\infty} \frac{d_r^{mn}}{(r+m)(r+m+1)} \frac{P_{m+r}^m(\cos\theta_i)}{\sin\theta_i} \tag{5.3.68}$$

$$f_{mn}^{(2)}(\theta_i) = \frac{2(2-\delta_{0m})}{\Lambda_{mn}} \sum_{r=0,1}^{\infty} \frac{d_r^{mn}}{(r+m)(r+m+1)} \frac{dP_{m+r}^m(\cos\theta_i)}{d\theta_i} \tag{5.3.69}$$

d_r^{mn} is calculated in section 5.2. The definition of Λ_{mn} is

$$\Lambda_{mn} = \sum_{r=0,1}^{\infty} \frac{(|m|+m+r)!}{(|m|-m+r)!} \frac{2}{2(|m|+r)+1} d_r^{mn*}(c) d_r^{mn}(c) \tag{5.3.70}$$

The incident plane waves propagate in the xz plane at angle θ_i to the z axis. In this section, *c* is real and $d_r^{mn}(c)$ is also real. The values of $d_r^{mn}(c)$ at different combinations of *c*, *m*, *n*, *r* are listed in Table V-2.

Table V-2. Example values of $d_r^{mn}(c)$.

$d_0^{00}(c=5)$	0.560317604	$d_1^{01}(c=10)$	0.118899627
$d_2^{00}(c=5)$	-0.695612643	$d_3^{01}(c=10)$	-0.234891914
$d_4^{00}(c=5)$	0.215476299	$d_5^{01}(c=10)$	0.171269083
$d_6^{00}(c=5)$	-0.032721208	$d_7^{01}(c=10)$	-0.06961685
$d_8^{00}(c=5)$	0.002935928	$d_9^{01}(c=10)$	0.018226738
$d_{10}^{00}(c=5)$	-0.000173179	$d_{11}^{01}(c=10)$	-0.003331058
$d_{12}^{00}(c=5)$	7.2083067E-06	$d_{13}^{01}(c=10)$	0.000448444
$d_{14}^{00}(c=5)$	-2.2270283E-07	$d_{15}^{01}(c=10)$	-4.6258553E-05
$d_{16}^{00}(c=5)$	5.3044690E-09	$d_{17}^{01}(c=10)$	3.7688450E-06
$d_{18}^{00}(c=5)$	-1.0031759E-10	$d_{19}^{01}(c=10)$	-2.4845627E-07

It is noted that the superscript '(1)' is used that $\bar{M}_{mn}^{r(1)}$, $\bar{N}_{mn}^{r(1)}$ because the incident waves are expanded in terms of income vector spheroidal waves.

After the expansion coefficients for both scattered fields and the corresponding incident fields are computed, The T matrix with vector spheroidal waves is obtained.

(c) The T Matrix Extraction for 3D Vector Cylindrical Waves

The scatter fields can be expanded into out-going 3D vector cylindrical waves, while exciting fields can be expanded into in-coming 3D vector cylindrical waves, with expressions as below.

$$\bar{E}^s(\bar{r}) = \sum_m \int_{-\infty}^{\infty} dk_z (\bar{M}_m(k_z,\bar{r}) a_m^{(M)}(k_z) + \bar{N}_m(k_z,\bar{r}) a_m^{(N)}(k_z)) \tag{5.3.71}$$

$$\bar{E}^{ex}(\bar{r}) = \sum_m \int_{-\infty}^{\infty} dk_z (Rg\bar{M}_m(k_z,\bar{r}) w_m^{(M)}(k_z) + Rg\bar{N}_m(k_z,\bar{r}) w_m^{(N)}(k_z)) \tag{5.3.72}$$

where the expressions for $\bar{M}_m(k_z,\bar{r})$, $\bar{N}_m(k_z,\bar{r})$, $Rg\bar{M}_m(k_z,\bar{r})$, and $Rg\bar{N}_m(k_z,\bar{r})$ are available in section 5.2. $a_m^{(M)}(k_z)$ and $a_m^{(N)}(k_z)$ are the expansion coefficients for the scattered fields while $w_m^{(M)}(k_z)$ and $w_m^{(N)}(k_z)$ are the expansion coefficients of the exciting fields.

The T matrix relates the exciting field coefficients to the scattered field coefficients.

$$a_m^{(\beta)}(k_z) = \sum_{\alpha=M,N} \sum_{m'} \int_{-\infty}^{\infty} dk_z' T_{mm'}^{(\beta,\alpha)}(k_z,k_z') w_{m'}^{(\alpha)}(k_z') \tag{5.3.73}$$

where $\alpha,\beta = M\ or\ N$ corresponding to the expansion coefficients of the 3D vector cylindrical waves $\bar{M}$ and $\bar{N}$, respectively. This notation is used in the remaining part of this chapter. $T_{mm'}^{(\beta,\alpha)}(k_z,k_z')$ are the elements of the T matrix.

It is noted that the T matrix with 3D vector cylindrical waves are a little different from the T matrix with vector spherical or spheroidal waves, as there is integration over dk_z. In numerical

computation, the integration can be transformed into summation. Thus, the integration over dk_z is similar to summation over n in the vector spherical or spheroidal waves.

Generally, the T matrix for an arbitrary-shaped object of moderate size can be extracted for commercial software such as HFSS. Section 5.3.1 (a) and (b) describe the procedures to extract the T matrix from HFSS with vector spherical and spheroidal wave expansions. The procedures to extract the T matrix with 3D vector cylindrical wave expansions are similarly, but the incident fields and the scattered fields on the enclosing cylindrical surface obtained from HFSS are expanded into 3D vector cylindrical waves instead of vector spherical waves. In this section, the hybrid method with 3D vector cylindrical waves are applied to forest of tree trunks which are modeled as tall cylinders that are much larger than a wavelength. For example, at the L-band (1.41 GHz), tree trunks that are 20 meters tall correspond to 94 wavelengths. In this section, the focus is to study forests at L-band. For these cases, the trees are as tall as 94 wavelengths. ICA is valid when the length of the cylinder is much longer than the wavelength. When using Body of Revolution (BOR), the length of the cylinder needs to be discretized into many sections for long cylinders, which requires much memory and computation CPU. For example, for the cylinders with length of 94 wavelength, parallel computing is needed for BOR while ICA can be run on a single computer with results obtained in seconds. For the tree trunks simulated in this section, ICA is much more efficient than BOR and ICA also provides satisfactory accuracies. Thus, we choose to use ICA instead of BOR to obtain the T matrix. Using ICA, the T matrix for a vertically oriented cylinder with radius *A*, length *L* and relative permittivity ϵ_p is derived as below.

The first step in extracting the T matrix is finding the scattered field from the cylinder. Without loss of generality, let the cylinder centered at [0,0,0]. According to Huygen's principle, the scattered fields is obtained as

$$\bar{E}^s(\bar{r}) = \int_{S'} dS' \{ik\eta \bar{\bar{G}}(\bar{r},\bar{r}') \cdot [\hat{n}' \times \bar{H}(\bar{r}')] + \nabla \times \bar{\bar{G}}(\bar{r},\bar{r}') \cdot [\hat{n}' \times \bar{E}(\bar{r}')]\} \tag{5.3.74}$$

where S' is the surface area of the cylinder and $\hat{n}'$ is the unit normal vector.

The Dyadic Green's function is then expanded using 3D vector cylindrical waves.

$$\bar{\bar{G}}(\bar{r},\bar{r}') = \frac{i}{8\pi} \sum_n (-1)^n \int_{-\infty}^{\infty} dk_z \frac{1}{k_\rho^2} \begin{bmatrix} \bar{M}_n(k_z,\bar{r}) Rg\bar{M}_{-n}(-k_z,\bar{r}') \\ +\bar{N}_n(k_z,\bar{r}) Rg\bar{N}_{-n}(-k_z,\bar{r}') \end{bmatrix} \tag{5.3.75 a}$$

$$\nabla \times \bar{\bar{G}}(\bar{r},\bar{r}') = \frac{ik}{8\pi} \sum_n (-1)^n \int_{-\infty}^{\infty} dk_z \frac{1}{k_\rho^2} \begin{bmatrix} \bar{N}_n(k_z,\bar{r}) Rg\bar{M}_{-n}(-k_z,\bar{r}') \\ +\bar{M}_n(k_z,\bar{r}) Rg\bar{N}_{-n}(-k_z,\bar{r}') \end{bmatrix} \tag{5.3.75 b}$$

To extract the T matrix, let the incident wave be

$$\bar{E}^{inc}(\bar{r}) = Rg\bar{\beta}_{m'}(k_z',\bar{r}) \tag{5.3.76}$$

Then, using ICA [4], the internal fields of the cylinder are obtained as

$$\bar{E}^{int}(\bar{r}') = c_{m'}^{(M,\beta)}(k_z') Rg\bar{M}_{m'}(k_{p\rho}',k_z',\bar{r}') + c_{m'}^{(N,\beta)}(k_z') Rg\bar{N}_{m'}(k_{p\rho}',k_z',\bar{r}') \tag{5.3.77}$$

$$\bar{H}^{int}(\bar{r}') = -\frac{ik_p}{k\eta}[c_{m'}^{(M,\beta)}(k_z') Rg\bar{N}_{m'}(k_{p\rho}',k_z',\bar{r}') + c_{m'}^{(N,\beta)}(k_z') Rg\bar{M}_{m'}(k_{p\rho}',k_z',\bar{r}')] \tag{5.3.78}$$

where $k_p = k\sqrt{\epsilon_p}$ is the wave number inside the cylinder. $c_{m'}^{(M,\beta)}(k_z')$ and $c_{m'}^{(N,\beta)}(k_z')$ are the coefficients of the vector cylindrical harmonics of order m', corresponding to the incident wave. These coefficients are obtained from ICA, as detailed in page 41-44 in [39]. $k_{p\rho}' = \sqrt{k_p^2 - k_z'^2}$. $k_{p\rho}'$ is writing explicitly in the expressions of $\bar{M}_{m'}$ and $\bar{N}_{m'}$ to incident they are the vector cylindrical harmonics inside the cylinder with wavenumber k_p, instead of k as above.

According to the boundary condition on the cylinder surface,

$$\hat{n}' \times \bar{H}(\bar{r}') = \hat{n}' \times \bar{H}^{int}(\bar{r}') \tag{5.3.79}$$

$$\hat{n}' \times \bar{E}(\bar{r}') = \hat{n}' \times \bar{E}^{int}(\bar{r}') \tag{5.3.80}$$

Next, substitute the expressions of the Dyadic Green's function and the internal fields into Huygen's principle to calculate $\bar{E}^s(\bar{r})$. It is noted that the Dyadic Green's function has summations of two parts, similarly for the curl of the Dyadic Green's function and the internal electric and magnetic fields. Thus, $\bar{E}^s(\bar{r})$ can be calculated as the summation of eight terms,

$$\bar{E}^s(\bar{r}) = \sum_{term=1}^{8} \bar{E}^s_{term} \tag{5.3.81}$$

Each term is calculated as below.

$$\bar{E}^s_1 = \int_{S'} dS' \left\{ \begin{array}{l} \dfrac{-k}{8\pi} \sum_n (-1)^n \int_{-\infty}^{\infty} dk_z \dfrac{1}{k_\rho^2} \bar{M}_n(k_z, \bar{r}) Rg\bar{M}_{-n}(k_z, \bar{r}') \\ \cdot[-i \dfrac{k_p}{k} c_{m'}^{(M,\beta)}(k_z') \hat{\rho}_{p'} \times Rg\bar{N}_{m'}(k_{p\rho}', k_z', \bar{r}')] \end{array} \right\} \tag{5.3.82}$$

The unit normal vector $\hat{n}'$ in this case is $\hat{\rho}_{p'}$, $\hat{\rho}$ direction at p'. This is because the integration to obtain the scattered fields in ICA is over the lateral surface, ignoring the two bases [4].

Substituting the expressions of the vector cylindrical waves as listed in section 5.2.3 and simplification lead to

$$\bar{E}^s_1 = \int_{-\infty}^{\infty} dk_z \frac{iAL}{4} c_{m'}^{(M,\beta)}(k_z') \frac{\sin((k_z - k_z')\frac{L}{2})}{(k_z - k_z')\frac{L}{2}} \frac{k_{p\rho}'^2}{k_\rho} J'_{m'}(k_\rho A) J_{m'}(k_{p\rho}' A) \bar{M}_{m'}(k_z, \bar{r}) \tag{5.3.83}$$

Similarly, for the other seven terms

$$\bar{E}^s_2 = \int_{S'} dS' \left\{ \begin{array}{l} \dfrac{-k}{8\pi} \sum_n (-1)^n \int_{-\infty}^{\infty} dk_z \dfrac{1}{k_\rho^2} \bar{M}_n(k_z, \bar{r}) Rg\bar{M}_{-n}(-k_z, \bar{r}') \\ \cdot[-i \dfrac{k_p}{k} c_{m'}^{(N,\beta)}(k_z') \hat{\rho}_{p'} \times \mathrm{Rg}\, \bar{M}_{m'}(k_{p\rho}', k_z', \bar{r}')] \end{array} \right\} = 0 \tag{5.3.84}$$

$$\bar{E}_3^s = \int_{S'} dS' \{ \frac{-k}{8\pi} \sum_n (-1)^n \int_{-\infty}^{\infty} dk_z \frac{1}{k_\rho^2} \bar{N}_n(k_z, \bar{r}) Rg\bar{N}_{-n}(-k_z, \bar{r}') \cdot [-i \frac{k_p}{k} c_{m'}^{(M,\beta)}(k_z') \hat{\rho}_{\bar{\rho}'} \times Rg\bar{N}_{m'}(k_{p\rho}', k_z', \bar{r}')] \}$$

$$= \int_{-\infty}^{\infty} dk_z [\frac{iAL}{4k_\rho^2} c_{m'}^{(M,\beta)}(k_z') \frac{\sin((k_z - k_z')\frac{L}{2})}{(k_z - k_z')\frac{L}{2}} \frac{m'}{kA} (k_z k_{p\rho}'^2 - k_\rho^2 k_z') J_{m'}(k_\rho A) J_{m'}(k_{p\rho}' A) \bar{N}_{m'}(k_z, \bar{r})]$$

(5.3.85)

$$\bar{E}_4^s = \int_{S'} dS' \{ \frac{-k}{8\pi} \sum_n (-1)^n \int_{-\infty}^{\infty} dk_z \frac{1}{k_\rho^2} \bar{N}_n(k_z, \bar{r}) Rg\bar{N}_{-n}(-k_z, \bar{r}') \cdot [-i \frac{k_p}{k} c_{m'}^{(N,\beta)}(k_z') \hat{\rho}_{\bar{\rho}'} \times Rg\bar{M}_{m'}(k_{p\rho}', k_z', \bar{r}')] \}$$

$$= \int_{-\infty}^{\infty} dk_z [\frac{iAL}{4} c_{m'}^{(N,\beta)}(k_z') \frac{\sin((k_z - k_z')\frac{L}{2})}{(k_z - k_z')\frac{L}{2}} \frac{-k_{p\rho}' k_p}{k} J_{m'}(k_\rho A) J_{m'}'(k_{p\rho}' A) \bar{N}_{m'}(k_z, \bar{r})]$$

(5.3.86)

$$\bar{E}_5^s = \int_{S'} dS' \left\{ \begin{array}{l} \frac{ik}{8\pi} \sum_n (-1)^n \int_{-\infty}^{\infty} dk_z \frac{1}{k_\rho^2} \bar{N}_n(k_z, \bar{r}) Rg\bar{M}_{-n}(-k_z, \bar{r}') \\ \cdot [c_{m'}^{(M,\beta)}(k_z') \hat{\rho}_{\bar{\rho}'} \times Rg\bar{M}_{m'}(k_{p\rho}', k_z', \bar{r}')] \end{array} \right\} = 0 \qquad (5.3.87)$$

$$\bar{E}_6^s = \int_{S'} dS' \{ \frac{ik}{8\pi} \sum_n (-1)^n \int_{-\infty}^{\infty} dk_z \frac{1}{k_\rho^2} \bar{N}_n(k_z, \bar{r}) Rg\bar{M}_{-n}(-k_z, \bar{r}') \cdot [c_{m'}^{(N,\beta)}(k_z') \hat{\rho}_{\bar{\rho}'} \times Rg\bar{N}_{m'}(k_{p\rho}', k_z', \bar{r}')] \}$$

$$= \int_{-\infty}^{\infty} dk_z [\frac{iAL}{4} c_{m'}^{(N,\beta)}(k_z') \frac{\sin((k_z - k_z')\frac{L}{2})}{(k_z - k_z')\frac{L}{2}} \frac{kk_{p\rho}'^2}{k_p k_\rho} J_{m'}'(k_\rho A) J_{m'}(k_{p\rho}' A) \bar{N}_{m'}(k_z, \bar{r})]$$

(5.3.88)

$$\bar{E}_7^s = \int_{S'} dS' \{ \frac{ik}{8\pi} \sum_n (-1)^n \int_{-\infty}^{\infty} dk_z \frac{1}{k_\rho^2} \bar{M}_n(k_z, \bar{r}) Rg\bar{N}_{-n}(-k_z, \bar{r}') \cdot [c_{m'}^{(M,\beta)}(k_z') \hat{\rho}_{\bar{\rho}'} \times Rg\bar{M}_{m'}(k_{p\rho}', k_z', \bar{r}')] \}$$

$$= \int_{-\infty}^{\infty} dk_z \{ \frac{iAL}{4} c_{m'}^{(M,\beta)}(k_z') \frac{\sin((k_z - k_z')\frac{L}{2})}{(k_z - k_z')\frac{L}{2}} [-k_{p\rho}' J_{m'}(k_\rho A) J_{m'}'(k_{p\rho}' A)] \bar{M}_{m'}(k_z, \bar{r}) \}$$

(5.3.89)

$$\bar{E}_8^s = \int_{S'} dS\{\frac{ik}{8\pi}\sum_n (-1)^n \int_{-\infty}^{\infty} dk_z \frac{1}{k_\rho^2} \bar{M}_n(k_z,\bar{r}) Rg\bar{N}_{-n}(-k_z,\bar{r}') \cdot [c_{m'}^{(N,\beta)}(k_z')\hat{\rho}_{\bar{\rho}'} \times Rg\bar{N}_{m'}(k_{p\rho}', k_z', \bar{r}')]\}$$

$$= \int_{-\infty}^{\infty} dk_z [\frac{iAL}{4} c_{m'}^{(N,\beta)}(k_z') \frac{\sin((k_z - k_z')\frac{L}{2})}{(k_z - k_z')\frac{L}{2}} \frac{m'}{k_\rho^2 k_p A} (k_z k_{p\rho}'^2 - k_\rho^2 k_z') J_{m'}(k_\rho A) J_{m'}(k_{p\rho}' A) \bar{M}_{m'}(k_z,\bar{r})]$$

(5.3.90)

The expressions for $\bar{E}^s(\bar{r})$ are obtained. After that, these expressions are compared with those of $\bar{E}^s(\bar{r})$ obtained from the T matrix method to extract the T matrix for the cylinder. When $\bar{E}^{inc}(\bar{r}) = Rg\bar{\beta}_{m'}(k_z', \bar{r})$, the scattered fields are as follows according to the T matrix method.

$$\bar{E}^s(\bar{r}) = \sum_m \int_{-\infty}^{\infty} dk_z [T_{mm'}^{M\beta}(k_z, k_z')\bar{M}_m(k_z,\bar{r}) + T_{mm'}^{N\beta}(k_z, k_z')\bar{N}_m(k_z,\bar{r})] \tag{5.3.91}$$

Comparing the $\bar{E}^s(\bar{r})$ derived from ICA as in the expressions of the eight terms above, the expressions for the T matrix of the cylinder are obtained as,

$$T_{mm'}^{(M,\beta)}(k_z,k_z') = \delta(m-m')\frac{iAL}{4k_\rho^2}\frac{sin((k_z-k_z')\frac{L}{2})}{((k_z-k_z')\frac{L}{2})}\left\{\begin{array}{l} c_m^{(M,\beta)}(k_z')k_\rho k_{p\rho}'\left[\begin{array}{l} k_{p\rho}' J_m'(k_\rho A) J_m(k_{p\rho}' A) \\ -k_\rho J_m(k_\rho A) J_m'(k_{p\rho}' A)\end{array}\right] + \\ c_m^{(N,\beta)}(k_z')\frac{m}{k_p A}(k_z k_{p\rho}'^2 - k_\rho^2 k_z') J_m(k_\rho A) J_m(k_{p\rho}' A)\end{array}\right\}$$

(5.3.92)

$$T_{mm'}^{(N,\beta)}(k_z,k_z') = \delta(m-m')\frac{iAL}{4k_\rho^2}\frac{sin((k_z-k_z')\frac{L}{2})}{((k_z-k_z')\frac{L}{2})}\left\{\begin{array}{l} c_m^{(M,\beta)}(k_z')\frac{m}{kA}(k_z k_{p\rho}'^2 - k_\rho^2 k_z') J_m(k_\rho A) J_m(k_{p\rho}' A) \\ +c_m^{(N,\beta)}(k_z')k_\rho k_{p\rho}'\left[\begin{array}{l} \frac{kk_{p\rho}'}{k_p} J_m'(k_\rho A) J_m(k_{p\rho}' A) \\ -\frac{k_p k_\rho}{k} J_m(k_\rho A) J_m'(k_{p\rho}' A)\end{array}\right]\end{array}\right\}$$

(5.3.93)

It is noted that there is a delta function $\delta(m-m')$ in the expressions of the T matrix. It is because there is summation over m in the scattered fields obtained from the T matrix method, while there is no summation over m in the simplified solutions of the scattered fields from ICA (i.e., the eight terms). Then, the delta function $\delta(m-m')$ is needed to cancel the summation of m in the results of the T matrix method to match the results from ICA. In the expressions of the T matrix of the cylinder above, m' is changed to m, which dose not change the results because of the delta function $\delta(m-m')$.

5.3.2 Numerical and Analytical Translation Addition Method

The second step in the hybrid method is wave transformations for all the single-objects pairs. To find the scattered fields from object centered at $\bar{r}_2$ to object centered at $\bar{r}_1$, the outgoing spherical waves centered at $\bar{r}_2$ need to be transformed to incoming spherical waves centered at object $\bar{r}_1$, as illustrated in Figure V.21 (a). This is also called translation addition theorem. Similarly, the translation addition theorem for vector spheroidal waves and 3D vector cylindrical waves are illustrated in Figure V.21 (b) and (c), respectively.

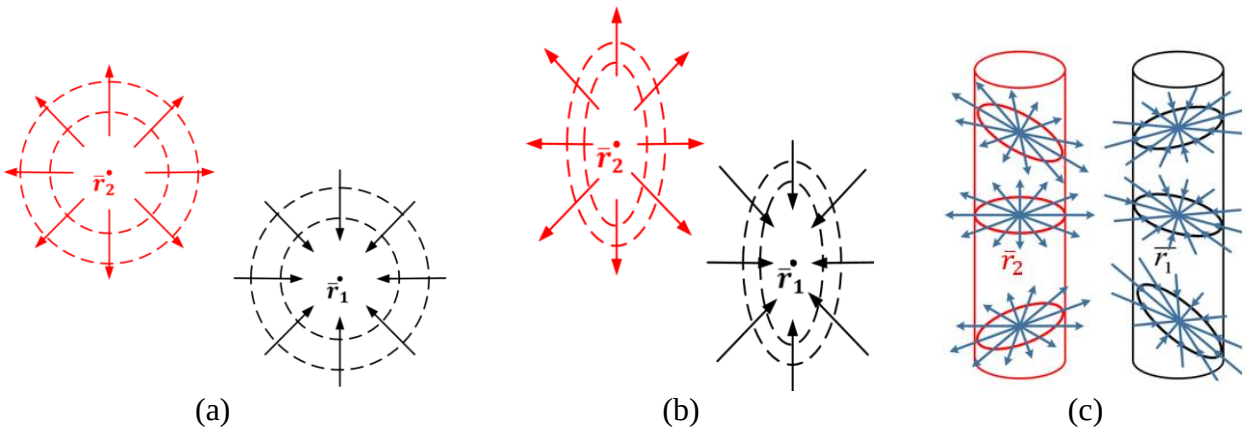

Figure V.21. Illustration of translation addition for (a) vector spherical waves, (b) vector spheroidal waves, and (c) 3D vector cylindrical waves.

(a) Translation Addition Method for Vector Spherical Waves

For vector spherical waves, the translation addition theorem is formulated as below [4].

$$\bar{M}_{mn}(k\bar{r}\bar{r}_a) = \sum_{\mu\nu}\left\{A_{\mu\nu mn}(k\bar{r}_b\bar{r}_a)Rg\bar{M}_{\mu\nu}(k\bar{r}\bar{r}_b) + B_{\mu\nu mn}(k\bar{r}_b\bar{r}_a)Rg\bar{N}_{\mu\nu}(k\bar{r}\bar{r}_b)\right\} \quad (5.3.94\text{ a})$$

$$\bar{N}_{mn}(k\bar{r}\bar{r}_a) = \sum_{\mu\nu}\left\{B_{\mu\nu mn}(k\bar{r}_b\bar{r}_a)Rg\bar{M}_{\mu\nu}(k\bar{r}\bar{r}_b) + A_{\mu\nu mn}(k\bar{r}_b\bar{r}_a)Rg\bar{N}_{\mu\nu}(k\bar{r}\bar{r}_b)\right\} \quad (5.3.94\text{ b})$$

where $\bar{M}_{mn}(k\bar{r}\bar{r}_a)$ and $\bar{N}_{mn}(k\bar{r}\bar{r}_a)$ are the outgoing vector spherical wave centered at $\bar{r}_a$. $Rg\bar{M}_{\mu\nu}(k\bar{r}\bar{r}_b)$ and $Rg\bar{N}_{\mu\nu}(k\bar{r}\bar{r}_b)$ are the incoming regular vector spherical waves centered at $\bar{r}_b$. $A_{\mu\nu mn}$ and $B_{\mu\nu mn}$ are the corresponding translation addition coefficients.

Thus, the key in the wave transformations is calculating the coefficients $A_{\mu\nu mn}$ and $B_{\mu\nu mn}$. [4] gives the analytical solutions of $A_{\mu\nu mn}$ and $B_{\mu\nu mn}$ for vector spherical waves

$$A_{\mu\nu mn}\left(k\bar{r}_o\right) = \frac{\gamma_{mn}}{\gamma_{\mu\nu}}(-1)^{\mu}\sum_p a(m,n\,|\,-\mu,\nu\,|\,p)a(n,\nu,p)h_p\left(kr_o\right)Y_p^{m-\mu}\left(\theta_o,\phi_o\right) \quad (5.3.95)$$

$$B_{\mu\nu mn}\left(k\bar{r}_o\right) = \frac{\gamma_{mn}}{\gamma_{\mu\nu}}(-1)^{\mu+1}\sum_p a(m,n\,|\,-\mu,\nu\,|\,p,p-1)b(n,\nu,p)h_p\left(kr_o\right)Y_p^{m-\mu}\left(\theta_o,\phi_o\right) \quad (5.3.96)$$

The definitions for γ_{mn}, $h_p\left(kr_o\right)$, and $Y_p^{m-\mu}\left(\theta_o,\phi_o\right)$ are listed in section 5.2. The remaining parameter is defined as below

$$a(m,n\,|\,\mu,\nu\,|\,p) = (-1)^{m+\mu}(2p+1)\left[\frac{(n+m)!(\nu+\mu)!(p-m-\mu)!}{(n-m)!(\nu-\mu)!(p+m+\mu)!}\right]^{1/2}\begin{pmatrix} n & \nu & p \\ m & \mu & -(m+\mu)\end{pmatrix}\begin{pmatrix} n & \nu & p \\ 0 & 0 & 0\end{pmatrix} \quad (5.3.97)$$

$$a(m,n\,|\,\mu,\nu\,|\,p,q) = (-1)^{m+\mu}(2p+1)\left[\frac{(n+m)!(\nu+\mu)!(p-m-\mu)!}{(n-m)!(\nu-\mu)!(p+m+\mu)!}\right]^{1/2}\begin{pmatrix} n & \nu & p \\ m & \mu & -(m+\mu)\end{pmatrix}\begin{pmatrix} n & \nu & q \\ 0 & 0 & 0\end{pmatrix} \quad (5.3.98)$$

$$a(n,\nu,p)=\frac{i^{\nu-n+p}}{2\nu(\nu+1)}\begin{bmatrix}2\nu(\nu+1)(2\nu+1)+(\nu+1)(n+\nu-p)\cdot(n+p-\nu+1)\\-\nu(n+\nu+p+2)(\nu+p-n+1)\end{bmatrix} \tag{5.3.99}$$

$$b(n,\nu,p)=-\frac{(2\nu+1)}{2\nu(\nu+1)}i^{\nu+p-n}\left[(n+\nu+p+1)(\nu+p-n)(n+p-\nu)(n+\nu-p+1)\right]^{1/2} \tag{5.3.100}$$

where $\begin{pmatrix} j_1 & j_2 & j_3 \\ m_1 & m_2 & -(m_1+m_2)\end{pmatrix}$ is the Wigner 3j symbols [105].

This analytic method is tedious and is not applicable to other kinds of vector waves such as vector spheroidal waves. Thus, a numerical method for translation addition is developed which is straightforward and robust. This method is similar to the numerical method of calculating the expansion coefficients of the scattered fields. To find $A_{\mu\nu mn}$, dot product with $Rg\bar{N}_{-\mu\nu}(k\overline{rr_b})$ and integration over the spherical surface is applied to both sides of equation (5.3.94 a), with the use of the orthogonality property. To find $B_{\mu\nu mn}$, dot product with $Rg\bar{M}_{-\mu\nu}(k\overline{rr_b})$ and integration over the spherical surface is applied to both sides of equation (5.3.94 a). After simplification, we obtain

$$A_{\mu\nu mn}(k\overline{r_b r_a})=\left[\gamma_{\mu\nu}j_\nu(kR_b)z_{3\mu\nu}\right]^{-1}\int_0^\pi d\theta sin\theta\int_0^{2\pi}d\phi\bar{M}_{mn}(k\overline{rr_a})\cdot\bar{C}_{-\mu\nu}(\theta,\phi) \tag{5.3.101}$$

$$B_{\mu\nu mn}(k\overline{r_b r_a})=\left[\gamma_{\mu\nu}\frac{[kR_b j_\nu(kR_b)]'}{kR_b}z_{3\mu\nu}\right]^{-1}\int_0^\pi d\theta sin\theta\int_0^{2\pi}d\phi\bar{M}_{mn}(k\overline{rr_a})\cdot\bar{B}_{-\mu\nu}(\theta,\phi) \tag{5.3.102}$$

where $\gamma_{\mu\nu}$, $z_{3\mu\nu}$, $\bar{C}_{-\mu\nu}(\theta,\phi)$ and $\bar{B}_{-\mu\nu}(\theta,\phi)$ are defined in section 5.2. The integrations are conducted numerically.

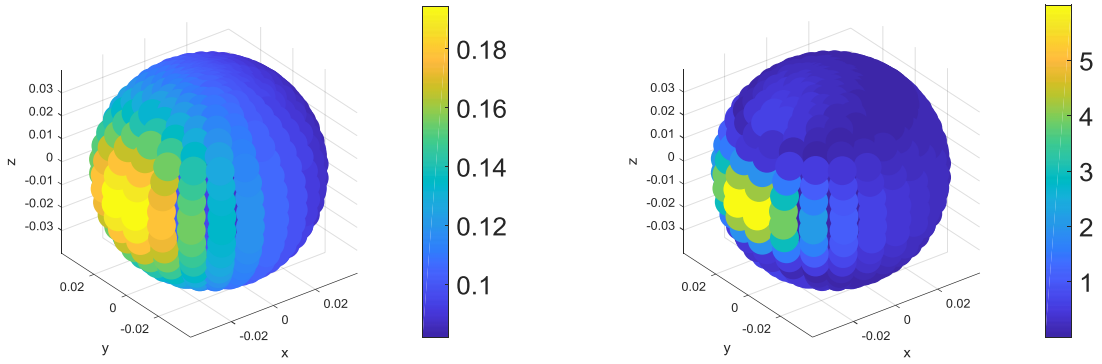

(a) (b)

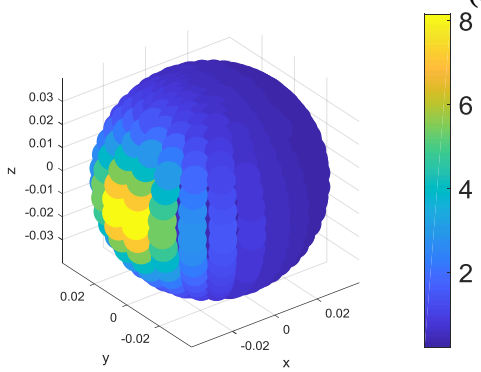

(c)

Figure V.22. $|\bar{M}_{mn}(\overline{rr_j})|$ on the spherical surface centered at $\overline{r_l}$, where $\overline{r_l} = [0,0,0]$, $\overline{r_j} = [-\frac{\lambda}{2}, 0,0]$ for (a) m=0, n=1; (b) m=0, n=5; (c) m=5, n=5.

The outgoing spherical harmonics $\bar{M}_{mn}(\overline{rr_j})$ is plotted in Figure V.22. It is observed that, its magnitude increases as m and n increases. However, the power of each order of spherical harmonics is the same, as proved blow.

Let $\bar{E} = \bar{M}_{mn}(kr,\theta,\phi)$. Then,

$$\bar{H} = \frac{1}{i\omega\mu}\nabla\times\bar{E} = -i\frac{1}{\eta}\bar{N}_{mn}(kr,\theta,\phi) \tag{5.3.103}$$

The expressions for $\bar{M}_{mn}(kr,\theta,\phi)$ and $\bar{N}_{mn}(kr,\theta,\phi)$ are available in section 5.2. For convenience in writing, let

$$\begin{aligned}\bar{M}_{mn}(kr,\theta,\phi) &= \gamma_{mn}FMC(n,kr)\bar{C}_{mn}(\theta,\phi)\\ \bar{N}_{mn}(kr,\theta,\phi) &= \gamma_{mn}FNP(n,kr)\bar{P}_{mn}(\theta,\phi)+\gamma_{mn}FNB(n,kr)\bar{B}_{mn}(\theta,\phi)\end{aligned} \tag{5.3.104}$$

where

$$\begin{aligned}FMC(n,kr) &= h_n(kr)\\ FNP(n,kr) &= \frac{n(n+1)h_n(kr)}{kr}\\ FNB(n,kr) &= \frac{\left[h_n(kr)+kr\left(h_n(kr)\right)'\right]}{kr}\end{aligned} \tag{5.3.105}$$

Then, the pointing vector is

$$\bar{S} = \frac{1}{2}\mathrm{Re}\left(\bar{E}\times\bar{H}^{*}\right) = \frac{1}{2}\mathrm{Re}\left\{i\sqrt{\frac{\varepsilon}{\mu}}\bar{M}_{mn}\left(kr,\theta,\phi\right)\times\bar{N}_{mn}{}^{*}\left(kr,\theta,\phi\right)\right\}$$

$$= \frac{1}{2}\mathrm{Re}\left\{i\sqrt{\frac{\varepsilon}{\mu}}\gamma_{mn}^{2}h_{n}\left(kr\right)\begin{bmatrix} FNP^{*}(n,kr)\bar{C}_{mn}\left(\theta,\phi\right)\times\bar{P}_{mn}^{*}\left(\theta,\phi\right) \\ +FNB^{*}(n,kr)\bar{C}_{mn}\left(\theta,\phi\right)\times\bar{B}_{mn}^{*}\left(\theta,\phi\right)\end{bmatrix}\right\}$$

$$= \frac{1}{2}\mathrm{Re}\left\{i\sqrt{\frac{\varepsilon}{\mu}}\gamma_{mn}^{2}h_{n}\left(kr\right)\begin{bmatrix} FNP^{*}(n,kr)\left(-\hat{\phi}\dfrac{im}{\sin\theta}P_{n}^{m}\left(\cos\theta\right)P_{n}^{m}\left(\cos\theta\right)-\hat{\theta}\dfrac{dP_{n}^{m}\left(\cos\theta\right)}{d\theta}P_{n}^{m}\left(\cos\theta\right)\right) \\ +FNB^{*}(n,kr)\left(\hat{r}\left[\left(\dfrac{m}{\sin\theta}P_{n}{}^{m}\left(\cos\theta\right)\right)^{2}+\left(\dfrac{d}{d\theta}P_{n}^{m}\left(\cos\theta\right)\right)^{2}\right]\right)\end{bmatrix}\right\}$$

(5.3.106)

The power for spherical harmonics of order mn is

$$P_{mn} = R^{2}\int_{0}^{\pi}d\theta\sin\theta\int_{0}^{2\pi}d\phi\hat{r}\cdot\bar{S}_{mn}$$

$$= \pi R^{2}\,\mathrm{Re}\left\{i\sqrt{\frac{\varepsilon}{\mu}}\gamma_{mn}^{2}h_{n}\left(kR\right)FNB^{*}(n,kR)\int_{0}^{\pi}d\theta\sin\theta\left[\left(\frac{m}{\sin\theta}P_{n}^{m}\left(\cos\theta\right)\right)^{2}+\left(\frac{d}{d\theta}P_{n}^{m}\left(\cos\theta\right)\right)^{2}\right]\right\}$$

$$= \pi R^{2}\sqrt{\frac{\varepsilon}{\mu}}\gamma_{mn}^{2}\int_{0}^{\pi}d\theta\sin\theta\left[\left(\frac{m}{\sin\theta}P_{n}^{m}\left(\cos\theta\right)\right)^{2}+\left(\frac{d}{d\theta}P_{n}^{m}\left(\cos\theta\right)\right)^{2}\right]\mathrm{Re}\left(ih_{n}\left(kR\right)\left(\frac{\left[krh_{n}\left(kr\right)\right]'}{kr}\right)^{*}\right)$$

(5.3.107)

The next step is to compute the integration. From section 5.2.1,

$$\int_{0}^{\pi}d\theta\sin\theta\int_{0}^{2\pi}d\phi\begin{Bmatrix}\left[\hat{\theta}\dfrac{im}{\sin\theta}P_{n}^{m}\left(\cos\theta\right)-\hat{\phi}\dfrac{d}{d\theta}P_{n}^{m}\left(\cos\theta\right)\right]e^{im\phi}\cdot \\ \left[\hat{\theta}\dfrac{-im}{\sin\theta}P_{n}^{-m}\left(\cos\theta\right)-\hat{\phi}\dfrac{d}{d\theta}P_{n}^{-m}\left(\cos\theta\right)\right]e^{-im\phi}\end{Bmatrix} = z_{2mn} = \left(-1\right)^{m}\frac{4\pi n\left(n+1\right)}{2n+1}$$

(5.3.108)

Use the following properties,

$$P_n^{-m}(\cos\theta) = (-1)^m \frac{(n-m)!}{(n+m)!} P_n^m(\cos\theta)$$
$$\frac{dP_n^{-m}(\cos\theta)}{d\theta} = (-1)^m \frac{(n-m)!}{(n+m)!} \frac{P_n^m(\cos\theta)}{d\theta} \tag{5.3.109}$$

After simplification, we obtain

$$2\pi(-1)^m \frac{(n-m)!}{(n+m)!} \int_0^\pi d\theta \sin\theta \left[\left(\frac{m}{\sin\theta} P_n^m(\cos\theta) \right)^2 + \left(\frac{d}{d\theta} P_n^m(\cos\theta) \right)^2 \right] = (-1)^m \frac{4\pi n(n+1)}{2n+1} \tag{5.3.110}$$

Thus,

$$\gamma_{mn}^2 \int_0^\pi d\theta \sin\theta \left[\left(\frac{m}{\sin\theta} P_n^m(\cos\theta) \right)^2 + \left(\frac{d}{d\theta} P_n^m(\cos\theta) \right)^2 \right]$$
$$= \left[\frac{(2n+1)(n-m)!}{4\pi n(n+1)(n+m)!} \right] \left[\frac{2n(n+1)}{2n+1} \frac{(n+m)!}{(n-m)!} \right] = \frac{1}{2\pi} \tag{5.3.111}$$

Substituting into the expressions for P_{mn},

$$P_{mn} = \frac{R^2}{2} \sqrt{\frac{\varepsilon}{\mu}} \operatorname{Re}\left(i h_n(kR) \left(h_n^*(kR) \right)' \right) \tag{5.3.112}$$

Next, we will prove that

$$\operatorname{Re}\left(i h_n(kR) \left(\frac{\left[kr h_n(kr) \right]'}{kr} \right)^* \right) = \left(\frac{1}{kR} \right)^2 \tag{5.3.113}$$

Using the following properties for spherical Hankel function,

$$h_n'(kR) = h_{n-1}(kR) - \left((n+1)/(kR) \right) h_n(kR)$$
$$h_n(kR) = \left((2n-1)/(kR) \right) h_{n-1}(kR) - h_{n-2}(kR) \tag{5.3.114}$$

Then,

$$
\begin{aligned}
&\mathrm{Re}\left(ih_n(kR)\left(h_n^*(kR)\right)'\right)\\
&=-\mathrm{Im}\left(h_n(kR)\left(h_n^*(kR)\right)'\right)\\
&=-\mathrm{Im}\left(h_n(kR)\left(h_{n-1}^*(kR)-\left((n+1)/(kR)\right)h_n^*(kR)\right)\right)=-\mathrm{Im}\left(h_n(kR)h_{n-1}^*(kR)\right)\\
&=-\mathrm{Im}\left(\left(\left((2n-1)/(kR)\right)h_{n-1}(kR)-h_{n-2}(kR)\right)h_{n-1}^*(kR)\right)=\mathrm{Im}\left(h_{n-1}^*(kR)h_{n-2}(kR)\right)\\
&=\mathrm{Im}\left(h_{n-2}(kR)\left(\left((2n-3)/(kR)\right)h_{n-2}(kR)-h_{n-3}(kR)\right)^*\right)=-\mathrm{Im}\left(h_{n-2}(kR)h_{n-3}^*(kR)\right)\\
&=...
\end{aligned}
\tag{5.3.115}
$$

Thus,

$$
-\mathrm{Im}\left(h_n(kR)h_{n-1}^*(kR)\right)=-\mathrm{Im}\left(h_{n-1}(kR)h_{n-2}^*(kR)\right)=-\mathrm{Im}\left(h_{n-2}(kR)h_{n-3}^*(kR)\right)=...=-\mathrm{Im}\left(h_1(kR)h_0^*(kR)\right)
\tag{5.3.116}
$$

Then,

$$
\begin{aligned}
&\mathrm{Re}\left(ih_n(kR)\left(h_n^*(kR)\right)'\right)\\
&=-\mathrm{Im}\left(h_n(kR)h_{n-1}^*(kR)\right)=-\mathrm{Im}\left(h_1(kR)h_0^*(kR)\right)\\
&=-\mathrm{Im}\left[-i\left(\frac{1}{(kR)^2}-\frac{i}{kR}\right)e^{ikR}\cdot\left(-i\frac{e^{ikR}}{kR}\right)^*\right]=\frac{1}{(kR)^2}
\end{aligned}
\tag{5.3.117}
$$

Finally,

$$
P_{mn}=\frac{R^2}{2}\sqrt{\frac{\varepsilon}{\mu}}\left(\frac{1}{kR}\right)^2=\frac{1}{2\eta k^2}
\tag{5.3.118}
$$

Thus, the power for each order of vector spherical harmonics is the same and does not depend on the order. P_{mn} also does not depend on R which satisfies the energy conservation.

As will be shown in section 5.4, the transformation coefficients obtained from the numerical method agrees with those from the analytical method. But the numerical method is more robust than the analytical method.

(b) Translation Addition Method for Vector Spheroidal Waves

The mathematical expressions for the translation addition theorem for vector spheroidal waves are

$$\bar{M}^{a(3)}_{\sigma,mn}\left(c,\xi_j,\eta_j,\phi_j\right)=\sum_{\mu,\nu}\left[\begin{array}{l}A^{I(M),e}_{(\sigma,mn)\mu\nu}\bar{M}^{a(1)}_{e,\mu\nu}\left(k\overline{rr_l}\right)+A^{I(M),o}_{(\sigma,mn)\mu\nu}\bar{M}^{a(1)}_{o,\mu\nu}\left(k\overline{rr_l}\right)\\+A^{I(N),e}_{(\sigma,mn)\mu\nu}\bar{N}^{a(1)}_{e,\mu\nu}\left(k\overline{rr_l}\right)+A^{I(N),o}_{(\sigma,mn)\mu\nu}\bar{N}^{a(1)}_{o,\mu\nu}\left(k\overline{rr_l}\right)\end{array}\right] \tag{5.3.119 a}$$

$$\bar{N}^{a(3)}_{\sigma,mn}\left(c,\xi_j,\eta_j,\phi_j\right)=\sum_{\mu,\nu}\left[\begin{array}{l}B^{I(M),e}_{(\sigma,mn)\mu\nu}\bar{M}^{a(1)}_{e,\mu\nu}\left(k\overline{rr_l}\right)+B^{I(M),o}_{(\sigma,mn)\mu\nu}\bar{M}^{a(1)}_{o,\mu\nu}\left(k\overline{rr_l}\right)\\+B^{I(N),e}_{(\sigma,mn)\mu\nu}\bar{N}^{a(1)}_{e,\mu\nu}\left(k\overline{rr_l}\right)+B^{I(N),o}_{(\sigma,mn)\mu\nu}\bar{N}^{a(1)}_{o,\mu\nu}\left(k\overline{rr_l}\right)\end{array}\right] \tag{5.3.119 b}$$

where σ is either 'e' or 'o'. These equations mean the outgoing vector spheroidal waves $\bar{M}^{a(3)}_{\sigma,mn}\left(c,\xi_j,\eta_j,\phi_j\right)$ and $\bar{N}^{a(3)}_{\sigma,mn}\left(c,\xi_j,\eta_j,\phi_j\right)$ centered at $\bar{r}_j$ are expressed the incoming vector spheroidal waves $\bar{M}^{a(1)}_{\sigma,\mu\nu}\left(k\overline{rr_l}\right)$ and $\bar{N}^{a(1)}_{\sigma,\mu\nu}\left(k\overline{rr_l}\right)$ centered at $\bar{r}_l$.

The transformation coefficients $A^{I(M),e}_{(\sigma,mn)\mu\nu}$, $A^{I(M),o}_{(\sigma,mn)\mu\nu}$, $A^{I(N),e}_{(\sigma,mn)\mu\nu}$, $A^{I(N),o}_{(\sigma,mn)\mu\nu}$, $B^{I(M),e}_{(\sigma,mn)\mu\nu}$, $B^{I(M),o}_{(\sigma,mn)\mu\nu}$, $B^{I(N),e}_{(\sigma,mn)\mu\nu}$, $B^{I(N),o}_{(\sigma,mn)\mu\nu}$. For generally cases, there is no analytical methods available to obtain these coefficients. In this section, a numerical method to find these coefficients will be developed. It is observed that the transformation coefficients are similar to the expansion coefficients of the scattered fields, except that $\bar{M}^{a(3)}_{\sigma,mn}\left(c,\xi_j,\eta_j,\phi_j\right)$ and $\bar{N}^{a(3)}_{\sigma,mn}\left(c,\xi_j,\eta_j,\phi_j\right)$ are vector spheroidal waves instead of scattered fields and the expansion basis functions are incoming waves instead of outgoing waves. Thus, similar method of calculating the expansion coefficients of scattered fields in section 5.3.1 can be used here. First, let us consider the translation addition theorem for $\bar{M}^{a(3)}_{\sigma,mn}\left(c,\xi_j,\eta_j,\phi_j\right)$. Following the method in section 5.3.1, we obtain

$$\begin{bmatrix} \bar{b}^{M(M,e)} \\ \bar{b}^{M(M,o)} \\ \bar{b}^{M(N,e)} \\ \bar{b}^{M(N,o)} \end{bmatrix} = \begin{bmatrix} \bar{\bar{C}}^{M,e,M,e}_{(1)} & \bar{\bar{C}}^{M,e,M,o}_{(1)} & \bar{\bar{C}}^{M,e,N,e}_{(1)} & \bar{\bar{C}}^{M,e,N,o}_{(1)} \\ \bar{\bar{C}}^{M,e,M,o}_{(1)} & \bar{\bar{C}}^{M,o,M,o}_{(1)} & \bar{\bar{C}}^{N,e,M,o}_{(1)} & \bar{\bar{C}}^{N,o,M,o}_{(1)} \\ \bar{\bar{C}}^{M,e,N,e}_{(1)} & \bar{\bar{C}}^{M,o,N,e}_{(1)} & \bar{\bar{C}}^{N,e,N,e}_{(1)} & \bar{\bar{C}}^{N,o,N,e}_{(1)} \\ \bar{\bar{C}}^{M,e,N,o}_{(1)} & \bar{\bar{C}}^{M,o,N,o}_{(1)} & \bar{\bar{C}}^{N,e,N,o}_{(1)} & \bar{\bar{C}}^{N,o,N,o}_{(1)} \end{bmatrix} \begin{bmatrix} \bar{A}^{I(M),e} \\ \bar{A}^{I(M),o} \\ \bar{A}^{I(N),e} \\ \bar{A}^{I(N),o} \end{bmatrix} \tag{5.3.120}$$

It is noted that subscripts '(1)' are used in the C matrices to denote that they are integration of inner product of incoming vector spheroidal waves instead of outgoing vector spheroidal waves as in section 5.3.1. The C matrices are calculated in the same way as described in section 5.3.1, except that the outgoing vector spheroidal waves are replaced by incoming vector spheroidal waves in the calculations. The b vectors are obtained by integrating of the inner product of $\hat{\xi}_{\bar{r}_l} \times \bar{M}^{a(3)}_{\sigma,mn}\left(c,\xi_j,\eta_j,\phi_j\right)$ and the incoming vector spheroidal waves centered at $\bar{r}_l$ over the spheroidal surface also centered at $\bar{r}_l$,

$$b^{M(V,\sigma')}_{\mu'v'} = \int_{\partial SO_l} \bar{V}^{a(1)}_{\sigma',\mu'v'} \cdot \left[\hat{\xi}_l \times \bar{M}^{a(3)}_{\sigma,mn}\left(c,\xi_l,\eta_l,\phi_l\right)\right] \tag{5.3.121}$$

where the subscript 'l' means centered at $\bar{r}_l$. In chapter V, 'a' is 'r'.

This integration is performed numerically. The key calculations in this numerical integration are calculating the values of $\bar{M}^{a(3)}_{\sigma,mn}\left(k\overline{rr_j}\right)$ at the points on the spheroidal surface centered at $\bar{r}_l$.

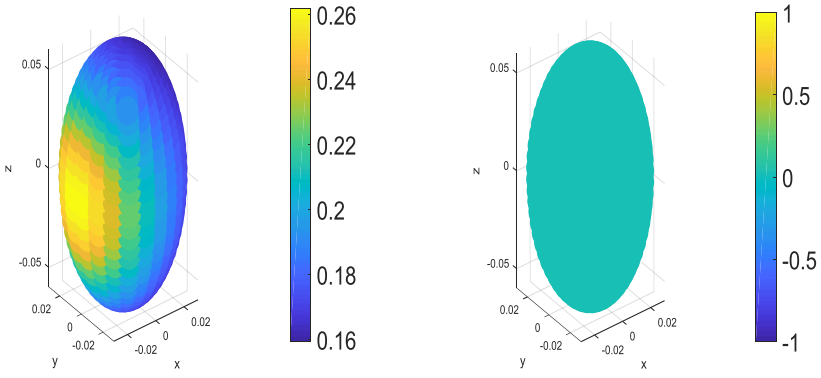

(a) (b)

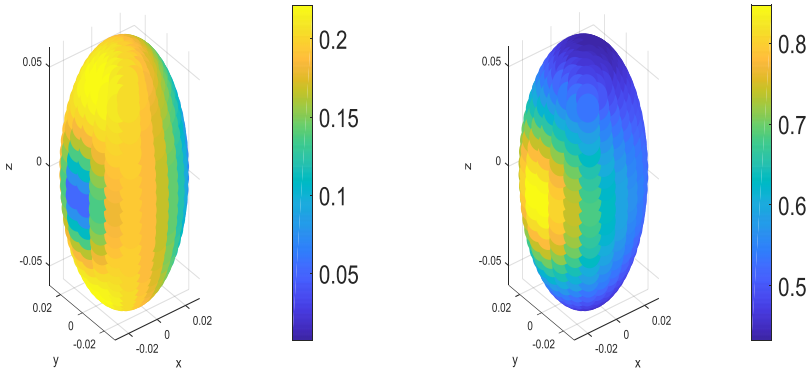

(c) (d)

Figure V.23. $|\bar{M}^{r(3)}_{\sigma,mn}(k\overline{rr_j})|$ on the spheroidal surface centered at $\bar{r}_l$, where $\bar{r}_l = [0,0,0]$, $\bar{r}_j = [-\frac{\lambda}{2},0,0]$ for (a) σ=e, m=0, n=1; (b) σ=o, m=0, n=1; (c) σ=e, m=1, n=2; (d) σ=o, m=1, n=2.

The magnitude of $\bar{M}^{a(3)}_{\sigma,mn}\left(k\overline{rr_j}\right)$ is plotted on the spheroidal surface centered at $\bar{r}_l$ in Figure V.23 It is observed that $\left|\bar{M}^{r(3)}_{o,01}(k\overline{rr_j})\right| = 0$. This can be verified by substituting m=0 and n=1 into the expression of $\bar{M}^{a(3)}_{o,mn}$ in section 5.2.1.

The following eight steps to obtain the transformation coefficients are summarized below.

Step 1: Generate quadrature points for integration on the spheroidal surface centered at $\bar{r}_l$. For each point (ξ_l,η_l,ϕ_l), transform it into the corresponding point (x_l,y_l,z_l) in the rectangular coordinate centered at $\bar{r}_l$, using the following relationship

$$\begin{aligned} x_l &= \frac{d_l}{2}\sqrt{\left(1-\eta_l^2\right)\left(\xi_l^2-1\right)}\cos\phi_l \\ y_l &= \frac{d_l}{2}\sqrt{\left(1-\eta_l^2\right)\left(\xi_l^2-1\right)}\sin\phi_l \\ z_l &= \frac{d_l}{2}\eta_l\xi_l \end{aligned} \tag{5.3.122}$$

Step 2: Transform (x_l,y_l,z_l) to the corresponding point (x_j,y_j,z_j) in the rectangular coordinate centered at $\bar{r}_j$. Let $\overline{r_jr_l} = \bar{r}_l - \bar{r}_j = [\Delta x,\Delta y,\Delta z]$, then

$$\left(x_j, y_j, z_j\right) = \left(x_l + \Delta x, y_l + \Delta y, z_l + \Delta z\right) \tag{5.3.123}$$

Step 3: Transform $\left(x_j, y_j, z_j\right)$ to the corresponding point $\left(\xi_j, \eta_j, \phi_j\right)$ in the prolate spheroidal coordinate centered at $\bar{r}_j$, using the following relationship

$$\begin{aligned}
\phi_j &= \text{atan2}\left(x_j, y_j\right) \\
\xi_j &= \frac{2}{d_j}\sqrt{\left(\frac{d_j^2}{4} + z_j^2 + x_j{}^2 + y_j^2\right) + \sqrt{\left(\frac{d_j^2}{4} + z_j^2 + x_j\%^2 + y_j^2\right)^2 - d_j^2 z_j^2}} \\
\eta_j &= \frac{2z_j}{d_j \xi_j}
\end{aligned} \tag{5.3.124}$$

where 'atan2' is a matlab function which computes the four-quadrant inverse tangent.

Step 4: Calculate $\bar{M}_{\sigma,mn}^{a(3)}\left(c, \xi_j, \eta_j, \phi_j\right)$ using the expressions in section 5.2.2.

Step 5: Transform $\bar{M}_{\sigma,mn}^{a(3)}\left(c, \xi_j, \eta_j, \phi_j\right)$ in the spheroidal coordinate centered at $\bar{r}_j$ into the rectangular coordinate.

$$\begin{aligned}
&\bar{M}_{\sigma,mn}^{a(3)}\left(c, \xi_j, \eta_j, \phi_j\right) = M_{\eta j}\left(c, \xi_j, \eta_j, \phi_j\right)\hat{\eta}_j + M_{\xi j}\left(c, \xi_j, \eta_j, \phi_j\right)\hat{\xi}_j + M_{\phi j}\left(c, \xi_j, \eta_j, \phi_j\right)\hat{\phi}_j \\
&= M_x\left(c, \xi_j, \eta_j, \phi_j\right)\hat{x} + M_y\left(c, \xi_j, \eta_j, \phi_j\right)\hat{y} + M_z\left(c, \xi_j, \eta_j, \phi_j\right)\hat{z}
\end{aligned} \tag{5.3.125}$$

The following relationship is used.

$$\begin{aligned}
M_x &= M_{\xi j}\left(\xi_j \frac{\left(1-\eta_j^2\right)^{\frac{1}{2}}}{\left(\xi_j^2 - \eta_j^2\right)^{\frac{1}{2}}}\cos\phi_j\right) + M_{\eta j}\left(-\eta_j \frac{\left(\xi_j^2 - 1\right)^{\frac{1}{2}}}{\left(\xi_j^2 - \eta_j^2\right)^{\frac{1}{2}}}\cos\phi_j\right) + M_{\phi j}\left(-\sin\phi_j\right) \\
M_y &= M_{j\xi}\left(\xi_j \frac{\left(1-\eta_j^2\right)^{\frac{1}{2}}}{\left(\xi_j^2 - \eta_j^2\right)^{\frac{1}{2}}}\sin\phi_j\right) + M_{j\eta}\left(-\eta_j \frac{\left(\xi_j^2 - 1\right)^{\frac{1}{2}}}{\left(\xi_j^2 - \eta_j^2\right)^{\frac{1}{2}}}\sin\phi_j\right) + M_{j\phi}\left(\cos\phi_j\right) \\
M_z &= M_{\xi j}\left(\eta_j \frac{\left(\xi_j^2 - 1\right)^{\frac{1}{2}}}{\left(\xi_j^2 - \eta_j^2\right)^{\frac{1}{2}}}\right) + M_{\eta j}\left(\xi \frac{\left(1-\eta_j^2\right)^{\frac{1}{2}}}{\left(\xi_j^2 - \eta_j^2\right)^{\frac{1}{2}}}\right)
\end{aligned} \tag{5.3.126}$$

Step 6: Transform $\bar{M}_{\sigma,mn}^{a(3)}\left(c,\xi_j,\eta_j,\phi_j\right)$ in the rectangular coordinate into the spheroidal coordinate centered at $\bar{r}_l$.

$$\begin{aligned}\bar{M}_{\sigma,mn}^{a(3)}\left(c,\xi_j,\eta_j,\phi_j\right)&=M_x\left(c,\xi_j,\eta_j,\phi_j\right)\hat{x}+M_y\left(c,\xi_j,\eta_j,\phi_j\right)\hat{y}+M_z\left(c,\xi_j,\eta_j,\phi_j\right)\hat{z}\\&=M_{\eta l}\left(c,\xi_j,\eta_j,\phi_j\right)\hat{\eta}_l+M_{\xi l}\left(c,\xi_j,\eta_j,\phi_j\right)\hat{\xi}_l+M_{\phi l}\left(c,\xi_j,\eta_j,\phi_j\right)\hat{\phi}_l\end{aligned}\tag{5.3.127}$$

$$\begin{aligned}M_{\eta_l}&=-\eta_l\frac{\left(\xi_l^2-1\right)^{\frac{1}{2}}}{\left(\xi_l^2-\eta_l^2\right)^{\frac{1}{2}}}\left(M_x\cos\phi_l+M_y\sin\phi_l\right)+\xi_l\frac{\left(1-\eta_l{}^2\right)^{\frac{1}{2}}}{\left(\xi_l^2-\eta_l^2\right)^{\frac{1}{2}}}M_z\\M_{\xi_l}&=\xi_l\frac{\left(1-\eta_l^2\right)^{\frac{1}{2}}}{\left(\xi_l^2-\eta_l^2\right)^{\frac{1}{2}}}\left(M_x\cos\phi_l+M_y\sin\phi_l\right)+M_z\frac{\left(\xi_l{}^2-1\right)^{\frac{1}{2}}}{\left(\xi_l^2-\eta_l^2\right)^{\frac{1}{2}}}\\M_{\phi_l}&=-M_x\sin\phi_l+M_y\cos\phi_l\end{aligned}\tag{5.3.128}$$

Step 7: Calculate the element of b vector $b_{\mu'\nu'}^{M\left(V,\sigma'\right)}=\int_{\partial SO_l}\bar{V}_{\sigma',\mu'\nu'}^{a(1)}\cdot\left[\hat{\xi}_l\times\bar{M}_{\sigma,mn}^{a(3)}\left(c,\xi_l,\eta_l,\phi_l\right)\right]$.

$$b_{\mu'\nu'}^{M\left(V,\sigma'\right)}=f^2\left(\xi^2-1\right)^{\frac{1}{2}}\int_0^{2\pi}d\phi\int_{-1}^{1}d\eta\left(\xi^2-\eta^2\right)^{\frac{1}{2}}\left(V_{\eta,\sigma',m'n'}^{a(3)}M_{\phi_l}-V_{\phi,\sigma',m'n'}^{a(3)}M_{\eta_l}\right)\tag{5.3.129}$$

Step 8: Finally, the transformation coefficients for $\bar{M}_{\sigma,mn}^{a(3)}$ are obtained as

$$\begin{bmatrix}\bar{A}^{I(M),e}\\\bar{A}^{I(M),o}\\\bar{A}^{I(N),e}\\\bar{A}^{I(N),o}\end{bmatrix}=\begin{bmatrix}\bar{\bar{C}}_{(1)}^{M,e,M,e}&\bar{\bar{C}}_{(1)}^{M,e,M,o}&\bar{\bar{C}}_{(1)}^{M,e,N,e}&\bar{\bar{C}}_{(1)}^{M,e,N,o}\\\bar{\bar{C}}_{(1)}^{M,e,M,o}&\bar{\bar{C}}_{(1)}^{M,o,M,o}&\bar{\bar{C}}_{(1)}^{N,e,M,o}&\bar{\bar{C}}_{(1)}^{N,o,M,o}\\\bar{\bar{C}}_{(1)}^{M,e,N,e}&\bar{\bar{C}}_{(1)}^{M,o,N,e}&\bar{\bar{C}}_{(1)}^{N,e,N,e}&\bar{\bar{C}}_{(1)}^{N,o,N,e}\\\bar{\bar{C}}_{(1)}^{M,e,N,o}&\bar{\bar{C}}_{(1)}^{M,o,N,o}&\bar{\bar{C}}_{(1)}^{N,e,N,o}&\bar{\bar{C}}_{(1)}^{N,o,N,o}\end{bmatrix}^{-1}\begin{bmatrix}\bar{b}^{M(M,e)}\\\bar{b}^{M(M,o)}\\\bar{b}^{M(N,e)}\\\bar{b}^{M(N,o)}\end{bmatrix}\tag{5.3.130}$$

These eight steps are performed for all the combinations of (σ,m,n) to obtain the transformation coefficient matrix $\bar{\bar{A}}\left(k\overline{rr_j}\right)$.

Similarly, methods are used to calculate the transformation coefficients $\bar{\bar{B}}\left(k\overline{rr_j}\right)$ for $\bar{N}_{\sigma,mn}^{a(3)}\left(c,\xi_j,\eta_j,\phi_j\right)$.

$$\begin{bmatrix} \bar{B}^{I(M),e} \\ \bar{B}^{I(M),o} \\ \bar{B}^{I(N),e} \\ \bar{B}^{I(N),o} \end{bmatrix} = \begin{bmatrix} \bar{\bar{C}}^{M,e,M,e}_{(1)} & \bar{\bar{C}}^{M,e,M,o}_{(1)} & \bar{\bar{C}}^{M,e,N,e}_{(1)} & \bar{\bar{C}}^{M,e,N,o}_{(1)} \\ \bar{\bar{C}}^{M,e,M,o}_{(1)} & \bar{\bar{C}}^{M,o,M,o}_{(1)} & \bar{\bar{C}}^{N,e,M,o}_{(1)} & \bar{\bar{C}}^{N,o,M,o}_{(1)} \\ \bar{\bar{C}}^{M,e,N,e}_{(1)} & \bar{\bar{C}}^{M,o,N,e}_{(1)} & \bar{\bar{C}}^{N,e,N,e}_{(1)} & \bar{\bar{C}}^{N,o,N,e}_{(1)} \\ \bar{\bar{C}}^{M,e,N,o}_{(1)} & \bar{\bar{C}}^{M,o,N,o}_{(1)} & \bar{\bar{C}}^{N,e,N,o}_{(1)} & \bar{\bar{C}}^{N,o,N,o}_{(1)} \end{bmatrix}^{-1} \begin{bmatrix} \bar{b}^{N(M,e)} \\ \bar{b}^{N(M,o)} \\ \bar{b}^{N(N,e)} \\ \bar{b}^{N(N,o)} \end{bmatrix} \tag{5.3.131}$$

The C matrix is the same as that for calculating $\bar{\bar{A}}\left(k\overline{rr_j}\right)$. The b vectors are obtained by integrating of the inner product of $\hat{\xi}_{\bar{r}_l} \times \bar{N}^{a(3)}_{\sigma,mn}\left(c,\xi_j,\eta_j,\phi_j\right)$ and the incoming vector spheroidal waves centered at $\bar{r}_l$ over the spheroidal surface also centered at $\bar{r}_l$,

$$b^{N\left(V,\sigma'\right)}_{\mu'\nu'} = \int_{\partial SO_l} \bar{V}^{a(1)}_{\sigma',\mu'\nu'} \cdot \left[\hat{\xi}_l \times \bar{N}^{a(3)}_{\sigma,mn}\left(c,\xi_l,\eta_l,\phi_l\right)\right] \tag{5.3.132}$$

In calculating $b^{N\left(V,\sigma'\right)}_{\mu'\nu'}$, the same eight steps are performed except that 'M' is changed to 'N'.

(c) Translation Addition Method for 3D Vector Cylindrical Waves

The analytical expressions translation addition theorem for 3D vector cylindrical waves are [4]

$$\bar{M}_m(k_z,\overline{rr_p}) = \sum_{\mu}\begin{bmatrix} H^{(1)}_{\mu-m}(k_\rho \mid \bar{\rho}_p - \bar{\rho}_q \mid)\exp(-i(\mu-m)\phi_{\overline{r_p r_q}}) \\ \cdot\exp(-ik_z(z_p - z_q))Rg\bar{M}_\mu(k_z,\overline{rr_q}) \end{bmatrix} \tag{5.3.133}$$

$$\bar{N}_m(k_z,\overline{rr_p}) = \sum_{\mu}\begin{bmatrix} H^{(1)}_{\mu-m}(k_\rho \mid \bar{\rho}_p - \bar{\rho}_q \mid)\exp(-i(\mu-m)\phi_{\overline{r_p r_q}}) \\ \cdot\exp(-ik_z(z_p - z_q))Rg\bar{N}_\mu(k_z,\overline{rr_q}) \end{bmatrix} \tag{5.3.134}$$

For 3D vector cylindrical waves, the numerical methods for wave transformations are not needed.

5.3.3 Solving the Foldy-Lax Multiple Scattering Equation

The final step in the hybrid method is solving the Foldy-Lax equations. For vector spherical waves, the Foldy-Lax equation formulation is available in [4]. The extracted T matrix and the transformation coefficients from section 5.3.1 and 5.3.2 are submitted to the Foldy-Lax equations. Similar formulation is used for vector spheroidal waves. For 3D vector cylindrical waves, the scattered field formulation of the Foldy-Lax equation is used instead of the usual exciting field formulation as used for the vector spherical and spheroidal waves. The detailed derivations are presented below.

As derived in chapter 4, the Foldy-Lax equations (FL) for N_t number of objects are

$$\bar{E}_q^{ex} = \bar{E}^{inc} + \sum_{p=1, p\neq q}^{N_t} \bar{E}_{qp}^{s} \tag{5.3.135}$$

where $\bar{E}_q^{ex}$ is the final exciting field on object q, $\bar{E}^{inc}$ is the incident field and $\bar{E}_{qp}^{s}$ is the scattered field from object p to q. It states that the final exciting on the object is the incident field plus the scattered fields from all the other objects except itself.

The exciting field is expanded into in-coming 3D vector cylindrical waves as in section 5.3.1. The incident field is also expanded into in-coming 3D vector cylindrical waves. In this chapter, incident plane wave is used which is commonly-used for remote sensing. Let the incident plane wave be $\bar{E}^{inc} = (\hat{v}E_{vi} + \hat{h}E_{hi})\exp(i\bar{k}_i \cdot \bar{r})$, where $\hat{v}$ and $\hat{h}$ are the vertical and horizontal polarization, respectively, and $\bar{k}_i = \hat{x}k\sin(\theta_i)\cos(\phi_i) + \hat{y}k\sin(\theta_i)\sin(\phi_i) + \hat{z}k\cos(\theta_i)$. The expansion coefficients for the incident plane wave are [4]

$$\bar{E}^{inc}(\bar{r}) = \sum_m \frac{i^m e^{-im\phi_i}}{k_{i\rho}} [iE_{hi} Rg\bar{M}_n(k_{iz}, \bar{r}) - E_{vi} Rg\bar{N}_n(k_{iz}, \bar{r})] \tag{5.3.136}$$

The scattered field from object p is expanded into out-going 3D vector cylindrical waves, where the expansion coefficients are related to the exciting field coefficients by the T matrix as expressed in section 5.3.1 (c). Then,

$$\bar{E}^s(\bar{r}-\bar{r}_p)=\sum_{\beta=M,N}\sum_{m}\int_{-\infty}^{\infty}dk_z\bar{\beta}_m(k_z,\bar{r},-\bar{r}_p)\sum_{m'}\int_{-\infty}^{\infty}dk_z'\begin{bmatrix}T_{mm',p}^{(\beta,M)}(k_z,k_z')w_{m',p}^{(M)}(k_z')\\+T_{mm',p}^{(\beta,N)}(k_z,k_z')w_{m',p}^{(N)}(k_z')\end{bmatrix} \tag{5.3.137}$$

where the subscript p means the coefficients and the T matrix are for the object p.

The next step is applying the vector translation addition theorem which transforms the out-going waves centered at r_p to in-coming waves centered tat r_q, as illustrated in section 5.3.2. After substituting the translation addition theorem into the scattered fields, the scattered field from object p is expanded in terms of in-coming 3D vector cylindrical waves centered at object q. In this way, $\bar{E}_q^{ex}$, $\bar{E}^{inc}$ and $\bar{E}_{qp}^{s}$ in FL are expanded in terms of in-coming 3D vector cylindrical waves. Matching the coefficients for different orders of waves leads to

$$\begin{aligned}w_{m'',q}^{(\beta)}(k_z)&=\frac{i^{m''}\exp(-im''\phi_i)}{k_{i\rho}}\exp(i\bar{k}_i\bar{r}_q)C_\beta\times\delta(k_z-k_{iz})\\&+\sum_{p=1,p\neq q}^{N_t}\sum_{mm'}\int_{-\infty}^{\infty}dk_z'\begin{Bmatrix}\exp(-i(m''-m)\phi_{\overline{r_pr_q}})H_{m''-m}^{(1)}(k_\rho|\bar{\rho}_p-\bar{\rho}_q|)\exp(-ik_z(z_p-z_q))\\\cdot[T_{mm',p}^{(\beta,M)}(k_z,k_z')\times w_{m',p}^{(M)}(k_z')+T_{mm',p}^{(\beta,N)}(k_z,k_z')w_{m',p}^{(N)}(k_z')]\end{Bmatrix}\end{aligned} \tag{5.3.138}$$

where $C_\beta=iE_{hi},when\ \beta=M;\ C_\beta=-E_{vi},when\ \beta=N.$

In the above equation of the exciting field formulation of the Foldy-Lax equation, the unknowns to be solved is the final exciting field coefficients of all the objects. It is noted that there is a delta function in the above equation caused by the incident plane wave expansion. To avoid the delta function, this exciting field formulation is modified to scattered field formulation where the unknowns are the final scattered field coefficients as below,

$$a_{m'',q}^{(\beta)}(k_z)=\sum_{m'}[T_{m''m',q}^{(\beta,N)}(k_z,k_{iz})C_N+T_{m''m',q}^{(\beta,M)}(k_z,k_{iz})C_M]\frac{i^{m'}\exp(-im'\phi_i)}{k_{i\rho}}\exp(i\bar{k}_i\bar{r}_q)$$
$$+\sum_{p=1,p\neq q}^{N_t}\sum_{mm'}\int_{-\infty}^{\infty}dk_z'\begin{Bmatrix}\exp(-i(m'-m)\phi_{\overline{r_pr_q}})H_{m'-m}^{(1)}(k_\rho'|\bar{\rho}_p-\bar{\rho}_q|)\exp(-ik_z'(z_p-z_q))\\ \cdot[T_{m''m',q}^{(\beta,N)}(k_z,k_z')a_{m,p}^{(N)}(k_z')+T_{m''m',q}^{(\beta,M)}(k_z,k_z')a_{m,p}^{(M)}(k_z')]\end{Bmatrix} \quad (5.3.139)$$

For rotational symmetric object such as a cylinder, the T matrix has a delta function as in it: $T_{mm'}^{(\beta,\alpha)}(k_z,k_z')=T_m^{(\beta,\alpha)}(k_z,k_z')\delta(m-m')$. This can simply the above equation into

$$a_{m'',q}^{(\beta)}(k_z)=[T_{m'',q}^{(\beta,N)}(k_z,k_{iz})C_N+T_{m'',q}^{(\beta,M)}(k_z,k_{iz})C_M]\frac{i^{m''}\exp(-im''\phi_i)}{k_{i\rho}}\exp(i\bar{k}_i\bar{r}_q)$$
$$+\sum_{p=1,p\neq q}^{N_t}\sum_{m}\int_{-\infty}^{\infty}dk_z'\begin{Bmatrix}\exp(-i(m''-m)\phi_{\overline{r_pr_q}})H_{m''-m}^{(1)}(k_\rho'|\bar{\rho}_p-\bar{\rho}_q|)\exp(-ik_z'(z_p-z_q))\\ \cdot[T_{m'',q}^{(\beta,N)}(k_z,k_z')a_{m,p}^{(N)}(k_z')+T_{m'',q}^{(\beta,M)}(k_z,k_z')a_{m,p}^{(M)}(k_z')]\end{Bmatrix} \quad (5.3.140)$$

We consider the cases that the cylinders are not that close to each other so that the evanescent waves can be ignored, for the application of Foldy-Lax equations with 3D vector cylindrical wave expansions. This means $\int_{-\infty}^{\infty}dk_z'\simeq\int_{-k}^{k}dk_z'$. Next, using the relationship $k_z=k\cos\theta$, the integration over k_z' is changed to the integration over θ', $\int_{-\infty}^{\infty}dk_z'=\int_{i\infty}^{\pi-i\infty}k\sin\theta'd\theta'$. For the case of cylinders, $\sin\theta'$ removes the $\frac{1}{\sqrt{k^2-k_z'^2}}$ singularity of $T_{m''}^{(\beta,\alpha)}(k_z,k_z')$ when $k_z'=k$. It is noted that when $k_z'>k$, the wave becomes evanescent. In this chapter for 3D vector cylindrical waves, we exclude the evanescent waves which are not important for the simulations of vegetation/forest canopy as will be shown in the following sections. Then, $\int_{-k}^{k}dk_z'=\int_{0}^{\pi}k\sin\theta'd\theta'$. Next, multiply $\sin(\theta)$ on both sides of the above equation and define $a(k_z)\sin\theta=a(\theta)$, $a(k_z')\sin\theta'=a(\theta')$, and $k\sin\theta T(k_z,k_z')=T(\theta,\theta')$. After that, changing the integration into numerical summation, the above equation becomes

$$a_{m'',q}^{(\beta)}(\theta_n) = [T_{m'',q}^{(\beta,N)}(\theta_n,\theta_i)C_N + T_{m'',q}^{(\beta,M)}(\theta_n,\theta_i)C_M]\frac{i^{m''}\exp(-im''\phi_i)}{kk\sin\theta_i}\exp(i\bar{k}_i\bar{r}_q)$$
$$+\sum_{p=1,p\neq q}^{N_t}\sum_{m,n'}(\Delta\theta)\left\{\begin{array}{l}\exp(-i(m''-m)\phi_{\overline{r_p r_q}})H_{m''-m}^{(1)}(k\sin\theta_{n'}\,|\,\bar{\rho}_p-\bar{\rho}_q\,|)\exp(-ik\cos\theta_{n'}(z_p-z_q))\\ \cdot[T_{m'',q}^{(\beta,N)}(\theta_n,\theta_{n'})a_{m,p}^{(N)}(\theta_{n'})+T_{m'',q}^{(\beta,M)}(\theta_n,\theta_{n'})a_{m,p}^{(M)}(\theta_{n'})]\end{array}\right\} \tag{5.3.141}$$

where θ_i is the incident angle, $\theta_n = n\Delta\theta$ and $\theta_{n'} = n'\Delta\theta$. The summation over n' is from 0 to N_{max}. In this chapter, uniform discretization is used and thus $\Delta\theta = \pi / N_{max}$. The unknowns in the above equation are the scattered field coefficients of the scattered fields from all the objects at two polarizations. Thus, the total number of unknowns are $2N_t(2M_{max}+1)N_{max}$. The unknowns are on both sides of the equation and can be written in the matrix form as $\bar{a} = \bar{c} + \bar{\bar{B}}\bar{a}$. Then, the scattered field coefficients are solved as $\bar{a} = (\bar{\bar{I}} - \bar{\bar{B}})^{-1}\bar{c}$.

After the scattered coefficients are solved, the final scattered fields from all the objects at observation point $\bar{r}$ is

$$\bar{E}^s(\bar{r}) = \sum_{q=1}^{N_t}\sum_{m,n}(\Delta\theta)k[\bar{M}_m(k\cos\theta_n,\bar{r}-\bar{r}_q)a_{m,q}^{(M)}(\theta_n) + \bar{N}_m(k\cos\theta_n,\bar{r}-\bar{r}_q)a_{m,q}^{(N)}(\theta_n)] \tag{5.3.142}$$

5.4 Results and Discussions

In this section, the results of the three steps of the hybrid method are verified. After that, the hybrid method is applied for NMM3D full-wave simulations of vegetation/forest.

5.4.1 The T Matrix Extraction

First, the extracted T matrix from off-the-shelf techniques is verified. For the T matrix with vector spherical wave expansions, analytical expression of the T matrix for a sphere is available [4]

$$\bar{\bar{T}}_{sphere} = \begin{bmatrix} \bar{\bar{T}}^{(11)} & 0 \\ 0 & \bar{\bar{T}}^{(22)} \end{bmatrix} \tag{5.4.1}$$

with $$T^{(11)}_{mnm'n'} = \delta_{mm'}\delta_{nn'}T^{(M)}_n;\ T^{(22)}_{mnm'n'} = \delta_{mm'}\delta_{nn'}T^{(N)}_n$$

$$T_n^{(M)} = -\frac{j_n\left(k_p a\right)\left[kaj_n(ka)\right]' - j_n(ka)\left[k_p a j_n\left(k_p a\right)\right]'}{j_n\left(k_p a\right)\left[kah_n(ka)\right]' - h_n(ka)\left[k_p a j_n\left(k_p a\right)\right]'}$$

$$T_n^{(N)} = -\frac{k_p^2 a^2 j_n\left(k_p a\right)\left[kaj_n(ka)\right]' - k^2 a^2 j_n(ka)\left[k_p a j_n\left(k_p a\right)\right]'}{k_p^2 a^2 j_n\left(k_p a\right)\left[kah_n(ka)\right]' - k^2 a^2 h_n(ka)\left[k_p a j_n\left(k_p a\right)\right]'}$$

where a is the radius of the sphere, k is the wavenumber in the background and k_p is the wavenumber inside the sphere.

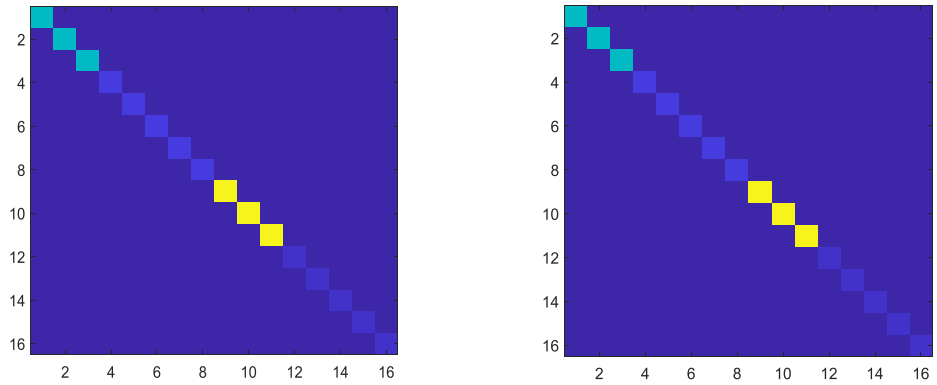

Figure V.24. T matrix from HFSS extraction (left) and analytical solution (right) for a sphere.

It is observed that the T matrix for the sphere is a diagonal matrix. The T matrix extracted from HFSS is compared with the analytical solution for a sphere with radius of 6 cm and permittivity of 27.22+5.22i at 1.41 GHz. In this case, $N_{max} = 2$ and the T matrix size is 16×16. Figure V.24 plots the absolute values of the T matrix from both methods. It is observed that the T matrix for the sphere extracted from HFSS is also a diagonal matrix and agrees well with the analytical solution. For the off-diagonal elements, the Root Mean Squared Error (RMSE) between the two solutions is 1.11×10^{-4}. It is noted that this numerical method of extracting the T matrix works for arbitrarily

shaped object such as complicated branches with leaves, as will be shown later. A sphere is used here only for verification.

For vector spheroidal waves, the analytical expression for the T matrix is not available. To verify the T matrix, we use the extracted T matrix to calculate the scattered fields and compare the scattered fields with those from HFSS. For incident plane wave, the expansion coefficients of the incident waves are detailed in section 5.3.1. Using the extracted T matrix, the expansion coefficients of the scattered waves are obtained using equation (5.3.2). Then, the scattered fields are

$$\bar{E}^s = \sum_{n=1}^{N\max}\sum_{m=0}^{n}\left[a_{mn}^{S(M),e}\bar{M}_{e,mn}^{a(3)} + a_{mn}^{S(N),e}\bar{N}_{e,mn}^{a(3)}\right] + \sum_{n=1}^{N\max}\sum_{m=1}^{n}\left[a_{mn}^{S(M),o}\bar{M}_{o,mn}^{a(3)} + a_{mn}^{S(N),o}\bar{N}_{o,mn}^{a(3)}\right] \qquad (5.4.2)$$

It is noted that the even and odd functions are written into two parts and the summation indexes are different for the even and odd functions. The m for the odd functions starts from m=1 instead of m=0. This is because for m=0, the odd functions are zero, as explained before in section 5.3.2. This can also be verified by substituting m=0 to the expressions for the odd functions in section 5.2.2.

Here, we want to compare the RCS. For RCS, $\xi \to \infty$. In this case, $l\xi \to r$ and $\eta \to \cos\theta$. Then,

$$\begin{aligned}
\hat{\eta} &= -\eta\frac{\left(\xi^2-1\right)^{\frac{1}{2}}}{\left(\xi^2-\eta^2\right)^{\frac{1}{2}}}\left(\hat{x}\cos\phi+\hat{y}\sin\phi\right)+\xi\frac{\left(1-\eta^2\right)^{\frac{1}{2}}}{\left(\xi^2-\eta^2\right)^{\frac{1}{2}}}\hat{z} \\
&\to -\eta\left(\hat{x}\cos\phi+\hat{y}\sin\phi\right)+\left(1-\eta^2\right)^{\frac{1}{2}}\hat{z} \qquad (5.4.3\text{ a}) \\
&= -\hat{x}\cos\phi\cos\theta-\hat{y}\sin\phi\cos\theta+\sin\theta\hat{z} = -\hat{\theta}
\end{aligned}$$

$$\begin{aligned}
\hat{\xi} &= \xi\frac{\left(1-\eta^2\right)^{\frac{1}{2}}}{\left(\xi^2-\eta^2\right)^{\frac{1}{2}}}\left(\hat{x}\cos\phi+\hat{y}\sin\phi\right)+\eta\frac{\left(\xi^2-1\right)^{\frac{1}{2}}}{\left(\xi^2-\eta^2\right)^{\frac{1}{2}}}\hat{z} \\
&\to \left(1-\eta^2\right)^{\frac{1}{2}}\left(\hat{x}\cos\phi+\hat{y}\sin\phi\right)+\eta\hat{z} \qquad (5.4.3\text{ b}) \\
&= \left(\hat{x}\cos\phi\sin\theta+\hat{y}\sin\phi\sin\theta\right)+\cos\theta\hat{z} = \hat{r}
\end{aligned}$$

$$\hat{\phi} = -\hat{x}\sin\phi + \hat{y}\cos\phi \tag{5.4.3 c}$$

Thus, in the far field direction,

$$E_v = E_\eta; \quad E_h = E_\phi \tag{5.4.4}$$

The asymptotic forms of $\bar{M}^{r(3)}_{(e,o),mn}$ and $\bar{N}^{r(3)}_{(e,o),mn}$ are [106]

$$M^{r(3)}_{(e,o),m,n,\eta} \to (-i)^{n+1} \frac{mS_{mn}(\cos\theta)}{\sin\theta} \frac{\exp(ikr)}{kr} \begin{bmatrix} \sin(m\phi) \\ -\cos(m\phi) \end{bmatrix} \tag{5.4.5 a}$$

$$M^{r(3)}_{(e,o),m,n,\phi} \to -(-i)^{n+1} \frac{dS_{mn}(\cos\theta)}{d\theta} \frac{\exp(ikr)}{kr} \begin{bmatrix} \cos(m\phi) \\ \sin(m\phi) \end{bmatrix} \tag{5.4.5 b}$$

$$N^{r(3)}_{(e,o),m,n,\eta} \to -(-i)^{n} \frac{dS_{mn}(\cos\theta)}{d\theta} \frac{\exp(ikr)}{kr} \begin{bmatrix} \cos(m\phi) \\ \sin(m\phi) \end{bmatrix} \tag{5.4.5 c}$$

$$N^{r(3)}_{(e,o),m,n,\phi} \to -(-i)^{n} \frac{mS_{mn}(\cos\theta)}{\sin\theta} \frac{\exp(ikr)}{kr} \begin{bmatrix} \sin(m\phi) \\ -\cos(m\phi) \end{bmatrix} \tag{5.4.5 d}$$

Thus, in the far field region,

$$E_{s,\eta} = \frac{\exp(ikr)}{kr} \sum_{m,n} \begin{bmatrix} \left(\alpha^{M,e}_{mn}\sin(m\phi) - \alpha^{M,o}_{mn}\cos(m\phi)\right)\left((-i)^{n+1}\frac{mS_{mn}(\cos\theta)}{\sin\theta}\right) \\ +\left(\alpha^{N,e}_{mn}\cos(m\phi) + \alpha^{N,o}_{mn}\sin(m\phi)\right)\left(-(-i)^{n}\frac{dS_{mn}(\cos\theta)}{d\theta}\right) \end{bmatrix} \tag{5.4.6}$$

$$E_{s,\phi} = \frac{\exp(ikr)}{kr} \sum_{m,n} \begin{bmatrix} \left(\alpha^{M,e}_{mn}\cos(m\phi) + \alpha^{M,o}_{mn}\sin(m\phi)\right)\left(-(-i)^{n+1}\frac{dS_{mn}(\cos\theta)}{d\theta}\right) \\ +\left(\alpha^{N,e}_{mn}\sin(m\phi) - \alpha^{N,o}_{mn}\cos(m\phi)\right)\left(-(-i)^{n}\frac{mS_{mn}(\cos\theta)}{\sin\theta}\right) \end{bmatrix} \tag{5.4.7}$$

Finally, using the relationship that $\begin{bmatrix} E^s_v \\ E^s_h \end{bmatrix} = \frac{\exp(ikr)}{r} \begin{bmatrix} S_{vv} & S_{vh} \\ S_{hv} & S_{hh} \end{bmatrix} \begin{bmatrix} E^i_v \\ E^i_h \end{bmatrix}$, and $\sigma_{pq} = 4\pi\left|S_{pq}\right|^2$, the RCS of the scatterer using the T matrix with vector spheroidal wave expansions is obtained.

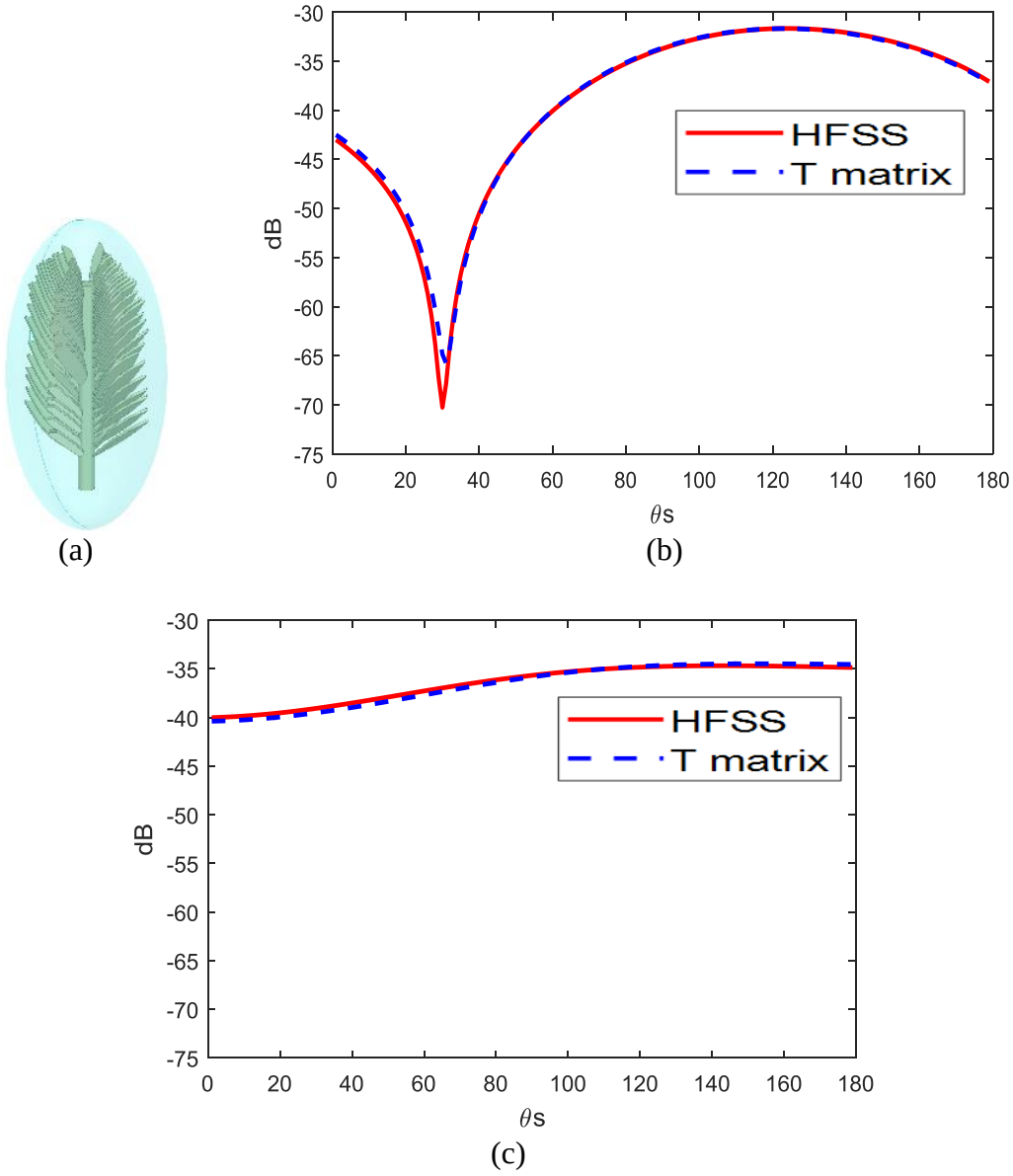

Figure V.25. (a) a branch with complicated leaves for simulation; RCS from HFSS compared with that from the T matrix for (b) σ_{vv} and (c) σ_{hh}.

The RCS are computed using two methods for a branch with complicated leaves (Figure V.25 (a)) : the T matrix method as explained above, and directly computed from HFSS. The results are shown in Figure V.25 (b) and (c). The length of the center stalk of the branch is 8cm and the permittivity is 27.22+5.22i with frequency at 1.41 GHz. The T matrix is extracted from HFSS using

the method in section 5.3. It can be seen that the results from the T matrix and HFSS compares well. This verifies the correctness of the T matrix with vector spheroidal wave expansions.

For 3D vector cylindrical waves, the correctness of the T matrix is verified by comparing the scattered or total fields from one cylinder calculated with three different methods: (a) using the T matrix to calculate the scattered field coefficient and then calculate the scattered fields; (b) using ICA to calculate the scattered fields directly as in [4]; (c) using the commercial full-wave solvers HFSS or FEKO to calculate the fields. The total fields are the scattered fields plus the incident fields. The total field $|E_{tot}|$ is the incident field plus the scattered field. Radar Cross Section (RCS) is also calculated which is defined as $\sigma = \lim_{r\to\infty} 4\pi r^2 \frac{|E_s|^2}{|E_i|^2}$. Method (a) calculates RCS by making the observation points at the far field region. Method (b) uses the far field approximation of the Green's function as detailed in [4].

The results are shown in Figure V.26 (a) for the RCS of a cylinder with radius 2cm and length 1.5m; and Figure V.26 (b) for the near field of a cylinder with radius 6cm and length 5m. The center of the cylinder is at [0,0,0]. the permittivity of the dielectric cylinders is set to be 30.7+5.5i, the incident angle θ_i is 140^o, the incident polarization is V-pol, the cylinder is vertically oriented and the frequency for simulation is L-band at 1.41 GHz.

The results from the T matrix matches those from ICA which shows the correctness of the T matrix derived from ICA. The results of ICA and the T matrix are also in good agreement with those from the commercial software. The errors are caused by the assumptions in ICA: the cylinder is considered as infinite cylinder in receiving the exciting fields and radiating as a finite cylinder without considering the top and bottom of the cylinder [4]. This error can be eliminated by extracting the T matrix of the cylinder from BOR. However, BOR [12, 92] needs to be made more

efficient for long cylinders such as 94 wavelengths in length. We simulate tall tree trunks up to 94 wavelengths. For these cases, ICA provides satisfactory accuracy with good efficiency. The main application of the hybrid method in this section is calculating the transmission and tau of forest for Earth remote sensing and ICA has been widely used in vegetation models for Earth remote sensing. The main purpose of this section is to develop the new method of Foldy-Lax with 3D vector cylindrical wave expansions for random media instead of extracting the T-matrix of a single object. This new method computes the multiple scattering of many objects instead of the scattering from a single object. Because of these reasons, we use the T-matrix extracted from ICA instead of BOR in this section.

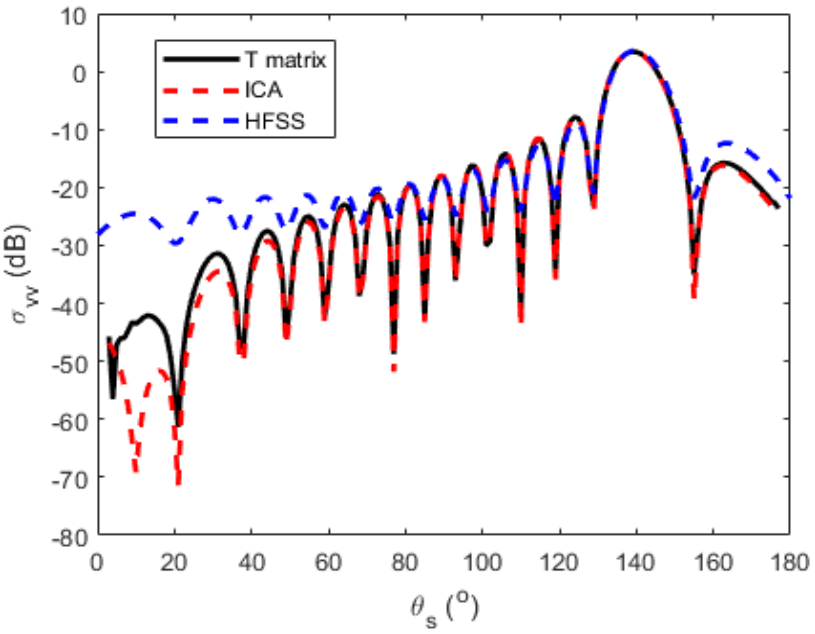

(a) RCS at $\phi_s = 0$.

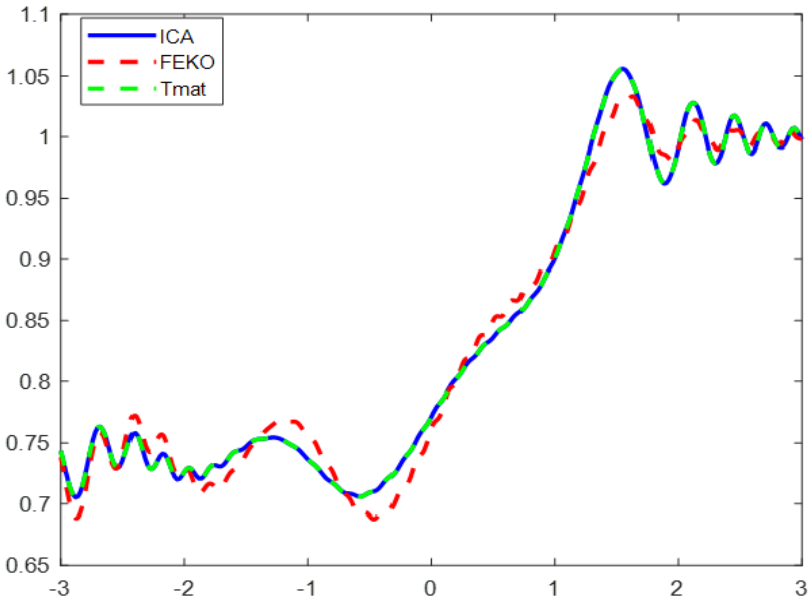

(b) Near Fields | *Etot* | plotted against z (m) at x = 1.5m and y = 0m.

Figure V.26. Comparisons between the methods using the T matrix, ICA and commercial full-wave solvers for one cylinder.

5.4.2 Translation Addition Theorem

After the T matrix extraction is validated, the next step is verifying the numerical translation addition theorem. First, for vector spherical waves, we randomly choose $\bar{r}_a = [0.1,0.1,0.1]$ and $\bar{r}_b = [0,0,0]$ without the loss of generality. Let the size of $A_{\mu\nu mn}(k\overline{r_b r_a})$ and $B_{\mu\nu mn}(k\overline{r_b r_a})$ both be 8×8. The results from the analytical and numerical solutions and their absolute errors are plotted in Figure V.27. It shows that the absolute errors for the matrix elements are all less than 10^{-15}. The RMSE between the two methods are 4.73×10^{-16} and 2.35×10^{-16} for $A_{\mu\nu mn}(k\overline{r_b r_a})$ and $B_{\mu\nu mn}(k\overline{r_b r_a})$, respectively. It means that the robust numerical method for wave transformations is accurate.

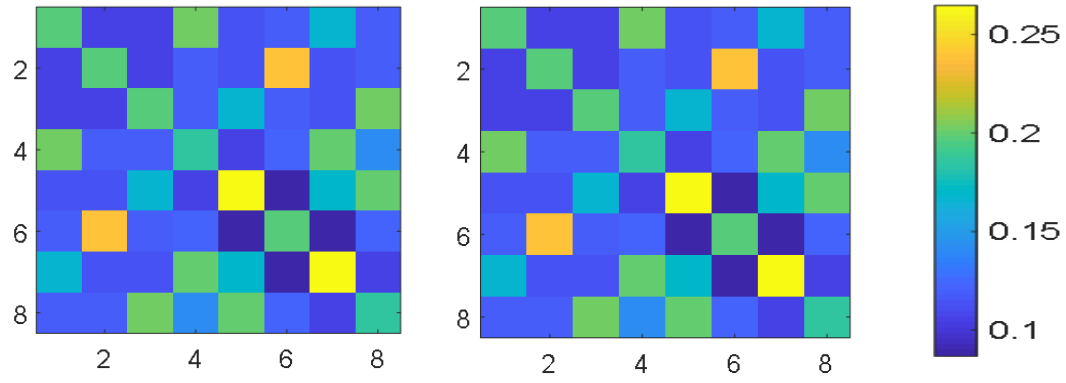

(a) $|A_{\mu\nu mn}|$ from analytical method (left) and numerical method (left)

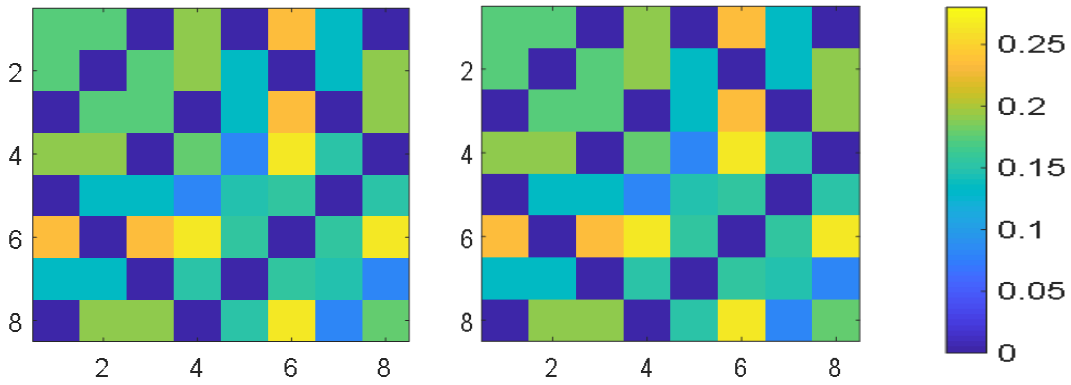

(b) $|B_{\mu\nu mn}|$ from analytical method (left) and numerical method (left)

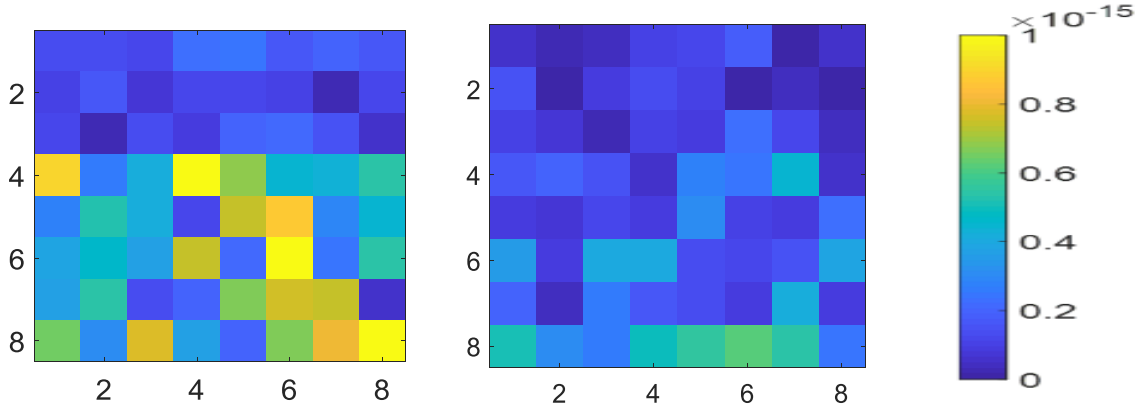

(c) Absolute error between the analytical and numerical wave transformation matrix: $A_{\mu\nu mn}$ (left), $B_{\mu\nu mn}$ (right).

Figure V.27. Analytical and numerical translation addition comparisons for vector spherical waves.

For vector spheroidal waves, there is no analytical translation addition theorem available for general cases. The $\bar{\bar{C}}_{(1)}$ matrix needed in the numerical translation addition method as in equation (5.3.120) can be verified. To verify $\bar{\bar{C}}_{(1)}$, we replace $\bar{M}_{mn}(k\overline{rr_2})$ by incident plane wave $\bar{E}^{inc}$ in the numerical translation addition method. With the same $\bar{\bar{C}}_{(1)}$, when $\bar{b}$ is integration using $\bar{E}^{inc}$, the resulting $\bar{A}$ and $\bar{B}$ are the expansion coefficient for incident plane waves. For incident plane waves, the analytical solutions of the expansion coefficients are available as listed in section 5.3. The expansion coefficients from the numerical method are compared with analytical solutions in Figure V.28, for both TE and TM polarizations. The incident plane waves are of $\phi_i = 0$ and $\theta_i = 10^o$ and 40^o. For $\theta_i = 10^o$, the real part of the expansion coefficient is in red while the imaginary part is in blue. For $\theta_i = 40^o$, the real part of the expansion coefficient is in magenta while the imaginary part is in green. The circle marker indicates the results of the analytical method while the cross marker indicates the results of the numerical method. It is observed that the results from analytical and the numerical method matches well. This means that the $\bar{\bar{C}}_{(1)}$ and the way of calculating $\bar{b}$ for the translation addition method is correct.

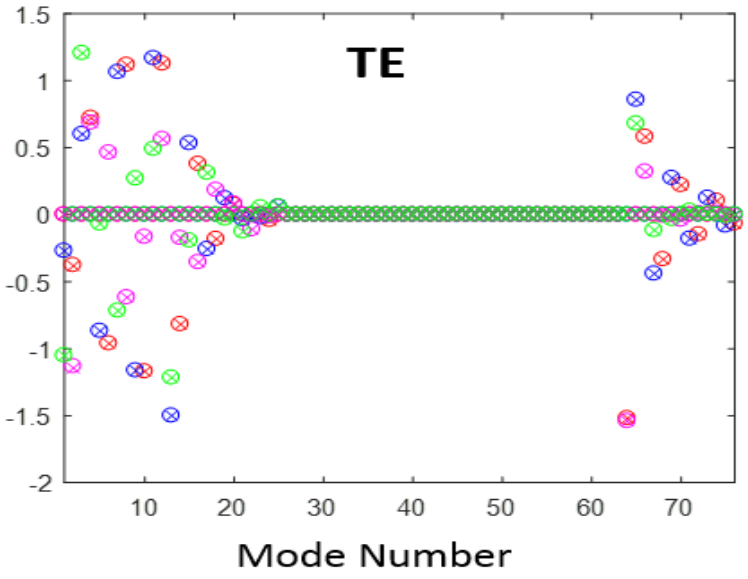

(a)

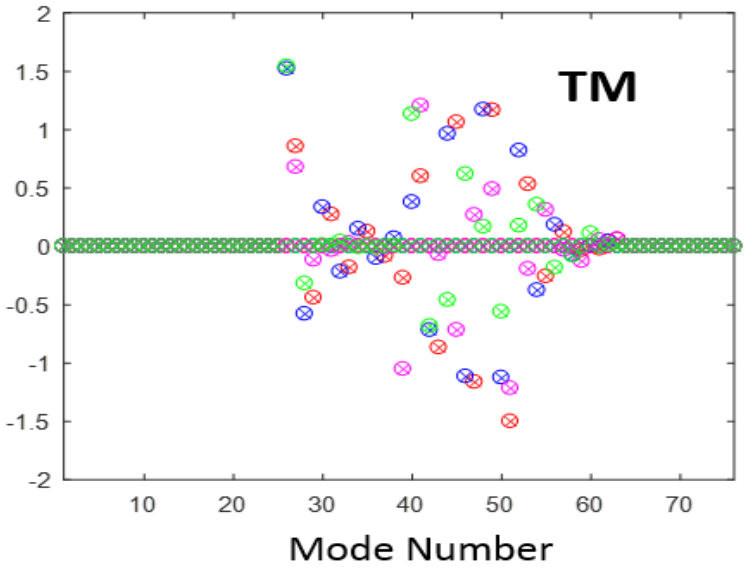

(b)

Figure V.28. Vector spheroidal wave expansion coefficients for incident plane waves using numerical method (maker of cross) and analytical method (maker of circle) for (a) TE and (b) TM polarizations.

5.4.3 Solving Foldy-Lax Equations

The methods developed in the first two steps (i.e., the T matrix extraction and numerical translation addition) of the hybrid method have been validated. Then, the resulted T matrix and translation addition matrix are submitted into the Foldy-Lax equations and we are ready to solve the equations to find the full-wave solutions of many vegetation scatterers. First, only serval vegetation scatterers are simulated which are feasible to be run on the commercial full-wave solvers such as HFSS and FEKO to provide validation. We calculate the scattering by three complicated branches attached with many irregular-shape leaves as shown in Figure V.29 (a). The permittivity of the vegetation scatterers is 27.22+5.22i and the simulation frequency is 1.41 GHz. The center position of the three branches are at [-7cm,0,0] [7cm,0,0], [0,8cm,8cm], respectively.

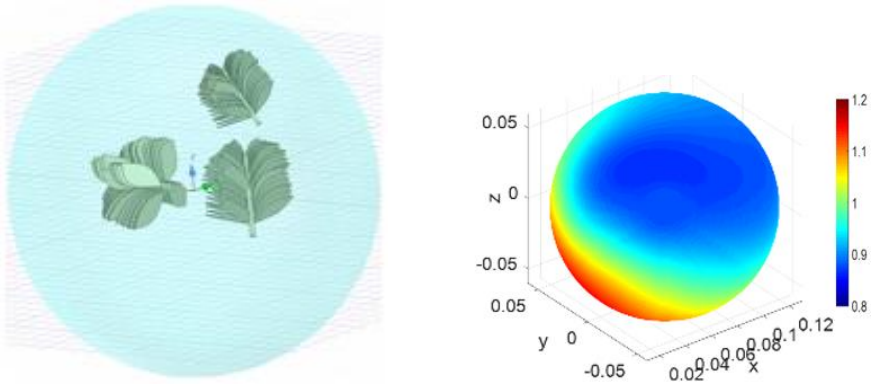

(a) (b)

Figure V.29. (a) Scattering of three complicated branches using hybrid method and HFSS brute force method; (b) Absolute value of the final exciting fields for one of the branches.

In the hybrid method, the T matrix of each branch is extracted from HFSS. Then the T matrices are substituted into FL, with numerical wave transformations applied. By solving the FL for the three branches, the wave interactions among them are taken into account. Let the incident plane wave at 40^o with magnitude 1. Figure V.29 (b) plots the final exciting fields ($|\bar{E}_m^{ex}|$) of the branch at lower right-hand-side on a spherical surface with diameter 12 cm enclosing the branch. It is

observed that the magnitudes of the exciting fields vary a lot. Thus, the exciting fields for the branches are not plane waves due to the influence of the other two branches.

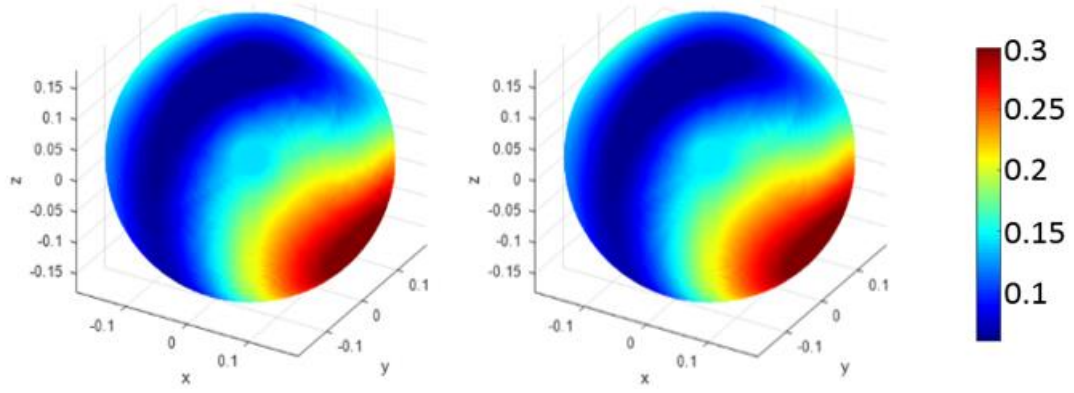

Figure V.30. Absolute value of the scattered fields on the enclosing sphere in Figure 7 for V-pol, from: hybrid method (left), HFSS brute force method (right).

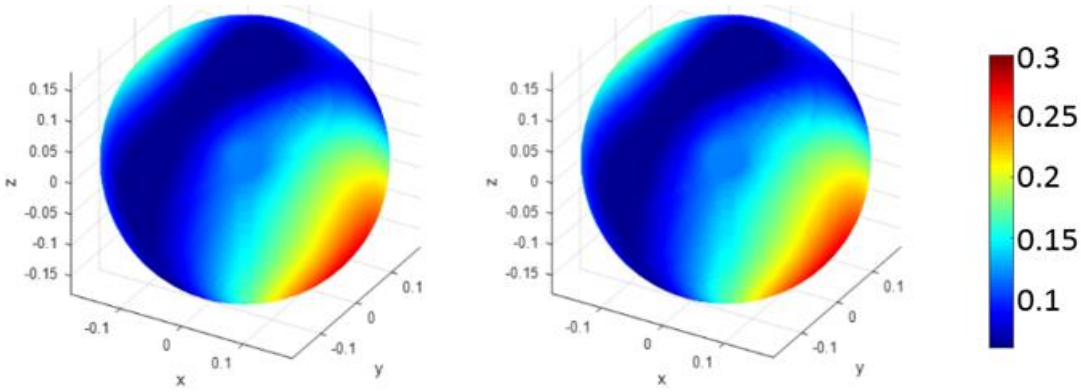

Figure V.31. Absolute value of the scattered fields on the enclosing sphere for H-pol, from: hybrid method (left), HFSS brute force method (right).

The total scattered fields from the three branches resulted from the hybrid method are compared with the HFSS brute force method. The HFSS brute force method simulates the three branches together in HFSS. For three branches, the HFSS brute force method is feasible. The scattered near fields on the enclosing sphere (shown in Figure V.29 (a) with radius 16 cm) are plotted in Figure V.30 and Figure V.31 for both V-pol and H-pol incident waves, respectively. The radar cross

sections σ_{VV} and σ_{HH} are also obtained and plotted in Figure V.32, for both methods. It can be seen that the results from the hybrid method agree with those from the HFSS brute force method.

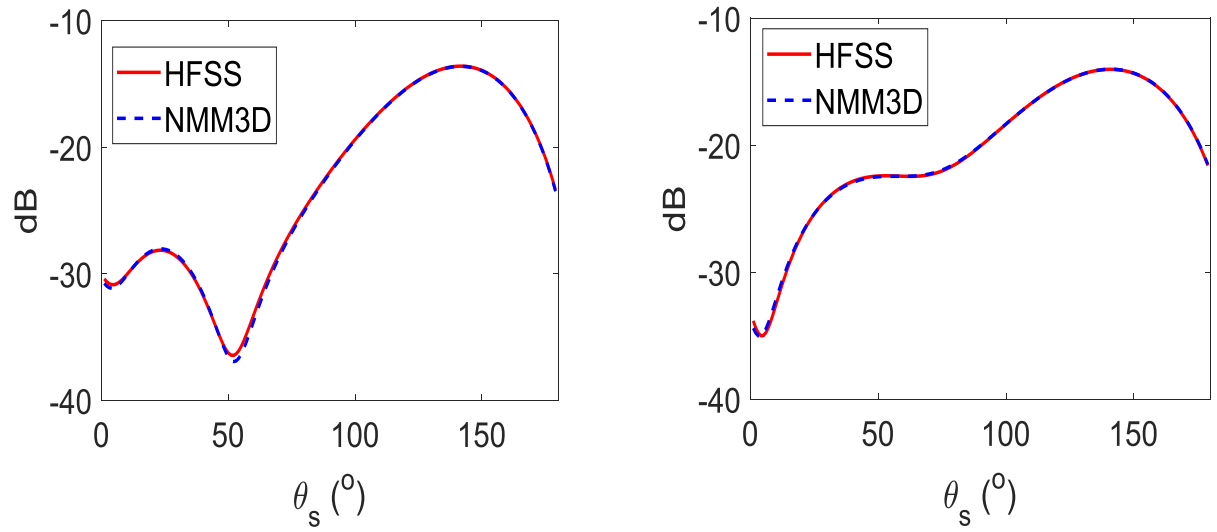

Figure V.32. (a) σ_{VV} and (b) σ_{HH} at different scattered angles from the two methods. NMM3D uses the hybrid method. θ_s is the angle with z-axis.

When simulating the case including a large number of objects or lots of empty space, the hybrid method is more efficient than the HFSS brute force method in terms of the CPU time and memory. Two reasons are discussed here. Firstly, the HFSS brute force method discretizes the whole volume including the empty space between the objects into tetrahedrons (as shown in Figure V.33, the rectangular box is the perfect matched layer (PML) defined in HFSS acting as an artificial absorbing boundary). In comparison, for the hybrid method, only the single object within the enclosing volume is discretized, when extracting the T matrix for each single object from HFSS. (i.e., Most of the empty space between the objects is not discretized in the hybrid method.) Secondly, the hybrid method uses the T matrix to account for the scattering properties of the objects while the HFSS brute force method calculates all the internal and surface fields of the objects. Figure V.34 (a) shows the total surface fields on the branch simulated using HFSS. Figure V.34 (b) shows the

total fields on the enclosing spherical / spheroidal surface of the branch which are used to extract the T matrix. It is observed that the fields shown in Figure V.34 (a) is much more complicated than those shown in Figure V.34 (b), since the near fields interaction is proportional to $1/distance^3$ [4]. Thus, the T matrix is much less complicated than the internal fields. Then, the use of the T matrix in the hybrid method significantly decreases the number of unknowns to be solved, compared with the HFSS brute force method.

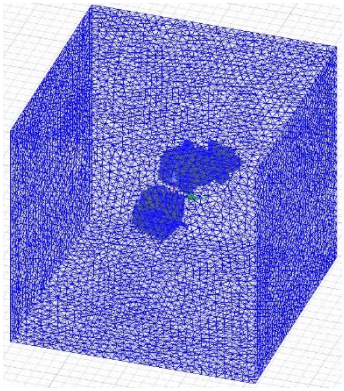

Figure V.33. The whole volume was discretized in HFSS.

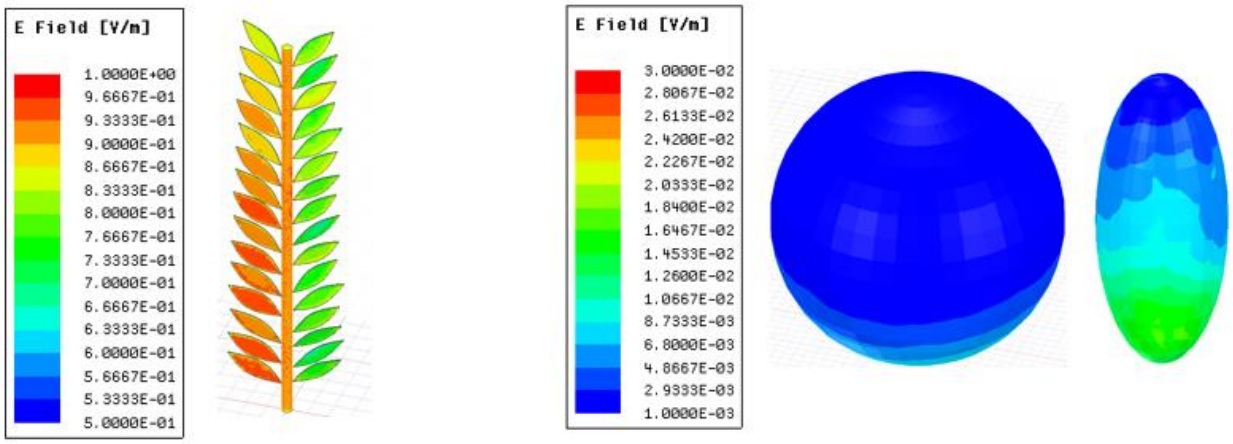

(a) (b)

Figure V.34. (a) Surface fields on a branch; (b) Fields on the enclosing spherical and spheroidal surface of the branch in (a).

Next, we simulate the case of 10 branches whose positions are shown in Figure V.35 (a). Each branch is similar to that in Figure V.29 (a). The simulations are performed a single PC with Intel

Core i7-4790 CPU and 32 GB RAM. The HFSS shows out of memory when simulating the 10 branches all together. However, it is feasible to simulate the 10 branches using the hybrid method. The T matrix for each branch is of size 48×48 ($N_{max} = 4$). Simulating each branch at different incident plane waves in HFSS for the T matrix extraction takes around 10 minutes each. Extracting the T matrix for each branch using the scattered fields exported from HFSS takes around 1 second each. Then, the T matrices for all the branches are stored for use in step 3 of the hybrid method (memory required is $48 \times 48 \times 10$). Finally, performing wave transformations and solving FL for the 10 branches takes around 5 seconds. The largest matrix stored and solved is of size 480×480, which is much less than the memory limit of the single PC. The radar cross sections σ_{VV} and σ_{HH} of the 10 branches calculated using the hybrid method are plotted in Figure V.35 (b).

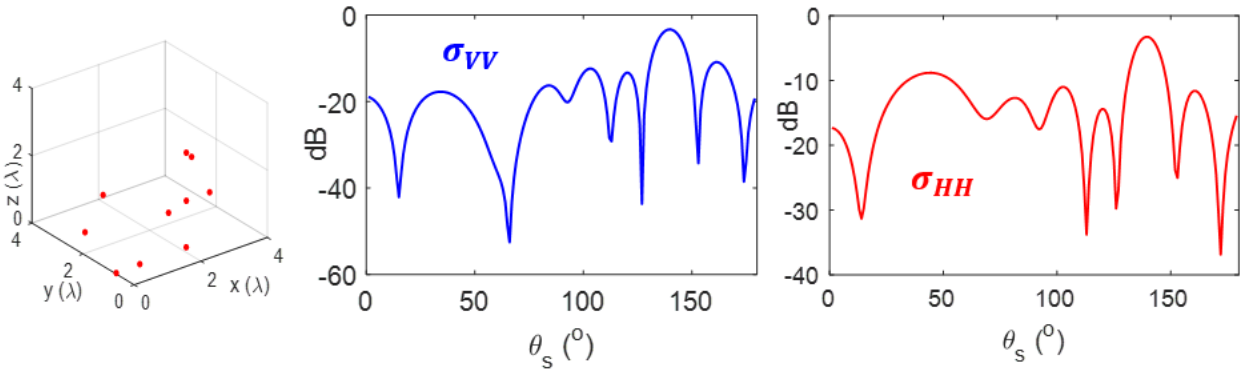

(a) (b)

Figure V.35. (a) Positions of the ten branches for simulation; (b) σ_{VV} (left) and σ_{HH} (right) at different scattered angles for the 10 branches.

This example of full-wave simulation of 10 branches illustrated that the hybrid method is much more efficient than the HFSS brute force method for large problems. For the vegetation canopy/trees, the volume fraction of the vegetation scatterers is typically less than 1% (i.e., more than 99% is air). It means that the volume discretized in the HFSS brute force method would be approximately 99 times more than that discretized for the T matrix extraction in the hybrid method.

Thus, the hybrid method is much more efficient than the HFSS brute force method for simulating the vegetation field. Full-wave simulations for vegetation/trees including a large number of objects are nearly impossible using the HFSS brute force method. However, the hybrid method can be readily used for these problems. Another advantage of the hybrid method is that the T matrix extraction for each single object which is the time-consuming part only needs to be conducted once. It is because the T matrix only depends on the geometry and material of the object, and is not related to the other properties such as the position of the object and the incident wave. The positions of the objects and the incident waves are taken into account by FL. Thus, if the positions of the objects are changed, the hybrid method only needs to solve FL again without re-calculating the T matrices, while the HFSS brute force method needs to re-calculate the whole problem again. This property of the hybrid method will save lots of time in the Monte Carlo simulations for vegetation/trees.

For 3D vector cylindrical waves, we simulate the case of two cylinders where there are interactions among cylinders. Each cylinder has a radius 2cm and length 1.5m, at the location of [0,0,0] and [0.3m,0,0], respectively. The permittivity of the cylinder is 30.7 + 5.5i, the simulation frequency is 1.41 GHz and the incident angle is vertical polarization at 140^o. The scattered/total fields are calculated using the hybrid method detailed in section 5.3 and compared with those from the full-wave solvers. The results are shown in Figure V.36 for both far fields (RCS σ_{VV}) and near fields. It is noticed that there are small differences in the results from the commercial software HFSS and FEKO. This can be caused by that different methods are used in HFSS and FEKO: HFSS uses Finite Element Method while FEKO uses the Method of Moment. It can be seen that the results from the hybrid method agree with those from the commercial full-wave solvers. This means the hybrid method is correct.

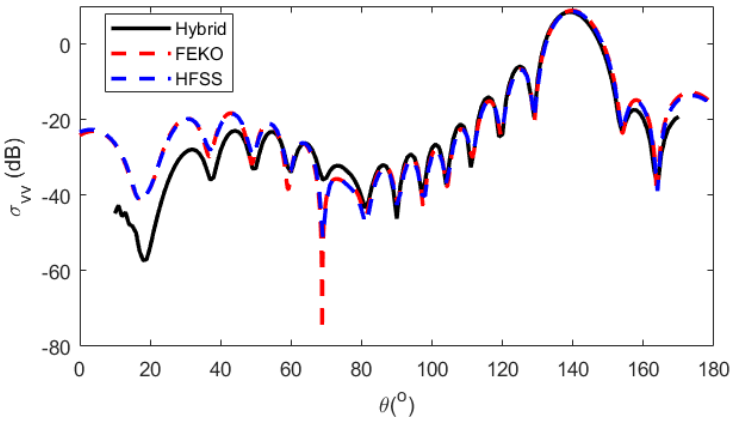

(a) σ_{VV} at $\phi_s = 0$.

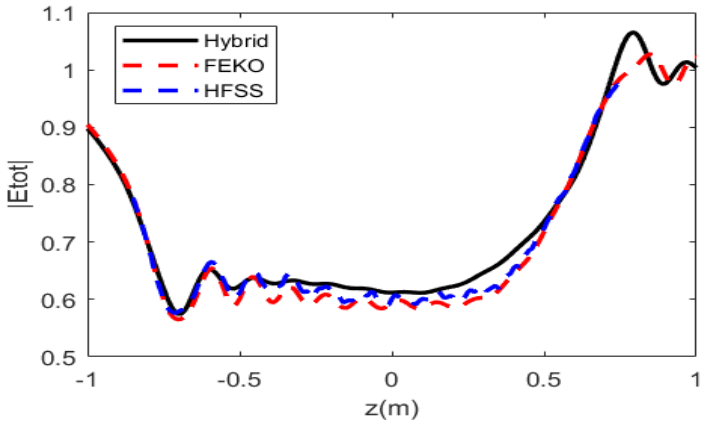

(b) Near Fields $|E_{tot}|$ plotted against z (m) at x=0.15m and y=0m.

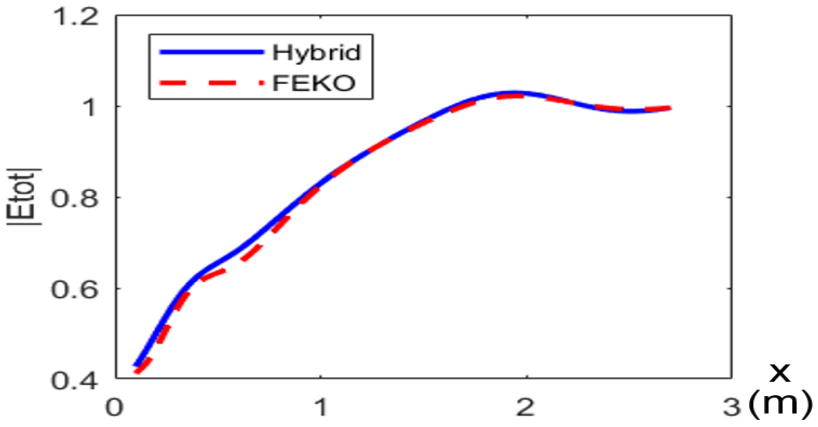

(c) Near Fields $|E_{tot}|$ plotted against x (m) at y=0 and z=-0.75m.

Figure V.36. Comparisons of the hybrid method and commercial full-wave solvers for two cylinders.

5.4.4 NMM3D Simulation Results of Vegetation/Forest

In this section, we apply the hybrid method for NMM3D full-wave simulations of vegetation/forest and calculate the transmission and optical thickness tau through the vegetation/forest canopy.

The normalized transmitted energy is defined as the transmitted energy at the bottom of the cylinders normalized by the energy when there are no cylinders,

$$T = \frac{1}{S}\iint_S \frac{\bar{S}^{tot}(\bar{r})\cdot(-\hat{z})}{\bar{S}^{inc}(\bar{r})\cdot(-\hat{z})} \tag{5.4.8}$$

where $\bar{S}(\bar{r}) = Re[\bar{E}(\bar{r})\times\bar{H}^{*}(\bar{r})]/2$. S is the size of the NMM3D 'receiver', put right below the vegetation/forest canopy.

The transmission is obtained by moving the 'receiver' all over the simulation area and then taking the average over the T at different locations. But there are edge effects when the 'receiver' is close to the edge of the simulation area. Edge effects are artificial effects caused by using finite area to simulate the infinite area of vegetation/forests. To avoid the effects, instead of moving the 'receiver', we fix the 'receiver' at the center of the simulation area and shuffling the plants/trees. Thus, the transmission t is obtained using Monte Carlo simulations by averaging over realizations,

$$t = \frac{1}{N}\sum_{n=1}^{N} T_n \tag{5.4.9}$$

where N is the total number of realizations.

A. Simulation setup

The dielectric cylinders can be used to represent tree trunks (Figure V.37). The parameters for the two simulation cases are shown in Table V-3. The simulations are performed at 1.41 GHz and the incident wave is vertical polarization. The simulation area needed depends on the height

of cylinders and the incident angle and the minimum length of the area ($L \times L$) is $L = 2h \times tan\theta_i$. We simulate two cases and the parameters are listed in Table V-3.

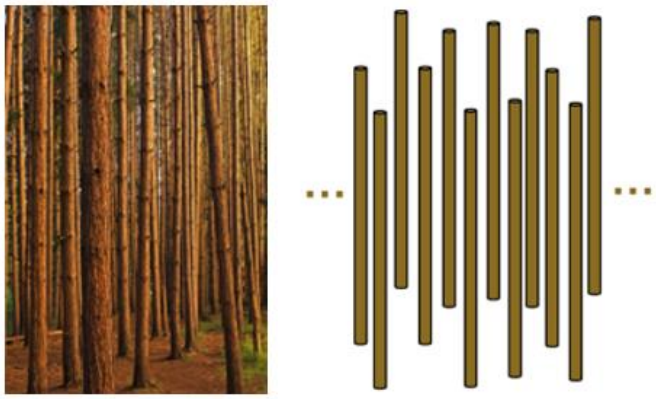

Figure V.37. Tree trunks (left) are modeled as dielectric cylinders (right).

Table V-3. Parameters for the two simulations cases.

	Height (h)	Diameter	Density
Case 1	20 m	12 cm	0.17 m^{-2}
Case 2	5 m	8 cm	2.2 m^{-2}

The minimum total number of cylinders needed for simulations is $N_t = L^2 \times Density$, which is 192 and 155 for Case 1 and 2, respectively. For the convenience of generating uniform distribution in a square area, we use 196 and 169 cylinders, the square root of which is integer, for Case 1 and 2, respectively. Uniform distribution is used for both cases. The top view of the centers of the cylinders in Case 2 for one realization is shown in Figure V.38. For Case 1, the number of discretizations in θ is 800 and the number of harmonics in ϕ is 9. Since there are two polarizations, the total number of unknown coefficients for each tree is $800 \times 9 \times 2 = 14,400$. Thus, the total number of unknown coefficients are $196 \times 14,400 = 2,822,400$. Thus, the matrix to be solved is of size $2,822,400 \times 2,822,400$. For Case 2, the number of discretizations in θ is 200,

the number of harmonics in ϕ is 5 and the matrix to be solved is of size $338,000 \times 338,000$. Parallel computing is used to solve the matrix.

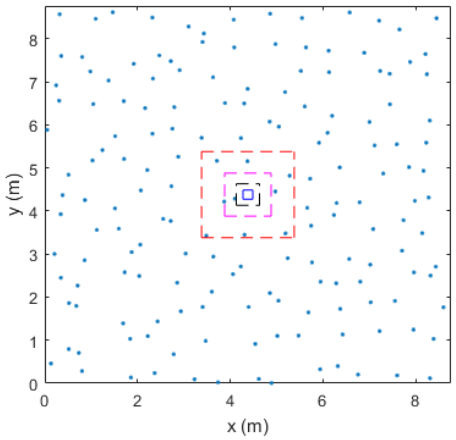

Figure V.38. Top view of the centers of the cylinders in Case 2 with 'receiver' of different sizes in the center.

B. Physically based iterative method for statistical moments

In the traditional approach, the exact solution of Maxwell's equation is obtained for each realization using conjugate gradient on the matrix equations. But such exact solution may not be useful because of random fluctuations from realization to realization. The results of many realizations are smoothed by taking average over realizations. In stochastic multiple scattering problems, the useful results are the statistical moments of the fields. In this paper, we use a new iterative method of determining the statistical moments of fields. Usually, statistical moments up to the 4th moments are useful.

In traditional method of solving such matrix equations, the equations are solved iteratively using conjugate gradient or similar algorithms for each realization. For example, when solving $\bar{\bar{Z}}\bar{x} = \bar{b}$, the iterations terminate when $\| \bar{\bar{Z}}\bar{x}_n - \bar{b} \| < err$, where $\bar{x}_n$ is the solution at nth iteration and err is a sufficiently small residual. This means Maxwell's equations are solved exactly for

each realization. The number of iterations for problems of the size of several millions are several thousands. To obtain statistical averaged, the solutions of Maxwell's equations of all these realizations, such as 5 to 20 realizations, are averaged. Thus, the total number of iterations for the averaged result would be tens of thousands. For example, for 10 realizations and 1000 iterations for each realization, there are a total of 10,000 iterations. The physically based iteration method are based (i) The exact solution of Maxwell equation for each realization may not be useful as the solution fluctuate from realization to realization and fluctuate at different locations of the receiver area, and (ii) In classical analytical theory such as radiative transfer theory, the averaged result is calculated and these averaged results converge usually in a few orders of multiple scattering. Thus ,we expect that on that the averaged multiple scattering solutions converge much faster. This turns out to be the case as shown in the examples below.

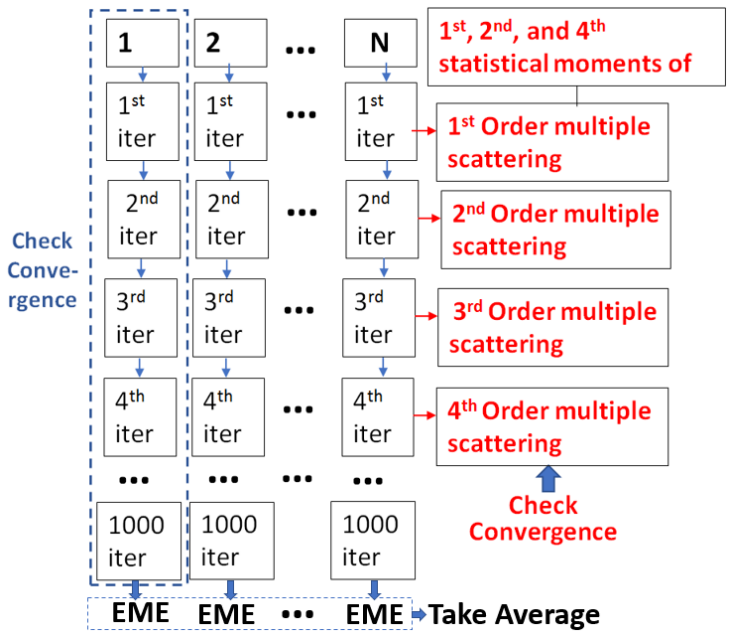

Figure V.39. Illustration of physically based iterative method for statistical moments over N realizations and the receiver area. 'EME' is short for 'Exact solutions of Maxwell's Equations'.

We iterate one multiple scattering order at a time. The averaging over 5 to 20 realizations and averaging over the receiver area are performed for each order. The averaged results usually

converge in several orders such as 4th of multiple scattering. Thus for 10 realizations, the total number of iterations is only 40, which is 250 times less than the traditional method of 10,000 iterations.

The physically multiple scattering iterated approach for averaged results is illustrated in Figure V.39. The traditional iterative method iterates until convergence of solution of Maxwell equation for each realization is achieved. The physically based iterative method for statistical moments iterates until the convergence of averaged result is achieved. In calculating the transmission t, the results is obtained as long as the averaged result is converged and thus the physically based iterative method can be applied. It is noted that, there are two kinds of statistical average in calculating the transmission: one is averaging over realizations of Monte Carlo simulations, and the other is integrating over the 'receiver' area since integration divided by the fixed area is the average. Figure V.40 shows the convergence of T over the order of multiples scattering for one realization of Case 2, where T is the integration over the receiver area of $2m \times 2m$ (red dash square in Figure V.38). It is observed that the value of T converges at 4th order of iteration.

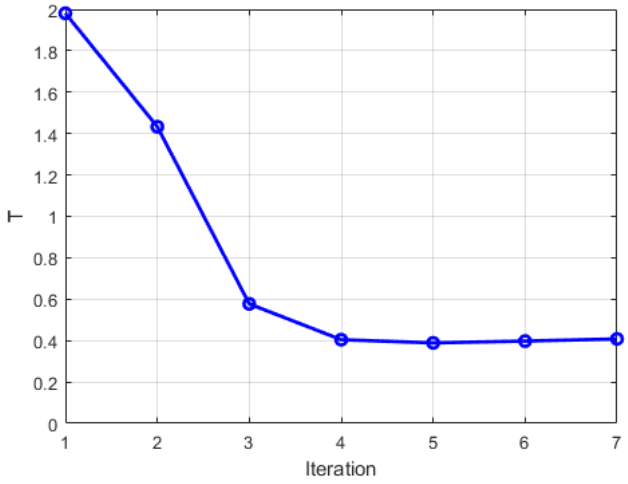

Figure V.40. Convergence of T over the order of multiple scattering.

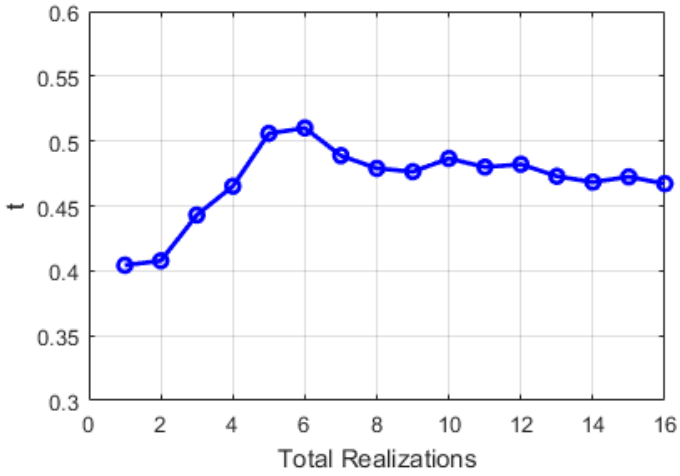

Figure V.41. Convergence of t over the number of realizations.

Figure V.41 shows the convergence of t over the number of realizations in Monte Carlo simulations of Case 2, where t is the transmission as defined above. It is observed that the transmission converges at around 8 realizations. In this case, total number of iterations to calculate the transmission using the physically based iterative method is only $4\times 8 = 32$.

C. Size of the receiver area

We examine the choice of the the size of the 'receiver' in calculating the transmission. The receiver size is a numerical parameter as the physical transmission should be independent of the choice of the numerical parameter. However, the receiver size cannot be too large to cause the edge effects, since the infinite canopy area is simulated using a finite area. We calculate the transmission of Case 2 using four different sizes of 'receiver': $2m\times 2m$, $1m\times 1m$, $0.5m\times 0.5m$, and $0.21m\times 0.21m$ (i.e., $\lambda\times\lambda$), as illustrated in Figure V.38. The T at different realizations is plotted in Figure V.42 for these different receiver sizes.

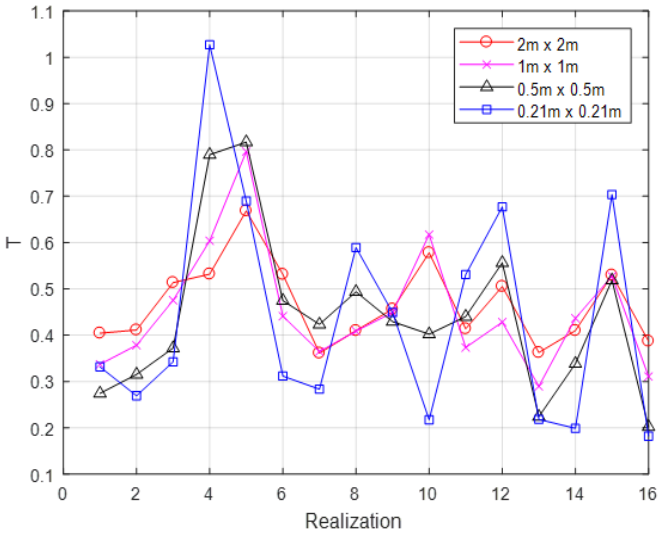

Figure V.42. T at different realizations for different receiver sizes.

It is observed that larger receiver size results in smaller fluctuations of T over different realizations. The standard deviation of T over the 16 realizations is listed in Table V-4, which shows the same conclusion that larger receiver size results in smaller standard deviations (i.e. less fluctuations). Smaller fluctuations of T means less number of realizations of Monte Carlo simulations are needed to calculate t. This is reasonable as explained below. When measuring the transmission, the receiver is moved all over the simulation area. The larger the receiver size is, the less number of movements are needed to cover all the simulation area. As illustrated in the beginning, to avoid the edge effects, we fixed the receiver at the center of the simulation area and shuffling the scatterers. The number of movements is positively correlated with the number of realizations of shuffling the scatterers in Monte Carlo simulations. Thus, less number of realizations is needed when receiver of larger area is used.

Table V-4. Receiver sizes and the standard deviation of T over 16 realizations.

Size	$2m \times 2m$	$1m \times 1m$	$0.5m \times 0.5m$	$0.21m \times 0.21m$ (i.e., $\lambda \times \lambda$)
Std.	0.0871	0.1308	0.1734	0.2420

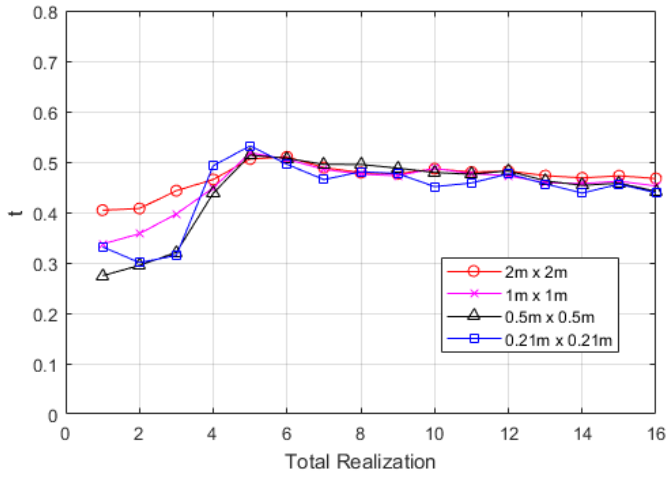

Figure V.43. Convergence of t over the number of realizations for different receiver sizes.

Next, T is averaged over realizations to calculate the transmission t. The value of average T as a function of total number of realizations is plotted in Figure V.43, for these different sizes of receivers. Comparing the red line with circle marker and the blue line with square marker, it is clear that larger receiver size needs less number of realizations to converge: $2m \times 2m$ receiver needs around 8 realizations to converge while $0.21m \times 0.21m$ needs around 16 realizations to converge. It is also observed that the averaged T converges to the about same value 0.45 for different receiver sizes. This shows that this method of calculating transmission is robust and does not depends on the receiver size as long as the receiver is not too large to cause the edge effects.

D. Comparisons with RTE/DBA for transmission and τ

In RTE/DBA, the transmission through randomly distributed cylinders are calculated as

$$t_R = exp(-\tau_R \sec(\theta_i)) \tag{5.4.10}$$

where the subscript R represents the method 'RTE/DBA' and τ is the optical thickness.

τ of RTE/DBA is calculated as

$$\tau_R = n_0(\sigma_s + \sigma_a)d \tag{5.4.11}$$

where n_0 is the number of cylinders per m^3 which is the number of cylinder per m^2 divided by the length of the cylinder. The n_0 is 0.0085 m^{-3} and 0.44 m^{-3} for Case 1 and 2, respectively. σ_s and σ_a are the scattering cross section and absorption cross section of one cylinder, which are calculated using the plane wave illumination. The length of the cylinder is represented by d.

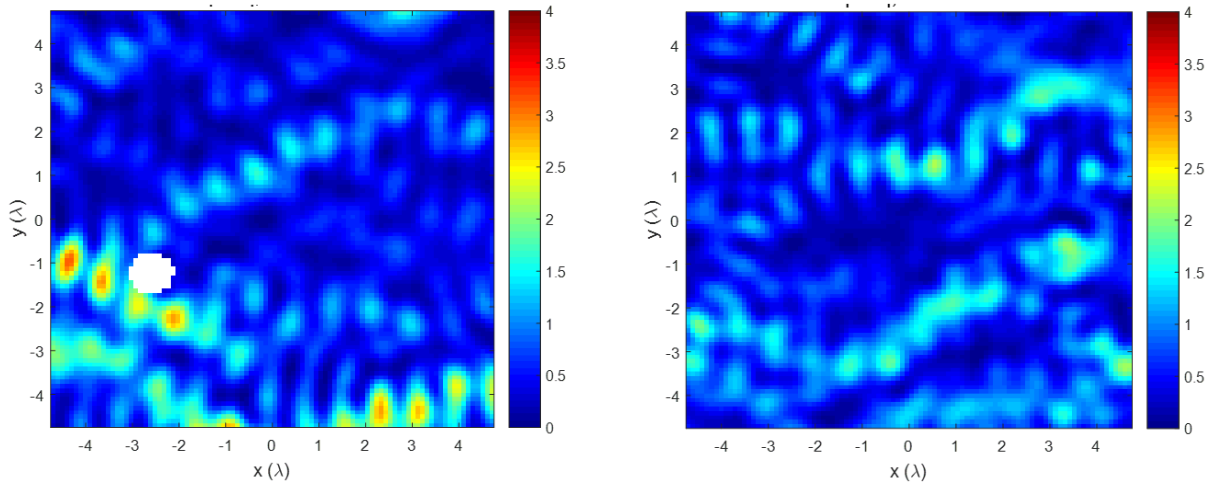

Figure V.44. Integrand of T for two realizations in Case 2.

As illustrated above, the transmission from the hybrid method for Case 2 is 0.45. For Case 1, following the simulations described above, the transmission is 0.66. The integrand of T for two realizations are plotted in Figure V.44. The receiver size is $2m \times 2m$ (i.e., $9.406\lambda \times 9.406\lambda$). The blank hole in the top figure shows a cylinder right above in the receiver area in this realization. The T for these two realizations (left and right of Figure V.44) is 0.6340 and 0.6434, respectively. The blank hole indicates the cross section area occupied by the cylinder which is excluded from the integration to obtain T. Thus, this area is left blank without plotting the integrand.

Using Maxwell's equations, we calculate transmission not τ. In order to compare with RTE/DBA, we defind the 'τ' of the hybrid method by $\tau_H = -ln(t_H)\sec(\theta_i)$, where the subscript H represents the hybrid method.

Table V-5. Transmission coefficient from RTE/DBA and the hybrid method.

Transmission	RTE/DBA	Hybrid Method
Case 1	0.35	0.66
Case 2	0.089	0.45

Table V-6. Optical thickness tau from RTE/DBA and the hybrid method.

Tau	RTE/DBA	Hybrid Method
Case 1	0.80	0.32
Case 2	1.85	0.61

The results for Case 1 and 2 from RTE/DBA and the hybrid method are tabulated in Table V-5 and Table V-6 for transmission and τ, respectively. For Case 1, the transmission from the hybrid method is around twice larger than the transmission from RTE/DBA while the τ from the hybrid method is only 40% of the τ computed using RTE/DBA. For Case 2, the transmission from the hybrid method is around five times larger than the transmission from RTE/DBA while the τ from the hybrid method is only 33% of the τ computed using RTE/DBA. Thus, the transmission from the hybrid method is much larger than that from RTE/DBA while the τ is much smaller than that from RTE/DBA. Because of the influences of the other cylinders, the final exciting fields on the cylinders are not plane wave anymore. Generally, the fields exciting on the bottom of the cylinder is less than those exciting on the top of the cylinder due to the attenuation. However, the σ_s and σ_a in RTE/DBA are calculated using plane wave exciting, which overestimates σ_s and σ_a. Thus, RTE/DBA overestimates τ and underestimates transmission. The results from the hybrid method also illustrates that the microwaves can penetrate through the gaps that are larger than the microwave wavelengths which are not accounted for in RTE/DBA based on the concept of homogenization.

5.5 Conclusions

The hybrid method combines the off-the-shelf techniques and the developing computational electromagnetics techniques, consisting of three steps: (1) the generalized T matrix extraction, (2) wave transformations, and (3) wave interactions among single objects. Vector spherical, spheroidal and cylindrical waves are used for the wave expansions. The T matrix extraction technique is applicable for arbitrary-shape objects which have no analytical solutions. The technology of extracting T matrix from HFSS with vector spherical wave expansions is validated using a sphere which has the analytical solutions for the T matrix. The extracted T matrix with vector spheroidal wave expansions is verified by comparing the scattered fields computed from the T matrix to those from the HFSS, for a branch with complicated leaves. For 3D vector cylindrical waves, the analytical expressions of the T matrix for a dielectric cylinder are derived and the correctness of the T matrix calculated from ICA is verified. The technique of numerical wave transformations is verified by the analytical solutions for vector spherical waves, resulting in RMSE on the order of 10^{-15}. The numerical method is more robust than the analytical method. The numerical method for wave transformations are also applied to spheroidal waves where the analytical method is not available. The results of the hybrid method are checked by the HFSS brute force method using three complicated branches attached with leaves. The full-wave simulation results from the hybrid method agree with those from the HFSS brute force method for both near fields and radar cross sections. The hybrid method is much more efficient in terms of CPU time and memory than the HFSS brute force method when simulating the case including a large number of objects or lots of empty space, such as vegetation canopy/trees. One reason is that the HFSS brute force method discretizes the whole volume including the empty space between the objects while the hybrid method only discretizes the single objects. When extracting the T matrix, each

single object is simulated on HFSS alone without the other objects. The multiple scattering of waves among the single objects are accounted for by solving FL. The hybrid method is also illustrated using 10 branches which cannot be simulated by the HFSS brute force method on the single PC. The hybrid method also has the advantage of only one-time computations of the T matrices since the T matrices are independent of positions and incident waves. This saves time when performing Monte Carlo simulations by randomly shuffling the objects. For 3D vector cylindrical waves, the scattered fields formulation of FL is used. Examples of cylindrical scatterers are illustrated and the correctness of the method is verified by HFSS. Both far and near fields are in good agreement with those from HFSS. The hybrid method is applied to calculate the transmission through a layer of dielectric cylinders representing tree trunks at L-band. Physically iterative method is developed to calculate the statistical moments by taking averages over each multiple scattering order. There are two kinds of averages to calculate the transmission: averages over the receiver area and averages over Monte Carlo simulations. It is found that the larger receiver size results in smaller fluctuations over realizations and thus smaller number of realizations needed for convergence. However, the receiver size does not affect the transmission in this simulation method which is robust. The transmission from the hybrid method is much larger than that from RTE/DBA while the optical thickness tau from the hybrid method is much smaller than that from RTE/DBA.

In the future, the hybrid method will be applied for modelling of irregularly shaped objects by extracting the T matrix from the commercial software which is suitable to irregularly shaped single object of moderate size such as a corn/soybean plant and a small tree with branches and leaves.

CHAPTER VI

Conclusions

This thesis focuses on electromagnetic modelling of vegetation/forests at microwave frequencies which is used for remote sensing of soil moisture. Both analytical and numerical models for vegetation/forests are studied. Chapter II and III are about the analytical models for vegetation-covered surfaces, using the distorted Born approximation (DBA), an improved coherent model and a unified model for combined active and passive, which were used for soil moisture retrieval in SMAP. Chapter IV and V are about Numerical Maxwell Model in 3D (NMM3D) full-wave simulations of vegetation/forests. The main contributions and novelty of this thesis are the development of the hybrid method for NMM3D full-wave simulations of vegetation/forest canopy, based on the generalized T matrix of the single object and Foldy-Lax equations of multiple scattering among many objects. This hybrid method is efficient for large-scale full-wave simulations of vegetation/forst. In NMM3D full-wave simulations, plants' structures gaps, heterogeneity and the wave interactions among scatterers are accounted for. We showed that the NMM3D results predict transmissions several times larger than that of the past two models. For passive remote sensing, a larger microwave transmission means the emission from soil can pass through the vegetation/forests to reach the radiometer. For radars, a much larger microwave transmission means the microwave can penetrate vegetation/forest canopy and thus can sense the soil moisture below. The advanced radiative transfer theory using NMM3D provides

the basis for improved physical model based retrievals of soil moistures from the stattellite measurements such as SMAP and combined SMAP and NISAR measurements.

The DBA is derived from the Foldy-lax equation with first-order iteration using the half-space Green's function. DBA is incoherent scattering model and it inclues three scattering mechanisms: volume scattering, double-bounce scattering and surface scattering. The surface scattering in DBA is computed by the attenuation of the vegetation canopy times the bare surface scattering from NMM3D. Wheat and canola data-cubes are generated based on this analytical scattering model to support soil moisture retrieval for the Soil Moisture Active Passive (SMAP) mission. The backscattering coefficients of the data-cubes compare well with the UAVSAR data collected during the SMAP validation experiment 2012 (SMAPVEX12) field campaign over a wide range of VWC and soil moisture. The data-cube based time-series retrieval algorithm for the SMAP mission is implemented to retrieve the soil moisture. The retrieved soil moisture is in good agreement with the in-situ soil moisture from SMAPVEX12. A coherent model with conditional probabilities is developed to compute the radar scattering from soybean fields. With the use of conditional probabilities, the unrealistic overlap of two branches at the same location is avoided. The new model is closer to the reality than the previous models, and produces smaller scattering compared with the previous coherent model predictions. However, it also generates significantly larger scattering than the incoherent model such as DBA. By comparisons with SMAPVEX 12 data, it is shown that this improved coherent model agrees well with observations in both the absolute values of backscattering and the polarization ratios between VV and HH backscattering coefficients. The accuracy of the time-series retrieval of soil moisture also improves by using the new data-cube based on the coherent model with conditional probabilities, compared with the incoherent data-cube.

A consistent model for combined active and passive microwave remote sensing is formulated in which the same physical model NMM3D-DBA (i.e., NMM3D for rough surfaces combined with DBA for vegetation) is used to calculate both backscatter and brightness temperature. The emissivity is obtained by integration of the bistatic scattering over the hemispherical solid angle. The novel feature of this combined active and passive approach is its use of the same model NMM3D-DBA and physical parameters for both active and passive for vegetation-covered surfaces to achieve a consistent modeling framework. In comparison, current approaches generally use different models and different parameters for active and passive with the tau-omega model most frequently used as the passive model with empirical input parameters. The NMM3D-DBA model results are validated using coincident airborne PALS low-altitude radiometer data and UAVSAR data taken during the SMAPVEX12 field campaign. On comparisons with the passive data, the results from NMM3D-DBA are comparable or better than those from the tau-omega model.

The analytical models such as radiative transfer equation (RTE) and DBA are based on some assumptions that are hard to justify for vegetation/forest, such as uniform random position of vegetation scatterers, uniform illumination of entire scatters and far field distance between each two scatterers. The physical process of radiative transfer at microwave frequencies are governed exactly by Maxwell's equations. The radiative transfer equation (RTE) make assumptions on radiative transfer and such assumptions can be invalid. Because of these issues, the new numerical approach of NMM3D full-wave simulations is developed. For the vegetation canopy composed of many vertically oriented dielectric thin cylinders, we develop the method of Foldy-Lax equations combined with the Z matrix of BOR (FL-BOR). The correctness of the FL-BOR simulation method is validated by comparing with the commercial software HFSS and the method FL-ICA

and by checking the energy conservation. The NMM3D simulations are performed at C-band for vertical polarization and applied to the extended-cylinders case and the short-cylinders case. The results are compared with those from effective permittivity (EP)/DBA/RTE. The results from the NMM3D and EP/DBA/RTE agree for the short-cylinders case. Because the short-cylinder case satisfies the assumptions of EP/DBA/RTE. For the examples of extended-cylinders case which resembles the grass canopy, the transmission from the NMM3D is 6.12 dB larger than that from EP/DBA/RTE while the optical thickness τ from the NMM3D is 5.0 times smaller than that from EP/DBA/RTE.

FL-BOR is limited to rational symmetric object and it is hard to be extended to cylinders with large radii. These limitations are resolved by the hybrid method developed in chapter V. The hybrid method is efficient for NMM3D full-wave simulations of vegetation/forest with realistic vegetation structures such as branches with complicated leaves. The hybrid method combines the off-the-shelf techniques (e.g. commercial software HFSS, FEKO; available computer codes ICA, BOR, ect.) and the developing computational electromagnetics techniques, consisting of three steps: (1) the generalized T matrix extraction, (2) wave transformations, and (3) wave interactions among single objects. Vector spherical, spheroidal and cylindrical waves are used for the wave expansions. The numerical T matrix extraction technique is applicable for arbitrary-shape objects which have no analytical solutions. A robust numerical method is developed for the translation addition theorem for vector spherical and spheroidal waves. The multiple scattering of waves among the single objects are accounted for by solving the Foldy-Lax equatons (FL). For 3D vector cylindrical waves, the scattered fields formulation of FL is used instead of the usual exciting field formulation. The results of the hybrid method are verified by the HFSS brute force method using three complicated branches attached with leaves. The hybrid method is much more efficient in

terms of CPU time and memory than the HFSS brute force method when simulating the case of including a large number of objects or lots of empty space, such as vegetation canopy/trees. One reason is that the HFSS brute force method discretizes the whole volume including the empty space between the objects while the hybrid method only discretizes the single objects. The hybrid method also has the advantage of only one-time computations of the T matrices since the T matrices are independent of positions and incident waves. This saves time when performing Monte Carlo simulations by randomly shuffling the objects. The hybrid method is applied to calculate the transmission through a layer of dielectric cylinders with up to 100-wavelength length and large radius, representing tree trunks at L-band. Physically iterative method is developed to calculate the statistical moments by taking averages over each multiple scattering order. There are two kinds of averages to calculate the transmission: averages over the receiver area and averages over Monte Carlo simulations. The transmission from the hybrid method is much larger than that from RTE/DBA while the optical thickness tau from the hybrid method is much smaller than that from RTE/DBA. A much larger microwave transmission means the microwave can better penetrate vegetation canopy and thus it can be used to retrieve soil moisture.

For future studies, the hybrid method with 3D vector cylindrical wave epansions will be combined with HFSS to perform full-wave simulations of crops such as wheat, soybean, corn, and canola. In addition to transmission, the NMM3D model will also be used to calculate the phase shift through the vegetation/canopy, which is important for SAR polarimetry and SAR interferometry. The NMM3D simulations also be extended to compute the passive information of brightness temperature. Brightness temperature is the physical temperature times emissivity. Because of the thermal equilibrium, the energy emitted equals the energy absorbed (i.e., emissivity equals absorption). Integration of the Poynting vector over the surface areas gives the absorption. This

method avoids the tedious integration of the bistatic scattering over all the hemispherical solid angle. This research work will help to build the next generation radiative transfer model which will be based on Maxwell's equations without RTE. Besides the current satellite mission such as Soil Moisture Active/Passive (SMAP) and Cyclone Global Navigation Satellite System (CYGNSS), this full-wave model can also be useful for future satellite missions such as NASA-ISRO Synthetic Aperture Radar (NISAR) and The Copernicus Imaging Microwave Radiometer (CIMR). CIMR is planned to launche CIMR-A in 2027 and CIMR-B shortly afterwards to provide enhanced global coverage. The CIMR mission will utilize radiometeris at multi-frequencies including L-, C-, X-, Ku-, and Ka-band. The observations at L-, C- and X-band can be useful for mapping of global soil moisture. Further enhancement can also be included such as including P-band and using broad-band radiometry at 0.5 ~3 GHz. Electromagnetic modelling of vegetation/forest at multiple freququencies is important for CIMR mission. The past RTE/DBA model has three key assumptions that are invalide and can cause large errors, as discussed in Chapters IV and V in detail. The problem becomes even more serious for multi-frequency models requiring different parameter tunings at the two frequencies. The hybrid method for full-wave simulations of vegetation/forest can provide us reliable simulation results under different conditions at multiple frequencies. The analysis of data with hybrid method will help us to define lookup tables and algorithms for multi-frequency soil moisture retrieval.

BIBLIOGRAPHY

[1] D. Entekhabi, E. G. Njoku, P. E. O'Neill, K. H. Kellogg, W. T. Crow, W. N. Edelstein, *et al.*, "The Soil Moisture Active Passive (SMAP) Mission," *Proceedings of the IEEE*, vol. 98, pp. 704-716, May 2010.

[2] F. T. Ulaby, D. G. Long, W. J. Blackwell, C. Elachi, A. K. Fung, C. Ruf, *et al.*, *Microwave radar and radiometric remote sensing* vol. 4: University of Michigan Press Ann Arbor, 2014.

[3] D. Entekhabi, S. Yueh, P. O'Neill, K. Kellogg, A. Allen, R. Bindlish, *et al.*, "SMAP Handbook, JPL Publication JPL 400-1567," *Jet Propulsion Laboratory, Pasadena, California*, vol. 182, 2014.

[4] L. Tsang, J. A. Kong, and R. T. Shin, *Theory of microwave remote sensing*: Wiley New York, 1985.

[5] H. Huang, S.-B. Kim, L. Tsang, X. Xu, T.-H. Liao, T. J. Jackson, *et al.*, "Coherent model of L-band radar scattering by soybean plants: Model development, evaluation, and retrieval," *IEEE Journal of Selected Topics in Applied Earth Observations and Remote Sensing*, vol. 9, pp. 272-284, 2016.

[6] S. B. Kim, M. Moghaddam, L. Tsang, M. Burgin, X. L. Xu, and E. G. Njoku, "Models of L-Band Radar Backscattering Coefficients Over Global Terrain for Soil Moisture Retrieval," *IEEE Transactions on Geoscience and Remote Sensing*, vol. 52, pp. 1381-1396, Feb 2014.

[7] S.-B. Kim, J. J. Van Zyl, J. T. Johnson, M. Moghaddam, L. Tsang, A. Colliander, *et al.*, "Surface soil moisture retrieval using the l-band synthetic aperture radar onboard the Soil Moisture Active–Passive satellite and evaluation at core validation sites," *IEEE Transactions on Geoscience and Remote Sensing*, vol. 55, pp. 1897-1914, 2017.

[8] E. G. Njoku and D. Entekhabi, "Passive microwave remote sensing of soil moisture," *Journal of Hydrology*, vol. 184, pp. 101-129, Oct 1 1996.

[9] H. Huang, T.-H. Liao, L. Tsang, E. G. Njoku, A. Colliander, T. J. Jackson, *et al.*, "Modelling and validation of combined active and passive microwave remote sensing of agricultural vegetation at L-band," *Progress In Electromagnetics Research*, vol. 78, pp. 91-124, 2017.

[10] H. McNairn, T. J. Jackson, G. Wiseman, S. Belair, A. Berg, P. Bullock, *et al.*, "The Soil Moisture Active Passive Validation Experiment 2012 (SMAPVEX12): Prelaunch Calibration and Validation of the SMAP Soil Moisture Algorithms," *IEEE Transactions on Geoscience and Remote Sensing*, vol. 53, pp. 2784-2801, May 2015.

[11] R. H. Lang and J. S. Sidhu, "Electromagnetic Backscattering from a Layer of Vegetation - a Discrete Approach," *IEEE Transactions on Geoscience and Remote Sensing*, vol. 21, pp. 62-71, 1983.

[12] A. W. Glisson and D. R. Wilton, "Simple and efficient numerical techniques for treating bodies of revolution," DTIC Document1979.

[13] H. Huang, L. Tsang, E. G. Njoku, A. Colliander, T.-H. Liao, and K.-H. Ding, "Propagation and scattering by a layer of randomly distributed dielectric cylinders using Monte Carlo simulations of 3D Maxwell equations with applications in microwave interactions with vegetation," *IEEE Access*, vol. 5, pp. 11985-12003, 2017.

[14] A. Tabatabaeenejad, M. Burgin, and M. Moghaddam, "Potential of L-Band Radar for Retrieval of Canopy and Subcanopy Parameters of Boreal Forests," *IEEE Transactions on Geoscience and Remote Sensing*, vol. 50, pp. 2150-2160, Jun 2012.

[15] Y. Kim and J. J. Van Zyl, "A time-series approach to estimate soil moisture using polarimetric radar data," *Geoscience and Remote Sensing, IEEE Transactions on*, vol. 47, pp. 2519-2527, 2009.

[16] A. T. Joseph, R. van der Velde, P. E. O'Neill, R. H. Lang, and T. Gish, "Soil moisture retrieval during a corn growth cycle using L-band (1.6 GHz) radar observations," *Geoscience and Remote Sensing, IEEE Transactions on*, vol. 46, pp. 2365-2374, 2008.

[17] R. D. De Roo, Y. Du, F. T. Ulaby, and M. C. Dobson, "A semi-empirical backscattering model at L-band and C-band for a soybean canopy with soil moisture inversion," *IEEE Transactions on Geoscience and Remote Sensing*, vol. 39, pp. 864-872, Apr 2001.

[18] Y.-C. Lin and K. Sarabandi, "Electromagnetic scattering model for a tree trunk above a tilted ground plane," *IEEE Transactions on Geoscience and Remote Sensing*, vol. 33, pp. 1063-1070, 1995.

[19] T. Senior, K. Sarabandi, and F. Ulaby, "Measuring and modeling the backscattering cross section of a leaf," *Radio Science*, vol. 22, pp. 1109-1116, 1987.

[20] K. Sarabandi, T. B. Senior, and F. Ulaby, "Effect of curvature on the backscattering from a leaf," *Journal of Electromagnetic Waves and Applications*, vol. 2, pp. 653-670, 1988.

[21] J. M. Stiles, K. Sarabandi, and F. T. Ulaby, "Microwave scattering model for grass blade structures," *IEEE transactions on geoscience and remote sensing*, vol. 31, pp. 1051-1059, 1993.

[22] V. L. Mironov, M. C. Dobson, V. H. Kaupp, S. A. Komarov, and V. N. Kleshchenko, "Generalized refractive mixing dielectric model for moist soils," *IEEE Transactions on Geoscience and Remote Sensing*, vol. 42, pp. 773-785, 2004.

[23] M. T. Hallikainen, F. T. Ulaby, M. C. Dobson, M. A. Elrayes, and L. K. Wu, "Microwave Dielectric Behavior of Wet Soil .1. Empirical-Models and Experimental-Observations," *IEEE Transactions on Geoscience and Remote Sensing*, vol. 23, pp. 25-34, 1985.

[24] C. Monfreda, N. Ramankutty, and J. A. Foley, "Farming the planet: 2. Geographic distribution of crop areas, yields, physiological types, and net primary production in the year 2000," *Global Biogeochemical Cycles*, vol. 22, Mar 1 2008.

[25] J. M. Stiles, K. Sarabandi, and F. T. Ulaby, "Electromagnetic scattering from grassland. II. Measurement and modeling results," *IEEE Transactions on Geoscience and Remote Sensing*, vol. 38, pp. 349-356, 2000.

[26] T. Chiu and K. Sarabandi, "Electromagnetic scattering interaction between a dielectric cylinder and a slightly rough surface," *IEEE Transactions on Antennas and Propagation*, vol. 47, pp. 902-913, 1999.

[27] A. Toure, K. P. B. Thomson, G. Edwards, R. J. Brown, and B. G. Brisco, "Adaptation of the Mimics Backscattering Model to the Agricultural Context - Wheat and Canola at L and C Bands," *IEEE Transactions on Geoscience and Remote Sensing*, vol. 32, pp. 47-61, Jan 1994.

[28] F. T. Ulaby, K. Sarabandi, K. Mcdonald, M. Whitt, and M. C. Dobson, "Michigan microwave canopy scattering model," *International Journal of Remote Sensing,* vol. 11, pp. 1223-1253, 1990.
[29] R. H. Lang and N. Khadr, "Effects of Backscattering Enhancement on Soil-Moisture Sensitivity," *International Space Year : Space Remote Sensing, Vols 1 and 2,* pp. 916-919, 1992.
[30] L. Tsang and J. A. Kong, *Scattering of electromagnetic waves: advanced topics* vol. 26: John Wiley & Sons, 2004.
[31] H. Huang, L. Tsang, E. G. Njoku, A. Colliander, K.-H. Ding, and T.-H. Liao, "Hybrid method combining generalized T matrix of single objects and Foldy-Lax equations in NMM3D microwave scattering in vegetation," in *2017 Progress in Electromagnetics Research Symposium-Fall (PIERS-FALL)*, 2017, pp. 3016-3023.
[32] S. W. Huang and L. Tsang, "Electromagnetic Scattering of Randomly Rough Soil Surfaces Based on Numerical Solutions of Maxwell Equations in Three-Dimensional Simulations Using a Hybrid UV/PBTG/SMCG Method," *IEEE Transactions on Geoscience and Remote Sensing,* vol. 50, pp. 4025-4035, Oct 2012.
[33] K. Sarabandi and T. Chiu, "Electromagnetic scattering from slightly rough surfaces with inhomogeneous dielectric profiles," *IEEE Transactions on Antennas and Propagation,* vol. 45, pp. 1419-1430, 1997.
[34] A. Colliander, T. Jackson, H. McNairn, S. Chazanoff, S. Dinardo, B. Latham, *et al.*, "Comparison of Airborne Passive and Active L-Band System (PALS) Brightness Temperature Measurements to SMOS Observations During the SMAP Validation Experiment 2012 (SMAPVEX12)," *IEEE Geoscience and Remote Sensing Letters,* vol. 12, pp. 801-805, Apr 2015.
[35] F. Marliani, S. Paloscia, P. Pampaloni, and J. A. Kong, "Simulating coherent backscattering from crops during the growing cycle," *IEEE Transactions on Geoscience and Remote Sensing,* vol. 40, pp. 162-177, 2002.
[36] S. H. Yueh, J. A. Kong, J. K. Jao, R. T. Shin, and T. Letoan, "Branching Model for Vegetation," *IEEE Transactions on Geoscience and Remote Sensing,* vol. 30, pp. 390-402, Mar 1992.
[37] T. Chiu and K. Sarabandi, "Electromagnetic scattering from short branching vegetation," *IEEE Transactions on Geoscience and Remote Sensing,* vol. 38, pp. 911-925, Mar 2000.
[38] N. Chauhan and R. Lang, "Radar backscattering from alfalfa canopy: a clump modelling approach," *International Journal of Remote Sensing,* vol. 20, pp. 2203-2220, 1999.
[39] L. Tsang, J. A. Kong, and K.-H. Ding, *Scattering of electromagnetic waves: theories and applications* vol. 27: John Wiley & Sons, 2004.
[40] K. Sarabandi and T. B. Senior, "Low-frequency scattering from cylindrical structures at oblique incidence," *IEEE Transactions on Geoscience and Remote Sensing,* vol. 28, pp. 879-885, 1990.
[41] J. M. Stiles and K. Sarabandi, "A scattering model for thin dielectric cylinders of arbitrary cross section and electrical length," *IEEE Transactions on Antennas and Propagation,* vol. 44, pp. 260-266, 1996.
[42] I.-S. Koh and K. Sarabandi, "A new approximate solution for scattering by thin dielectric disks of arbitrary size and shape," *IEEE transactions on antennas and propagation,* vol. 53, pp. 1920-1926, 2005.

[43] S. W. Huang, L. Tsang, E. G. Njoku, and K. S. Chan, "Backscattering Coefficients, Coherent Reflectivities, and Emissivities of Randomly Rough Soil Surfaces at L-Band for SMAP Applications Based on Numerical Solutions of Maxwell Equations in Three-Dimensional Simulations," *IEEE Transactions on Geoscience and Remote Sensing*, vol. 48, pp. 2557-2568, Jun 2010.

[44] S.-B. Kim, S. Huang, L. Tsang, J. Johnson, and E. Njoku, "Soil moisture retrieval over low-vegetation surfaces using time-series radar observations and a lookup table representation of forward scattering," in *Geoscience and Remote Sensing Symposium (IGARSS), 2011 IEEE International*, 2011, pp. 146-149.

[45] S. Hensley, K. Wheeler, G. Sadowy, C. Jones, S. Shaffer, H. Zebker, *et al.*, "The Uavsar Instrument: Description and First Results," *2008 IEEE Radar Conference, Vols. 1-4*, pp. 827-832, 2008.

[46] I. E. Mladenova, T. J. Jackson, R. Bindlish, and S. Hensley, "Incidence Angle Normalization of Radar Backscatter Data," *IEEE Transactions on Geoscience and Remote Sensing*, vol. 51, pp. 1791-1804, Mar 2013.

[47] T. L. Rowlandson, A. A. Berg, P. R. Bullock, E. R. Ojo, H. McNairn, G. Wiseman, *et al.*, "Evaluation of several calibration procedures for a portable soil moisture sensor," *Journal of Hydrology*, vol. 498, pp. 335-344, Aug 19 2013.

[48] M. H. Cosh, T. J. Jackson, R. Bindlish, J. S. Famiglietti, and D. Ryu, "Calibration of an impedance probe for estimation of surface soil water content over large regions," *Journal of Hydrology*, vol. 311, pp. 49-58, Sep 15 2005.

[49] F. T. Ulaby and M. A. El-Rayes, "Microwave dielectric spectrum of vegetation-Part II: Dual-dispersion model," *IEEE Transactions on Geoscience and Remote Sensing*, pp. 550-557, 1987.

[50] Y.-C. Lin and K. Sarabandi, "A Monte Carlo coherent scattering model for forest canopies using fractal-generated trees," *IEEE Transactions on Geoscience and Remote Sensing*, vol. 37, pp. 440-451, 1999.

[51] Y.-C. Lin and K. Sarabandi, "Retrieval of forest parameters using a fractal-based coherent scattering model and a genetic algorithm," *IEEE Transactions on Geoscience and Remote Sensing*, vol. 37, pp. 1415-1424, 1999.

[52] K. Sarabandi and Y.-C. Lin, "Simulation of interferometric SAR response for characterizing the scattering phase center statistics of forest canopies," *IEEE Transactions on Geoscience and Remote Sensing*, vol. 38, pp. 115-125, 2000.

[53] R. H. Lang and H. A. Saleh, "Microwave inversion of leaf area and inclination angle distributions from backscattered data," *IEEE transactions on geoscience and remote sensing*, pp. 685-694, 1985.

[54] F. Ulaby, R. Moore, and A. Fung, "Microwave remote sensing: Active and passive. Volume 2-Radar remote sensing and surface scattering and emission theory," 1982.

[55] Y. Du, Y. Luo, W.-Z. Yan, and J. A. Kong, "An electromagnetic scattering model for soybean canopy," *Progress In Electromagnetics Research*, vol. 79, pp. 209-223, 2008.

[56] E. Attema and F. T. Ulaby, "Vegetation modeled as a water cloud," *Radio science*, vol. 13, pp. 357-364, 1978.

[57] S. B. Kim, L. Tsang, J. T. Johnson, S. Huang, J. J. van Zyl, and E. G. Njoku, "Soil Moisture Retrieval Using Time-Series Radar Observations Over Bare Surfaces," *IEEE Transactions on Geoscience and Remote Sensing*, vol. 50, pp. 1853-1863, May 2012.

[58] T. Jackson and T. Schmugge, "Vegetation effects on the microwave emission of soils," *Remote Sensing of Environment,* vol. 36, pp. 203-212, 1991.
[59] A. Monerris and T. Schmugge, "Soil moisture estimation using L-band radiometry," in *Advances in Geoscience and Remote Sensing*, ed: InTech, 2009.
[60] Y. H. Kerr and E. G. Njoku, "A semiempirical model for interpreting microwave emission from semiarid land surfaces as seen from space," *Geoscience and Remote Sensing, IEEE Transactions on,* vol. 28, pp. 384-393, 1990.
[61] Y. Oh, K. Sarabandi, and F. T. Ulaby, "Semi-empirical model of the ensemble-averaged differential Mueller matrix for microwave backscattering from bare soil surfaces," *IEEE Transactions on Geoscience and Remote Sensing,* vol. 40, pp. 1348-1355, Jun 2002.
[62] J. D. Bolten, V. Lakshmi, and E. G. Njoku, "Soil moisture retrieval using the passive/active L- and S-band radar/radiometer," *IEEE Transactions on Geoscience and Remote Sensing,* vol. 41, pp. 2792-2801, Dec 2003.
[63] R. Bindlish, T. Jackson, R. J. Sun, M. Cosh, S. Yueh, and S. Dinardo, "Combined Passive and Active Microwave Observations of Soil Moisture During CLASIC," *IEEE Geoscience and Remote Sensing Letters,* vol. 6, pp. 644-648, Oct 2009.
[64] P. Ferrazzoli, G. Luzi, S. Paloscia, P. Pampaloni, G. Schiavon, and D. Solimini, "Comparison between the Microwave Emissivity and Backscatter Coefficient of Crops," *IEEE Transactions on Geoscience and Remote Sensing,* vol. 27, pp. 772-778, Nov 1989.
[65] L. Guerriero, P. Ferrazzoli, and R. Rahmoune, "A synergyc view of L-band active and passive remote sensing of vegetated soil," in *Microwave Radiometry and Remote Sensing of the Environment (MicroRad), 2012 12th Specialist Meeting on*, 2012, pp. 1-3.
[66] N. S. Chauhan and D. M. Levine, "Discrete Scatter Model for Microwave Radar and Radiometer Response to Corn - Comparison of Theory and Data," *IEEE Transactions on Geoscience and Remote Sensing,* vol. 32, pp. 416-426, Mar 1994.
[67] R. H. Lang, "Scattering from a layer of discrete random medium over a random interface: application to microwave backscattering from forests," *Waves in Random Media,* vol. 14, pp. S359-S391, Apr 2004.
[68] J. M. Stiles and K. Sarabandi, "Electromagnetic scattering from grassland Part I: A fully phase-coherent scattering model," *IEEE Transactions on Geoscience and Remote Sensing,* vol. 38, pp. 339-348, Jan 2000.
[69] E. G. Njoku and J. A. Kong, "Theory for Passive Microwave Remote-Sensing of near-Surface Soil-Moisture," *Transactions-American Geophysical Union,* vol. 58, pp. 554-554, 1977.
[70] A. Colliander, E. G. Njoku, T. Jackson, S. Chazanoff, H. McNairn, and P. J., "Retrieving Soil Moisture for Non-Forested Areas Using PALS Radiometer Measurements in SMAPVEX12 Field Campaign," *Submitted to Remote Sensing of Environment, in review*.
[71] T. Le Toan, F. Ribbes, L.-F. Wang, N. Floury, K.-H. Ding, J. A. Kong, *et al.*, "Rice crop mapping and monitoring using ERS-1 data based on experiment and modeling results," *IEEE Transactions on Geoscience and Remote Sensing,* vol. 35, pp. 41-56, 1997.
[72] L.-F. Wang, J. A. Kong, K. Ding, T. Le Toan, F. Ribbes, and N. Floury, "Electromagnetic scattering model for rice canopy based on Monte Carlo simulation," *Progress In Electromagnetics Research,* vol. 52, pp. 153-171, 2005.
[73] S. Tretyakov, *Analytical modeling in applied electromagnetics*: Artech House, 2003.

[74] S. K. Chan, R. Bindlish, P. E. O'Neill, E. Njoku, T. Jackson, A. Colliander, *et al.*, "Assessment of the SMAP passive soil moisture product," *IEEE Transactions on Geoscience and Remote Sensing,* vol. 54, pp. 4994-5007, 2016.

[75] J. G. Fleischman, S. Ayasli, E. M. Adams, and D. R. Gosselin, "Foliage penetration experiment .1. Foliage attenuation and backscatter analysis of SAR imagery," *IEEE Transactions on Aerospace and Electronic Systems,* vol. 32, pp. 135-144, Jan 1996.

[76] M. F. Toups, S. Ayasli, and J. G. Fleischman, "Foliage penetration experiment .2. Analysis of foliage-induced synthetic pattern distortions," *IEEE Transactions on Aerospace and Electronic Systems,* vol. 32, pp. 145-155, Jan 1996.

[77] P. Liang, L. E. Pierce, and M. Moghaddam, "Radiative transfer model for microwave bistatic scattering from forest canopies," *IEEE Transactions on Geoscience and Remote Sensing,* vol. 43, pp. 2470-2483, 2005.

[78] T-H Liao, S. Kim, S. Tan, L. Tsang, C. Su, and T. Jackson "Multiple Scattering Effects with Cyclical Corrections in Active Remote Sensing of Vegetated Surface Using Vector Radiative Transfer Theory," *IEEEE Journal of Selected Topics in Applied Earth Observations and Remote Sensing,* 2015.

[79] J. S. Lee and E. Pottier, "Polarimetric Radar Imaging: From Basics to Applications," *Polarimetric Radar Imaging: From Basics to Applications,* pp. 1-398, 2009.

[80] I. Hajnsek, T. Jagdhuber, H. Schcon, and K. P. Papathanassiou, "Potential of Estimating Soil Moisture Under Vegetation Cover by Means of PolSAR," *IEEE Transactions on Geoscience and Remote Sensing,* vol. 47, pp. 442-454, Feb 2009.

[81] T. Jagdhuber, I. Hajnsek, A. Bronstert, and K. P. Papathanassiou, "Soil Moisture Estimation Under Low Vegetation Cover Using a Multi-Angular Polarimetric Decomposition," *IEEE Transactions on Geoscience and Remote Sensing,* vol. 51, pp. 2201-2215, Apr 2013.

[82] A. H. Sihvola and J. A. Kong, "Effective Permittivity of Dielectric Mixtures," *IEEE Transactions on Geoscience and Remote Sensing,* vol. 26, pp. 420-429, Jul 1988.

[83] K. H. Ding, X. L. Xu, and L. Tsang, "Electromagnetic Scattering by Bicontinuous Random Microstructures With Discrete Permittivities," *IEEE Transactions on Geoscience and Remote Sensing,* vol. 48, pp. 3139-3151, Aug 2010.

[84] X. L. Xu, L. Tsang, and S. Yueh, "Electromagnetic Models of Co/Cross Polarization of Bicontinuous/DMRT in Radar Remote Sensing of Terrestrial Snow at X- and Ku-band for CoReH2O and SCLP Applications," *IEEE Journal of Selected Topics in Applied Earth Observations and Remote Sensing,* vol. 5, pp. 1024-1032, Jun 2012.

[85] K. Sarabandi, P. F. Polatin, and F. T. Ulaby, "Monte Carlo simulation of scattering from a layer of vertical cylinders," *IEEE transactions on antennas and propagation,* vol. 41, pp. 465-475, 1993.

[86] P. F. Polatin, K. Sarabandi, and F. T. Ulaby, "Monte-Carlo simulation of electromagnetic scattering from a heterogeneous two-component medium," *IEEE Transactions on Antennas and Propagation,* vol. 43, pp. 1048-1057, 1995.

[87] S. Chandrasekhar, "Radiative heat transfer," *Dover Publications, New York,* vol. 11, pp. 11-12, 1960.

[88] A. Ishimaru, *Wave propagation and scattering in random media* vol. 2: Academic press New York, 1978.

[89] U. Frisch, "Wave propagation in random media," Centre National de la Recherche Scientifique, Paris1970.

[90] B. Peterson and S. Strom, "T Matrix for Electromagnetic Scattering from an Arbitrary Number of Scatterers and Representations of E(3)," *Physical Review D,* vol. 8, pp. 3661-3678, 1973.
[91] L. Tsang, K. H. Ding, and C. E. Mandt, "Monte Carlo simulations of the extinction rate of dense media with randomly distributed dielectric spheres based on solution of Maxwell's equations," *Optics letters,* vol. 17, pp. 314-316, 1992.
[92] W. C. Gibson, *The method of moments in electromagnetics* vol. 1: Chapman & Hall/CRC London, UK, 2008.
[93] L. Tsang, J. A. Kong, K.-H. Ding, and C. O. Ao, *Scattering of electromagnetic waves: numerical simulations* vol. 25: John Wiley & Sons, 2004.
[94] L. Tsang, K.-H. Ding, G. Zhang, C. Hsu, and J. A. Kong, "Backscattering enhancement and clustering effects of randomly distributed dielectric cylinders overlying a dielectric half space based on Monte-Carlo simulations," *IEEE Transactions on Antennas and Propagation,* vol. 43, pp. 488-499, 1995.
[95] S. H. Yueh, S. J. Dinardo, A. Akgiray, R. West, D. W. Cline, and K. Elder, "Airborne Ku-band polarimetric radar remote sensing of terrestrial snow cover," *IEEE Transactions on Geoscience and Remote Sensing,* vol. 47, pp. 3347-3364, 2009.
[96] L. Zhu, J. P. Walker, L. Tsang, H. Huang, N. Ye, and C. Rüdiger, "Soil moisture retrieval from time series multi-angular radar data using a dry down constraint," *Remote Sensing of Environment,* vol. 231, p. 111237, 2019.
[97] K. Goïta, A. E. Walker, and B. E. Goodison, "Algorithm development for the estimation of snow water equivalent in the boreal forest using passive microwave data," *International Journal of Remote Sensing,* vol. 24, pp. 1097-1102, 2003.
[98] J. Zheng, Y. Wang, and N. L. Nihan, "Quantitative evaluation of GPS performance under forest canopies," in *Proceedings. 2005 IEEE Networking, Sensing and Control, 2005.*, 2005, pp. 777-782.
[99] Y. Oh, Y.-M. Jang, and K. Sarabandi, "Full-wave analysis of microwave scattering from short vegetation: An investigation on the effect of multiple scattering," *IEEE transactions on geoscience and remote sensing,* vol. 40, pp. 2522-2526, 2002.
[100] A. Lopes and E. Mougin, "Microwave coherent propagation in cylindrical-shaped forest components: interpretation of attenuation observations," *IEEE Transactions on Geoscience and Remote Sensing,* vol. 28, pp. 315-324, 1990.
[101] S.-B. Kim, H. Huang, T.-H. Liao, and A. Colliander, "Estimating vegetation water content and soil surface roughness using physical models of L-band radar scattering for soil moisture retrieval," *Remote Sensing,* vol. 10, p. 556, 2018.
[102] C. Flammer, *Spheroidal wave functions*: Courier Corporation, 2014.
[103] S. Zhang, J. Jin, and R. E. Crandall, "Computation of special functions," *American Journal of Physics,* vol. 65, pp. 355-355, 1997.
[104] L.-W. Li, X.-K. Kang, and M.-S. Leong, *Spheroidal wave functions in electromagnetic theory*: Wiley Online Library, 2002.
[105] A. R. Edmonds, *Angular momentum in quantum mechanics* vol. 4: Princeton university press, 1996.
[106] S. Asano and G. Yamamoto, "Light scattering by a spheroidal particle," *Applied optics,* vol. 14, pp. 29-49, 1975.